Electron, ion and neutral heating in hollow cathode plasma thrusters

Scott James Doyle

Doctor of Philosophy

University of York

Physics

September 2019

Abstract

As the space community moves towards deploying greater numbers of ever smaller satellite platforms, the development of miniaturised, low power micro-propulsion sources is essential. Power and space limitations restrict the use of Hall effect and gridded ion thrusters, commonly employed on larger satellites, while the volatile and toxic hydrazine propellant employed in traditional cold-gas and monopropellant thrusters pose concerns for large-scale commercial applicability. In response to this, a growing number of novel approaches to electric spacecraft propulsion are being developed for a variety of space missions. Among these, radio-frequency (rf), electrothermal plasma thrusters are of specific interest as they enable efficient volumetric neutral gas heating, while maintaining charge neutral operation. Understanding the mechanisms whereby electrical power is coupled into the electron, ion and neutral species for these conditions is crucial for optimising the performance and range of application of these thrusters.

This thesis demonstrates the capability to control the particle heating mechanisms in hollow cathode rf electrothermal micropropulsion sources via the application of multi-harmonic 'tailored' voltage waveforms. Modulation of the electrical asymmetry of such waveforms, through varying the phase offset between successive harmonics, results in a direct variation of the phase-resolved sheath dynamics. This enables the preferential deposition of power into either electrons or ion species, selectively enhancing the ionisation rate or neutral gas heating efficiency, respectively. Further, by considering the neutral depletion arising from neutral gas heating, this work predicts the formation of collisionless ion populations within otherwise collisional plasmas. These outcomes are achieved in tandem through the use of 2D fluid/Monte-Carlo numerical simulations with comparison to experimental measurements of the lab-based prototype *Pocket Rocket* hollow cathode microthruster. Application of these electrical control schemes to plasma sources for spacecraft propulsion enables the prospect of variable thrust and variable specific impulse operation, significantly increasing the in-mission versatility of electric thrusters.

Contents

List of Tables

List of Figures

Symbols and Abbreviations

Symbol	Description
PR	*Pocket Rocket*,
	Al_2O_3, Internal Diameter = 2.1 mm
Mini-PR	Miniature *Pocket Rocket*,
	Al_2O_3, Internal Diameter = 1.0 mm
FFT	Fast Fourier Transform
CCP	Capacitively Coupled Plasma
ICP	Inductively Coupled Plasma
EAE	Electrical Asymmetry Effect
HCE	Hollow Cathode Effect
EEDF	Electron Energy Distribution Function
IEDF	Ion Energy Distribution Function
HPEM	Hybrid Plasma Equipment Model
FKPM	Fluid Kinetic Poisson Module
EETM	Electron Energy Transport Module
PCMCM	Plasma Chemistry Monte-Carlo Module
R_{bulk}	Ohmic resistance of plasma bulk
L_{bulk}	Inductance of plasma bulk
R_{sheath}	Ohmic resistance of plasma sheath
C_{sheath}	Capacitance of plasma sheath
A_p	Powered electrode(s) area in contact with plasma
A_g	Grounded electrode(s) area in contact with plasma
V_{pp}	Peak-to-peak radio-frequency voltage, $V_{pp} = \lvert\phi^+_{rf}\rvert + \lvert\phi^-_{rf}\rvert$
I_{rf}	Peak-to-peak radio-frequency current
J_p	Plasma current density
∇_x	Spatial derivative operator, $\nabla_x = (\frac{d}{dx}, \frac{d}{dy}, \frac{d}{dz})$
∇_v	Velocity derivative operator, $\nabla_v = (\frac{d}{dv_x}, \frac{d}{dv_y}, \frac{d}{dv_z})$
π	Circle constant, 3.14159265359...
exp	Exponential function, Euler's number = 2.7182818284...
k_b	Boltzmann constant, $1.38064852 \times 10^{-23}$ [m^2 kg s^{-2} K^{-1}]

N_A	Avogadro's constant, $6.02214086 \times 10^{23}$ [mol^{-1}]
c	Speed of light in vacuum, 2.99792458×10^{8} [m s^{-1}]
e	Elementary charge, $1.60217662 \times 10^{-19}$ [C]
ϵ_0	Vacuum permittivity, $8.854187817 \times 10^{-12}$ [F m^{-1}]
μ_0	Vacuum permeability, $4\pi \times 10^{-7}$ [H m^{-1}]
κ_{th}	Bulk thermal conductivity:
	Al_2O_3, 0.18 [$\text{W cm}^{-1}\ \text{K}^{-1}$]
	Macor, 0.015 W cm^{-1} [K^{-1}]
	Aluminium Metal, 2.5 [$\text{W cm}^{-1}\ \text{K}^{-1}$]
	Copper Metal, 4.0 [$\text{W cm}^{-1}\ \text{K}^{-1}$]
	Gas Phase Species, 0.0 [$\text{W cm}^{-1}\ \text{K}^{-1}$]
c_i	Specific heat capacity:
	Argon, 0.52 [$\text{J g}^{-1}\ \text{K}^{-1}$]
α_{tac}	Thermal accommodation coefficient:
	Argon, 0.9
	Al_2O_3, 0.4
	Macor, 0.4
α_{tma}	Tangential momentum accommodation coefficient:
	Argon, 0.95
σ_c	Bulk electrical conductivity:
	Al_2O_3, [$1 \times 10^{-14}\ \Omega^{-1}\ \text{cm}^{-1}$]
	Macor, [$1 \times 10^{-17}\ \Omega^{-1}\ \text{cm}^{-1}$]
	Conducting Metals, [$5 \times 10^{7}\ \Omega^{-1}\ \text{cm}^{-1}$]
ϵ_r	Relative permittivity or dielectric constant:
	Al_2O_3, 9.8
	Macor, 5.8
	Conducting Metals, 1.0
	Gas Phase Species, 1.0
γ_s	Energy independent secondary electron emission coefficient:
	Al_2O_3, 0.2
	Conducting Metals, 0.0
$\mathbf{E}$	Electric field vector potential
$\mathbf{B}$	Magnetic field vector potential
$\mathbf{v}$	3D velocity vector, (v_x,v_y,v_z)
$\mathbf{x}$	3D Cartesian vector, (x,y,z)
ϕ	Arbitrary electric potential
ϕ_{rf} or $\phi_{rf}(\tau)$	Radio-frequency voltage waveform amplitude
ϕ_{rf}^{+}	Positive amplitude of radio-frequency voltage

ϕ_{rf}^{-}	Negative amplitude of radio-frequency voltage
ϕ_k	Voltage amplitude of k'th harmonic component
ϕ_{fp}	Phase-averaged floating potential
ϕ_S	Phase-averaged sheath potential
ϕ_{dc}	Phase-averaged DC surface potential
η_{dc}	Phase-averaged DC self-bias voltage
ν	Arbitrary frequency
ν_{rf}	Applied voltage frequency
ω_{rf}	Applied angular radio-frequency, $\omega_{rf} = 2\pi\nu_{rf}$
τ_{rf}	Radio-frequency phase cycle, $\tau_{rf} = {}^{1}/_{\nu_{rf}}$
$S_x(\tau)$	Phase-resolved sheath edge location, (radial or axial)
S_x	Phase-averaged sheath extent, (radial or axial)
τ_i	Ion transit time through sheath
n	Number of applied harmonics, fundamental harmonic n = 0
k	Frequency harmonic number, normalised to fundamental harmonic
θ_k	Phase offset of k'th harmonic relative to fundamental harmonic
θ	Phase offset of highest harmonic relative to fundamental harmonic
ϵ_s	EAE symmetry parameter
ω_{pe}	Electron plasma frequency
ω_{pi}	Ion plasma frequency
δ_s	Skin Depth
λ_D	Debye Length
v_B	Bohm Velocity
c_s	Speed of sound
k_n	Knudsen number
L	Characteristic distance, relevant to flow
S_y	Sputtering yield
μ_e	Electron mobility
μ_i	Ion mobility
D_e	Electron Diffusion Coefficient
D_i	Ion Diffusion Coefficient
v_e	Electron drift velocity
v_i	Ion drift velocity
λ_{mfp}	Collisional mean-free-path
$\sigma(\epsilon)$	Energy resolved collision cross-section
ν_{coll}	Collision frequency
k_{ij}	Collision rate coefficient between species i and j
k_{ei}	Elastic energy loss rate coefficient for species i

$k_{ei,L}$	Inelastic energy rate loss coefficient for species i
ΔH	Change in enthalpy
$\bar{\bar{v}}_i$	Viscosity tensor for species i
$A_{Arr,i}$	Arrenhius coefficient for species i
α_i	Activation energy for species i
R_i	Reaction rate for species i
S_i	Source function for species i
ι_{tot}	Total ionisation rate
ι_α	Ionisation rate from α-mode heating mechanisms
ι_γ	Ionisation rate from γ-mode heating mechanisms
P_e	Deposited radio-frequency power into electrons
P_i	Deposited radio-frequency power into ions
P_{rf}	Total deposited radio-frequency power
η_{th}	Thermal efficiency of power transfer between species
ϵ	Scalar energy of given particle or transition
$f(v)$	Maxwellian ion velocity distribution function
$f(\epsilon)$	Maxwellian ion energy distribution function
$f_e(\epsilon)$	Maxwellian electron energy distribution function
$f_g(\epsilon)$	Gaussian ion energy distribution function
$\langle v_s \rangle$ or $\hat{v}_s$	Mean velocity of species s
$\langle \epsilon_s \rangle$ or $\hat{\epsilon}_s$	Mean energy of species s
A_i	Spontaneous emission coefficient for level i
A_{ik}	Transition coefficient from level i to k
A_{ic}	Cascade transition coefficient for level i
τ_{eff}	Effective lifetime of particle in state i
g_{ik}	Optical escape factor
k_q	Quenching coefficient
$E_{i,0}$	Electron impact ionisation function from ground to level i
$E_{m,i}$	Electron impact ionisation function from metastable level m to level i
m	Arbitrary mass
m_s	Mass of species s
M_s	Molar mass of species s
m_e	Electron rest mass, $m_e = 9.10938356 \times 10^{-31}$
m_i	Ion species mass
m_g	Gas phase species mass
ρ_s	Density of species s
Q_x	Absolute surface charge of surface x
q_i	Absolute charge of ion species

Z_i	Specific charge of ion species
Γ_e	Electron flux
Γ_i	Ion species flux
T_e	Electron Temperature
T_i	Ion species Temperature
T_g	Neutral Gas Temperature
ΔT_g	Change in gas temperature from 325 K
n_e	Plasma (electron) number density
n_i	Ion species number density
n_{eff}	Effective positive ion number density, $n_{eff} = (n_{i^+}\text{-}n_{i^-})$
n_g	Neutral gas species number density
n_{ph}	Photon number density
ρ	Space charge density, $\rho = n_i$ - n_e
m_0	Spacecraft initial mass (pre-burn)
m_f	Spacecraft final mass (post-burn)
R_f	Spacecraft payload to propellant ratio, $R_f = {}^{m_f}/_{m_0}$
$\dot{m}$	Mass flow rate of propellant
v_e	Exhaust velocity of propellant
a	Rate of acceleration
$g_\oplus$	Gravitational acceleration on Earth at sea-level
F_T	Gross thrust force
ΔF_T	Net thrust force
I_m	Total impulse
I_{sp}	Specific Impulse
Δv	Change in velocity
P	Arbitrary Pressure
P_z	Pressure at thrust plane
P_0	Expansion chamber base pressure
d or x	Arbitrary distance

Acknowledgments

Firstly, I thank my supervisors James Dedrick and Deborah O'Connell for keeping me on track despite my habit of becoming fixated on new and shiny ideas. I wish to thank James Dedrick in particular for his ceaseless (and often-times worrying) attention to detail and for many hours of discussions, not just related to my research but to all aspects of life and academia.

I wish to acknowledge all fellow Ph.D. students here at York, special mentions include: Dave Shaw, who having known me for approximately 6 years is still willing to make polite conversation, Dave Meehan for his conference companionship and no nonsense approach to life, James Ellis for his spontaneous and rewarding hugs and Greg Smith for his office decoration skills and taste in hats. I would also like to express my sincerest gratitude to Andrew Gibson, who's gentle nature and endless knowledge have made my Ph.D. far more enjoyable and fruitful.

I am indebted to the entirety of the support staff at the York Plasma Institute, with special thanks to Ruth Lowman and Kathryn Harvey for helping to organize the plethora of trains, flights, hotels and buffets that keep academic life moving. Donna Cook for her straightforward and principled approach to financial matters, despite the often unusual requests placed upon her. Richard Armitage, Adam Stroughair, Mark Laughton and Kari Niemi for their invaluable assistance in setting up and maintaining the *Pocket Rocket* plasma source, without which this thesis would be significantly shorter. Finally I wish to thank Peter Hill for much needed technical support and for letting me multi-class as a sorcerer-warlock.

In addition to the staff and students at York, I wish to thank my international collaborators. Christine Charles and Rod Boswell for allowing me to visit their labs and encouraging me to 'leap before looking' from time to time. Mark Kushner for allowing me the use of his HPEM code and for his dispiritingly efficient work ethic, of which I wish to emulate. Finally I would like to thank Gregory Daly for his ongoing support and interest in my work.

I would also like to thank my parents and grandparents for their support over the decade I have spent in further education. Last but not least I would like to thank my extraordinary partner, Issy, for her love and patience (mostly patience) with the writing process and for her ongoing support in all matters.

Declaration

This thesis has not previously been accepted for any degree and is not being concurrently submitted in candidature for any degree other than Doctor of Philosophy of the University of York. This thesis is the result of my own investigations, except where otherwise stated. All other sources are acknowledged by explicit references.

All numerical simulations were initialised, run and analysed by the author utilizing the hybrid plasma equipment model (HPEM) code, provided by Prof. Mark Kushner of the university of Michigan, US. Experiments were carried out at the university of York plasma propulsion laboratory, the laboratory was set-up and furnished with help from Mr Richard Armitage, Mr Adam Stroughair and Mr Mark Laughton and the author. The Pocket Rocket source was conceived and designed by Prof. Christine Charles and the York prototype was constructed in-house by Mr Jason Flatt. The experimental apparatus for the phase resolved optical emission spectroscopy was set-up and the data was recorded, analyzed and interpreted by the author only. The Solayl current voltage probes were calibrated by Solayl and operated by the author.

The work presented herein was funded by the Engineering and Physical Sciences Research Council (EPSRC), grant reference number: EP/m508196/1.

Publications and Conference Contributions

This thesis has resulted in a number of publications in peer reviewed journals. In addition, a subset of the results discussed in this thesis have been presented at scientific conferences.

Publications:

- *"Decoupling ion energy and flux in intermediate pressure plasmas utilizing tailored voltage waveforms"*
  S. J. Doyle, A. R. Gibson, R. W. Boswell, C. Charles and J. P. Dedrick
  Plasma Sources Sci. Technol., In Preparation. (2020)

- *"Efficient low-frequency ionization and plasma heating in a radio frequency electrothermal microthruster"*
  S. Leigh, **S. J. Doyle**, G. Smith, A. R. Gibson, R. W. Boswell, C. Charles and J. P. Dedrick.
  Plasma Sources Sci. Technol., In Review. (2020)

- *"Characterisation and control of an ion-acoustic plasma instability downstream of a diverging magnetic nozzle"*
  S. J. Doyle, A. Bennet, D. Tsifakis, J. P. Dedrick, R. W. Boswell, and C. Charles
  Frontiers in Physics, In Review. (2020)

- *"Inducing locally structured ion energy distributions in intermediate-pressure plasmas"*
  S. J. Doyle, A. R. Gibson, R. W. Boswell, C. Charles, M. J. Kushner and J. P. Dedrick
  Physics of Plasmas, vol. **26**, Issue. **7**, 073519, (2019)

- *"Disrupting the spatio-temporal symmetry of electron heating in atmospheric pressure plasmas"*
  A. R. Gibson, Z. Donkó, L. Alelyani, L. Bischoff, G. Hübner, J. Bredin, **S. J. Doyle**, I. Korolov, K. Niemi and T. Mussenbrock
  Plasma Sources Sci. Technol., vol. **28**, 01LT01, (2019)

- *"Control of electron, ion and neutral heating in a radio-frequency electrothermal microthruster via dual-frequency voltage waveforms"*
  S. J. Doyle, A. R. Gibson, R. W. Boswell, C. Charles and J. P. Dedrick
  Plasma Sources Sci. Technol., vol. **28**, 035019, (2019)

- *"Spatio-temporal plasma heating mechanisms in a radio-frequency electrothermal microthruster"*
  S. J. Doyle, A. R. Gibson, J. Flatt, T. S. Ho, R. W. Boswell, C. Charles, P. Tian, M. J. Kushner and J. P. Dedrick
  Plasma Sources Sci. Technol., vol. **27**, 085011, (2018)

- *"Enhanced control of the ionization rate in ratio-frequency plasmas with structured electrodes via tailored voltage waveforms"*
  S. J. Doyle, T. Lafleur, A. R. Gibson, P. Tian, M. J. Kushner and J. P. Dedrick
  Plasma Sources Sci. Technol., vol. **26**, p. 125005, (2017)

Conference proceedings:

- *"Lab to Launch"*
  C. Charles, D. Tsifakisa, A. Bennet, R. W. Boswell, W. Braun, J. Rivas-Davila, K. Takahashi, A. Ando, E. Dudas, A. Benidar, R. Georges, **S. J. Doyle**, J. P. Dedrick, F. Filleul, J. Cater and N. Rattenbury.
  70th International Astronautical Congress: **IAC-19-C4.4.1**, (2019)

- *"Spatially resolved plasma power deposition in a radio-frequency electrothermal microthruster"*
  S. J. Doyle, A. R. Gibson, R. W. Boswell, C. Charles, M. J. Kushner and J. P. Dedrick
  Association Aéronautique et Astronautique de France, **SP2018**, p. 00451, (2018)

Conference presentations:

- *"Control of ion energy distribution functions in intermediate pressure plasmas"*
  - Student Excellence Award Recipient 2019
  46th Gaseous Electronics Conference (GEC)
  College Station, US, Nov 2019

- *"Characterization of beam-plasma instability downstream of a divergent magnetic nozzle"*
  46th IOP Plasma Physics Conference (PPC)
  Loughborough, UK, April 2019

- *"Inducing localised beam-like ion energy distribution functions in intermediate-pressure plasmas"*
  1st York Computational Plasma Physics Workshop
  York, UK, March 2019

- *"Enhanced control of ionisation rate and IEDFs in structured rf-CCPs via dual-frequency voltage waveforms"*
  4th York Plasma Institute Industrial Plasmas Workshop
  York, UK, March 2019

- *"Control of electron, ion and neutral dynamics in radio-frequency electrothermal microthrusters"*
  16th Technological Plasma Workshop, (TPW)
  Coventry, UK, October 2018

- *"Spatial control of power deposition in radio-frequency electrothermal micro-thrusters via tailored voltage waveforms"*
  24th Europhysics Conference on Atomic and Molecular Physics of Ionized Gases (ESCAMPIG)
  Glasgow, UK, July. 2018

- *"Spatially resolved plasma power deposition in a radio-frequency electothermal microthruster"*
  6th Association Aéronautique et Astronautique de France Space Propulsion Conference (3AF)
  Seville, Spain, May 2018

- *"Spatio-temporal plasma heating mechanisms in a radio-frequency electrothermal microthruster"*
  45th IOP Plasma Physics Conference (PPC)
  Belfast, UK, April 2018

- *"Phase resolved optical emission from a radio-frequency electrothermal microthruster"*
  20th Workshop on the Exploration of Low-Temperature Plasma Physics (WELTPP)
  WELTPP, Netherlands, December 2017

- *"Enhanced control of the ionization rate in radio-frequency plasmas with structured electrodes via tailored voltage waveforms"*
  1st IOP Conference on Computational Plasma Physics (CPPC)
  York, UK, November 2017

- *"Enhanced control of the ionization rate in radio-frequency plasmas with structured electrodes via tailored voltage waveforms"*
  15th Technological Plasma Workshop, (TPW)
  Coventry, UK, October 2017

- *"The effect of tailored voltage waveforms on neutral gas heating in a radio-frequency driven electrothermal microthruster"*
  69th Gaseous Electronics Conference, (GEC)
  Bochum, Germany, October 2016

Chapter 1

Introduction

This research project was motivated by a prospective performance enhancement of the *Pocket Rocket* hollow cathode microthruster, a novel radio-frequency plasma propulsion system designed for use on microsatellites. Through the application of multi-frequency voltage waveforms an enhanced degree of control is achieved over the behaviour and energies of particles within the plasma. This control is employed to facilitate variable thrust and thermal efficiency operation. Investigating the mechanisms by which this control is afforded and the influence gained over plasma properties relevant to electrothermal propulsion forms the central theme of this thesis. As such, is it useful to begin with the fundamentals of rocketry, focusing on electric propulsion systems in particular (sections 1.1 and 1.2), following on to a brief consideration of microsatellites (section 1.3), and finishing with an introduction to the relevant plasma theory (section 1.4).

1.1 Introduction to Rocketry

Hero of Alexandria (*c.* 67 AD) is often credited with the development of the first device making use of the reaction principle[1]. Employing the law that every action has an equal an opposite reaction, his *aeolipile* utilized directed jets of steam to provide motion some 1600 years before Newton's birth. The Chinese continued to develop rockets as fireworks and weapons (*c.* 1000 AD), but the mathematical principles of rocketry were not understood until 1903 when a Russian school teacher named Konstantin Tsiolkovsky laid down what has become known as the rocket equation[2]. This equation states that in order to achieve an acceleration a rocket must expel mass, i.e. a rocket in free flight can accelerate in a positively defined direction by expelling mass in a negatively defined direction. The rocket equation (Eq. 1.4) can be readily derived by first considering the momentum imparted by an expelled mass of propellant m, at a velocity v_e:

$$F_T = \frac{d(mv_e)}{dt} = m\frac{dv_e}{dt} + v_e\frac{dm}{dt} \tag{1.1}$$

and therefore:

$$F_T = ma + v_e\dot{m} \tag{1.2}$$

Where the thrust, F_T, denotes force exerted by the escaping propellant, a denotes acceleration of the spacecraft and $\dot{m}$ denotes the mass loss rate from the spacecraft. For terrestrial vehicles this equation simplifies down to Newton's second law as the change in mass with time is negligible. However, for space vehicles this term remains significant, owing to their high propellant to mass ratio. The change in velocity can be obtained by rearranging equation 1.2 for the acceleration of the spacecraft and performing an integration between an initial mass of m_0 and a final mass m_f while assuming a constant exhaust velocity[3], as shown in equation 1.3:

$$\int \frac{dv}{dt} = -v_e \int_{m_0}^{m_f} \dot{m}\ \frac{1}{m}\ dm \tag{1.3}$$

the result of which yields the rocket equation:

$$\Delta v = v_e\ ln\left(\frac{m_0}{m_f}\right) \tag{1.4}$$

Here, Δv represents the total change in velocity of the spacecraft after a 'burn' of propellant of mass $m = (m_0 - m_f)$. In orbital mechanics, the radius of an object's orbit is defined primarily by its velocity relative to the object that it is orbiting. Therefore, a natural parameter to quote when transferring between orbits is the change in velocity Δv that would be required. Often, the rocket equation is employed in the form expressed in equation 1.5,

representing the initial mass of fuel required for a fixed Δv:

$$\frac{m_f}{m_0} = exp\left\{\frac{\Delta v}{v_e}\right\} \tag{1.5}$$

Here, the importance of the exit velocity becomes apparent as it can be seen that for a fixed Δv requirement, the mass of propellant required can be exponentially reduced if the exhaust velocity is increased. To illustrate this, equation 1.5 has been plotted in figure 1.1 for exit velocities in the range 1 - 16 kms^{-1}.

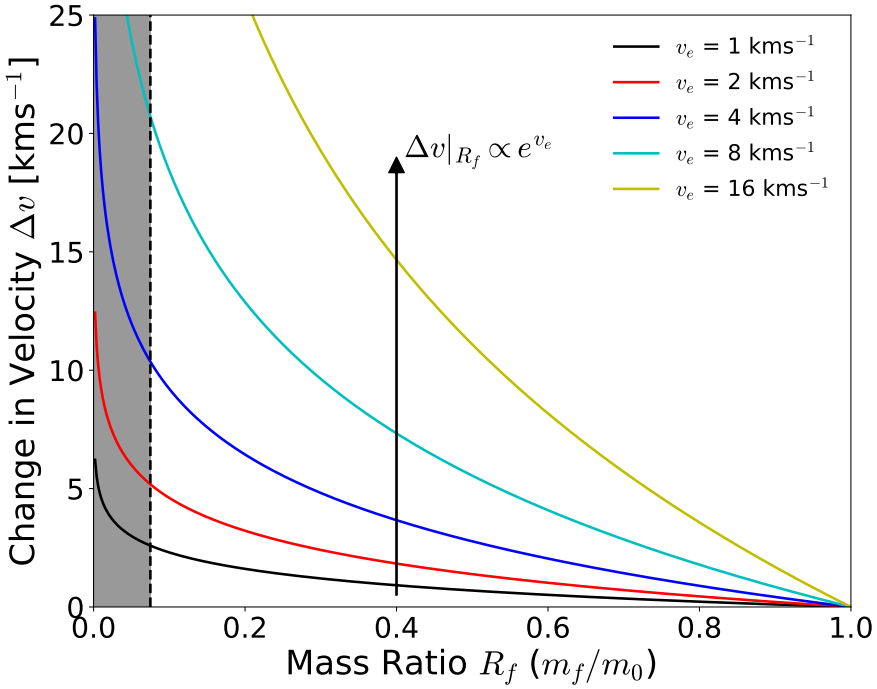

Figure 1.1: Change in velocity Δv achieved for varying craft mass ratio ($R_f = {}^{m_f}/_{m_0}$) at exhaust velocities between 1 - 16 kms^{-1}. The vertical dashed line indicates the engineering limit for propellant mass ratios, while the solid arrow denotes the transition between isotachs for a fixed mass ratio.

Increasing the Δv available for a given spacecraft requires either that more of the spacecraft mass consists of propellant, or that that propellant leaves the spacecraft with a higher exhaust velocity. Increasing the mass ratio increases the velocity gained along an isotach, a line of constant exhaust velocity. However, engineering limits place the lower end of the mass ratio at between 0.05 - 0.1, marked by the dashed line, at which point almost all of the spacecraft mass is propellant[3]. For a fixed mass ratio, increasing the exhaust velocity allows the movement between isotachs, providing a greater Δv for the same mass of propellant used. Examples of typical Δv requirements: stationkeeping in low Earth orbit (LEO) ranges from 7 - 100 ms^{-1} year^{-1}, while a transit from LEO to low lunar orbit is $\approx$ 6 kms^{-1}, thrust dependant[4]. An increased exhaust velocity either permits longer lifetimes in orbit for missions with a fixed propellant mass, or reduces the propellant needed for missions with a

fixed Δv requirement.

The efficiency of propellant can also discussed in terms of the specific impulse, I_{sp}, defined as effective exit velocity per unit weight (on Earth) of propellant, as shown in equation 1.6:

$$I_{sp} = \frac{v_e}{g_\oplus} = \frac{I_m}{\dot{m} g_\oplus} \tag{1.6}$$

Where the specific impulse relates to the thrust via the propellant flow rate:

$$F_T = v_e \dot{m} = g_\oplus I_{sp} \dot{m} \tag{1.7}$$

Here, $g_\oplus$ is acceleration due to gravity at sea-level on Earth and I_m is the impulse produced by a propellant mass-flow rate of $\dot{m}$. Measured in units of seconds, the specific impulse nominally describes the length of time that a propulsion system can continue to accelerate it's own initial mass at 1 g. This is perhaps most clearly shown in equation 1.7 where a higher specific impulse enables the same net thrust for a reduced propellant mass flow rate. A higher specific impulse therefore represents a more efficient use of propellant, achieving higher a Δv with the same initial propellant mass. This property makes the specific impulse a useful metric when comparing different methods of propulsion or when employing different molecular mass propellants.

1.2 Methods of Propulsion

A wide array of spacecraft propulsion sources are employed on modern space vehicles, ranging from cold-gas and chemical to electric in nature[3,4]. However, irrespective of the physical mechanism employed, the end goal of a propulsion source is to produce a high velocity and preferably also high mass propellant stream. This section introduces and contrasts traditional chemical propulsion techniques against the most common electrical techniques.

1.2.1 Chemical and Cold-Gas Propulsion

Traditional propulsion sources, such as mono-propellant and bi-propellant chemical thrusters, employ reactive propellants in which the energy provided for heating is contained within the propellant itself[5]. Mono-propellant or 'cold-gas' thrusters make use of a pressurized container of a single propellant, often hydrazine or hydrogen peroxide[6,7], which decomposes and heats when passed over a catalyst. Since the temperature of this propellant is low, the propellant efficiency achievable by such thrusters is limited. The low specific impulses are offset by the simplicity, reliability and inexpensiveness of cold-gas systems. Bi-propellant chemical thrusters employ separate fuel and oxidiser components, often liquid hydrogen or kerosene and liquid oxygen, respectively[3]. The flexibility and tunability afforded by variable propellant configurations enables the generation of higher thrusts and specific impulses as compared to cold-gas thrusters, at the expense of increased cost and complexity.

Regardless of the method utilized, all chemical thrusters achieve heating of the propellant through collisional processes, where the heating power is supplied via the stored chemical potential energy. In a collisional system, the mean velocity $\langle v \rangle$ of a given propellant species with mass m_g can be described in terms of the first moment of the velocity distribution, shown in equation 1.8:

$$\langle v \rangle = \int_0^\infty v f(v) dv = \sqrt{\frac{8 k_b T_g}{\pi m_g}} \approx v_e \tag{1.8}$$

Here, T_g is the effective temperature of the gas species, k_b is Boltzmann's constant and $f(v)$ describes the particle velocity distribution function. While the majority of collisional systems can generally be assumed to have a Maxwellian velocity distribution, see equation 1.26, the exact distribution of any given species is subject to operational parameters such as particle densities, local pressure gradients and the supplied heating power[8,9]. Assuming a Maxwellian velocity distribution, the mean particle velocity in equation 1.8 increases with the square root of the gas temperature for a fixed propellant species mass. Therefore, recalling equation 1.5 and approximating $v_e = \langle v \rangle$, the achievable delta v and specific impulse scale as $\Delta v \propto e^{\sqrt{T_g/m_g}}$ and $I_{sp} \propto \sqrt{T_g/m_g}$, respectively, for thrusters employing a thermalised propellant, irrespective of the method of heating.

This reliance on the neutral gas temperature, coupled with the internal energy storage, sets fundamental propellant efficiency limits for traditional cold gas and chemical propulsion systems[3]. This limit can be defined in terms of the ratio between the specific enthalpy and specific heat capacity of the chosen propellant mixture. Lower molecular mass propellants achieve higher temperatures for the same specific enthalpy, and can therefore achieve higher specific impulses at the expense of a reduced thrust force. Ultimately however, for any propellant there is a maximum change in temperature achievable per mass of said propellant, setting a theoretical upper limit for the average particle velocity, and hence specific impulse, for chemical thrusters.

Achieving higher specific impulses requires externally supplying the heating power, effectively decoupling the source of the propellant heating from the properties of propellant itself. While this confers several benefits such as a wider choice of propellants and the capability to discretely vary the external heating power, it introduces the problem of how to couple the externally supplied power into the propellant. Fundamentally, power is typically supplied through either nuclear or electrical means, the latter of which forms the focus of this work. Most nuclear propulsion techniques couple heat convectively, the propellant effectively acting as the coolant for the fissile fuel rods[3], as such the gas heating and specific impulse limits are set by the melting temperature of the fissionable material. While possessing the highest energy density of the techniques discussed, nuclear propulsion employs large, dangerous and expensive components, the discussion of which is outside the scope of this thesis. Electric propulsion couples electrical energy into the propellant, heating it either through direct or indirect ohmic dissipation, or through directly accelerating charged particles through interactions with electromagnetic fields[4,5]. The remainder of this section introduces each of these approaches individually, providing an overview of the advantages and disadvantages of each approach.

1.2.2 Electric Propulsion

The concept of electric propulsion (EP) has been the topic of discussion and research for over 100 years, with the first recorded mentions of employing electricity for the generation of thrust being attributed to Tsiolkovsky in 1911[3]. The first device created for the explicit purpose of accelerating charged particles for propulsion purposes is attributed to R. H. Goddard, when in 1917 he filed a U.S. patent entitled *"Method of and Means for Producing Electrified Jets of Gas"*, detailing the worlds first electrostatic ion accelerator. The first EP system deployed in space saw use aboard the Soviet Zond 2 spacecraft. Launched in 1964, the satellite employed a pulsed plasma thruster (PPT), the operation of which involves utilizing a high current electrical discharge to ablate and subsequently accelerates propellant from a solid bar of Teflon[10]. In the decades since its first deployment, interest in the development of EP systems has increased substantially. Primarily driven by the requirement for more

efficient station keeping and the capability to perform collision avoidance maneuvers, an ever increasing percentage of satellites are being equipped with electric thrusters.[4,5,11–14].

The coupling of electrical power into the propellant can be achieved in several ways; through the direct *electrostatic* acceleration of charged particles, the *electromagnetic* acceleration of charged propellant via Lorentz forces, or through *electrothermal*, or ohmic, dissipation into predominately neutral propellant. These three categories of electric propulsion are introduced and discussed in sections 1.2.3, 1.2.4 and 1.2.5, respectively, where schematic examples of thrusters employing the most prominent electric propulsion technologies are shown in figure 1.2.

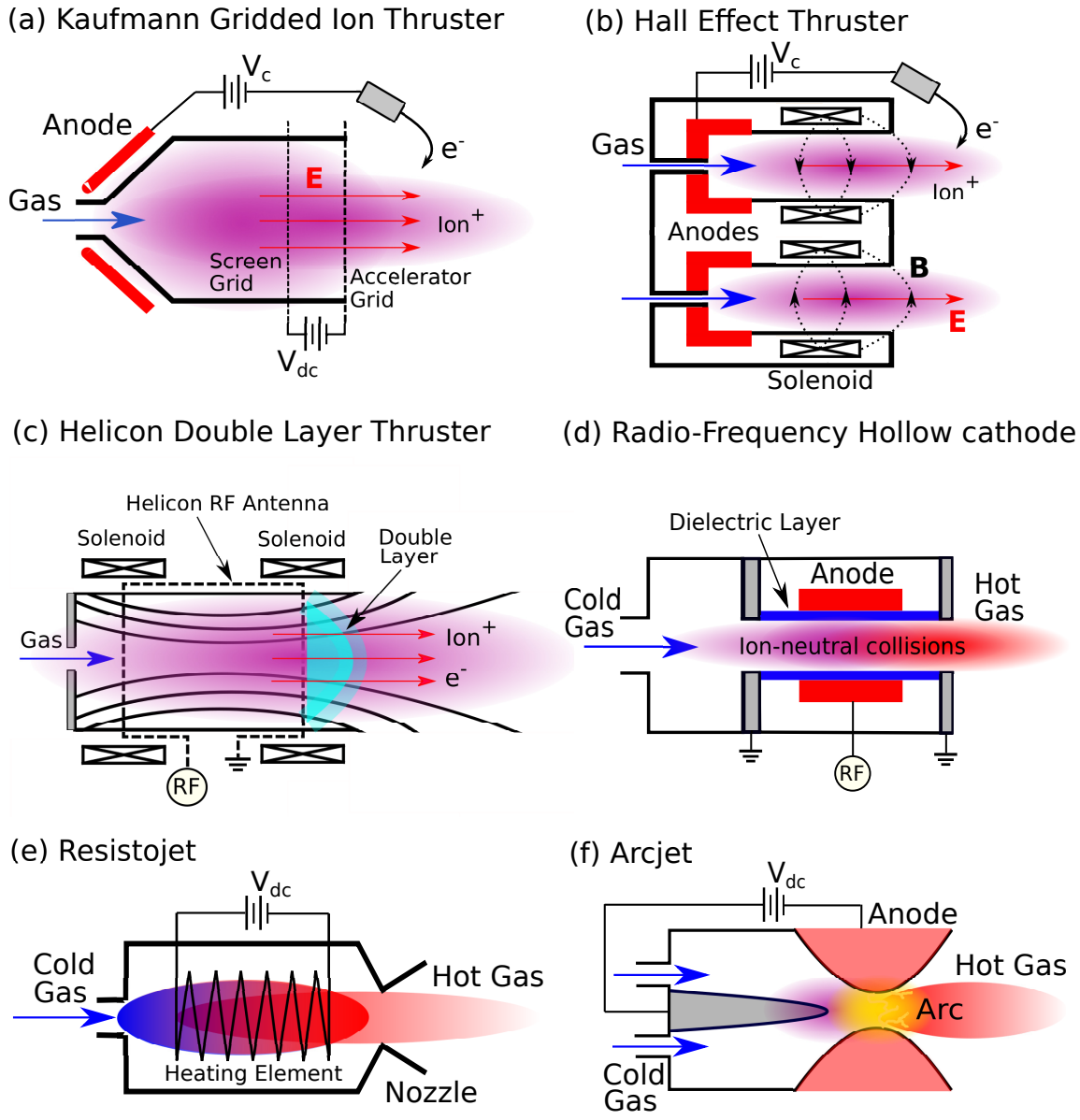

Figure 1.2: Schematic examples of commonly employed (a) electrostatic, (b), (c) electromagnetic and (d - f) electrothermal propulsion sources.

1.2.3 Electrostatic Propulsion

Electrostatic propulsion devices employ an electric field to directly accelerate ions to high velocities, magnetic fields may be employed for auxiliary purposes but are not crucial to the acceleration mechanism[14]. Generally speaking, electrostatic propulsion provides higher specific impulse at the cost of reduced thrust as compared to cold-gas or chemical propulsion[15].

The most commonly employed electrostatic propulsion device is the Kaufmann type gridded ion thruster[14,16], the main features of which are shown in figure 1.2 (a). While the precise configuration varies, gridded ion thrusters all employ an upstream ionisation chamber and a series of DC charged grids positioned downstream. Positive ions accelerated through the significant potential gradient ($\approx$ 1 kV) between the ionisation region and the grid achieve exit velocities in the range $25,000 \leq v_e \leq 40,000$ m s^{-1}, resulting in specific impulses far in excess of that achievable through chemical means[3]. Note that, as electrons are confined by the accelerating grids, an additional neutraliser cathode is required to maintain charge neutral operation. Dual-ion thrusters attempt to address this issue by employing rf power supplies and electronegative propellants (typically oxygen, chlorine or iodine), which enable charge neutral operation through alternate pulses of positive and negative ions[17–19].

Field emission electric propulsion (FEEP) devices employ liquid propellants, typically caesium or indium, from which ions are extracted and accelerated via the application of a strong electric field[20–22]. Colloid, or electrospray, thrusters operate in a similar manner through the application of a significant voltage ($\approx$ 10 kV) to a needle or capillary through which the liquid propellant is passed[22,23]. In both devices, ions extracted from the liquid propellant can reach extremely high velocities ($\geq$ 100 km s^{-1}), achieving some of the highest specific impulses in currently employed electric propulsion sources. This comes at the expense of significantly reduced thrusts (typically $F_T \leq 1$ mN) as compared to other electric propulsion sources.

1.2.4 Electromagnetic Propulsion

Electromagnetic propulsion employs both electric and magnetic fields to accelerate ionised propellant either directly through the Lorentz force or indirectly through induced currents and plasma drifts, such as the $\mathbf{E} \times \mathbf{B}$ drift[14]. Electromagnetic propulsion provides higher specific impulses as compared to cold-gas or chemical propulsion, and higher thrusts as compared to electrostatic propulsion, at the expense of greater complexity and higher power requirements[15].

Hall-effect thrusters, shown in figure 1.2 (b), represent the most commonly employed electromagnetic thruster, and have been extensively flown on over 100 satellites[3]. The Hall-effect thruster consists of a toroidal cavity with an upstream ionisation chamber and a downstream pair of co-axial magnetic coil windings. The DC power applied to the upstream electrode creates an axially aligned **E**-field, while the magnetic coils generate a cylindrically symmet-

ric magnetic field. The Hall current forms from electrons, trapped within the source by a toroidally aligned $\mathbf{E} \times \mathbf{B}$ drift. The Hall-current and the magnetic field interact to produce an axially aligned $\mathbf{J} \times \mathbf{B}$ force, resulting in positive ion acceleration[16,24]. As with gridded ion thrusters, the selective acceleration of positive ions necessitates an additional neutraliser to maintain charge neutral operation, adding weight and complexity to the system. Further, both Hall-effect and gridded ion thrusters exhibit significant etching of internal components from ion bombardment, reducing their operational lifetime.

Helicon thrusters, such as the helicon Double Layer Thruster (HDLT) shown in figure 1.2 (c), are capable of accelerating both ions and electrons, negating the need for an external neutraliser[25–28]. The HDLT employs a radio-frequency helical antenna capable of producing high density plasmas through capacitive, inductive or wave coupling to the plasma[29]. Solenoids positioned co-axially around the source produce an axially aligned diverging magnetic field. A current-free double layer, consisting of a rapid drop in plasma potential, is formed downstream of the exit solenoid as plasma expands through this diverging magnetic field[30,31]. While helicon thrusters enable charge-neutral operation, their relatively high power requirements ($\approx$ 500 W) and complexity pose issues for commercial employment on satellites. Note however that, mini-helicon thrusters are under development that are expected to operate on less than 50 W[32].

1.2.5 Electrothermal Propulsion

Electrothermal propulsion sources directly heat the propellant gas, either through ohmic dissipation or through the volumetric[33,34] and stochastic[9,35] collisional transfer of energy from electrostatically accelerated ions into neutral propellant. Thrust is generated through the thermodynamic expansion of the resulting hot propellant gas, analogous to chemical or cold-gas operation. To achieve high temperatures and exhaust velocities, electrothermal thrusters typically operate at higher pressures than electrostatic and electromagnetic thrusters, which leads to efficient gas heating. Higher thrusts, in combination with reduced complexity and lower operating powers as compared to other electric propulsion sources make electrothermal thrusters an attractive option for commercial satellite operation. These benefits come at the cost of reduced specific impulses which typically only slightly exceed cold-gas and chemical propulsion methods[5,14,15].

Resistojets, shown in figure 1.2 (e), are a commonly employed class of electrothermal thruster, consisting of a chamber through which propellant is convectively heated by a DC powered heating element[4,36]. Propellant use varies, with some resistojets employing nitrogen, helium and even water[22], however traditionally decomposed hydrazine is employed[14,37]. The simplicity and versatility of resistojets have lead to wide adoption on satellites for attitude control and drag-compensation.

Arcjets, shown in figure 1.2 (f), directly heat the propellant by passing it through a elec-

trical arc maintained between an annular DC powered electrode and an on-axis grounded electrode[14,16]. In contrast to the resistojet, where power is indirectly coupled into the propellant via conduction and convection, here power is directly ohmically dissipated within the propellant, improving the heating efficiency substantially. Further, volumetric heating of the propellant relaxes material restrictions on the maximum gas temperature, as the walls can be maintained at a lower temperature than the propellant. Typical propellants include inert or noble gasses[38,39], however hydrazine and other volatile propellants have been employed[14,16].

Micro-electro-mechanical systems (MEMS) thrusters represent a lightweight, low power alternative to traditional electrothermal propulsion[40]. Working along the same principles as monopropellant thrusters and resistojets, MEMS typically breakdown volatile propellants such as hydrazine within an ohmically heated chamber[41]. The micro-scale of the MEMS manufacturing process greatly reduces the propulsion system's 'dry mass' and enables operation at very low powers, typically 0.5 - 2 W, making them suitable for deployment on microsatellite platforms. These benefits come at the cost of significantly reduced thrusts, typically of the order 100 μN, and relatively low thermal efficiencies.

Resistojets, and especially arcjets, require high powers (100 - 1000 W) to operate effectively and are typically employed on larger satellite platforms[42]. MEMS meanwhile are capable of low power operation ($\leq$ 5 W) but produce only limited thrusts, resulting in long burn times and a reduced capability to perform unexpected avoidance manoeuvrers[40]. A desirable alternative comes in the form of radio-frequency electrothermal thrusters (RFETs), also known as 'rf plasma thrusters'[13]. RFETs, shown in figure 1.2 (d), employ a low power radio-frequency discharge to volumetrically heat propellant, benefiting from enhanced spatial heating as compared to resistojets, enhanced thrusts as compared to MEMS and reduced power requirements as compared to arcjets[4,5]. The rf power is coupled either capacitively or inductively into the propellant, maintaining a weakly ionised plasma within the source, ion acceleration and subsequent collision with neutral particles facilitates power transfer into the propellant. RFETs typically employ heavy noble gasses such as argon[43] or xenon[44], however lighter gasses such as hydrogen[34] have been employed in attempts to increase the specific impulse. The rf power coupling enables separation between the powered electrode and the propellant, significantly reducing component degradation and enabling longer lifetimes. In addition, the non-local rf power coupling provides a degree of flexibility in the geometry of the source, enabling co-axial or 'hollow cathode' designs, altering the thermal efficiency and spatial power deposition into the propellant[45,46]. Of the propulsion techniques discussed, rf electrothermal thrusters present considerable potential for application on the next generation of micro-satellites, offering low power operation and high thermal efficiencies while maintaining a lightweight, simple and flexible geometry[13].

1.3 Microsatellites

Over the past decade there has been growing interest in the development of compact microsatellite platforms for use in scientific, commercial and defense applications[12,14,47]. While not strictly defined, microsatellites typically refer to platforms with a total mass less than 100 kg, a total power output of less than 100 W and a total volume less than 1 m^3[22]. CubeSats represent a modular approach to microsatellite development, see figure 1.3, employing commercial off-the-shelf components to enable cheaper and more reliable construction[48–50].

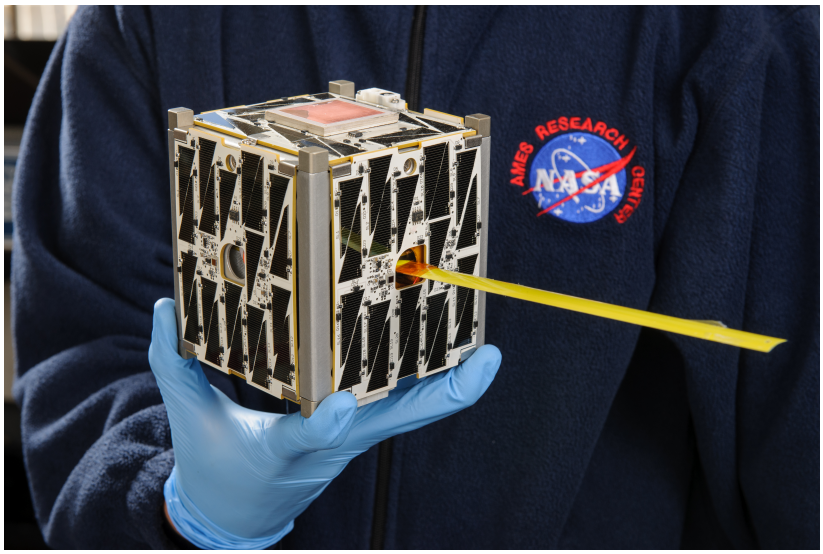

Figure 1.3: Image of a single CubeSat unit (1U), showing photovoltaic cells and extended communication antenna, with human for scale[51].

CubeSats are constructed from modular 10 cm^3 units, with a maximum mass per unit of 1.33 kg, typical configurations employ between 1 - 12 of these units. Their small size and weight enables many CubeSats to be deployed from a single launch vehicle, reducing deployment cost substantially. Originally CubeSats were developed to suit the requirements of the academic sector, primarily suited for education and technological demonstration purposes. However, recent growth in the commercial space sector has seen growing interest in CubeSat development. To date over 1000 CubeSats have been deployed in space, with a projected 3000 more to follow in the next six years[51]. Current and future planned missions range from communications[42], remote sensing[52–54], autonomous vehicle control[55], orbital debris management[56] and even interplanetary data aquisition[57]. CubeSats therefore represent the capability to operate low-cost, low-risk missions with potential high value scientific or commercial return[58]. Further, the large scale adoption of microsatellites and CubeSats offers the prospect of novel distributed mission paradigms through the use of coordinated swarms or constellations of microsatellites[59,60]. For the same dry mass of satellite launched, constellations present a greater ‘collection area’ for communications and remote sensing applications. Further, constellations provide a significant increase in redundancy over larger

more sophisticated satellites, reducing the impact of individual component failures.

From a practical standpoint microsatellites require essentially the same on-board systems as larger satellite platforms. This includes onboard control and communication systems, power supplies, cooling systems and propulsion systems[42]. While significant progress has been made in most of these areas, the majority of microsatellites are still launched without onboard propulsion[52,58]. Reaction wheels are sometimes employed to maintain attitude control, however uncontrolled orbital dynamics and orbital decay lead to limited operational lifetimes and concerns regarding collision avoidance[61]. The strict volume and weight restrictions make traditional propulsion systems unattractive for the majority of microsatellite platforms. Therefore, the continued development of microsatellites would benefit from lightweight, low power, electric propulsion sources[58,62].

1.3.1 Micro Propulsion Considerations

Microsatellites are most commonly employed in Low Earth Orbit (LEO) as these orbits require the least amount of energy for satellite placement*. Microsatellites in LEO experience significant atmospheric drag and, without drag compensation provided by onboard propulsion, will typically de-orbit and require replacement on the order of 1 - 5 years[3,63]. Further, without propulsion a microsatellite has no possibility of altering course following detachment from the launch vehicle, limiting mission parameters and restricting the use of constellations or swarms[55]. Finally, operation in LEO raises the consideration of orbital debris mitigation, specifically dealing with collision avoidance manoeuvrers and end-of-life deorbiting.

Micro propulsion sources face far stricter limitations on volume, mass and power requirements as compared to their larger counterparts. The specific characteristics required vary substantially depending on the mission objectives, however some general requirements remain the same, these being power, thermal efficiency and thrust[58]. Comparisons of key parameters for various currently employed low-to-mid power propulsion technologies are shown in table 1.1. As discussed previously, CubeSats are limited to 1.33 kg per unit, restricting not only the propellant mass, but also the dry mass of the propulsion system and associated power supply. Photovoltaic solar cells represent the primary power source for most satellite systems, where CubeSats typically achieve approximately 6 W per unit[42], with larger systems ($\geq$ 3U) capable of generating 20 - 30 W by deploying external solar panels[58]. Neutraliser free, charge-neutral electric propulsion is therefore desirable in reducing not only the power requirements but also the dry mass of the propulsion system[64]. While not a strict requirement, microsatellites designed for use in constellations and those capable of collision avoidance manoeuvrers require a relatively high maximum thrust ($\approx$ 1 mN) to enable a timely response[61].

*LEO refers to any orbital inclination with an orbital radius of less than 2000 km. Note that polar orbits, beneficial for terrestrial observation satellites, while still technically within the LEO category require a substantially higher Δv at launch due to their misalignment with the axis of rotation of the Earth.

Technology	Propellant	Thrust (mN)	I_{sp} [s]	Power [W]	Efficiency	Refs.
Cold-Gas	Nitrogen	0.1 - 5	45 - 75	n/a	n/a	22
Monopropellant	Hydrazine	1 - 4450	162 - 230	n/a	n/a	22
	H_2O_2	1 - 1.82	100 - 180	n/a	n/a	22
Resistojet	Hydrazine	—	300 - 400	100 - 1000	65 - 90%	14,37
	H_2O	0.125	127 - 150	100	—	22
	Various	109 - 335	93 - 385	167 - 506	—	36
Arcjet	Hydrazine	—	345 - 471	650 - 1400	29 - 36%	14,16
	Ammonia	—	600 - 900	1000 - 10000	—	14
	Nitrogen	—	254 - 284	40 - 90	50 -70%	38
	Helium	0.014 - 0.031	313	119	36%	39
	Hydrogen	—	700 - 1200	10000	—	14
Hollow Cathode	Argon	1.13 - 2.0	30 - 70	1.8 - 4.8	30 - 55%	43,65,66
	Xenon	0.8 - 2.4	24 - 32	10 - 70	$\approx$ 15 -32%	44
	Hydrogen	0.002 - 1	$\approx$ 3000	100 - 1000	$\approx$ 75%	34
MEMS	Various	0.013 - 1.07	54	0.5 - 2	4 - 18%	40,41
Gridded-Ion	Xenon	0.1 - 1.5	$\approx$ 3000	20 - 60	45%	16
	Xenon/SF_6	$\approx$ 5.5	$\approx$ 7000	700	$\approx$ 33%	18,19
FEEP	Cesium	0.001 - 1.4	9000	3 - 93	95%	22
	Indium	0.001 - 0.14	2000 - 8000	1	95%	20,21
Colloid	Various	$<$ 0.007	300 - 1500	2	75%	22,23
Hall-Effect	Xenon	0.1 - 16	830 - 1718	50 - 300	6 - 34%	15,16,24
Mini-Helicon	Argon	1 - 4	600 - 1200	50- 300	1 - 20%	27,30
	Xenon	1	1000	50	20%	32

Table 1.1: A summary of key operational parameters for various modern micro-propulsion technologies. Entries proceded by a $\approx$ symbol indicate extrapolated or estimated values, while entries consisting of — denote unknown or unstated values.

Space debris is a growing concern for space agencies worldwide, the avoidance and management of existing debris and the reduction of new debris are at the forefront of current satellite development[56]. There are currently an estimated 22,000 pieces of space debris larger than 10 cm and an estimated 600,000 objects sized between 1 - 10 cm[67]. Since 2006 the likelihood of a collision between any given satellite in LEO and a piece of debris over 1 cm in size has increased from 17 - 20%[68] to over 50% per year[69]. This increase is attributed to two events, namely the testing of a Chinese anti-satellite ballistic missile on the non operational Chinese weather satellite, Fengyun-1C (FY-1C) and an accidental collision between *Iridium 33*, a US communications satellite, and *Kosmos 2251*, a retired Russian communica-

tion satellite[69]. The continued routine use of LEO necessitates that future satellites plan for collision avoidance, requiring the use of suitable on-board propulsion. The requirement for manoeuvrable microsatellites with on-board propulsion systems is therefore well established. As such, an increasing percentage of 'all-electric' microsatellites are being equipped with compact, low-power, charge-neutral, electric propulsion sources[5,11,22,40,70].

1.3.2 The *Pocket Rocket* Microthruster

This thesis assesses the performance and capability of a hollow cathode enhanced radio-frequency electrothermal plasma micro-thruster known as the *'Pocket Rocket'*[70,71], currently under development in a collaboration including the Space Plasma, Power and Propulsion laboratory (SP3) at the Australian National University and the York Plasma Institute (YPI) at the University of York. The *Pocket Rocket* (PR) was initially concieved by Rod Boswell and Christine Charles as a low-power alternative to cold-gas and resistojet sources[44,71]. An image of the downstream plume of the thruster is shown in figure 1.4 for operation in argon with a 0.5% nitrogen admixture. A schematic and full details of the operation of the *Pocket Rocket* microthruster are presented in section 2.1.1. Much of the initial development was performed by Charles and Greig, demonstrating that the primary neutral gas heating mechanism arises from ion-neutral charge exchange collisions within the discharge volume[72–75]. Further work by Teck-Seng Ho has investigated the cold gas and heated flow in detail, including a fluid dynamic analysis of prospective nozzle geometries[66,76,77]. Direct thrust measurements employing xenon propellant in a miniature version of the PR, dubbed the *mini-PR*, have been performed in the Wombat space simulation chamber at SP3[44,78]. In addition, the thruster and power supply have recently been demonstrated to fit within a standard 1U CubeSat frame, see Ref. 47 for a schematic of the thruster *in-situ*.

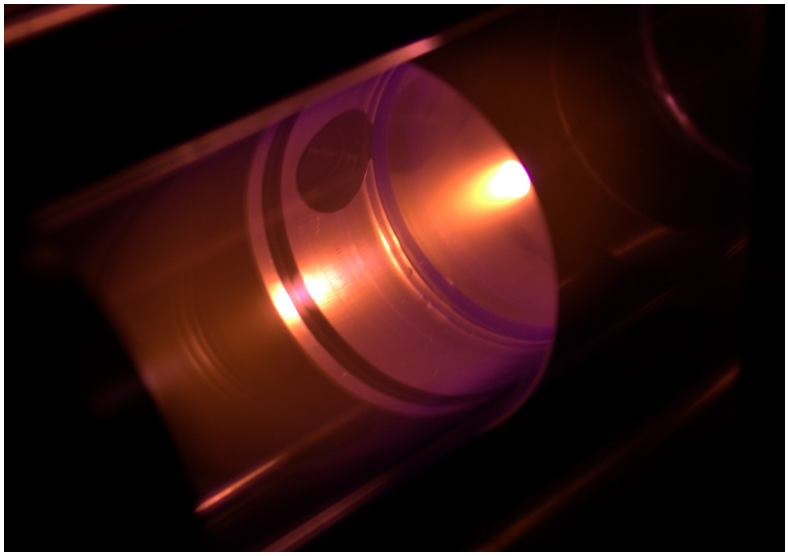

Figure 1.4: Neutral plume downstream of the *Pocket Rocket* source in argon with 0.5% nitrogen admixture. Plenum pressure 1.5 Torr in argon, 300 V at 13.56 MHz.

Previous work has established the *Pocket Rocket* as a viable micro propulsion device, capable of providing thrust in the mN range and specific impulses of between 50 - 60 s while employing less than 10 W (in argon). This places the *Pocket Rocket* as an intermediary between traditional cold gas, resistojet and arcjet thrusters. In comparison to these contemporaries, the *Pocket Rocket* benefits from increased thermal efficiencies and reduced material considerations as compared to resistojets, significantly lower power consumption as compared to arcjets and the capability to employ inert propellant as compared to cold-gas thrusters which typically employ toxic, hypergolic propellants such as hydrazine. The latter of these benefits is particularly advantageous for commercial applications, where access to traditional propellants can be limited and introduce additional safety concerns. Current development of the *Pocket Rocket* at SP3 is primarily focused on increasing mission readiness, continued development of the power and gas supply sub-systems and inclusion of a downstream nozzle in preparation for the first in-situ deployment onboard a 1U cubesat.

The work presented in this thesis expands upon previous work by outlining enhanced operation of the *Pocket Rocket* through employing electrical control schemes involving the use of variable or multi-frequency voltage waveforms with the aim of achieving higher thermal efficiencies and variable thrust output. Such capabilities are desirable for application on the next generation of micro-satellites, enabling low power operation in combination with more flexible mission constraints as required for distributed or constellation mission paradigms. Before progressing to demonstrate these control mechanisms, a summary of the relevant plasma physics and associated underpinning theory is given in section 1.4

1.4 Plasma Theory

Plasma is the fourth and most prevalent state of matter in the visible universe and can exist over a wide range of temperatures and pressures. Some commonly encountered examples of plasmas include fluorescent light bulbs, atmospheric lightning and the aurora. Plasmas may be formed through the deposition of sufficient power into a material, typically a gas, such that the electrons are stripped from their parent atoms and can exhibit independent dynamics. The description of plasmas therefore differs from that of unionised gasses as the collective behaviour of the constituent particles is determined not only through short ranged kinetic interactions, but also through long ranged electromagnetic interactions [79].

1.4.1 Fundamentals of Plasmas

Consider an atmospheric pressure, neutral, monatomic gas at room temperature. The motion of the atoms within this gas can be described stochastically as a 'random-walk' and are governed by short range collisional interactions. Next, consider stripping a single electron from each atom within the gas, resulting in the formation of a plasma[†]. Charged particles within this plasma are now subject to long range electromagnetic forces, introducing collective behaviour into the system. First, notice that although the plasma now contains many charged particles, notably positively charged ions and negatively charged electrons, the net charge of the whole system is still zero. This concept is known as quasineutrality and represents the conservation of charge within a plasma. In discussing quasineutrality further it is useful to define the Debye length λ_D, shown in equation 1.9:

$$\lambda_D = \sqrt{\frac{\epsilon_0 k_b T_e}{n_e e^2}} \tag{1.9}$$

Here, T_e is the mean electron temperature, n_e is the plasma (electron) density, ϵ_0 is the permittivity of free space, k_b is Boltzmann's constant and e is the electronic charge. The Debye length represents the capability of a plasma to shield free charges. Consider the case of a freely moving positively charged ion within a plasma. Electrons, electrostatically accelerated towards the ion, will form a cloud of negative charge surrounding the ion. Additional electrons will 'see' this as a cloud of negative charge and be repelled. The distance at which the free charge is obscured by the plasma is equal to the the Debye length and defines the length scale over which collective electromagnetic interactions occur. Note that externally imposed electromagnetic fields may still interact on length scales larger than the Debye length.

Before examining the effects of an externally imposed electromagnetic field in detail, first consider a uniform plasma consisting of equal numbers of fixed positive charges and freely moving negative charges. The quasineutrality of the system can be broken if the negative

[†]Note that the majority of terrestrial plasmas contain many more neutrals than ions, for the plasmas discussed in this work the fraction of ions relative to neutrals is typically ≤ 1 %

charges are uniformally displaced by a distance δ_x from the positive charges. Coulomb forces arising from this displacement ($\mathbf{F}_x = q\mathbf{E}_x$) act to reduce the charge separation, resulting in oscillatory motion for any non-zero mass charge carrier. In the absence of a damping force, this oscillatory motion will continue at a frequency ω_{pe} that depends only upon the electron density[79]:

$$\omega_{pe} = \sqrt{\frac{e^2 n_e}{\epsilon_0 m_e}} \tag{1.10}$$

As before, n_e is the plasma (electron) density, ϵ_0 is the permittivity of free space, and m_e and e are the electron mass and charge, respectively. By virtue of the charge separation resulting from thermal motion, all undisturbed plasmas posses this oscillatory motion and therefore, the electron plasma frequency ω_{pe}, can be thought of as the natural resting frequency of a plasma. The electron plasma frequency for plasmas studied in this work is typically in the range $\omega_{pe} \approx$ 1 - 10 GHz and similar motion is observed for the heavier ion species, albeit at reduced frequencies ($\omega_{pi} \approx$ 0.1 - 1 MHz).

Returning to the discussion of externally applied electromagnetic fields, consider an imposed time varying electric field applied at a frequency ν, where $\nu \geq \omega_{pe}$. In this scenario, electrons within the plasma are able to respond on timescales faster than the variation in the applied field and power can be deposited into the system through electron acceleration and subsequent collisional interactions. Note that as $\omega_{pi} \leq \omega_{pe}$, the heavier ion species will, in most cases, only respond to the time-averaged dc component of the applied field. As power is coupled into charged particles within the plasma, the applied field amplitude is dampened exponentially over a lengthscale δ_s, shown in equation 1.11:

$$\delta_s = \frac{c}{\omega_{pe}} \tag{1.11}$$

where c is the speed of light in a vacuum. For the plasmas presented in this work, the skin depth is typically on the order of 1 - 5 λ_D. For electromagnetic fields applied at frequencies where $\nu \leq \omega_{pe}$, electrons within the plasma are unable to respond to the time-varying component of the applied field, resulting in undamped wave propagation through the plasma and neglegable power coupling[80].

1.4.2 Thermodynamic Equilibria

Power supplied from applied electromagnetic fields is initially coupled into a plasma through the charged particle species only, typically through Lorentz forces. The transfer of that power between charged species occurs through short and long-range interactions, while transfer of power into non-charged species occurs through short-range collisional interactions. The steady-state distribution of energy within a plasma therefore depends upon the collisional

transfer of power through the numerous constituent particle species.

Plasmas whose constituent species exist in a state of thermodynamic equilibrium are described as *high-temperature* or *thermal* plasmas, examples include welding arcs and fusion plasmas[81,82]. Plasmas which have species that are not in thermodynamic equilibrium, such as those discussed in this thesis, are described as *low-temperature* or *non-thermal* plasmas[11,83–85]. Low-temperature, non-thermal plasmas are typically characterised by the lack of thermal equilibrium between the high temperature electrons and the relatively low temperature ions and neutrals. This thermodynamic disequilibrium is maintained through coupling power primarily to the lighter electron species, i.e. employing an applied voltage frequency ν where $\omega_{pi} \leq \nu \leq \omega_{pe}$. The low electron inertia relative to the heavy ion species prevents significant heating of the ions through electron-ion collisions. The result is a plasma where the average electron temperature ($\approx$ 1 - 5 eV) can be varied approximately independently from the bulk ion/neutral temperatures ($\approx$ 0.01 - 0.1 eV).

Control over the fractional power deposition into heavier ion and neutral species is beneficial for aerospace concerns where maximising the neutral gas temperature is desirable, making non-thermal plasmas attractive options as thermal propulsion systems[71]. Low-temperature plasmas are also of interest for many industrial and biomedical applications as the electron temperature can be controlled, allowing for variable temperature chemistry, while keeping the ion and neutral population at approximately room temperature[11,84].

Particles in a plasma volume can collide on varying timescales, such collisions can be elastic or inelastic depending on the specific collision process[9]. In electropositive[‡] low-temperature plasmas the most common interactions involving a charged particle, namely an electron e^- or ion A^+, are elastic collisions with neutral atoms B. These collisions may lead to the inelastic ionisation of the neutral atom and the release of an additional electron (1.12), or they may lead to the elastic excitation of the neutral (1.13).

$$e^- + B = A^+ + 2e^- \tag{1.12}$$

$$e^- + B = B^* + e^- \tag{1.13}$$

In addition, fast ions can undergo ion-neutral charge exchange collisions 1.14 with slow neutrals:

$$A^+ + B = B + A^+ \tag{1.14}$$

This elastic process occurs when the electron shells of a neutral atom and negative ion come into contact, resulting in the transfer of an electron from the atom to the ion[34]. The end result is that populations of fast ions and slow neutrals exchange charge and maintain

[‡]Reactions involving negative ion species and photoionisation are not considered here.

momentum resulting in populations of fast neutrals and slow ions. Ion-neutral charge exchange therefore facilitates the coupling of electrical energy into neutral thermal motion, altering the neutral gas temperature. Additional ion/neutral heating can be achieved via the application of lower frequency voltage components ($\nu \leq \omega_{pi}$) or transient dc bias voltages[86–89].

When discussing collisional behaviour it is useful to define two parameters, the mean-free-path and the collision frequency. The mean-free-path λ_{mfp} for a given species is defined as the average distance that particle will travel before undergoing a collision[79]:

$$\lambda_{\text{mfp}} = \frac{1}{\sigma(\epsilon) n_g} \tag{1.15}$$

Where $\sigma(\epsilon)$ is the energy resolved interaction cross-section for the related collisional process and n_g is the background gas density. The collision frequency ν_{coll} is then simply the product of the inverse mean-free-path and the distance subtended by a particle per unit time, i.e. it's velocity:

$$\nu_{\text{coll}} = \lambda_{\text{mfp}}^{-1} \langle v_x \rangle = n_g \sigma(\epsilon) \langle v_x \rangle \tag{1.16}$$

Here, $\langle v_x \rangle$ is the average velocity of species 'x'. While a plasma is not considered 'collisional' or 'collisionless' based solely on the collision frequency, as a rule of thumb a plasma may be considered collisional if $\nu_{\text{coll}} \geq 10 \langle v_x \rangle$[90]. Note that the 'collisionality' of a plasma is determined not only by the background gas pressure, but also the energy resolved cross-section for the specific collisional process. Therefore, varying the mean energy, and hence velocity, of a particle species can alter the plasma collisionality, this is addressed in more detail in section 1.5.3.

1.5 Radio-Frequency Capacitively Coupled Plasmas

Radio-frequency (rf) plasma discharges employ a high-frequency alternating voltage to couple power into charged particles within the plasma. Typical applied voltage frequencies include 13.56 MHz and its harmonics as these are reserved for industrial, scientific and medical (ISM) use[§]. Power is coupled into the plasma either through applying the rf voltage waveform to a metal plate in direct contact with the plasma or via an antenna indirectly coupled to the plasma, denoted capacitive and inductive coupling, respectively[79,85]. In this work, capacitive coupling is employed, where the powered electrode is separated from the plasma by a dielectric layer.

Radio-frequency capacitively coupled plasma sources (rf-CCPs) typically consist of two or more electrodes, a powered electrode and a grounded electrode, separated by a gas-filled

[§]ITU Radio Regulations, CHAPTER II – Frequencies, ARTICLE 5 Frequency allocations

chamber. A 13.56 MHz radio-frequency voltage waveform is applied to one electrode, while the other is grounded, forming a time varying electric field between the two plates. Free electrons within the gas respond to the applied rf voltage and undergo energetic collisions with the neutral atoms, resulting in electron induced ionisation and the release of additional free electrons. The resulting electron avalanche results in a breakdown of the neutral gas and the formation of a plasma between the two plates.

The strength of the applied field required for breakdown varies depending upon the separation d between the two plates and the background pressure P of the plasma. Plotting the breakdown potential against the product of these two parameters ($P \times d$) produces a function known as a Pachen curve. Paschen curves for six commonly employed gasses are shown in figure 1.5.

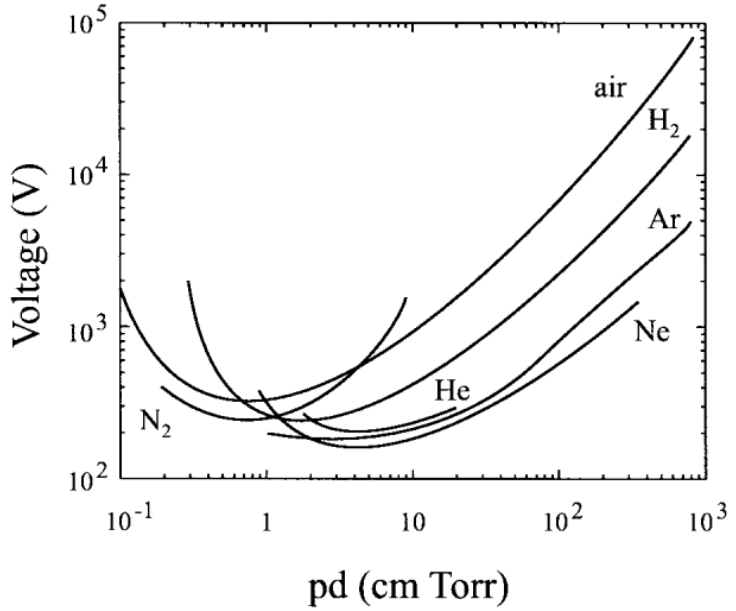

Figure 1.5: Paschen curves showing the DC breakdown voltages for six commonly employed species of gas with respect to varying pressure distance product ($P \times d$). Image reproduced from Ref. 91.

The curves in figure 1.5 exhibit two regions of proportionality to the applied voltage surrounding a minimum breakdown condition. The voltage required for breakdown increases slowly with increasing $P \times d$. This relationship can be quantified by noting that the collision frequency, equation 1.16, scales linearly with pressure. Conversely, if the pressure is reduced too far then the number of collisions, and hence ionisations, becomes too small to sustain the plasma. The same is true if the spacing between the electrodes reduces such that $d << \lambda_{\text{mfp}}$. Finally, the minimum voltage for breakdown typically decreases with increasing atomic mass, due primarily to the increasing impact cross-section $\sigma(\epsilon)$ and in part to the reduction in the ionisation potential due to Debye shielding within the atom, note however that this most apparent for higher atomic mass nuclei, e.g. xenon. Upon breakdown the plasma stratifies into two distinct regions, the plasma bulk and the plasma sheath, separating the bulk from

the electrodes.

1.5.1 Plasma Sheaths

A plasma sheath exists as a positive space charge region between the plasma bulk and plasma facing material surfaces. They act to confine the mobile plasma species (electrons) and accelerate the less mobile species (ions) out of the plasma bulk. Consider the plasma volume adjacent to the powered electrode immediately following breakdown. Free electrons within this volume, being more mobile, are lost to the powered electrode surface faster than the heavier ion species. This enforces an overall negative charge at the electrode surface. The resulting drop in potential from the plasma bulk to the electrode wall sets up an electric field retarding further electrons while accelerating positive ions into the sheath region. The resulting steady state spatial variation in particle species density and electrostatic potential through the sheath are shown in figure 1.6.

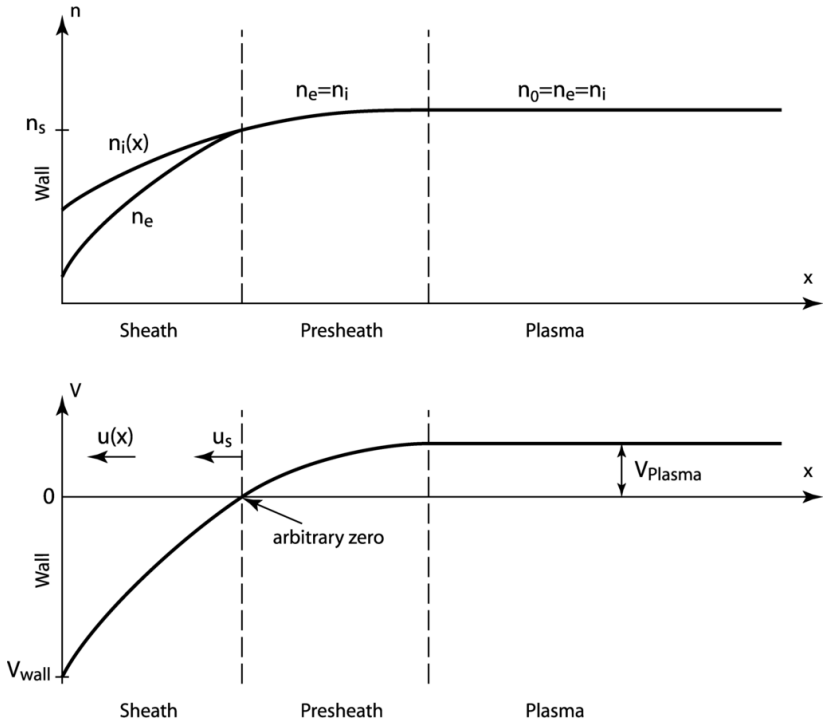

Figure 1.6: Generalized example of (a) the ion n_i and electron n_e densities and (b) the plasma potential (V_{plasma}) through a high voltage Child-Langmuir sheath. Reproduced from Ref 9.

Within the sheath region, positive ion densities will exceed electron densities due to the aforementioned negative surface charge repelling lower energy electrons, see figure 1.6 (a) and (b). This implies that quasineutrality is broken within the sheath region. Despite the absolute number density of ions and electrons differing, the ion Γ_i and electron Γ_e fluxes incident upon the electrode must balance for the plasma to remain in steady state:

$$\int_0^\tau \Gamma_e \mathrm{d}\tau = \int_0^\tau \Gamma_i \mathrm{d}\tau \tag{1.17}$$

Here, $\Gamma_e = m_e v_e$, $\Gamma_i = m_i v_i$ and τ represents one rf phase cycle. In the absence of additional external forces, and despite the reduction in electron density within the sheath, the electron flux towards the wall would still exceed the ion flux due to the greater average electron temperature, as discussed previously. Therefore, in order to maintain the flux balance in equation 1.17, the ions must enter the sheath region with a minimum velocity, v_B, known as the Bohm velocity[92]:

$$v_B = \sqrt{\frac{eT_e}{m_i}} \tag{1.18}$$

Ions are accelerated to the Bohm velocity in the pre-sheath, a region where quasineutrality is approximately maintained, but the plasma potential reduces due to the reducing charge density. Once within the sheath, ions are accelerated through the sheath potential towards the electrode surface and impact the surface at high energies ($1 - 10$'s eV) relative to the average bulk ion energy ($\approx$ 0.01 - 0.1 eV). Note that as a negative potential gradient is required to increase the ion flux and maintain charge continuity, it follows that the plasma potential must always be higher than the wall potential for a steady state plasma[9]. Therefore, as the voltage applied to the electrode surface varies, the sheath must respond to maintain the ion and electron fluxes.

An estimation of the instantaneous electric field through the sheath $\mathbf{E}(x,\tau)$ can be obtained from Poisson's equation by assuming a negligible electron density ($n_e(x,\tau) = 0$) and temporally and spatially invariant ion density ($n_i(x,\tau) = \hat{n}_i$) through the sheath.

$$\nabla_x \cdot \mathbf{E}(x,\tau) = \frac{-\rho}{\epsilon_0} \approx \frac{e\hat{n}_i}{\epsilon_0} \tag{1.19}$$

Integrating equation 1.19 through a sheath of thickness $S_x(\tau)$, at phase τ we obtain:

$$\mathbf{E}(x,\tau) \approx \frac{e\hat{n}_i}{\epsilon_0}(x - S_x(\tau)) \tag{1.20}$$

where $x \geq S_x(\tau)$ and $\mathbf{E}(x,\tau) = 0$ for $x \leq S_x$. The instantaneous sheath extent is obtainable through noting that $\phi(\tau) = -\nabla_x \cdot \mathbf{E}(x,\tau)$ as follows:

$$\phi(\tau) = -\int_0^{S_x} \frac{e\hat{n}_i}{\epsilon_0}(x - S_x(\tau))\mathrm{d}x = \frac{e\hat{n}_i}{\epsilon_0}\frac{S_x^2(\tau)}{2} \tag{1.21}$$

and therefore,

$$S_x(\tau) = \left(\frac{2\epsilon_0\phi(\tau)}{e\hat{n}_i}\right)^{1/2} \tag{1.22}$$

Note that due to the assumptions made when considering equation 1.19, equation 1.22

does not implicitly account for collisions within the sheath volume. Despite this, a more rigerous derivation considering non-zero, spatially varying, ion and electron density distributions through the sheath obtains a similar result[93].

In this work the sheath edge is defined employing the Brinkmann sheath criterion[94]. Within this model, illustrated in figure 1.7, spatial and temporal variations in the ion and electron densities within the sheath are considered, allowing for a consideration of ionisation within the sheath volume.

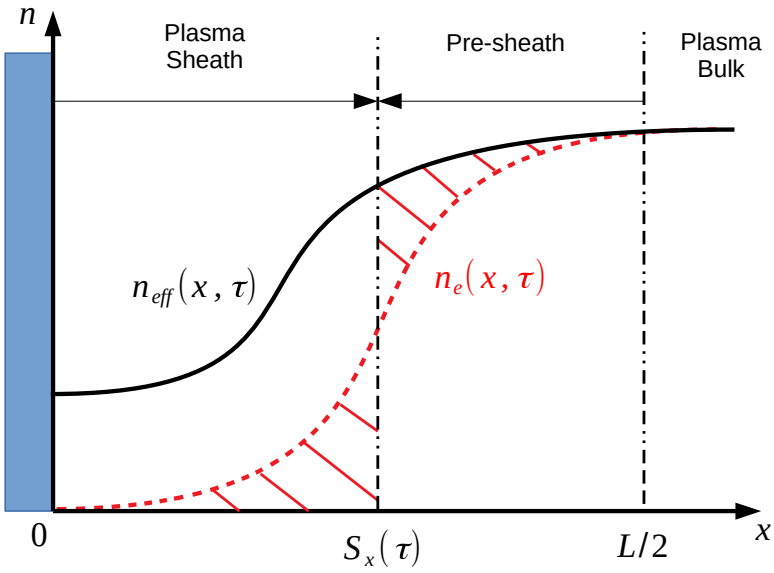

Figure 1.7: Generalized example of the Brinkmann sheath model, indicating the effective positive charge n_{eff} and electron n_e spatial density distributions. Floating material surface is denoted in blue.

Here, $L/2$ represents the centre of the plasma bulk, defined as the radius of most positive plasma potential. The sheath edge is defined as the point about which the ion and electron densities from $L/2$ towards the wall are equal. A formal derivation of the Brinkmann sheath criterion can be found in Ref. 94, the solution is stated here for brevity:

$$\int_0^{S_x(\tau)} n_e(x,\tau)\mathrm{d}x = \int_{S_x(\tau)}^{L/2} n_{\mathrm{eff}}(x,\tau) - n_e(x,\tau)\mathrm{d}x \tag{1.23}$$

The effective positive charge density is denoted n_{eff} where generally $n_{\mathrm{eff}} = n_{i+} - n_{i-}$, however when dealing with electropositive plasmas $n_{\mathrm{eff}} \approx n_{i+}$. In practice, n_{eff} is integrated radially from the material surface towards $L/2$, while the electron density is integrated from $L/2$ towards the material wall. The radius for which equation 1.23 is true is taken as the sheath edge.

Equations 1.22 and 1.23 describe the behaviour of the sheath on two important timescales: on timescales below an rf phase-cycle τ, the instantaneous sheath extent varies in response to the applied rf voltage $\phi_{rf}(\tau)$, where the ion density within the sheath can be considered

constant. However, on timescales above τ, the phase-averaged sheath extent depends upon the local ion and electron densities and is hence related to the local ionisation rate. These two timescales cannot necessarily be treated independent of each other, noting that the movement of the sheath itself gives rise to a flux of electrons as the electron density profile readjusts in response to the applied electric field, see figure 1.7. This time varying electron flux results in collisions at the sheath edge and subsequent additional sheath heating mechanisms. In essence; the plasma density at the sheath edge defines the sheath mobility, the sheath mobility defines the ionisation rate, re-defining the plasma density at the sheath edge, forming a closed system.

1.5.2 Plasma Heating Mechanisms

Capacitively coupled rf plasma sources exhibit different electron heating mechanisms depending upon the pressure, applied voltage and geometry. These heating mechanisms can broadly be broken up into collisional and collisionless (stochastic) heating[19,95]. At the pressures employed in this work collisionless heating forms a negligible component of the total electron heating, therefore a detailed discussion is omitted.

Collisional electron heating occurs primarily at the moving sheath edge. From the frame of reference of an electron, the sheath edge appears as a negative potential gradient moving towards or away from the electron. The sheath edge can therefore be thought of as a 'hard wall', from which the electrons will electrostatically 'bounce' if they come into contact with it[96]. In such a collision the electron will gain momentum in proportion to twice the wall velocity, such as with the ballistic case of a rigid ball reflected from a moving wall, e.g. a squash ball impacting a racket. Therefore, the greatest change in electron velocity, and hence greatest collisionally deposited power, occurs at rf-phases where the rate of change of the applied voltage is greatest. For example, low power capacitively coupled discharges are typically sustained through ionisations during sheath expansion and contraction, corresponding to phases of peak temporal voltage modulation (dV/dt)[9]. Sheath collapse heating, e.g field reversal,[97,98] and sheath expansion heating, e.g stochastic,[35,99] occur during phases of peak dV/dt, increasing and decreasing voltage respectively, and are indicative of α-mode operation.

At higher applied voltages, positive ion bombardment onto material surfaces becomes significant, leading to an increased production of secondary electrons, which are subsequently accelerated through the sheath, back into the plasma, reaching maximum energies during full sheath extension[100,101]. As they are accelerated electrostatically through a large sheath potential, secondary electrons poses high, non-thermal, energies relative to the collisionally excited electrons. Owing to the non-thermal energy distribution, secondary electrons typically exhibit a long mean-free-path, enabling the deposition of power deeper into the plasma bulk through electron-electron collisions and electron-ion ionisation collisions. Sec-

ondary electron heating can be enhanced through the hollow cathode effect (HCE), leading to higher specific power deposition[102,103]. Electron heating mechanisms observed for phases of peak positive or negative applied voltage amplitude are indicative of γ-mode operation.

To illustrate the origin of these mechanisms, consider a volume of plasma subtended by the sheath adjacent to the powered electrode during a single rf phase cycle:

- *Sheath Collapse Heating*[97,98]
  During the phase of sheath collapse, ($+\mathrm{d}\phi_{rf}/\mathrm{dt}$), electrons are accelerated out of the plasma bulk and towards the powered electrode surface. Within an rf phase cycle, positive current is lost at an approximately time independent rate due to the ions responding only to the phase-averaged negative sheath potential. The majority of electrons however, are unable to leave the plasma bulk while the sheath exists due to the same, now confining, electric field. As the applied voltage at the electrode increases beyond the plasma potential the sheath collapses and the low energy electrons are free to exit the bulk. The fraction of rf phase for which the sheath is collapsed is typically smaller than the fraction for which it is extended, necessitating a relatively high electron flux is required to transfer an equivalent negative current. The degree to which sheath collapse heating is observed is therefore proportional to the fraction of the rf cycle for which the sheath is collapsed and inversely proportional to the electron density, as higher electron fluxes can be maintained at a lower mean electron velocity.

- *Sheath Expansion Heating*[35,99]
  During the phase of sheath expansion, ($-\mathrm{d}\phi_{rf}/\mathrm{dt}$), electrons are accelerated away from the electrode surface by the rapidly changing surface potential. In essence this represents the inverse of sheath collapse heating, however the motive force comes not from charge imbalance, but from the applied rf voltage amplitude directly. The degree to which sheath expansion heating is observed is proportional to the applied voltage frequency, i.e. to the sheath expansion velocity, and indirectly proportional to the plasma density, for the same reasoning as with sheath collapse heating.

- *Secondary Electron Heating*[100,101]
  During the phase of maximum sheath extension (most negative ϕ_{rf}), secondary electrons released from the electrode surface due to ion bombardment are accelerated through the sheath potential to super-thermal energies ($\approx$ 10 - 100 eV). Ions impacting material surfaces can release secondary electrons through the Auger process[104]. These electrons are then accelerated away from the wall back into the plasma, where they can undergo multiple ionisation reactions before thermalising back into the bulk electron population. The degree to which secondary electron heating is observed is proportional to the ion flux incident on the material surface and the sheath potential through which the secondary electrons are accelerated through. Secondary electron heating is also

sensitive to the geometry of the capacitive discharge[102,103], enabling spatially localised enhanced ionisation rates through the Hollow Cathode Effect (HCE)[102,103], this effect is discussed in more detail in section 1.6.1.

Having established that electron heating mechanisms are significantly affected by the phase-resolved movement of the plasma sheath, it is now important to discuss the ion heating mechanisms in capacitively coupled plasmas. In contrast to electron heating, ion heating is primarily dominated by the phase-averaged sheath behaviour, owing to their reduced mobility. This implies that, in non-magnetised plasmas[¶], the primary ion heating mechanism arises from electrostatic acceleration through the sheath potential gradient. Quantifying that last statement, if we consider a simplified system including only the electrostatic force on an ion of mass m_i accelerated through a constant sheath potential ϕ_S, then the average ion velocity is computable as equation 1.24:

$$\hat{v}_i = \left(\frac{2e\phi_S}{m_i}\right)^{1/2} \tag{1.24}$$

and hence the ion transit time τ_i across a phase-averaged sheath width of $\hat{S}_x$ is:

$$\tau_i = \frac{\hat{S}_x}{\hat{v}_i} = \hat{S}_x \left(\frac{m_i}{2e\phi_S}\right)^{1/2} \tag{1.25}$$

For cases where $\tau_{rf} << \tau_i$, (high-frequency regime) and in the absence of collisional effects, the resulting ion energy distribution function (IEDF) typically resembles a single peak centered at the phase-averaged plasma potential[105]. However, if the applied voltage frequency is reduced such that it is comparable to the ion transit time across the sheath $\tau_{rf} >> \tau_i$ (low-frequency regime), a bi-modal ion energy distribution is observed[106]. This effect arises due to the ions now responding directly to the varying sheath potenetial, with the greatest number of ions reaching energies corresponding to the extrema in sheath potential at the fully extended and fully collapsed sheaths[107]. It is clear therefore, that the degree to which the ion heating can be thought independent of the phase-resolved sheath dynamics depends upon the applied voltage frequency, the ion mass and the operating pressure[108].

1.5.3 Ion Energy Distribution Functions

The primary ion heating mechanism in rf-CCPs arises from acceleration through the phase-averaged sheath potential, as previously discussed. So far, the effect from collisions has been neglected, resulting in an effectively mono-energetic ion beam. In reality, ion-neutral collisional interactions play a significant role in determining the ion energy distribution function (IEDF) within the plasma sheath[109]. In cases where the plasma can be considered collisional,

[¶]The helical motion of ions in magnetised plasmas gives rise to additional resonant heating effects including, but not limited to, ion cyclotron resonance heating (ICRH) and Landau damping.

for example at higher pressures ($\geq$ 10 pa), the IEDF is significantly weighted towards the lower ion energies[110]. This shift results from the effects of ion scattering following ion-ion and ion-neutral collisions and from low energy neutrals entering the ion population through ion-neutral charge exchange collisions (see equation 1.14)[111]. Examples of heavy particle energy distribution functions in highly collisional, weakly collisional and collisionless plasmas are shown in figure 1.8.

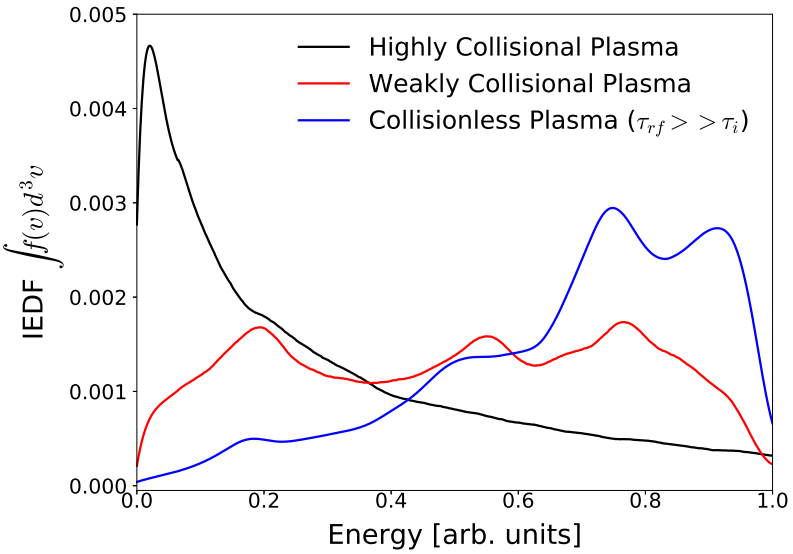

Figure 1.8: Examples ion energy distribution functions in a highly collisional plasma sheath (black), a weakly collisional plasma sheath (red) and a low-frequency regime ($\tau_{rf} >> \tau_i$) collisionless plasma sheath (blue).

As described previously, the IEDFs in highly collisional plasmas are weighted towards the low energies due to the high collision frequency, and hence short timescale over which energy is transferred through the ion population, i.e. the thermalisation timescale. Reducing the pressure of the system increases the mean-free-path and reduces the collision frequency, equations 1.15 and 1.16), leading to a reduction in the capability for highly energetic species to thermalise. As a result the IEDF of a weakly collisional plasma possesses multiple structures, the position and size of which are strongly dependant upon the specific operating conditions and sheath dynamics[112,113]. For the case shown in figure 1.8, the plasma exhibits a low energy structure predominately arising from collisional effects, and two high energy structures arising from resonances between the ion mean-free-path and the sheath potential. Reducing the pressure of the system yet further, such that the ion mean-free-path is of order the source geometry, results in an essentially collisionless ion population. IEDFs formed in collisionless conditions typically exhibit either one or two high energy peaks, as described previously, where the bi-modal structure exhibited in figure 1.8 indicates operation in the low-frequency regime ($\tau_{rf} >> \tau_i$).

The mathematical description of these distribution functions was initially developed

by Maxwell and given additional statistical rigour by Boltzmann. The resulting Maxwell-Boltzmann distribution function $f(v)$ describes the probability distribution of particle velocities (or energies) in a highly collisional highly entropic system [114], the general form of which when considering three spatial dimensions is shown in equation 1.26:

$$f(v)d^3\mathbf{v} = 4\pi \langle v_i \rangle^2 \left(\frac{m_i}{2\pi k_b T_i} \right)^{3/2} exp \left\{ \frac{-m_i \langle v_i \rangle^2}{2k_b T_i} \right\} d^3\mathbf{v} \tag{1.26}$$

where the velocity distribution function $f(v)$ is normalised[‖] such that:

$$\int_0^\infty f(v)d^3\mathbf{v} = n_i \tag{1.27}$$

Here, $d^3\mathbf{v}$ is an element of 3D velocity space (dv_x, dv_y, dv_z) and is dependant upon the geometry of the system, while m_i, $\langle v_i \rangle$ and T_i represent the mass, average velocity and translational temperature of species i, respectively. Assuming an isotropic velocity distribution, the mean velocity $\langle v_i \rangle$ of a species of particle with mass m_i can be described in terms of the first moment of the velocity distribution $f(v)$, shown in equation 1.28:

$$\langle v_i \rangle = \int_0^\infty v_i f(v) dv = \left(\frac{8k_b T_i}{\pi m_i} \right)^{1/2} \tag{1.28}$$

When discussing collisional interactions both the mean and modal velocities are of importance. The modal energy of a Maxwell-Boltzmann distribution $\hat{v}_i$ represents the energy at which the largest fraction of particles exist. Here, $\hat{v}_i$ is obtained as the positive real solution of the first differential of $f(v)$:

$$\frac{\mathrm{d}f(v)}{\mathrm{d}v} = 0 \implies \hat{v}_i = \left(\frac{2k_b T_i}{m_i} \right)^{1/2} \tag{1.29}$$

The modal energy becomes of importance when discussing particle species with flattened or arbitrarily structured energy distribution functions, where the mean energy may correspond to a region between structures, and therefore represents an insignificant number of particles. One final distribution function of importance when discussing energy distribution functions is the Gaussian $f_g(v)$ distribution, simply stated here for brevity:

$$f_g(v) = \left(2\pi v_\delta^2\right)^{-1/2} exp \left\{ \frac{-(v_i - \hat{v}_i^2)}{2v_\delta^2} \right\} \tag{1.30}$$

Here, $\hat{v}_i$ is both the mean and modal velocity and v_δ is the velocity variance, i.e. the square of the standard deviation of velocities from the mean. It is possible to quantitatively describe any reasonable particle energy distribution function through a linear combination of collisional and collisionless components described by equations 1.26 and 1.30, respectively [112].

[‖] Strictly speaking the probability distribution function is normalised to unity, multiplying by n_i is simply a convenient nomenclature.

For the case of the weakly collisional plasma in figure 1.8, the IEDF consists of a low energy Maxwellian component and two high energy Gaussian components. Controlling the IEDF within plasmas therefore relies on altering the relative contributions from collisional and collisionless effects. Recalling that collisional heating predominately arises from sheath edge effects and the majority of the collisionless acceleration depends upon the phase-averaged sheath potential, it becomes clear that controlling the sheath dynamics provides control of the resulting IEDF. Beyond varying the background pressure and gas species, control of the phase-resolved sheath dynamics can be achieved through the application and modulation of physical and electrical asymmetries.

1.6 Plasma Asymmetries

Thus far we have considered the formation of capacitively coupled plasmas in the context of the collective behaviour of their constituent particles, independent of the plasma source geometry. When addressing the formation of a plasma sheath only the behaviour adjacent to the powered electrode was considered. This simplified picture implicitly neglects charge continuity through the whole system. In this section, charge continuity and particle fluxes into all plasma interacting surfaces will be considered, enabling a consideration of asymmetrical behaviour and the formation of dc self-biases.

1.6.1 Physical Asymmetry

For the majority of plasma sources, there exists a physical asymmetry between the powered A_p and grounded A_g areas in contact with the plasma[11,79]. Discussing these asymmetries in terms of an equivalent circuit has the benefit that conserved quantities, such as currents, can be dealt with in a natural manner. An illustration of a simplified physically asymmetric plasma source and equivalent electrical circuit is shown in figure 1.9. Here collisional power deposition is accounted for by ohmic losses within the bulk, R_{bulk} and sheaths R_{sheath}. Electron inertia within the plasma bulk is modelled as an inductor L_{bulk}, and the powered and grounded sheaths, representing space charge regions, are modelled by capacitors of capacitance C_{sheath}.

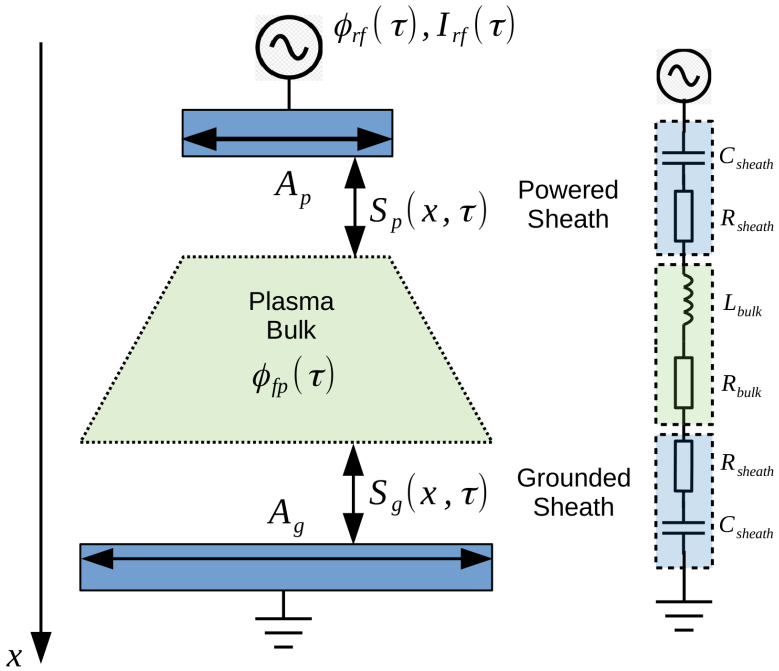

Figure 1.9: Illustration of an asymmetric capacitively coupled plasma, detailing powered and grounded electrode areas and sheath extents with an equivalent circuit diagram.

As previously discussed, for a plasma to maintain quasineutrality the total charge entering

and leaving the system must equate over an rf phase-cycle[99]. Current enters the system through powered surfaces, leaves through grounded surfaces and, for the purposes of this discussion, floating surfaces can be thought of as current neutral. Therefore, in the case shown in figure 1.9 where $A_g > A_p$, the current density towards the powered electrode must exceed that towards the grounded electrode. Increasing the current density at the powered electrode necessitates the formation of an additional accelerating potential at the powered electrode, this is the dc self-bias voltage[65,85]. The dc self-bias voltage therefore represents a difference between the voltage drop through the powered and grounded electrode sheaths. To quantify the voltage drop through a plasma sheath it is now useful to return to our circuit model, and beginning with a consideration of Child's law[79].

$$I_{rf}(\tau) = C\frac{\mathrm{d}\phi_{rf}(\tau)}{\mathrm{d}t} \tag{1.31}$$

Here, $\phi_{rf}(\tau)$ and $I_{rf}(\tau)$ are the instantaneous voltage and current through a capacitor of capacitance C. The voltage drop across a capacitor can therefore be represented through an integration of equation 1.31:

$$\phi_{rf}(\tau) = C^{-1}\int_0^\tau I_{rf}(\tau)\mathrm{d}t \tag{1.32}$$

Modelling the powered electrode sheath in figure 1.9 as a capacitor, where $C_p = \epsilon_p A_p/\hat{s}_p$, the phase-averaged voltage drop through the powered sheath $\hat{\phi}_{Sp}$ is given by equation 1.33:

$$\hat{\phi}_{Sp} = \frac{\hat{S}_p}{\epsilon_p A_p}\int_0^\tau I_{rf}(\tau)\mathrm{d}t \tag{1.33}$$

Here, $\hat{S}_p$ represents the phase-averaged powered sheath extent, A_p is the powered sheath area in contact with the plasma and ϵ_p is the relative permittivity within the powered electrode sheath. Equation 1.33 is true for all sheaths, employing electrode area A_x, phase-averaged sheath extent $\hat{S}_x$ and relative permittivity ϵ_x for the x'th sheath. Recalling that the dc self-bias voltage η_{dc} forms to maintain charge fluxes to each surface (equation 1.17), it must therefore vary in proportion to the potential drop through the powered and grounded sheaths, given by:

$$\eta_{dc} \propto \frac{\hat{\phi}_{Sp}}{\hat{\phi}_{Sg}} = \frac{\frac{\hat{S}_p}{\epsilon_p A_p}\int_0^\tau I_{rf}(\tau)\mathrm{d}t}{\frac{\hat{S}_g}{\epsilon_g A_g}\int_0^\tau I_{rf}(\tau)\mathrm{d}t} \tag{1.34}$$

Enforcing current continuity through all surfaces and approximating $\epsilon_p \approx \epsilon_g$, we obtain:

$$\eta_{dc} \propto \frac{\hat{\phi}_{Sp}}{\hat{\phi}_{Sg}} \approx \frac{A_g}{A_p}\frac{\hat{S}_p}{\hat{S}_g} \tag{1.35}$$

A more rigorous treatment, detailed in Ref. 79, involves a consideration of the charge

distribution within the sheath and arrives at a similar solution, albeit the dc self-bias voltage varies super-linearly with respect to the electrode area:

$$\eta_{dc} \propto \left(\frac{A_g}{A_p}\right)^k \left(\frac{\hat{S}_{Sp}}{\hat{S}_{Sg}}\right) \tag{1.36}$$

Finally, substituting equation 1.22 for $\hat{S}_p$ and $\hat{S}_g$, we obtain:

$$\eta_{dc} \propto \left(\frac{A_g}{A_p}\right)^k \left(\frac{\hat{n}_{i,g}}{\hat{n}_{i,p}} \frac{\hat{\phi}_{Sp}}{\hat{\phi}_{Sg}}\right)^{1/2} \tag{1.37}$$

Here the coefficient k may be analytically computed as $k = 4$, however in practice $2 \lessapprox k \lessapprox 3$ and depends upon the precise geometry of the reactor, the electrode materials and the volume of the reactor vessel[79]. Equation 1.37 indicates that, in addition to the physical asymmetry, the dc self-bias voltage varies with respect to the ion density distribution and the variation in sheath potential between the powered and grounded electrodes. These relations are demonstrated in figure 1.10, showing the powered electrode dc self-bias voltage in a parallel plate geometry for varying electrode area ratios, varying applied voltage amplitudes and varying background pressures in argon.

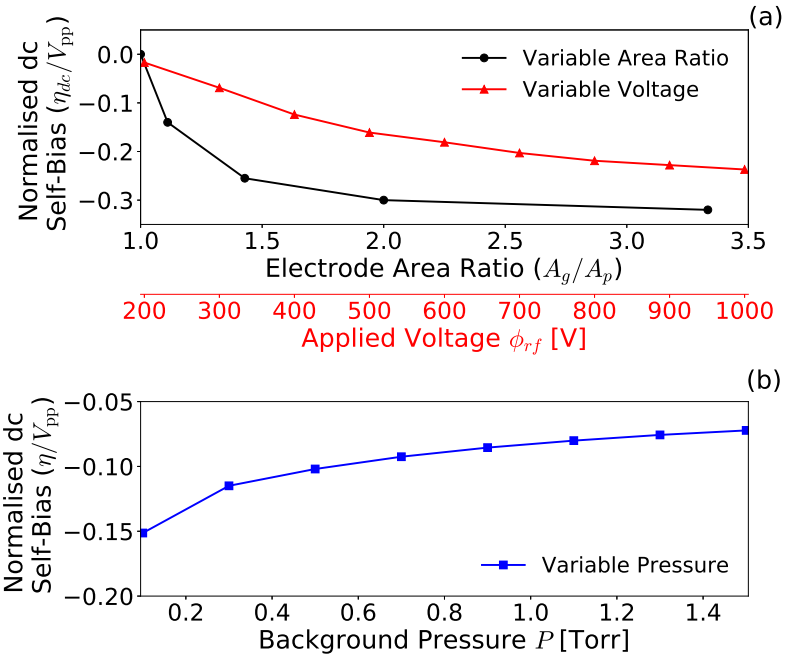

Figure 1.10: Normalised dc self-bias voltage at the powered electrode with respect to (a) the grounded to powered electrode area ratio (A_g/A_p) and applied voltage amplitude ϕ_{rf} and (b) the background pressure P in a parallel plate CCP discharge. Conditions: 13 - 200 Pa (0.1 - 1.5 Torr) in argon, 200 - 1000 V at 13.56 MHz.

Reducing the powered electrode area in figure 1.10 (a) increases the grounded to powered

area ratio (A_g/A_p) and results in the formation of a negative dc self-bias voltage on the powered electrode. This bias forms to enforce the equal positive flux through both the grounded and the now smaller powered electrode areas, as previously discussed. The dc self-bias voltage exhibits a strong correlation with the electrode area ratio, consistent with the theoretical treatment in equation 1.37, converging towards $\eta_{dc} \approx -0.35\ V_{pp}$ for increasing grounded electrode area. Increasing the applied voltage amplitude, for a fixed grounded to powered electrode ratio ($A_g/A_p = 1.0$), results in the formation of a negative dc self-bias voltage, exhibiting a similar trend as before, albeit with a reduced proportionality. As power is primarily deposited within the powered electrode sheath, the ion density adjacent to the powered electrode increases at a faster rate than that adjacent to the grounded electrode. While this alone is enough to enforce a dc self-bias voltage, the increased ion density adjacent to the powered electrode reduces the powered electrode sheath extent, see equation 1.22. This results in an increased powered electrode sheath capacitance, and therefore the potential drop through the narrower powered electrode sheath must be greater than through the wider grounded sheath, see equation 1.32, leading to a variation in the dc self-bias voltage[115]. Increasing the background pressure for a fixed electrode area ratio ($A_g/A_p = 1.0$) for a 500 V discharge, shown in figure 1.10 (b), results in a reduction in the magnitude of the dc self-bias voltage. An increased background pressure results in an increased ion density, reducing both the powered and grounded sheath widths at approximately the same rate. As it is the relative difference which determines the capacitive portion of the physical asymmetry, see equation 1.36, the magnitude of the dc self-bias voltage subsequently reduces.

Building upon the theory presented in equation 1.37 and the relationships observed in figures 1.10 (a) and (b), it can be seen that the magnitude of the dc self-bias voltage is maximised for high voltage, low pressure asymmetric discharges. These constraints have lead to the development of the hollow cathode source geometry, which forms the source geometry relevant to this work, introduced in more detail in section 2.1.1.

1.6.2 The Hollow Cathode Effect

Hollow cathode discharges are typically characterized by a hollow annular powered electrode cavity electrically connected to a larger grounded area and can be operated with radio-frequency[116] or dc[117] power. They are employed over a wide range of pressures from atmospheric[118] to high vacuum[100,119,120] and can form part of the gas source[71,121] or operate external to it[103,122]. Hollow cathodes are employed a large variety of industrial processes including: etching and deposition[116,123], CO_2 dissociation[124], light sources[125] and spacecraft propulsion[34,43,65,126]. A representative example of a capacitively coupled discharge within a hollow cathode geometry is shown in figure 1.11.

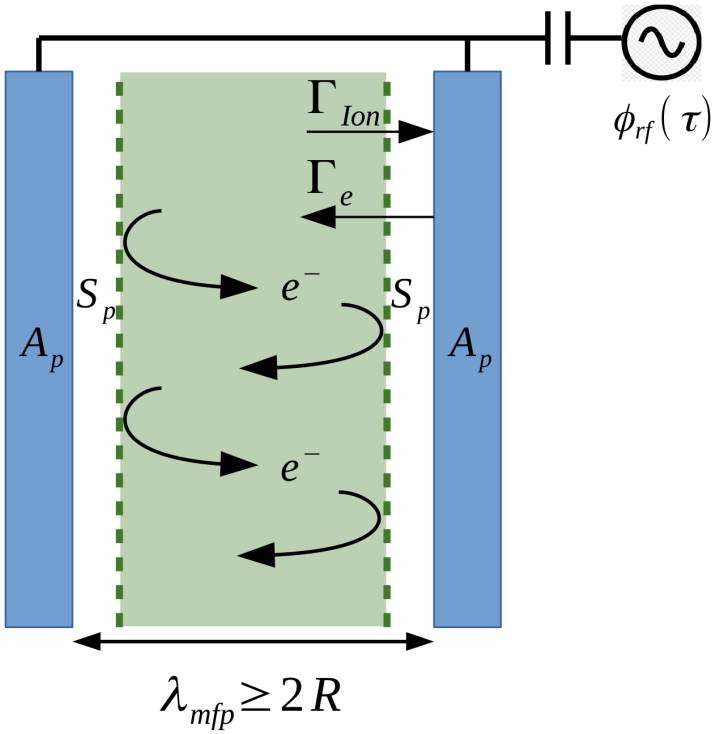

Figure 1.11: Illustration of an hollow cathode geometry capacitively coupled plasma, detailing hollow powered electrode, radial sheath extents and ion induced secondary electron emission with reflected electron trajectories.

For *pd* (pressure × distance) values in the range of 0.01 - 10 Torr cm the hollow cathode effect (HCE) can be initiated, resulting in a large increase in plasma density for a given voltage[103,117,127]. This capability to locally increase the plasma density adjacent to the powered electrode, coupled with the inherent physical asymmetry, enables the formation of substantial dc self-bias voltages in hollow cathode sources[65,113]. One of the proposed mechanisms of the HCE arises from the pendular motion of electrons produced within the electrode cavity, illustrated in figure 1.11, resulting in an increased number of ionisation events per secondary electron[100]. Positive ions impacting on the inside surface of the hollow cathode produce secondary electrons that are subsequently accelerated through the plasma sheath[101]. These electrons typically have non-thermal 'beam-like' energy distributions with a mean energy much higher than electrons produced through collisions in the plasma bulk. These high energy electrons reflect from the opposite cathode sheath, return to the original sheath, and reflect again leading to pendular motion within the cavity. Note that pendular motion requires suitably energetic electrons such that 1) their mean-free-path λ_{mfp} is greater than the diameter of the source and 2) the electron transit time across the source diameter be shorter than the rf phase period. Pendular electrons predominately slow by ionisation collisions which, when coupled with the higher specific power deposition of the pendular motion, produces a high plasma density[100,127]. Hollow cathodes operated at low pressures ($\leq$ 13 Pa) can also enforce higher electron energies by enhancing the maximum sheath

expansion within/adjacent to the hollow cathode cavities[122].

While hollow cathode geometries have been shown to enhance the ion and electron heating mechanisms, they represent a somewhat inflexible solution. The geometry of a hollow cathode source cannot be easily modified in real-time, limiting the control achievable over the HCE and resulting discharge parameters. The extent of the HCE has been shown to vary with respect to the dc self-bias voltage present on the cathode surface[65,102,103]. Therefore, methods enabling remote variation of the dc self-bias voltage, and thereby controlling the HCE, are of interest. Control of the dc self-bias, and hence the HCE, via the application of multi-harmonic or tailored voltage waveforms represents a promising mechanism to influence the ionisation and particle heating mechanisms in hollow cathode plasma sources.

1.6.3 The Electrical Asymmetry Effect

A dc self-bias voltage may also be achieved through purely electronic means by use of multi-frequency or 'tailored' rf waveforms through the 'Electrical Asymmetry Effect' (EAE) [87,128,129]. The concept of multi-frequency driven plasmas was first demonstrated by Goto *et. al.* in 1990 [130] and expanded upon subsiquently [131]. Through applying a high frequency to the powered electrode and a second lower frequency to the grounded electrode, control of the dc self-bias voltage present on a substrate on the grounded electrode was achieved. While plasma sources employing waveforms supplied by separate power supplies are still employed, tailored voltage waveforms are typically supplied to the powered electrode as a single arbitrary voltage waveform. By tailoring the applied voltage waveform it is possible to independently control parameters such as plasma density, electron and ion energies and ion flux incident upon the electrode [132–134]. Such independent control is not achievable through single frequency operation as any increase in the plasma density is nessecarily achieved through an increased applied voltage, which will consequentially also increase the ion acceleration through the sheath [135]. This limitation is demonstrated in figure 1.12, as reproduced from Ref. 105, showing the mean ion energy respect to the ion flux incident upon the powered electrode in a parallel plate discharge for varying single frequency operation between 13.56 MHz to 81.36 MHz.

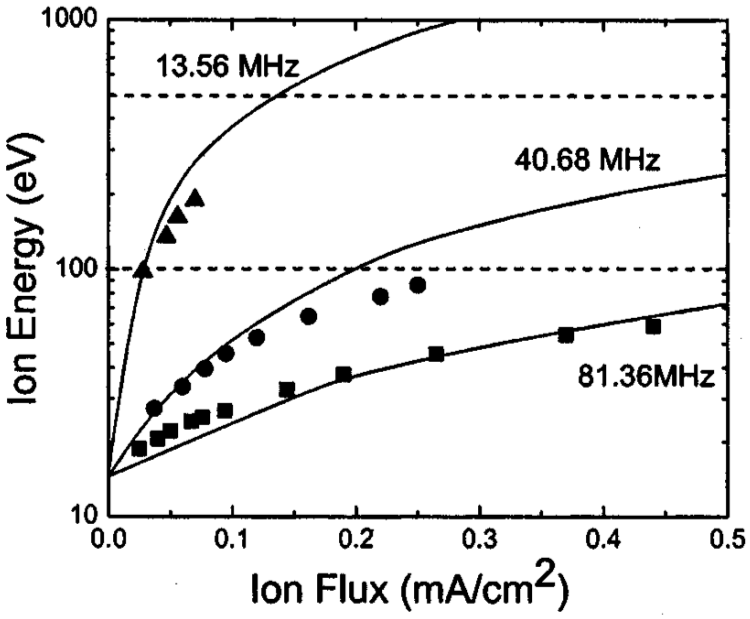

Figure 1.12: Plot illustrating the relationship between the mean ion energy and the ion flux in for varying voltages at three applied voltage frequencies. Reproduced with permission from Perret *et. al.*, Ref. 105, Appl. Phys. Lett. 86 021501. Copyright 2005 American Institute of Physics.

Figure 1.12 demonstrates that, for a single frequency discharge, the range of ion fluxes and ion energies attainable lie along a single line. Varying the applied frequency alters the

shape and gradient of this line but does not provide a wider range over any other applied frequency. As an example, excitation at 13.56 MHz is capable of achieving high ion energies but not high fluxes, while excitation at 81.36 MHz attains high fluxes at the expense of high energies. In addition, practical concerns such as the substantial variation in the matching required to encompass such a wide range of applied voltage frequencies results in control via varying single frequency operation becoming intractable.

For the purposes of electrothermal propulsion, discrete control of the ion flux and ion energy is desired. The capability to optimise the ion energy for desired particle interactions, for example ion-neutral collisions, while independently maximising the ion flux is of particular interest. In this work, discrete control of the dc self-bias voltage, and hence mean ion energy and flux, in capacitively coupled rf plasmas is achieved through the application of multiple voltage harmonics with varying phase offsets to produce distinct rf waveforms that exhibit either amplitude or slope asymmetries[128,136–138]. Such 'tailored' voltage waveforms present the capability to transition between the fixed ion energy and flux curves shown in figure 1.12, broadening the range of accessible ion energy and flux combinations.

This investigation focuses on tailored voltage waveforms that consist of two components, a fundamental frequency (typically 13.56 MHz) and one of its harmonics[87,128]. Aspects specific to these dual-frequency waveforms will be addressed in more detail in chapter 5, a more general introduction to tailored voltage waveforms is briefly presented here. By adjusting the phase shift between successive harmonics, it is possible to influence the dc self-bias voltage through altering the electrical asymmetry of the rf waveform[87]. As the applied voltage waveforms employed here comprise exclusively of harmonics of a fundamental frequency, they can be described by the following equation[138]:

$$\phi_{\mathrm{rf}}(t) = \sum_{k=1}^{n} \left(\frac{\phi_0}{n}\right) \sin(k\omega_0 \mathrm{t} + \theta_k) \tag{1.38}$$

Where, $\phi_{\mathrm{rf}}(t)$ is the time dependent voltage of the combined waveform, ϕ_0 is its maximum amplitude, $\omega_0 = 2\pi\nu_0$ is the fundamental angular frequency, θ_k is the phase offset of harmonic k and n is the total number of applied harmonics. For a sufficient number of harmonics, any desired waveform profile can be generated in this fashion by individually tailoring the desired amplitudes and phases[138]. The 'magnitude' of the EAE produced via application of an arbitary tailored voltage waveform can be described through the symmetry parameter[139], ϵ_s, as shown in equation 1.39.

$$\epsilon_s = \frac{\hat{n}_{Sp}}{\hat{n}_{Sg}} \left(\frac{Q_{Sg}}{Q_{Sp}}\right)^2 \left(\frac{A_p}{A_g}\right)^2 \frac{I_{Sg}}{I_{Sp}} = \left|\frac{\phi_{Sg}}{\phi_{Sp}}\right| \tag{1.39}$$

Here, $\hat{n}_{Sp}$, $\hat{n}_{Sg}$ are the sheath averaged ion densities, Q_{Sg}, Q_{Sp} are the maximum electrode surface charges, A_p, A_g represent electrode surface areas, ϕ_{Sg}, ϕ_{Sp} are the maximum voltage drops across each respective sheath, where subscripts p and g denote the powered

and grounded electrodes, respectively. The parameters I_{Sp} and I_{Sg} are represent the sheath integrals, defined as:

$$I_{Sx} = 2\int_0^1 \frac{n_i(x)}{\hat{n}_{Sx}}\xi \; d\xi \qquad \text{where} \qquad \xi = \frac{x}{S_x} \tag{1.40}$$

where S_x is the maximum sheath extension. The dc self-bias voltage η_{dc} resulting from an EAE of magnitude ϵ_s, can be readily calculated through an application of Kirchhoff's law[140]. The result for the typical case where the change in voltage across the plasma bulk is very small is shown in equation 1.41.

$$\eta_{dc} = -\frac{\phi_{rf}^{+} + \epsilon_s \phi_{rf}^{-}}{1+\epsilon_s} \tag{1.41}$$

Where, ϕ_{rf}^{+} and ϕ_{rf}^{-} are the maximum and minimum amplitudes of the applied voltage waveform respectively. Here, we are assuming a larger grounded electrode area than powered electrode area resulting in a negative dc self-bias voltage at the powered electrode.

Ignoring losses due to ion collisions, the resulting energy gained by an ion accelerated through the phase-averaged powered (equation 1.42) and grounded sheaths (equation 1.43) are therefore given by:

$$E_i = \hat{\phi_S} + \eta_{dc} = \frac{1}{2}\phi_{rf}^{+} \tag{1.42}$$

$$E_i = \hat{\phi_S} = \frac{1}{2}\left|\phi_{rf}^{-}\right| \tag{1.43}$$

Where symbols are as previously described. Note that in practice the ion energies vary throughout the rf phase cycle with respect to $\phi_S(\tau)$, equations 1.42 and 1.43 represent mean expected energies. Separate control of the ion flux and ion energy can be achieved in a two harmonic system by offsetting the phase angle of the two harmonics. Increasing this offset has the effect of linearly changing the ion energy, by altering η_{dc}, while keeping the ion flux approximately constant[136,138]. However, in reality this control is not completely independent as varying the dc self-bias voltage also influences ionisation mechanisms, such as secondary electron energies, resulting in slightly altered ion densities and fluxes. The introduction of three or more harmonics allows for a finer control over the ion energy distribution, increasing the separation achieved[141,142]. The efficiency of multi-harmonic 'tailored' waveform capacitive plasma systems has been limited as matching networks typically reflect much of the power applied outside of a single frequency. However, recent experimental work on multiple frequency phase matching has shown positive results for up to three harmonics[143]. Continued work and optimization of tailored voltage waveforms for plasmas is being performed for both industrial and propulsion based applications[102,137,144].

1.7 Thesis Outline

The remainder of this thesis is arranged as follows:

Chapter 2 introduces key concepts relevant to *low-temperature* plasma diagnostics and outlines the experimental methodologies and numerical techniques employed in this work, detailing their advantages and limitations.

Chapter 3 discusses the electron, ion and neutral gas heating mechanisms in the *Pocket Rocket*. Experimental validation of the employed 2D fluid/Monte-Carlo hybrid numerical model is presented for operation at 13.56 MHz.

Chapter 4 investigates the effects on the neutral gas heating and IEDF within the powered electrode sheath region with increasing applied rf frequency through experimentally validated simulations. The formation of structured IEDFs is discussed with respect to the interaction between the ion mean-free-path and phase-averaged sheath extent.

Chapter 5 considers the effects of dual-frequency tailored voltage waveforms on the rf power deposition and neutral gas heating when employed in the *Pocket Rocket*. The prospect of variable thrust and specific impulse are considered within a laboratory context.

Chapter 6 summarises the key conclusions and proposes a roadmap for future research.

Chapter 2

Numerical & Experimental Methodologies

This chapter introduces the numerical and experimental techniques employed in this work. The operating principles of the York-based *Pocket Rocket*, an rf capacitively coupled hollow cathode microthruster, are introduced. The experimental set-up and apparatus, including the rf power circuit, power measurement techniques and voltage waveform tailoring method are detailed. Phase resolved optical emission spectroscopy (PROES) is introduced with a consideration of the assumptions made when comparing to the numerically obtained comparisons. This is followed by an overview of the range of numerical approaches commonly employed to simulate radio-frequency plasmas, after which the model employed in this work, the Hybrid Plasma Equipment Model (HPEM), is introduced. The principles of the fluid and kinetic modules in HPEM are discussed in detail, with specific consideration given to the determination of plasma collisionality and the applicability of the fluid solvers within different regions of the simulation geometry. Finally, a two step method for the determination of steady-state material temperatures is introduced and the method by which thrust and specific impulse are computed is presented.

2.1 Experimental Methodologies

In this section the experimental set-up and measurement methodologies are introduced and discussed. The operating principles of the York based radio-frequency capacitively coupled microthruster source, the *Pocket Rocket*, are introduced and the range of operation is detailed. An overview of the optical and electrical equipment employed in this work is given, including a discussion of the method by which tailored voltage waveforms are created and introduced into the source. Finally, the primary optical diagnostic employed in this study, phase-resolved optical emission spectroscopy (PROES) is detailed with reference to the corona model, including any necessary assumptions made in the analysis.

2.1.1 The *Pocket Rocket* Microthruster

Introduced in section 1.3.2, the *Pocket Rocket* source is a low power ($\leq$ 50 W) asymmetric radio-frequency capacitively coupled electrothermal microthruster[71,74,76,145,146]. The thruster is conventionally powered by a 13.56 MHz rf voltage resulting in a weakly ionised ($\approx$ 0.01% ionisation fraction) plasma, facilitating the coupling of electrical energy into the propellant[70]. Thrust is produced by the expulsion of hot ($\geq$ 1000 K) neutrals, themselves heated via ion-neutral charge exchange collisions within the plasma bulk and sheaths[72]. A cutaway schematic highlighting the key components of the *Pocket Rocket* is shown in figure 2.1.

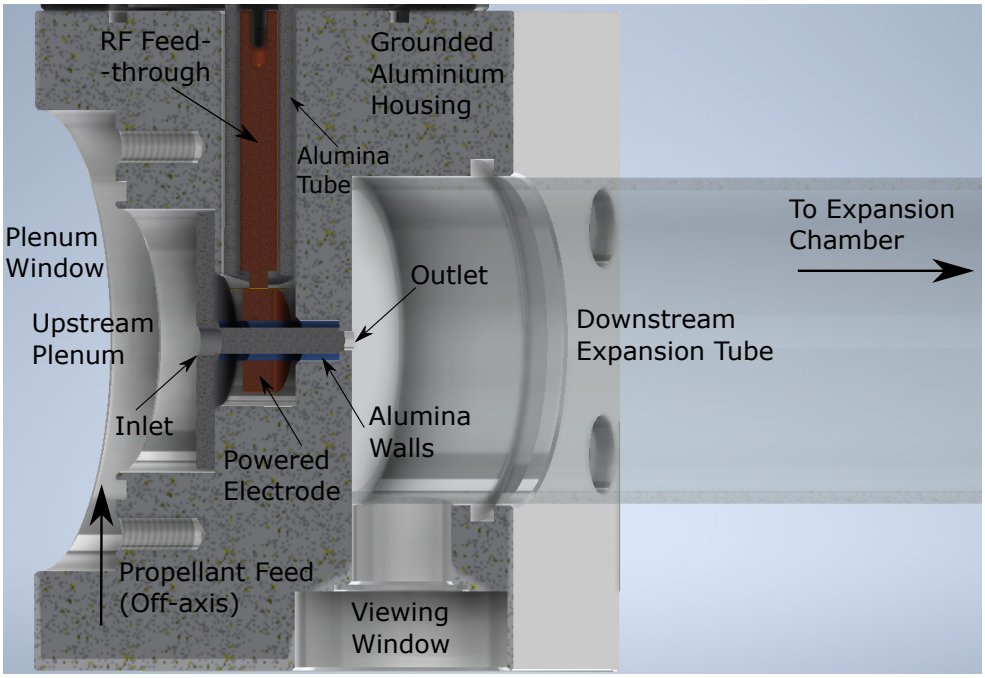

Figure 2.1: Cutaway schematic illustrating the key components of the *Pocket Rocket* rf electrothermal microthruster. The housing is formed of aluminium, containing a copper rf feedthrough isolated by an alumina sleeve and connected to the annular powered electrode. The powered electrode is insulated by a macor housing (not shown) and seperated from direct contact with the plasma by an alumina tube, which serves as a dielectric barrier.

The *Pocket Rocket* source facilitates the coupling of electrical power into neutral propellant through ion-neutral charge exchange collisions, where the ions primarily serve as an intermediary. Ions within the thruster source are radially accelerated through the sheath potential, enhanced by means of a dc self-bias voltage that forms as a negative surface charge on the insulating alumina dielectric walls, located between the plasma and the powered electrode. This negative dc self-bias voltage forms due to the physically asymmetric geometry of the *Pocket Rocket*, and enforces equal positive and negative charge loss to both the smaller powered electrode and larger grounded electrode areas[9], see section 1.6. The requirement for equal net charge loss through the smaller powered electrode area maintains a significant positive ion flux through the powered electrode sheath[132]. Ions accelerated through the sheath potential collide with neutral propellant traversing the axial pressure gradient, resulting in neutral heating via ion-neutral charge exchange[73], generating thrust.

Relatively few ions are capable of escaping the thruster due to the substantial radial acceleration within the source arising from the dc self-bias voltage, ambipolar forces then constrain the electrons. The outlet plume is therefore effectively charge neutral, removing the requirement for an additional external neutralizer[71,72]. With no need for an external neutralizer, the size, complexity and power requirements of the Pocket Rocket are reduced relative to other, non-charge neutral, EP sources[64]. Ions impacting the radial wall can release secondary electrons through the Auger process[104]. These electrons are then accelerated away

from the wall back into the plasma through the sheath potential, reaching high energies ($\geq$ 50 eV)[73,88] relative to the ionisation potential of the propellant (15.76 eV for argon)[74]. Secondary electrons can therefore undergo multiple ionisation interactions, resulting in a locally increased plasma density. The hollow cathode geometry of the *Pocket Rocket* source (see section 1.6.2) amplifies this effect as secondary electrons, capable of traversing through the bulk plasma, are reflected from the opposite sheath and back into the bulk, further increasing their ionisation efficiency.

The *Pocket Rocket* is typically operated within an intermediate pressure regime, between 133 - 666 Pa (1 - 5 Torr), as this represents the Paschen minimum for ignition[126]. This results in a relatively steep pressure gradient through the thruster during operation, typically terminated by a *choked* or *shocked* flow region where the neutral axial velocity exceeds the local sound speed[66,76]. The formation of this shocked boundary prevents downstream conditions from affecting the upstream pressure gradient and therefore the conditions within the source can be considered effectively independent of those in the expansion region.

The *Pocket Rocket* has been observed to operate in two modes, a low-powered α-mode, sustained through ionisations during sheath expansion and contraction, and hence show plasma heating at phases of peak temporal voltage modulation (dV/dt)[9]. And a high-powered γ-mode, where the plasma is sustained through ionisation by ion bombardment induced secondary electrons and hence exhibits plasma heating at phases corresponding to the most negative applied voltage. Secondary electrons typically exhibit a non-thermal energy distribution and primarily deposit power into the plasma through ionisation collisions, as compared to elastic or excitation interactions[102,103]. Operation in γ-mode is desirable due to the enhanced ionisation from secondary electrons, leading to higher positive ion fluxes and higher neutral gas temperatures[65].

2.1.2 *Pocket Rocket* Experimental Apparatus

The majority of this thesis describes the effects on plasma heating mechanisms within the *Pocket Rocket* microthruster operated employing a variety of single and multi-frequency rf voltage waveforms. This work is achieved in tandem through experimental and numerical analysis, where experimentally obtained measurements are employed to validate the numerical models. The experimental set-up and apparatus employed in this study are shown in figure 2.2.

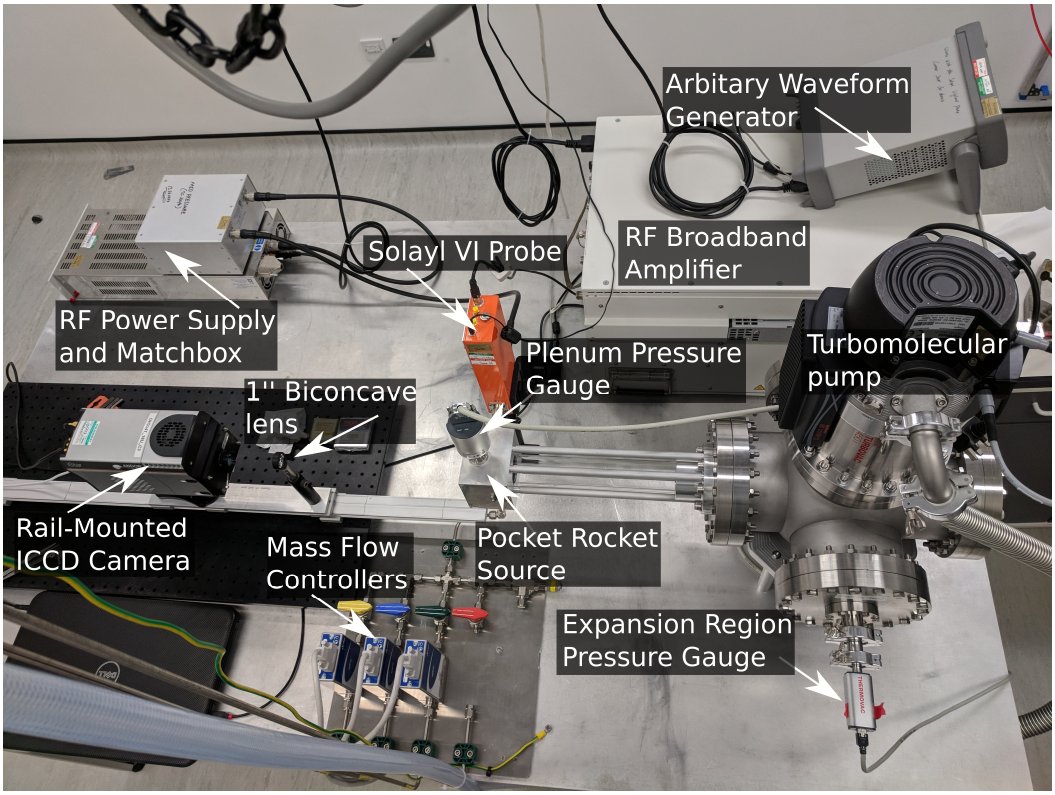

Figure 2.2: The experimental set-up and apparatus employed in this study.

The apparatus employed in this study can be broken down into three key sub-components: 1) The gas supply and vacuum system, 2) the rf power circuit, including the *Pocket Rocket*, and 3) the optical and electrical diagnostics. The *Pocket Rocket* source, power coupling circuit and optical configuration are illustrated in figure 2.3. The thruster consists of an 18 mm long, 4.2 mm inside diameter, 1.0 mm thick, alumina tube through which propellant is passed. A 5 mm long copper electrode is positioned around the midpoint of this tube, supported in a macor housing, and two grounded aluminium rings, of length 4 mm and 2 mm, are positioned around the inlet and the outlet, respectively. The grounded electrodes are separated by 3 mm and 4 mm from the powered electrode on the downstream and upstream sides, respectively. The source is mounted to, and electrically isolated from, an expansion chamber by a 300 mm long Pyrex glass tube. The system is operated in vacuum, where a base pressure of 1.33 Pa (0.01 Torr) is achieved employing the use of a scroll pump (not shown). Gas is introduced through a plenum at the upstream side of the source. The operating pressure is measured by a gauge fitted to the plenum and a Pyrex glass window positioned at the rear of the plenum enables optical access along the axial length of the source. When employed in argon a plenum pressure of between 186 - 226 Pa (1.4 - 1.7 Torr) is typical for a 100 sccm (1.786 mg min^{-1}) flow-rate, resulting in a downstream expansion chamber pressure of 113 Pa (0.85 Torr).

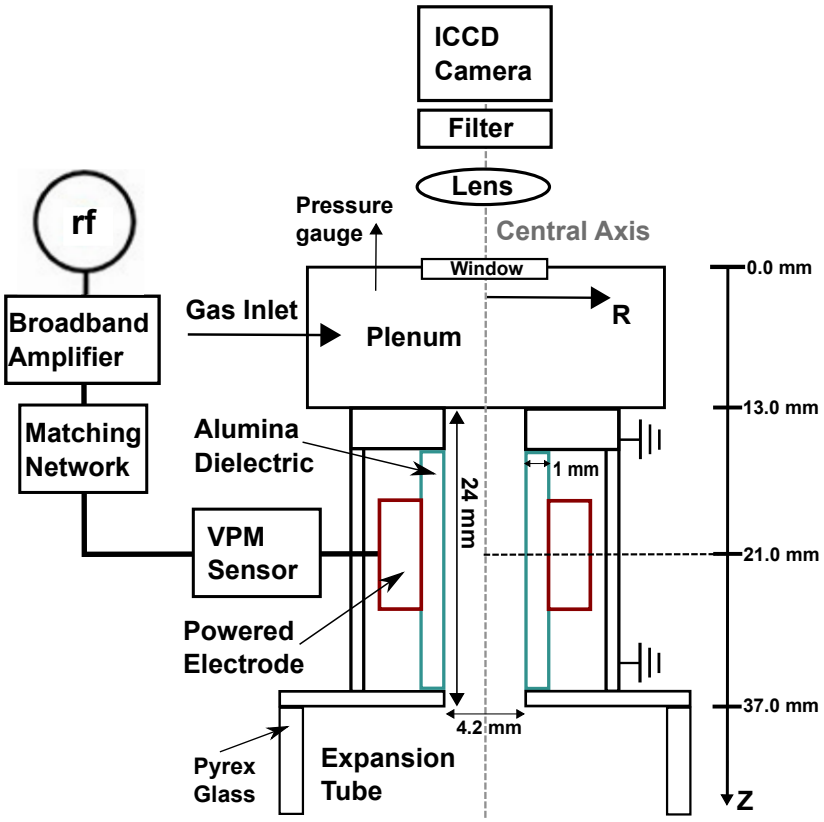

Figure 2.3: Schematic of the *Pocket Rocket* source (not to scale), including the power coupling circuit and the orientation of the optical equipment with respect to the plasma source.

Power can be supplied via a dedicated fixed frequency power supply or via an amplified arbitrary seed voltage waveform, the latter method is employed unless otherwise specified. Typical operation of the source involved the application of a 13.56 - 40.68 MHz driving voltage frequency at between 120 - 450 V voltage amplitude supplied via an external circuit comprising: an arbitrary waveform generator (Keysight 33621A, 120 MHz), broadband amplifier (IFI SCCX100, 0.01 - 220 MHz) and matching network (Coaxial Power Systems MMN150), connected as shown in figure 2.3. Voltage, current and power are measured with a SOLAYL SAS Vigilant Power Monitor (VPM)[147], placed in series directly before the source. Power deposited into the plasma is obtained via the subtractive method, as the difference between the power deposited with and without a gas flow at a fixed applied voltage.[148,149].

Tailored voltage waveforms were constructed through the superposition of up to five harmonics of 13.56 MHz with varying phase and amplitude offsets resulting in the desired waveform shape. When employing tailored voltage waveforms a feedback system between the arbitrary waveform generator, the Solayl SAS probe and a software suite was employed as shown in figure 2.4.

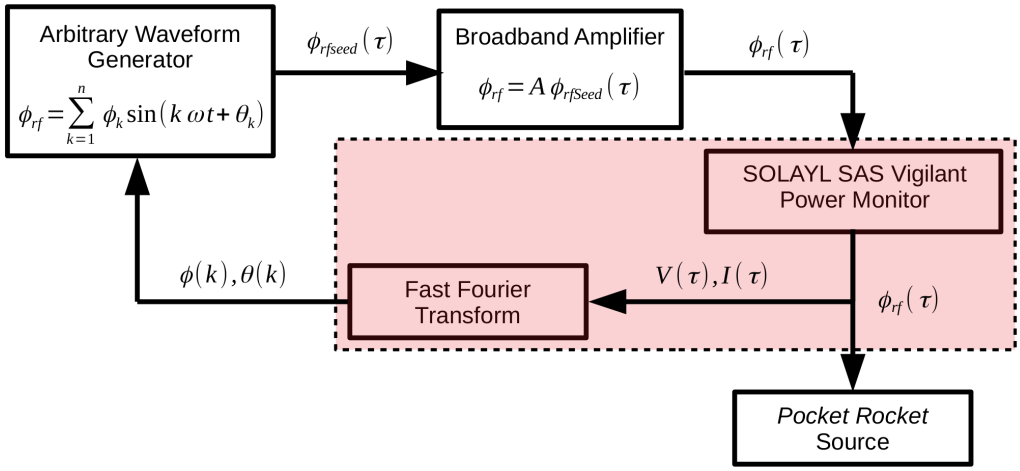

Figure 2.4: Schematic of the tailored voltage waveform feedback mechanism, sections employing the Solayl SAS monitoring probe or associated software are highlighted in red.

The feedback system is employed as follows, first a desired waveform shape is determined in the solayl software by manually specifying the desired harmonic amplitudes $\phi(k)$ and phase offsets $\theta(k)$. The harmonic components are superimposed in the arbitrary waveform generator, creating a tailored seed waveform ϕ_{rfSeed}, where typically $\phi_{rfSeed} \leq 1$ V. The seed waveform is amplified to the desired voltage amplitude before passing through the Solayl SAS monitor and onto the *Pocket Rocket* source. If all electrical components were perfectly matched this system alone would be sufficient, however impedance mismatches between the rf circuit and the plasma, as well as non-white noise imparted during the amplification stage, deforms the tailored waveform en-route to the *Pocket Rocket*.

Reduction of this deformation is achieved through taking real-time fast Fourier transforms (FFT) of the waveform voltage and current signals measured by the Solayl probe. The difference between the input harmonic components $\phi(k)$ and $\theta(k)$ and the measured harmonic components post amplification are employed to modify the next iteration of input components, attempting to compensate for the impedance mismatches. This iterative loop is repeated until the measured waveform shape conforms to the desired input shape. The feedback loop can then be disabled during measurement, and/or re-enabled should the impedance of the system change (during an α - γ mode transition for example), ensuring that the waveform shape and amplitude remains constant. This feedback mechanism enabled the generation of tailored voltage waveforms within $\approx 2-5\%$ of the desired amplitude and temporal shape.

2.1.3 Phase Resolved Optical Emission Spectroscopy

The optical emission from the thruster is measured with respect to time within the rf voltage cycle by phase-resolved optical emission spectroscopy (PROES) [150,151]. This technique provides information on the ionisation and excitation dynamics of phase-dependent species,

i.e. electrons, in the discharge[140]. Here, optical emission from the Ar($2p_1$ - $1s_2$) transition at 750.4 nm is measured in phase with the driving voltage. This state is chosen as it is predominately ($\geq$ 90%) populated from the ground state by direct electron impact excitation[152,153]. The phase resolved optical emission is post-processed to extract the electron impact excitation rate of the Ar($2p_1$) state, enabling direct comparison to simulation.

The PROES set-up consists of a 1" biconcave lens positioned in-front of the plenum window, which produces an image of the plasma focused at the midpoint of the alumina tube, shown in figure 2.3 as a dotted line. Images are recorded by an ICCD camera (Andor iStar DH344T-18U-73, 1024 $\times$ 1024 array, pixel size: 13 $\times$ 13 μm^2), fitted with a 750.466 nm bandpass filter (LOT-QuantumDesign, 1 nm FWHM), which is positioned at the focal point of the lens. Phase-resolved images are obtained by triggering the camera on the output of arbitrary waveform generator and a digital delay generator (Stanford Research Systems DG645) in series provides a variable delay τ_{Delay} in the triggering time. Figure 2.5 illustrates the PROES technique over two rf cycles.

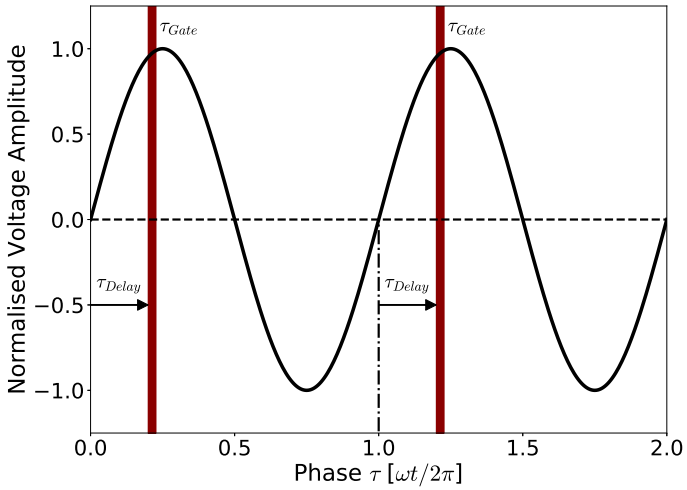

Figure 2.5: Illustration of the PROES diagnostic technique over two rf cycles, showing the optical gate width τ_{Gate} and the digital delay between successive exposures τ_{Delay}.

PROES images in this study are taken with an optical gate width τ_{Gate} = 1.7 ns at a sampling frequency of 500 kHz for a total integrated exposure time of $\tau_{Exposure}$ = 100 ms. Following this, the delay is stepped forward by 2.0 ns and the exposure repeated, building up a series of images representing the temporally resolved emission, where each image corresponds to the average of $\tau_{Exposure}/\tau_{Gate} \approx 5 \times 10^7$ rf cycles. As the ICCD camera is aligned axially with the source, the measured optical emission is integrated along the axial line-of-sight within the source. In addition, as the plasma is optically thin at the wavelengths of interest, emission from the full length of the source region is able to reach the camera. Therefore, the experimental depth of field (DoF) was assumed to be 24 mm, equal to the axial length of the source region. To a reasonable approximation, the contribution of the DoF can be considered

flat with respect to axial depth[154]. To replicate a 24 mm DoF in simulated PROES images, discussed in detail in section 3.1, the simulated excitation is integrated 12 mm either side of the simulated imaging plane, parallel to the source axis.

The PROES diagnostic relies upon the corona model describing the change in populations of excited and ionised states for a system under partial-local thermodynamic equilibrium[79]. The change in population of an excited state n_i at any given time is described by a system of coupled differential equations. These include the electron impact excitation rate from ground to level i, the sum of the excitation rates from metastables to level i, the sum of the cascade contributions due to de-excitation from levels above i and the decay rate from level i as described in equation 2.1:

$$\frac{\mathrm{d}n_i(t)}{\mathrm{d}t} = \overbrace{n_0 E_{i,0}(t)}^{\text{Direct Transition}} + \overbrace{\sum_m n_m E_{m,i}(t)}^{\text{Metastables}} + \overbrace{\sum_c A_{ic} n_c(t)}^{\text{Cascades}} - \overbrace{A_i n_i(t)}^{\text{Spontanious}} \tag{2.1}$$

Here, n_0,n_i,n_m and n_c are the ground state, i'th state, metastable state and cascade state populations, respectively. A_i is the Einstein coefficient for state i, A_{ic} is the cascade probability out of state i, while $E_{m,i}(t)$ and $E_{i,0}(t)$ are the electron impact excitation functions for metastable excitation and ground excitation, respectively. Note, that $E_{m,i}(t)$ and $E_{i,0}(t)$ can be obtained from the product of the electron density, n_e, and the energy dependent rate coefficient for the relevant process as follows:

$$E_{i,0}(t) = n_e \int_0^\infty \sigma_i(\epsilon) \sqrt{\frac{2\epsilon_{i0}}{m_e}} f_e(\epsilon) d\epsilon \tag{2.2}$$

Where, $\sigma_i(\epsilon)$ is the energy dependent collision cross section for level i, $f_e(\epsilon)$ is the EEDF, ϵ_{i0} is the energy between state i and ground, and m_e is the electron mass. By assuming that the $\mathrm{Ar}(2p_1)$ excited state is not heavily populated through cascade processes or step-wise (metastable) excitation, the excitation function $\mathrm{E}_{i,0}(t)$ can be equated directly to the number of photons emitted $n_{\mathrm{Ph,i}}(t,r)$ via[151]:

$$E_{i,0}(t) = \frac{1}{n_0 A_{ik}} \left(\frac{\mathrm{d}n_{\mathrm{Ph,i}}(t,r)}{\mathrm{d}t} + \frac{1}{\tau_{\mathrm{eff}}} n_{\mathrm{Ph,i}}(t,r) \right) \tag{2.3}$$

where the photon flux $n_{\mathrm{Ph,i}}(t,r)$ is given as:

$$n_{\mathrm{Ph,i}}(t,r) = A_{ik} n_i(t,r) \tag{2.4}$$

Here, $\mathrm{n}_i(t,r)$ and A_{ik} are the radially resolved population density and transition probability out of state i, respectively. The effective lifetime of state i is denoted by τ_{eff}, taking into account spontaneous emission and collisional quenching given by:

$$\frac{1}{\tau_{\mathrm{eff}}} = \sum_k A_{ik} g_{ik} + \sum_q k_q n_q \tag{2.5}$$

Where $g_{ik} = 1$ is the optical escape factor[155,156] and k_q, m_q are the quenching coefficient and density of quenching species q, respectively. In this work quenching is assumed to be performed only by neutral argon where the quenching coefficients are evaluated for a neutral gas temperature of 1000 K[73].

The excitation structures in PROES images relate directly to electron fluxes, with the emission intensity proportional to the flux density, or current. This fact, alongside the single dimension of spatial resolution, provides a method for spatially and temporally locating electron heating mechanisms. As mentioned previously in section 2.1.1, the electron heating mechanisms in the *Pocket Rocket*, and indeed radio-frequency plasmas in general, are primarily dictated by the movement of the sheath. Recall also, that the ion heating, and consequentially neutral heating, is substantially affected by the sheath dynamics as the ions 'see' and are accelerated through the phase-averaged sheath potential. The phase-averaged sheath dynamics therefore dictate the ion power deposition, while the phase-resolved sheath dynamics dictate the electron power deposition. Therefore, if comparisons between the excitation structures in measured PROES images and simulated PROES comparisons agree we can be relatively confident that the sheath dynamics, and hence the ion and electron heating mechanisms, within the simulation are accurate. This is the central premise upon which the validation of the numerical model is based.

2.2 Modelling Non-Equilibrium Plasmas

The numerical modelling of non-equilibrium, low-temperature plasmas poses a number of challenges, from the simultaneous consideration of physical mechanisms scaling over twelve orders of magnitude (1 ps - 10 s), to the wide range of collisional and collisionless conditions that must be seamlessly transitioned between and not forgetting a consideration of the gas phase chemistry[86,157]. It is little surprise then that there exists no single 'correct' method by which to simulate a low-temperature plasma. The currently accepted 'gold-standard' for plasma simulation are the Particle-in-Cell (PIC) models, where individual (or often macro) particle motion is considered kinetically[108,158–160]. However, with charged particle densities on the order of $10^{14} - 10^{19}$ m^{-3} and neutral particle densities typically a few orders of magnitude above that, full PIC solutions often represent a computationally intractable solution with current technology. For this reason, a number of numerical techniques have been developed, employing physical approximations and abstractions to simplify the problem but yet still produce physically reliable solutions. Before introducing two of these techniques, it is important to first define the term 'numerical modelling' in this context.

Numerical modelling refers to a system of equations and boundary conditions that are capable of non-analytically approaching a converged solution through an iterative process. Although analytical models of plasmas do exist, due to their inherently self-referential collective behaviour, plasma parameters can rarely be extracted purely analytically. However, through carefully considered assumptions it is often possible to describe localised regions or processes within a plasma through an analytical approach, see the previous treatment of the plasma sheath and electrical asymmetries in sections 1.5.1 and 1.6 as examples. This naturally limits the application of these models to conditions where the assumptions are known to be true, however the reduction in complexity can often be worth the limitations.

The remainder of this section will briefly introduce two of the most common numerical techniques, namely *fluid* models and *kinetic* models. Note that zero-dimensional *global* models will not be discussed here for purposes of brevity although they do represent a commonly employed technique[?] .

2.2.1 Fluid Models

Fluid models and techniques approach the computational intractability of modelling plasmas by doing away with the single particle model and focusing on the macroscopic properties of a plasma[161–164]. Particle species densities, fluxes and temperatures are solved for through taking moments of the Boltzmann equation (equation 2.8), obtaining conservation relations for particle species mass, momentum and energy[114]. The EEDF, required for determination of electron reaction rates and transport coefficients, is often solved for through a zero-dimensional Boltzmann solver ahead of the fluid simulation or iteratively within the

simulation model[161,165].

The benefits of this approach are a significantly reduced computational expense compared to fully kinetic codes, enabling higher dimensional (often 2D or 3D) geometries and very complex plasma chemistries. However for what they achieve in computational speed, fluid models suffer when it comes to capturing collisionless effects. As the Boltzmann equation describes particles in thermal equilibrium, particle species energy distribution functions are implicitly assumed to be collisional in nature, i.e. they can be reliably approximated by a Maxwellian fit, see equation 1.26. Therefore, by definition fluid models are unable to capture or predict collisionless effects, which begin to dominate over collisional interactions at very low pressures (< 10 Pa)[164].

2.2.2 Kinetic Models

Kinetic models employ either individual or macro-particles, the motion of which is dictated by electromagnetic and mechanical forces within the simulation volume[108,159,160]. Where macroparticles (or super-particles) typically consist of groups of approximately 10^5 - 10^7 particles treated as a single packet. The most commonly employed kinetic models include the Particle-in-Cell (PIC) model and the Monte-Carlo collisional model[159,166]. Particle energy distribution functions fall directly out of the range of energies observed in the macro-particles of a particular species within a given spatial and temporal range. Collisions are typically handled by a Monte-Carlo algorithm where the chance for and type of collisions observed are determined stochastically from normalised reaction cross-sections[167].

The benefits of kinetic modelling are that it minimises the assumptions placed upon the particle energy distribution functions, and is considered reliable over a wider range of operational conditions as compared to fluid and global models. In more conceptual terms, kinetic models also more closely maintain the physically understood system of particle interactions in real plasmas. However, the computational expense of kinetic modelling limits simulation geometry (most PIC models employ 1D or 2D geometries) and also places an upper limit on the number of particle species that can be concurrently modelled.

2.2.3 Hybrid Models

Each method of plasma modelling introduces advantages and disadvantages which influence the choice of simulation geometry and boundary conditions. Hybrid modelling attempts to weigh the advantages of one method against the disadvantages of another to achieve the best compromise of computational expense and reliably modelled phenomena[165,166]. This paradigm relies on the capability to separate physical mechanisms into those which can be captured by the applied modelling techniques. A commonly employed approach involves combining aspects of fluid modelling for heavy particle collisional plasma species and aspects of kinetic modelling for lighter species (e.g. secondary electrons emitted from

material surfaces[166]), or species which otherwise cannot be assumed to be collisional. If care is taken to appropriately determine which physical mechanisms are treated by which numerical method then a wider range of physical mechanisms can be captured, while reducing the computational expense. An example of a hybrid model, and the model employed in this work, is the Hybrid Plasma Equipment Model (HPEM), which employs a 2D fluid model in conjunction with a Monte-Carlo collision model.

2.3 Hybrid Plasma Equipment Model

The Hybrid Plasma Equipment Model is a modular 2D fluid/Monte-Carlo simulation suite developed by Prof. Mark Kushner and the Computational Plasma Science and Engineering Group at the University of Michigan. Comprehensive overviews of the code and its operation are given in Refs 165 and 168. In this work HPEM has been employed as compiled directly from source code employing a custom made 'RFVOLT_USER' subroutine enabling the application of tailored voltage waveforms, see appendix 8.1. A schematic illustrating the operation of the hybrid plasma equipment model is shown in figure 2.6 below:

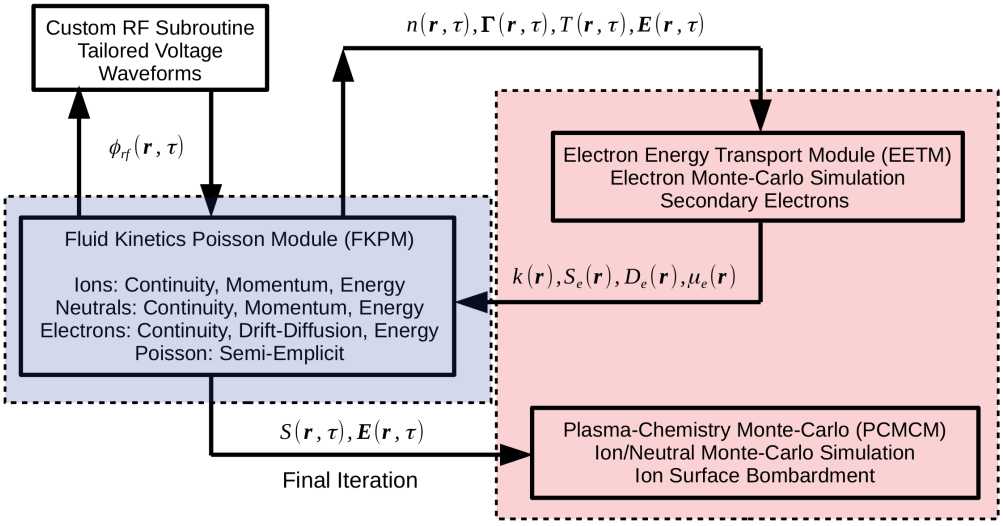

Figure 2.6: Flowchart detailing the operation of the Hybrid Plasma Equipment Model as employed in this work. Modules highlighted in red employ kinetic Monte-Carlo algorithms, while modules in blue employ fluid approaches. The Plasma-Chemistry Monte-Carlo Module (PCMCM) is only employed at the final iteration.

The HPEM employs a modular framework, allowing substantial flexibility in the algorithms employed to represent desired physical mechanisms. Figure 2.6 illustrates the three core modules employed in this work, the Fluid Kinetic Poission Module (FKPM), the Electron Energy Transport Module (EETM) and the Plasma-Chemistry Monte-Carlo Model (PCMCM). A custom subroutine was employed within the FKPM to allow for the applica-

tion of non-sinusoidal voltage waveforms, this will be discussed in more detail at the end of this section.

The FKPM represents the fluid component of the HPEM model and employs moments of the Boltzmann equation to determine charged and neutral species continuity equations (equations 2.9, 2.12 and 2.13), supplemented by the electron drift-diffusion equation (equation 2.10). The solution to Poisson's equation is obtained semi-implicitly, where the potential at the future iteration is determined from the potential at the current iteration plus an incremental prediction. This prediction employs implicit electrons and predictor-corrector ions, where the divergence of charged particle fluxes as obtained from drift-diffusion equations and the electron flux is simultaneously solved for through continuity of charge. Within the FKPM, these methods are employed within a single, commonly shared, rectilinear simulation mesh. Particle species densities and temperatures as well as electrostatic potentials and magnetic field strength are solved for at the mesh cell verticies, whereas particle fluxes and electric fields are solved for at the mid-points between vertices[165]. The spatially and temporally resolved particle species densities $n(\mathbf{x},\tau)$, fluxes $\mathbf{\Gamma}(\mathbf{x},\tau)$, temperatures $T(\mathbf{x},\tau)$, electrostatic potentials $\phi_{rf}(\mathbf{x},\tau)$, and electric field strengths, $\mathbf{E}(\mathbf{x},\tau)$ are then supplied to the EETM and PCMCM.

The EETM contains two different solution methods for obtaining the spatially resolved (time averaged) electron mobilities $\mu_e(\mathbf{x})$, diffusion coefficients $D_e(\mathbf{x})$, electron reaction rates $k_e(\mathbf{x})$ and source functions $S_e(\mathbf{x})$. Namely either through a solution to the zero-dimensional, two-term approximated, Boltzmann equation or through a sub-mesh Monte-Carlo kinetic algorithm. Note that in this work, secondary electrons are treated independently from the fluid solved 'bulk' electron population, and therefore have different transport and diffusion coefficients. A similar Monte-Carlo kinetic algorithm is employed to determine the ion energy distribution functions incident on material surfaces at pre-defined locations within the simulation geometry. Note that the PCMCM is only called on the final iteration of the simulation, no information is returned into the FKPM. In addition, the EETM and PCMCM employ localised rectilinear sub-meshes, where the mesh geometry and resolution are the same as in the FKPM.

2.3.1 Fluid Electron Energy Transport

Before progressing further into operation of the FKPM it is important to underpin how the particle mobility and transport coefficients are determined, as these are required for a solution to the continuity equations. This work is performed in the EETM and represents the fluid component of that module, the kinetic approach to the following solution is discussed in detail in section 2.3.3.

In the first step, the electron energy distribution function (EEDF), and associated mean electron temperature $\hat{T}_e$, within each simulation cell are determined from a zero-dimensional

two-term approximation of the Boltzmann equation[114]. These solutions make use of a range of reduced electric fields (E/N), specified manually within the input deck, in combination with the electron impact cross-sections for each included collisional interaction, specified in the plasma chemistry set. Determination of the mean electron temperature in each cell allows for the computation of the electron mobility μ_e, the electron diffusion coefficient D_e and ultimately the desired reaction rate coefficients for use in the FKPM conservation equations. The electron mobility and electron diffusion coefficient are calculated as in equations 2.7 and 2.6:

$$D_e = \frac{k_b \hat{T}_e \mu_e}{e} \tag{2.6}$$

$$\text{Where} \qquad \mu_e = \frac{v_{ed}}{eE} \tag{2.7}$$

Where v_{ed} and E are the scalar values of the electron drift velocity and electric field, respectively. The ion mobility and diffusion coefficients D_i are calculated in the same manner by simply employing the mean ion species temperature $\hat{T}_i$ in equation 2.7 and ion specific charge $Z_i e$ in equation 2.6. Employing the zero-dimensional Boltzmann approach to obtaining reaction rate coefficients allows for a consideration of a wider range of EEDF shapes, and a more reliable determination of ionisation and excitation rates. However, extraction of reliable particle species densities and hence excitation rates for comparison with measured rates requires a consideration of mass, momentum and energy conservation.

2.3.2 Fluid Kinetics Poission Module (FKPM)

As previously indicated, the particle continuity equations within the FKPM are obtained from the first three moments of the Boltzmann equation, shown in Eq. 2.8. The Boltzmann equation describes the evolution of the particle energy distribution function $f(\epsilon)$ in a seven dimensional Cartesian geometry with spatial vectors (x, y, z), velocity vectors (v_x, v_y, v_z) and with respect to time t:

$$\frac{\delta f(\epsilon)}{\delta t} + \mathbf{v} \cdot \nabla f(\epsilon) - \frac{Z_s e}{m_s} [\mathbf{E} + \mathbf{v} \times \mathbf{B}] \cdot \nabla_{\mathbf{v}} f(\epsilon) = |\frac{\delta f(\epsilon)}{\delta t}|_{coll} \tag{2.8}$$

where, $\mathbf{v} = (v_x, v_y, v_z)$ is the 3D velocity vector, $\mathbf{E}$ and $\mathbf{B}$ are the electric and magnetic field vectors in real space (x, y, z), respectively and Z_s and m_s represent the specific charge and atomic mass of the species s, respectively. The final term on the right hand side represents the thermal relaxation of the energy distribution through collisional interactions, the exact form of this collision operator depends on the number of particle species and types of collisional interactions included within the model.

The precise nature of the continuity equations employed within HPEM can vary depend-

ing upon the species. The conservation of mass for all species is the same and is shown in equation 2.9, where the number density n_s within any given cell is determined from the mass continuity between adjacent cells.

$$\frac{\delta n_s}{\delta t} = -\nabla \cdot \mathbf{\Gamma}_s + S_s \tag{2.9}$$

Here, $\mathbf{\Gamma_s}$ is the particle flux of species s between adjacent cells and S_s is the particle source function arising from ionisation and/or inelastic heavy particle collisions. Obtaining the particle flux between cells differs slightly between electron and heavier ion and neutral species. The electron flux $\mathbf{\Gamma}_e$ and collisional energy transfer are accounted for via the second and third moments of the Boltzmann equation (equations 2.10 and 2.11, respectively), where momentum is conserved via drift diffusion:

$$\mathbf{\Gamma}_e = -n_e \mu_e \mathbf{E} - D_e \nabla n_e \tag{2.10}$$

Here, μ_e and D_e are the electron mobility and electron diffusion coefficient as described by equations 2.7 and 2.6, determined from the mean electron temperature obtained from solutions of the zero-dimensional Boltzmann equation, described previouly. In this work, equation 2.10 is implemented using Scharffeter-Gummel fluxes, see Ref. 169, as this implimentation was previously found to provide the best numerical stability within this pressure range[168]. The electron energy conservation equation is shown in equation 2.11:

$$\frac{\delta \mathbf{\Gamma}_e}{\delta t} = -\nabla \mathbf{\Gamma}_e - e\mathbf{\Gamma}_e \mathbf{E} \pm \sum_j n_e n_j k_{L,ej} \pm \sum_j 3\frac{m_e}{m_j} k_{ej} k_b n_e (T_e - T_j) \tag{2.11}$$

Here, j represents species for which electron impact collisions are specified, n_j, m_j and T_j represent the number density, atomic mass and temperature of species j and k_{ej} and $k_{L,ej}$ represent the elastic and inelastic energy loss rate coefficients, respectively, for collisions between electrons and species j. Reaction rates k_{ej} and $k_{L,ej}$ are again determined from the mean electron temperatures obtained from the solutions of the zero-dimensional Boltzmann equation, described previously.

For ions and neutrals, the species flux Γ_i and temperature T_i are obtained from more complete versions of the momentum and energy continuity equations (equations 2.12 and 2.13), taking into account viscous and entropic/enthalpic losses. Neutral species exclude the terms with the electric fields, while the viscosity terms are not included for ions due to the low density of ions relative to neutral particles.

$$\frac{\delta \mathbf{\Gamma}_i}{\delta t} = \underbrace{-\frac{1}{m_i}\nabla\left(n_i k_b T_i\right)}_{\text{Thermal motion}} \overbrace{-\nabla\cdot\left(n_i v_i^2\right)}^{\text{Self-collisions}} \underbrace{+\frac{q_i}{m_i} n_i \mathbf{E}}_{\text{Lorentz force}} \overbrace{-\nabla\cdot\overline{\overline{v}}_i}^{\text{Viscous forces}} \underbrace{-\sum_j \frac{m_j}{m_i m_j} n_i n_j \nu_{ij}\left(v_i - v_j\right)}_{\text{Elastic collisions}} \tag{2.12}$$

Here T_i, m_i and v_i are the mean temperature, mass and velocity of species i, respectively. $\overline{\overline{v}}_i$ is the viscosity tensor for species i, ν_{ij} is the collision frequency between species i and j, E is the electric field strength and k_b is Boltzmann's constant. The summation term is performed for each heavy particle species j for which collision rates have been defined. Electron-neutral and electron-ion collisions solved for in the model include elastic, excitation and ionization reactions. As described in Ref. 170, cascade processes, multi-step ionization and heavy particle mixing between excited species are also included, the interaction cross-sections and rate coefficients for which are obtained from Refs. 171–175. In the case of heavy particle reactions rate coefficients are used in Arrhenius form[165].

The conservation of energy between ion and neutral species is accounted for by equation 2.13, enabling a self-consistent computation of heavy particle species temperatures. Equation 2.13 describes conduction, convection, thermodynamic work and changes in enthalpy ΔH. The final term also considers inelastic reactions, with rate coefficients k_{ij}, that result in the formation of new species and accounts for ion-neutral charge exchange heating. The general form of the energy continuity equation for heavy particles is written as:

$$\begin{aligned}\frac{\delta N_i c_i T_i}{\delta t} = {} & \overbrace{\nabla\cdot\kappa_i\nabla T_i}^{\text{Heat conduction}} \overbrace{-P_i\nabla\cdot v_i}^{\text{PdV work}} \overbrace{-\nabla\cdot\left(n_i v_i \epsilon_i\right)}^{\text{Heat convection}} \overbrace{+\frac{n_i q_i^2}{m_i v_i}\mathbf{E}^2}^{\text{Electrostatic potential}} \\ & \underbrace{+\sum_j \frac{m_j}{m_i m_j} n_i n_j \nu_{ij} k_b\left(T_j - T_i\right)}_{\text{Elastic collisions}} \underbrace{\pm\sum_j n_i n_j k_{\Delta H_{ij}} \Delta H}_{\text{Change in enthalpy}} \underbrace{\pm\sum_j 3 n_i n_j k_{ij} k_b T_j}_{\text{Inelastic collisions}}\end{aligned} \tag{2.13}$$

Where c_i is the specific heat capacity, κ_i is the species conductivity, P_i is the partial pressure and $\epsilon_i = c_i T_i$ is the specific energy of species i. The change in enthalpy for an exothermic or endothermic reaction is ΔH and the rate coefficient for reactions with a change in enthalpy is given as $k_{\Delta H_{ij}}$. Equation 2.13 can be extended into metal and ceramic components to provide material temperatures. For material nodes, terms 1, 5, 6 and 7 are retained, accounting for thermal conduction and sources of heat due to ion collisions and surface neutralisation of ions.

Ion-neutral charge exchange collisions are employed within the final term of equation 2.13. During a symmetric charge exchange collision, the temperatures of the ion and neutral are exchanged, resulting in a significant heating source for neutrals and cooling of the ions. Ions

impacting material surfaces deposit their kinetic energy and remaining potential energy after their Auger based neutralisation[73]. Conductive and convective thermal energy transport to material surfaces is solved for through a temperature gradient dependant model, discussed in section 2.4.3.

The system of equations outlined so far are closed by the inclusion of the semi-implicit Poisson's equation, (equation 2.14), from which the updated electric potential ϕ is obtained[165]:

$$\nabla\phi = -\frac{1}{\epsilon_0}\sum_{s}^{n_s}(eZ_s n_s - \nabla\cdot\Gamma_s) + (en_e - \nabla\cdot\Gamma_e) \tag{2.14}$$

for all charged particle species s, where symbols are as defined previously. Note that here and elsewhere ϕ refers to an arbitrary potential, while ϕ_{rf} is reserved strictly for applied rf voltages. Here, the number density and change in flux of particle species s is taken into account when determining the resulting charge density. The inclusion of the electron drift-diffusion flux, (equation 2.10), imparts a degree of implicitness, as the electron component of the resulting potential is entirely self-referential.

2.3.3 Monte-Carlo Collision Models

Following the FKPM, the particle densities, fluxes, temperatures and electric potentials solved under the closed system of equations 2.9 - 2.14 are passed into the EETM as shown in figure 2.6. The electron transport coefficients are then determined either through the zero-dimensional Boltzmann approximation, as described in section 2.3.1, or computing the electron energy distribution function directly by employing a Monte-Carlo kinetic model on a sub-mesh, separate from the main simulation mesh.

In this work, two species of electrons are considered: a thermalised, fluid treated, 'bulk' electron population with a mean electron temperature typically below $\approx$ 3 eV and a non-thermal, kinetically treated, secondary electron population with a mean electron temperature typically above 50 eV. Secondary electron emission following ion bomardment of material surfaces is introduced using an energy independent model, where the secondary electron flux is proportional only to the incident ion flux and the secondary electron emission coefficient[104,176]. A secondary electron emission coefficient of 0.2 is employed in this work based upon measurements performed on aluminium and alumina surfaces under argon ion bombardment[177]. Once created, secondary electron macro-particles are launched from the material surface with an initial energy of 3 eV and are further accelerated through the local potential gradient, determined in the FKPM, where their motion and collisions are tracked using a Monte-Carlo algorithm[167].

Collisions within the Monte-Carlo algorithm are handled stochastically, employing elec-

tron collision rates interpolated from the relevant energy resolved interaction cross-sections as defined in the gas-phase chemistry set. A mean time between collisions is determined, employing a pseudo-collision-frequency based upon the calculated collision rate with a stochastic component. Collisions are 'rolled for' at each of these mean times between collisions, the outcome of which dictates if a collision occurred (a *real* collision) or did not occur (a *null* collision)[111]. In the case of a real collision, the type of collision is determined by comparing a further random number and a normalised form of the included collision cross-sections[165]. The angle through which macro-particles are scattered is also computable employing a similar method, where the scatter angle is determined from the angles of incidence with a stochastic component. The process repeats for a pre-determined timescale (typically 5 rf cycles) and the resulting angularly resolved EEDFs are obtained directly from the distribution of electron macro-particle energies. The secondary electron mobility, transport coefficients and reaction rates are then computed from the mean temperature of this distribution and passed back into the FKPM.

The simulation proceeds in this manner, passing updated variables back and forth between the FKPM and the EETM, where an iteration is defined as one cycle through all of the included modules. As the simulation converges, the change in the calculated parameters between any two iterations reduces until they can be considered effectively constant. Following the final iteration the converged ion densities and electric field strengths are sent to the PCMCM. The PCMCM employs a similar Monte-Carlo kinetic algorithm as the EETM, where ion macro-particles are created adjacent to specified material surfaces on a separate rectilinear mesh. The spatial distribution of the ion macro-particles is proportional to the converged density distribution. The same collision algorithm is employed as with the secondary electron macro-particles and the resulting angularly resolved ion energy distribution function incident upon the chosen material surfaces is determined.

2.3.4 Plasma Chemistry

The charged particle species included in the simulation consist of two argon ion species; Ar^+, Ar_2^+ and two electron species; e^- and e_γ^-, the treatment of which was discussed previously in section 2.3.1. Neutral argon is included with an atomic model consisting of seven energy levels and a single energy level diatomic argon metastable, namely: Ar, Ar($1s_2$), Ar($1s_3$), Ar($1s_4$), Ar($1s_5$), Ar($4p$), Ar($4d$) and Ar_2^*. Here Ar($4p$) and Ar($4d$) are lumped excited states where Ar($4p$) consists of Ar($4p$, $3d$, $5s$, and $5p$), while Ar($4d$) contains Ar($4d$, $6s$, and Rydberg states). The full reaction mechanism is as discussed in Ref. 170. Note that the population of the Ar($4p$) lumped state is employed as a proxy for the Ar($2p_1$) state and is employed when comparing the measured PROES excitation from Ar($2p_1$ - $1s_2$)[178], see section 2.1.3. At the pressures and energies employed the plasma is expected (and was

observed) to be optically thin, therefore an explicit simulation of radiation transport is not included here.

Collisional interactions considered within the reaction mechanism include gas-phase electron-neutral and electron-ion collisions, including elastic, excitation and ionization reactions[170]. Heavy particle interactions consider elastic and inelastic collisions including multi-step ionization, cascade processes, and heavy particle mixing between excited species and ion-neutral charge exchange collisions the interaction cross-sections for which are obtained from Refs. 171–175. Ion-neutral charge exchange reactions are included with a with temperature dependant rate coefficient of 5.66×10^{-16} m^{-3} $(T_g/300)^{0.5}$ where T_g is the neutral-gas temperature[179].

Reaction rate coefficients not computed by the electron energy transport module are provided in Arrenhius form, where the reaction rates for heavy particle and electron impact interactions are as shown in equations 2.15 and 2.16, respectively:

$$R_i = A_{Arr,i} \left(\frac{T_i}{298} \right)^n exp \left(\frac{-k_b \alpha_i}{T_i} \right) \tag{2.15}$$

$$R_e = A_{Arr,i} (T_e)^n exp \left(\frac{-k_b \alpha_i}{T_e} \right) \tag{2.16}$$

Here, $R_i = k_i n_i$ represents the reaction rate for species i, $A_{Arr,i}$ represents the associated Arrenhius coefficient, n is the order of the reaction, α_i is the process specific activation energy, while T_e and T_i are the electron and ion species temperatures respectively.

2.4 Pocket Rocket Mesh Geometry and Standard Operating Conditions

Following module choices and formulation of the plasma chemistry model, the simulation geometry must be defined. In this work the simulation geometry consists of the York based *Pocket Rocket* source, including the downstream plenum and 40 mm of expansion chamber. The axial and radial dimensions of the source region are modelled to scale, however the radial extent of the plenum and expansion tube are reduced by a factor of three to reduce simulation expense. This reduction is not expected to significantly affect the quality of comparison between the simulation and experimental measurements as the physical asymmetry 'seen' by the plasma remains approximately the same in both cases. The Pocket Rocket mesh geometry is illustrated in figure 2.7. An external circuit (not shown) comprising: an rf voltage source and blocking capacitor was connected to the powered electrode. Note that the alumina dielectric layer also prevents a dc current back to the power source and maintains the time averaged dc self-bias voltage as a negative surface charge.

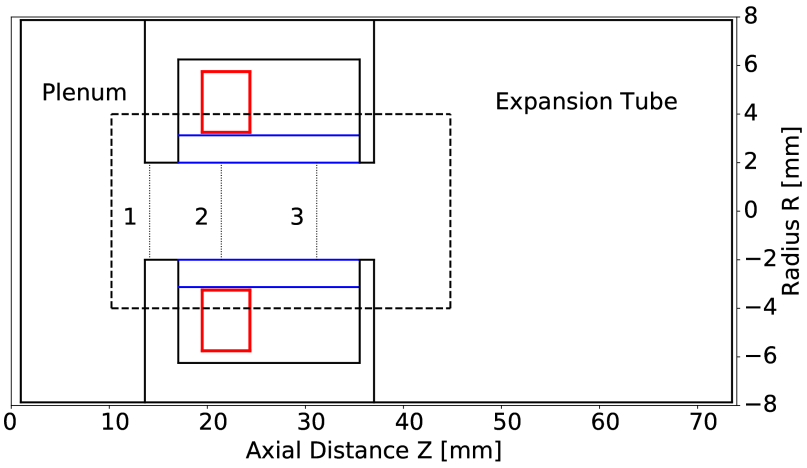

Figure 2.7: Illustration of the simulation domain (not to scale). The domain is radially symmetric around R = 0.0 mm. Gas is introduced into the plenum and extracted at the end of the expansion tube. An rf voltage is applied to the electrodes, denoted in red, and couples to the plasma through an alumina tube, denoted in blue. The source region, highlighted by dotted lines, contains three sub-regions of interest: upstream (Z = 14.2 mm), the powered electrode (Z = 21 mm) and downstream (Z = 31 mm), denoted regions 1, 2 and 3, respectively. Energy distribution functions are obtained from the surface of the alumina wall adjacent to the powered electrode (region 2).

The numerical mesh consisted of 64 × 152 (R × Z) cells in a cylindrically symmetric geometry, corresponding to a radial resolution of 0.125 mm per cell and an axial resolution of 0.5 mm per cell. A higher radial resolution is required to resolve the electric field gradient through the powered electrode sheath. The powered electrode was driven by an rf voltage of amplitude 120 - 450 V. The source was operated in argon with an input flow rate of 100 sccm at the gas inlet and a fixed pressure of 0.85 Torr at the outlet, resulting in a plenum pressure

of between 200 - 226 Pa (1.5 - 1.7 Torr) at 450 V, closely matching the experimental setup. As the plasma is considered to be collisional at this pressure, the bulk ion and electron energy distribution functions are assumed to be predominately Maxwellian in shape, with a superimposed advective axial velocity v_Z, agreeing with the fluid approximations considered previously in section 2.3.2.

Material properties were manually set for the alumina, Macor, aluminium and copper components, values were chosen assuming clean, smooth surfaces[180,181]. Relative permittivities (ϵ/ϵ_0) for alumina and Macor were set to 9.8 and 5.8, respectively. The bulk electrical conductivities for alumina and Macor were set to 1×10^{-14} Ω^{-1}cm^{-1} and 1×10^{-17} Ω^{-1}cm^{-1}, respectively. All materials were initiated at 325 K unless otherwise stated and the bulk thermal conductivities for alumina and Macor were set to 0.18 Wcm^{-1}K^{-1} and 0.015 Wcm^{-1}K^{-1}, respectively and for aluminium and copper as 2.5 Wcm^{-1}K^{-1} and 4 Wcm^{-1}K^{-1}, respectively. Secondary electron emission coefficients for alumina and Macor surfaces are set to $\gamma = 0.2$ and for all other surfaces $\gamma = 0.0$.

Simulated radial excitation profiles are taken from the upstream plenum side of the source, the centre of the powered electrode and the expansion region downstream of the source, shown in figure 2.7 as axial locations of 1, 2 and 3, respectively. The energy distribution functions for ions impacting the radial wall adjacent to the powered electrode (region 2) and the subsequently emitted secondary electrons are obtained from the PCMCM and EETM Modules as detailed previously in section 2.3.3. Ion energy distribution functions are obtained from region 2 corresponding to the axial location of highest power deposition, highest neutral gas heating and highest dc self-bias voltage, the details of which are given in chapter 3. The kinetic treatment of the sheath accelerated ions and secondary electrons ensures that, aside from the initial launch energy of the electrons, there are no further assumptions made regarding the shape of these energy distributions.

2.4.1 Spatial and Temporal Convergence

When discussing convergence it is useful to first define two types of convergence; (1), temporal convergence, representing the iterative convergence of a single simulation towards a steady state solution and (2), spatial convergence, representing the invariance of the temporally converged steady state solution to the mesh resolution. Temporal convergence is confirmed for each simulation presented in this study, a representative example is presented in figure 2.8 (a), for a 200 Pa (1.5 Torr) argon discharge, supplied a 450 V, 13.56 MHz sinusoidal voltage waveform. The spatial convergence of the mesh geometry shown in figure 2.7 is demonstrated in figure 2.8 (b), for temporally resolved simulations employing the same conditions as previously described.

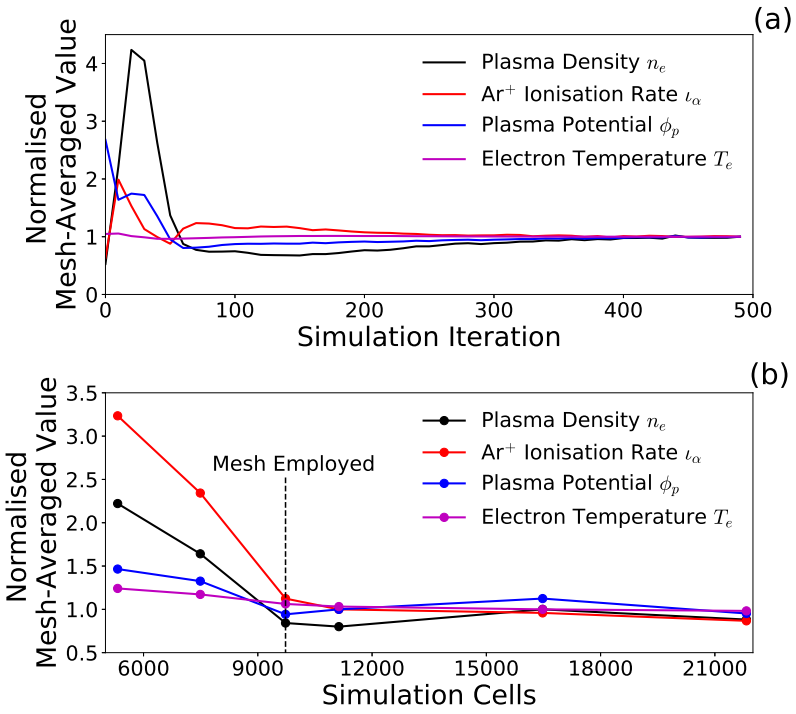

Figure 2.8: Iterative (a) temporal and (b) spatial convergence of the *Pocket Rocket* PR mesh geometry for 'standard' operating conditions, employing an argon input flowrate of 100 sccm, resulting in an upstream plenum pressure 200 Pa (1.5 Torr) and expansion region pressure of 133 Pa (0.85 Torr), with an applied voltage of 450 V at 13.56 MHz.

Figure 2.8 (a) shows the temporal convergence of the mesh-averaged plasma density, Ar^+ ionisation rate, plasma potential and electron temperature for 'standard' operating conditions employing the *Pocket Rocket* geometry shown in figure 2.7. The increased degree of noise in the Ar^+ ionisation rate and plasma density as compared to the plasma potential and electron temperature, arises from the stochastic contribution from the kinetic Monte-Carlo solved secondary electron population. Here, the simulation is considered converged if the largest change in a mesh-averaged value is below 0.1%, this is achieved by iteration 400 for the standard operating conditions. As described previously, one iteration represents a single cycle through all of the employed modules, see figure 2.6. Converting between iteration count and real time is not trivial, as the exact 'real time' simulated in each module varies significantly with operating conditions and the exact solvers employed. For this work approximately $\approx 10\ \mu s$ per iteration can be assumed, and therefore figure 2.8 (a) represents ≈ 5 ms of 'real time'.

The temporally resolved values shown in figure 2.8 (a) correspond to a mesh of geometry $R, Z = 64, 152$, containing 9728 cells as denoted by the dashed line in figure 2.8 (b). Here, five variants of the mesh shown previously in figure 2.7 were run employing standard operating conditions for 500 iterations, each achieving temporal convergence. For the parameters shown, increasing the mesh resolution reduced the mesh-averaged values until remaining

approximately constant for meshes containing above ≈ 10,000 cells, indicating spatial convergence. The first mesh geometry to spatially converge is chosen for application in this work as it represents the optimised trade-off between simulation reliability and simulation expense, both of which increase with increasing mesh resolution.

2.4.2 Determining Collisionality & Flow Regimes

The study of intermediate pressure (≈ 1 Torr) rf plasma jets has shown that pressure gradients substantially influence the plasma heating mechanisms within the source[44]. Sources indended for use as space propulsion naturally posses a pressure gradient between the gas inlet and the vacuum expansion region, as such the neutral gas and electron heating mechanisms can vary spatially across this region. This effect is compounded as the neutral gas temperature and local ionization fraction are coupled to the local collisionality, leading to a non-linear relationship between axial neutral transport and the effectiveness of plasma and neutral gas heating mechanisms[182–185].

In this work an argon (Ar) plasma is employed with a variable input flow rate and a fixed output pressure boundary condition. To enable specifying an outlet pressure boundary condition, modifications were required to the model. As previously described, the FKPM employs a multi-fluid model in which a momentum equation (equation 2.12) is solved for each ion and neutral species. Implementing a self-consistent pressure boundary condition requires a consideration of the pressure gradient between cells. First, the numerical mesh points corresponding to the furthermost downstream (i.e. vacuum pump) pressure in contact with the plasma are specified. Starting from the specified downstream radial plane, and for each neutral species, the densities at the nearest plasma cells to the pump cell are averaged and placed at the vertices of the pump cells. These collected densities are then used to compute mole fractions. The partial pressure of each species at the pump face is then the mole-fraction of that species multiplied by the outlet pressure boundary condition, determined from experiment. The inlet boundary condition is the flow rate, which determines the momentum of each species at the face of the upstream gas inlet. Working upstream from the pump cells, the pressure gradient is averaged to the next row of cells at the following iteration. Over successive iterations the pressure gradient between the inlet and outlet cells naturally results from the calculation.

From the description above, the neutral flow between adjacent cells is globally determined by the input flow rate and the output pressure boundary. However, with the introduction of any material surface the interaction becomes more complex. In general neutral particle fluxes into material surfaces are reflected, minus a fraction determined by material specific sticking coefficients, leading to the geometry influencing the flow regime. Specifically, as the integrated mass flux through a radial plane must be conserved, and the input flow rate is balanced to the output pressure, any restriction of the flow volume will naturally

result in increased momentum fluxes through the restricted region. Increased momentum fluxes result in altered collision rates, increasing the neutral gas heating and quenching of excited states within the plasma. The 'collisionality' of such a system is often described by the Knudsen number[90], K_n, the ratio between the atomic mean free path λ_{mfp} and a characteristic dimension of the imposed, flow restricting, geometry L:

$$K_n = \frac{\lambda_{\text{mfp}}}{L} = \frac{1}{n_{Ar}\sigma_{Ar}2R} = \left(\frac{k_b T_g}{PV}\right)\frac{1}{\sigma(\epsilon)_{Ar}2R} \tag{2.17}$$

Here, n_{Ar} is the Ar ground state density, related to the pressure P, neutral gas temperature T_g and discharge volume V by the ideal gas law, $\sigma(\epsilon)_{Ar}$ is the argon-argon collisional cross-section and R is the radius of the discharge region (2.1 mm in the *Pocket Rocket*, see section 2.1.1). The resultant flow regime is empirically defined in terms of the computed Knusden number: Continuum flow ($K_n \leq 0.001$), slip-flow ($0.001 \leq K_n \leq 0.1$), transitional flow, ($0.1 \leq K_n \leq 10$), free molecular flow ($K_n \geq 10$)[80,90].

Continuum flow is dominated by viscous forces, where the fluid exhibits substantial momentum losses at fluid boundaries and is well modelled by approximating zero fluid motion parallel to material surfaces. The fluid therefore possesses a significant gradient between the flow velocity at the centre of the flow channel and at the edge of the flow channel. If the pressure is reduced or the channel widened, the fluid moves into the rarified slip regime. The slip flow regime, as the name suggests, implies that there exists a non-zero fluid velocity relative to the material surface. This intermediate slip boundary layer impacts the fluid flow, most notably reducing the momentum loss to the walls. By $1 \leq K_n \leq 10$ the fluid is substantially rarified and short-range collisional interactions are becoming less important, and by $K_n \geq 10$, concepts such as thermodynamic pressure and internal viscosity no longer have meaning and a kinetic model must be applied.

For the conditions simulated in this work, the *Pocket Rocket* operates in the boundary between the slip-flow and the transitional flow regimes ($0.01 \leq K_n \leq 0.35$)[80]. In both cases viscous losses to the walls are accounted for in equation 2.12 and a slip condition[186] is applied at all plasma-material interfaces to maintain non-zero fluid velocities at material surfaces[187]. This boundary reduces the viscous losses to the walls in proportion to both the advective neutral flow perpendicular to the material surface and the tangential momentum accomodation coefficient, where for argon $\alpha_{tma} = 0.95$[188].

2.4.3 Determining Wall Temperatures

Thermal energy transport from the neutral gas towards the material surfaces is accounted for using the approach described in Ref. 189, based upon a temperature 'jump' across the computational cell adjacent to the surface[190]. The gradient of this temperature jump is proportional to the gradient in temperature between the two materials multiplied by a ther-

mal energy accommodation coefficient α_{tac}. In reality the value of α_{tac} is dependent on a variety of conditions including the pressure, the gas species employed and the fluid flow regime. In general, argon thermal energy accommodation coefficients have been found to be relatively independent of the surface material[191]. In this work a value of $\alpha_{tac} = 0.4$ is applied to the alumina surfaces, while metal surfaces have a value of $\alpha_{tac} = 1.0$. These are based on extrapolating the temperature dependence of the thermal energy accommodation coefficient as measured by Yamaguchi et al[188] for argon atoms incident on platinum surfaces to a temperature of 1000 K.

In addition to conductive and convective heating of material surfaces, the ion flux incident on the radial wall results in additional heating of the wall material. Previous work has shown that wall heating in the Pocket Rocket occurs over a relatively long timescale ($\approx$ 100 s)[73]. As typical simulation timescales are in the range 100 μs - 10 ms, this wall heating cannot easily be implicitly accounted for[165]. To approximate the effects arising from steady-state wall heating, two sets of simulations are performed employing argon plasma flowing through an alumina tube: one with a fixed initial wall temperature of 325 K and a second with an initial wall temperature derived from a two-step procedure, described below. The maximum on-axis neutral gas temperatures with respect to applied voltage for both sets of simulations are shown in figure 2.9.

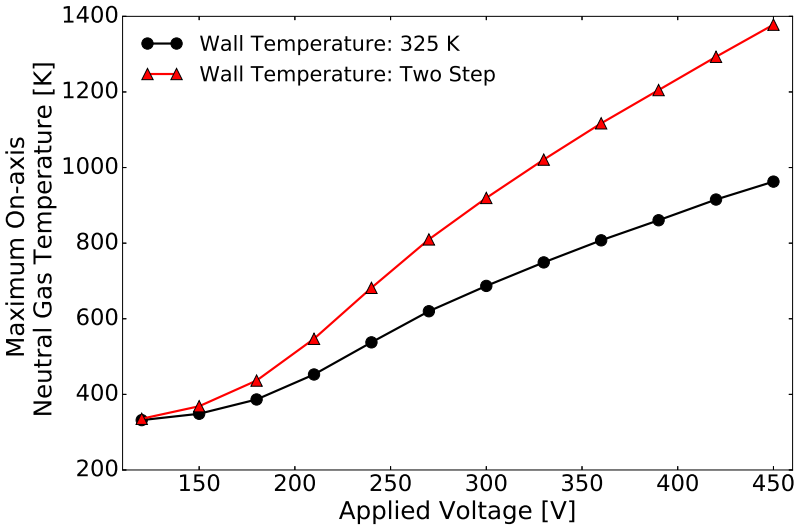

Figure 2.9: Phase-averaged on-axis (R = 0 mm) neutral gas temperatures with respect to applied voltage with 325 K walls (black circles) and with the wall temperature determined by the two step method (red triangles). Plenum pressure 186 - 226 Pa (1.4 - 1.7 Torr) in argon for 13.56 MHz driving voltage amplitudes between 120 V - 450 V.

For cases where the wall temperature is initiated at 325 K, the on-axis neutral gas temperature in figure 2.9 varies as expected when compared to previously simulated cases employing the computational fluid dynamics code CFD-ACE+[73,146]. As the initiated temperature of the walls increases, conductive heat losses are reduced and the on-axis neutral gas temper-

ature increases, as shown in figure 2.9. Setting the initial wall material temperature was achieved using a two-step method, performed as follows. In the first step, the maximum on-axis neutral gas temperature was computed using a 'cold' wall at 325 K. In the second step, the simulations were re-run with the wall temperature initialized as the maximum value of on-axis neutral gas temperature determined in the first step. The two step method therefore results in higher on-axis neutral gas temperatures, with temperature increase being proportional to the applied voltage. A reliable determination of the neutral gas temperature is required for calculation of the resulting thrust and specific impulse.

2.4.4 Determining Thrust

The specific impulse is calculated as in equation 1.6, where v_e is taken as the mean neutral velocity across a radial plane at the exit aperture of the thruster. The simulated thrust F_T was obtained by integrating the ion and neutral axial flux across the same radial plane with a consideration of the differential pressure, the general form of which is shown in equation 2.18. The method employed here is adapted from that employed by Ref. 43:

$$F_T = \int_0^R A_c \left(\sum_{k=0}^{n} v_{kn} \dot{m}_{kn} \right) + A_c \left(\sum_{k=0}^{n} v_{ki} \dot{m}_{ki} \right) \mathrm{d}R + \int_0^R A_c \Delta P \mathrm{d}R \tag{2.18}$$

when considering only neutral Ar and Ar^+ this simplifies to:

$$F_T = \int_0^R A_c (v_{Ar} \dot{m}_{Ar}) + A_c (v_{Ar^+} \dot{m}_{Ar^+}) \mathrm{d}R + \int_0^R A_c \Delta P \mathrm{d}R \tag{2.19}$$

where R is the radius of the source (2.1 mm), A_c is the cross-sectional area of a simulation cell (in cylindrical coordinates), v_{Ar} and v_{Ar^+} are the neutral Ar and Ar^+ ion velocities respectively. The mass flux rates through the plane of integration are denoted by $\dot{m}_{Ar}$ and $\dot{m}_{Ar^+}$ for Ar and Ar^+, respectively. Here the neutral mass flux rate is defined $\dot{m}_{Ar} = m_{Ar} \Gamma_{Ar}$, for the argon ion mass m_{Ar} and argon flux Γ_{Ar}, the argon ion mass flux rate is defined in the same way for the Ar^+ flux. The differential pressure across the plane of integration is accounted for as ΔP, defined as $\Delta P = P_Z - P_0$ where P_Z is the pressure at the plane of integration and P_0 is the output pressure (typically 113 Pa (0.85 Torr) in experiment). In reality when operating in vacuum, a portion of the pressure thrust will be converted into radial momentum of the neutrals, this is not accounted for in this treatment.

Chapter 3

Spatio-Temporal Plasma Heating Mechanisms in a Radio-Frequency Electrothermal Microthruster

In this chapter the ion, neutral and electron heating mechanisms in a capacitively coupled physically asymmetric rf electrothermal microthruster are investigated employing phase-resolved optical emission spectroscopy and 2D fluid/Monte-Carlo numerical simulations. Fundamental electron heating mechanisms are introduced and discussed with relevance to their spatio-temporal location within the plasma source and the applied rf phase cycle during a voltage induced α-γ mode transition. The mechanics underlying this mode transition are described with respect to the dc self-bias voltage and radial ion flux adjacent to the powered electrode within the thruster. Finally, the extent to which the neutral gas heating is affected by this mode transition is investigated and the impact this has on the thrust and specific impulse produced is discussed. Operating conditions within this chapter are maintained at a 13.56 MHz driving voltage waveform supplied at between 120 - 450 V (0.2 - 5 W). Unless otherwise stated, the thruster is operated employing 100 sccm of argon gas, resulting a plenum pressure between 186 - 226 Pa (1.4 - 1.7 Torr).

The results and conclusions presented in this chapter are based upon those published by the author in Ref. 65.

3.1 Phase-Resolved Electron-Impact Excitation Rate: Comparing Experiments to Simulations

Before progressing into an analysis of the simulated spatio-temporal heating mechanisms within the *Pocket Rocket*, the simulations must first be validated against experimental measurements. Here, this is performed by comparing the measured and simulated rf phase-resolved PROES images for varying applied voltage amplitudes. Simulated PROES images are produced from an imaging plane aligned with the centre of the powered electrode (Z = 21 mm). A 24 mm depth-of-field is then applied through a a top hat integration scheme to account for the optically thin nature of the plasma in experiment[154]. Simulated PROES images, and their associated waveforms, are shifted in phase such that the excitation structures align with those measured in experiment.

Measured phase-resolved Ar($2p_1$) excitation rates are shown in figures 3.1 (a) and (b) and simulated Ar($2p_1$) excitation rates are shown in figures 3.1 (c) and (d), for an applied voltage frequency of 13.56 MHz at 135 V (α-mode) and 445 V (γ-mode), respectively. The associated applied rf voltage waveforms and dielectric surface potentials adjacent to the powered electrode (Z = 21 mm, R = 2.1 mm) are shown in figures 3.1 (e) and (f), respectively.

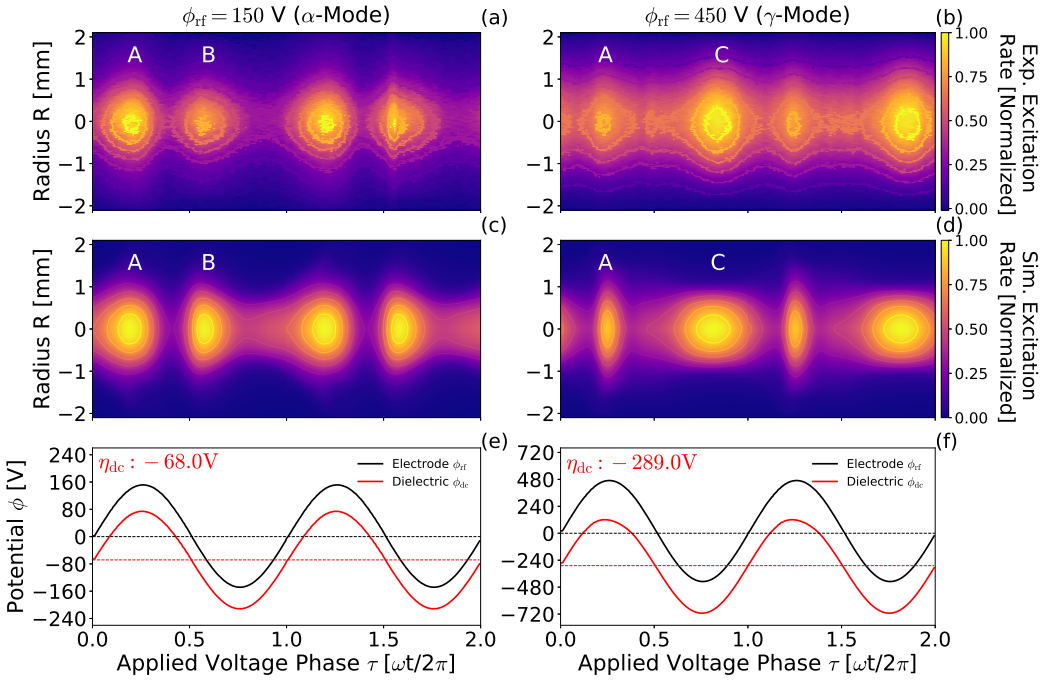

Figure 3.1: Measured (a), (b) and simulated (c), (d) phase-resolved Ar($2p_1$) excitation rates for 13.56 MHz applied voltage frequency discharges at 135 V and 445 V applied voltage amplitudes, respectively. Associated applied rf voltage waveforms and dielectric surface potentials adjacent to the powered electrode (Z = 21 mm, R = 2.1 mm) are shown in panels (e) and (f) for the 135 V and 445 V discharges, respectively, where the dc self-bias voltage is denoted by the red dashed line. Operating conditions: Plenum pressure 186, 226 Pa (1.4, 1.7 Torr) argon, applied voltages of 135 V, 445 V at 13.56 MHz, wall temperatures of 332 K, 963 K.

Close agreement is observed between experiment and simulation at 135 V (figures 3.1 (a) and (c)). Two excitation structures, labelled A and B, occur per phase cycle in both the simulated and measured Ar($2p_1$) excitation rates. Peak A is wider temporally than peak B and coincides with an increasing applied voltage at the powered electrode, thereby accelerating electrons towards the dielectric, this is the phase of sheath collapse. Peak B occurs for decreasing voltage at the powered electrode and dielectric, accelerating electrons into the bulk plasma, this is the phase of sheath expansion. Under these conditions the discharge is operating in α-mode, characterised by electron heating predominately observed during phases of sheath movement, i.e. expansion and collapse. The phases of highest sheath velocity also correspond to phases of peak dV/dt in the applied rf waveform in figure 3.1 (e). Due to the formation of a negative surface charge on the alumina surface, the reasoning for which is discussed in section 1.6, the waveform 'seen' by the plasma exhibits a time-averaged dc self-bias voltage of -68 V. As the thickness of the alumina dielectric is relatively small (1.1 mm) no phase-offset is observed between the applied voltage waveform and the dielectric surface potential.

If the applied voltage amplitude is increased to 445 V, the discharge exhibits a rapid increase in emission intensity entering a 'bright'[192], or γ-mode of operation, shown in figures 3.1 (b) and (d) for the measured and simulated excitation, respectively. Here, the measured and simulated excitation rates again show close agreement, exhibiting two excitation structures per rf-cycle. When compared to figures 3.1 (a) and (c), the excitation during sheath collapse at the powered electrode, peak A, is still visible, however this structure occurs over a shorter time interval. The excitation during sheath expansion at the powered electrode, peak B, is no longer visible and a new excitation structure, peak C, appears just after maximum sheath extension at $\omega t/2\pi \approx 0.75$. Peak C represents excitation from secondary electrons released from the alumina surface via ion bombardment and subsequently accelerated through the sheath potential. Operation in γ-mode is typically characterised by electron heating predominately occurring at phases of either full sheath extension or full sheath collapse, i.e. when the sheath is not moving. For operation employing 100 sccm of argon at 13.56 MHz, the *Pocket Rocket* transitions into γ-mode for voltages higher than 385 V in experiment and at voltages higher than 390 V in simulation. With reference to the heating mechanisms observed in figures 3.1 (a - d), transition into γ-mode may also be characterised as the voltage for which the integrated excitation from peak C becomes larger than A and B combined.

In both simulation and experiment the background excitation rate is higher in γ-mode than in α-mode, suggesting the existence of a time-independent excitation mechanism. Note that in simulation this arises in part from the secondary electron contribution as the Ar($2p_1$) excitation rates are obtained from the summation of the phase-resolved fluid 'bulk' electron excitation rate and the phase-averaged kinetic secondary electron excitation rate. The temporally-resolved effects from the secondary electron population (i.e. peak C) are ob-

served primary through high energy fluid electrons produced via elastic electron-electron collisions with secondary electrons. In addition, the relaxation of secondary electrons into the fluid population produces a time-varying fluid electron temperature, further indicating the temporal behaviour of the secondary electrons.

3.1.1 Phase resolved excitation across the α-γ mode transition

An α-γ mode transition is observed experimentally as a sharp increase in the optical emission intensity for applied voltage amplitudes of 385 V and above. To examine the evolution of this transition in more detail, the simulated and measured Ar($2p_1$) excitation rates for voltages between 150 - 450 V, in steps of 30 V, are shown with respect to applied voltage phase in figures 3.2 (a) and (b), respectively.

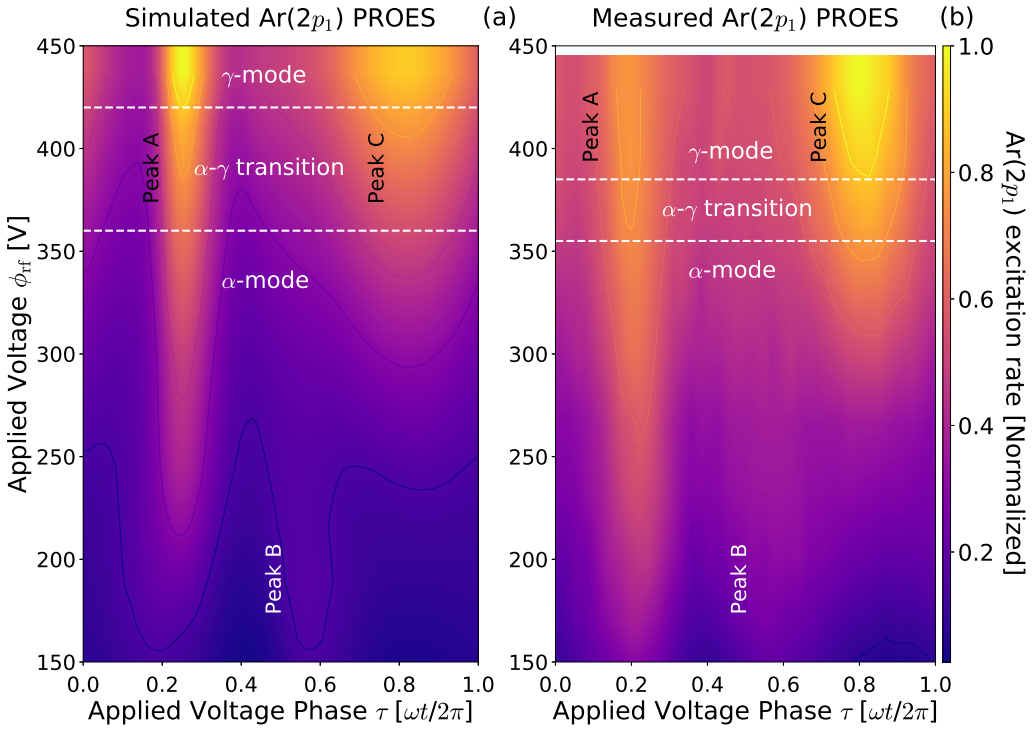

Figure 3.2: Simulated (a) and measured (b) Ar($2p_1$) excitation rates, including excitation from fluid and secondary electrons, with respect to applied rf voltage phase and voltage amplitude. Sheath collapse heating (A), sheath expansion heating (B) and heating via secondary electron interactions (C) are denoted explicitly. The voltage ranges representing transitions between α-mode and γ-mode operation are denoted by the white dashed lines. Operating Conditions: plenum pressure 186 - 226 Pa (1.4 - 1.7 Torr), 13.56 MHz, wall temperature 334 - 963 K.

Close agreement is observed between the measured and simulated Ar($2p_1$) excitation rates in figures 3.2 (a) and (b), with sheath collapse (A), sheath expansion (B) and heating via secondary electrons (C) observed over approximately the same voltage ranges in both cases. A voltage induced $\alpha - \gamma$ transition is observed in both simulation and experiment, the experimental transition occurs between 360 - 385 V, while in simulation the transition occurs

between 360 - 420 V. Here, the voltages for which an $\alpha - \gamma$ transition occurs are defined by the ratio between the excitation due to secondary electron induced excitation (peak C) and the excitation arising from sheath collapse and expansion (peaks A and B, respectively). Specifically, the discharge is said to be in α-mode if the excitation rate associated with peak C ($E_{2p1,C}$) is less than 0.9 of the excitation rate from peaks A and B ($E_{2p1,A}$, $E_{2p1,B}$), conversely the discharge is in γ-mode if peak C is equal to or greater than peaks A and B, and the discharge is said to be in the transition region where the ratio is between 0.9 - 1.0, explicitly defined below:

$$0.0 < \frac{E_{2p1,A} + E_{2p1,B}}{E_{2p1,C}} \leq 0.9 \qquad \alpha - \text{mode} \tag{3.1}$$

$$0.9 < \frac{E_{2p1,A} + E_{2p1,B}}{E_{2p1,C}} < 1.0 \qquad \text{transition} \tag{3.2}$$

$$\frac{E_{2p1,A} + E_{2p1,B}}{E_{2p1,C}} \geq 1.0 \qquad \gamma - \text{mode} \tag{3.3}$$

The $\alpha - \gamma$ transition in figure 3.2 (a) occurs at a slightly higher applied voltage and over a greater voltage range in simulation as compared to experiment. The later onset of γ-mode in simulation implies that the influence of the secondary electron population is slightly underestimated in simulation. This underestimation could arise from the ion-energy dependency of the secondary electron emission coefficient, or from thermionic emission of electrons from the hot alumina walls, neither of which are currently captured within the model[101,193]. Alternatively, recalling that the total Ar($2p_1$) excitation presented here is obtained as the phase-resolved fluid component and phase-averaged kinetic component, it is perhaps not unusual that the kinetic component (i.e. excitation via secondary electrons) is underestimated, considering that the secondary electron ionisation rate is exponentially self-referential. This may also explain the more gradual $\alpha - \gamma$ transition observed in simulation as compared to experiment, as the temporal averaging of the secondary electron ionisation rate artificially reduces the maximum possible growth rate in simulation.

3.1.2 Power Dissipated in the Plasma

The simulated and measured plasma power deposited with respect to increasing applied voltage amplitude is shown in figure 3.3. The simulated plasma power is shown for both the 325 K 'cold wall' and the two step method 'hot wall' cases. The measured plasma power is obtained via the subtractive method as described previously in section 2.1.2.

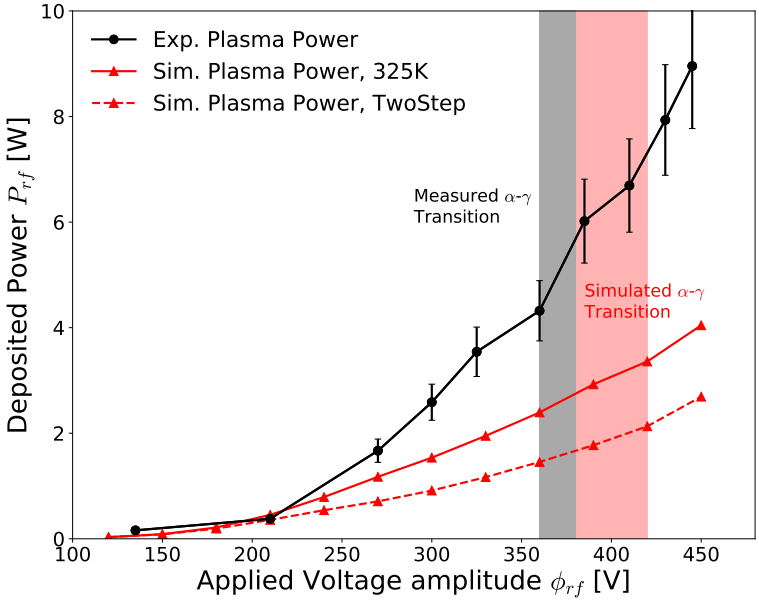

Figure 3.3: Measured and simulated plasma power with respect to applied voltage amplitude. The voltage interval within which the α-γ transition occurs is shown by shaded regions. Operating Conditions: plenum pressure 200 - 240 Pa (1.5 - 1.8 Torr) in experiment, 186 - 226 Pa (1.4 - 1.7 Torr) in simulation, for 13.56 MHz driving voltage, simulation wall temperature 332 - 963 K.

The measured and simulated plasma powers show close agreement for applied voltages up to approximately 250 V, beyond which the measured plasma power increases more rapidly with voltage. An α-γ mode transition occurs for applied voltages between 360 - 385 V accompanied by an increase in deposited plasma power. An α-γ mode transition is also observed in simulation over a similar voltage range between 360 - 420 V, however the same increase in P_{rf} is not observed in either the cold (325 K) or variable temperature wall cases.

The difference between the measured and simulated plasma powers could arise due to power deposition in non-plasma components within the circuit, which are not accounted for in the model. Additionally, the secondary electron emission and thermal accommodation coefficients will affect the power deposition to the plasma. These values are not precisely known in the experiment, and can change depending on material temperature and surface cleanliness[189,193,194]Finally, note that by increasing the initial wall temperature with the applied voltage using the two step method, the conductive losses from the neutral gas to the walls are reduced for a fixed thermal accommodation coefficient. Less power is required to attain higher neutral gas temperatures as the power required to maintain the high wall temperature is effectively removed from the simulation. This results in a lower simulated plasma power deposition for a given applied voltage when employing the two step method.

The results presented in figures 3.1, 3.2 and 3.3 show a good agreement between measurement and simulation, reliably capturing the phase-resolved sheath dynamics, dc self-bias formation and associated α-γ transition. However, phase-averaging of the secondary electron dynamics leads an underestimation in the simulated plasma density and power deposition.

3.2 Spatio-Temporal Ionisation Dynamics in the *Pocket Rocket*

Having validated the simulated excitation within the *Pocket Rocket* to that measured in experiment in section 3.1, it is now possible to employ the numerical analysis in a discussion of the spatial and temporal ionisation mechanisms.

3.2.1 Temporally Resolved Ionisation Dynamics

Figure 3.4 shows the the simulated phase-resolved Ar^+ ionisation rates ι_{tot} with respect to applied voltage over the range 150 - 450 V. The associated alumina surface bias and phase-averaged sheath extents adjacent to the powered electrode (Z = 21 mm) for applied voltage amplitudes of 150 V, 300 V and 450 V are shown in figures 3.4 (b) and (c), respectively, where a Savitzk-Golay filter has been applied to smooth the sheath extents.

The total Ar^+ ionisation rate ι_{tot} shown in figure 3.4 (a) is integrated through a 24 mm depth of field including ionisation from the entire source region, as performed previously in figure 3.1, Sheath collapse heating (peak A) is observed for all applied voltages in figure 3.4 increasing in magnitude and reducing in temporal extent with increasing applied voltage. In addition, the peak occurs later in the phase-cycle with increasing applied voltage, more closely aligning with the phase of maximum applied voltage, as opposed to the phase of increasing applied voltage. This phase drift and the temporal narrowing of peak A arise due to the increasingly negative sheath potential and the differing ion and electron mobilities leading to the build up of an increasing excess negative charge within the plasma bulk within an rf cycle. Increasing the applied voltage results in a larger dc self-bias voltage and a greater phase-averaged radial ion flux as shown previously in figures 3.8 (a) and (b).

To maintain quasi-neutrality within the bulk there must exist an equal phase-averaged electron flux to the walls to compensate the positive ion loss from the plasma within a single rf cycle[195]. During the phase of sheath collapse, between approximately $0.1 \leq \frac{\omega t}{2\pi} \leq 0.3$ in figure 3.4 (c), electrons are able to leave the bulk plasma to conserve current continuity. However, due to the increasingly negative sheath potential fewer electrons are able to leave the plasma until the sheath has fully collapsed, leading to the temporal drift in the peak A. Naturally, a reduced portion of the rf phase-cycle for which electrons are able to leave the plasma leads to higher electron velocities required to maintain the same flux, resulting in the observed higher rates of ionisation and excitation. Note that due to the relatively limited radial resolution ($\approx$ 9 cells), the sheath extents presented in figure 3.4 (c) do not fully collapse, however electrons within the simulation are observed to leave the plasma during phases of minimum sheath extension, indicating that a sheath collapse has occurred.

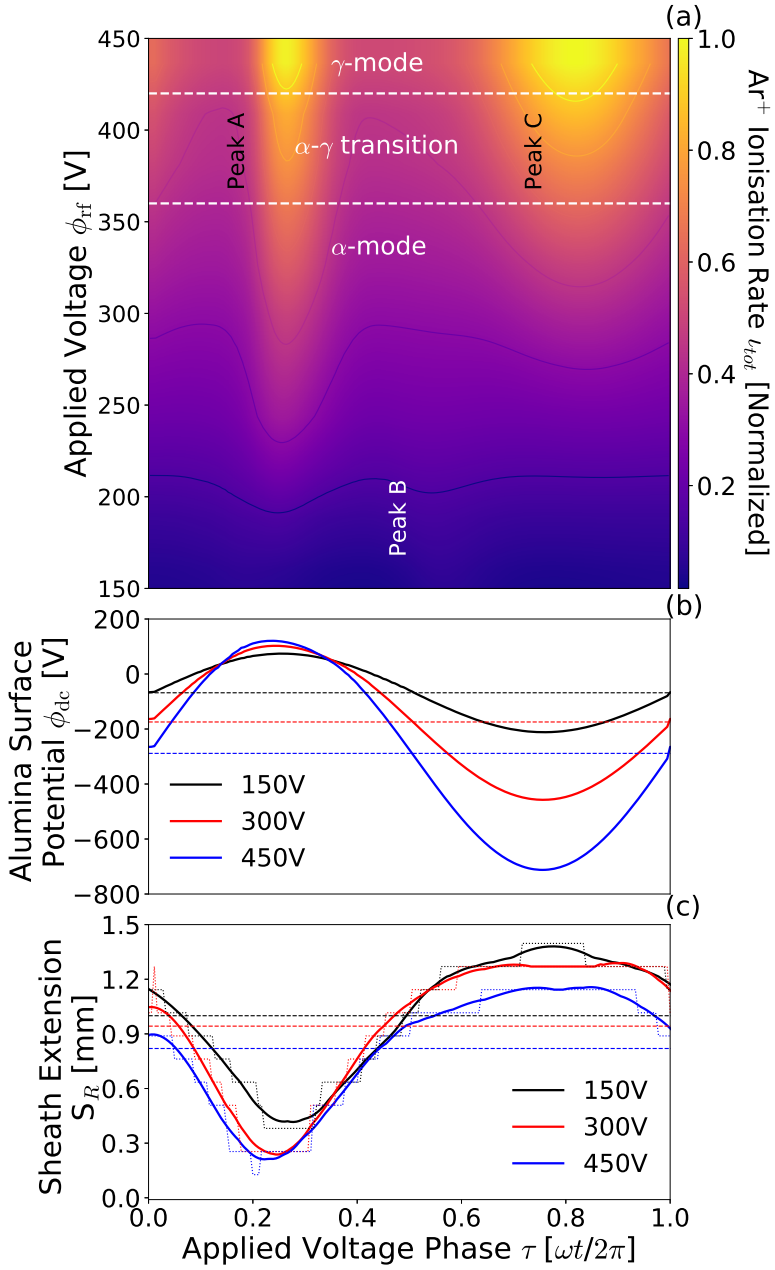

Figure 3.4: Simulated (a) on-axis phase-resolved Ar^+ ionisation rate, (b) dielectric surface potential and (c) sheath extension adjacent to the powered electrode (region 2), (R, Z) = (2.1 mm, 21 mm), for applied voltages 150 V, 300 V, 450 V. Dashed lines in (b) and (c) indicate phase-averaged alumina surface potentials and sheath extensions, respectively. The dotted lines in (c) indicate computed sheath extents employing the Brinkmann Criterion, while solid lines are smoothed employing a Savitzky–Golay filter. Operating conditions: plenum pressures 186 - 226 Pa, (1.4 - 1.7 Torr) argon, 13.56 MHz, wall temperatures 349 K - 963 K, respectively.

At 13.56 MHz, sheath expansion heating (peak B) is observed for applied voltages below $\approx$ 210 V. Peak B is observed for phases where the alumina surface potential is decreasing, repelling electrons from the surface and re-forming the sheath region. Due to the relatively

high pressures ($\geq$ 1 Torr), the maximum sheath extension, and hence velocity, is relatively low resulting in a small contribution to the total ionisation, from electrons accelerated via sheath expansion heating.

Secondary electron heating (peak C) occurs just after the phase of most negative alumina surface potential ($\frac{\omega t}{2\pi} = 0.77$). As discussed previously, peak C arises from highly energetic secondary electrons released from the alumina surface, which are then accelerated through potentials of up to 700 V through the fully extended sheath, see figure 3.4 (b). While the electron energy varies in response to the applied voltage amplitude, the secondary electron production varies in response to the radial Ar^+ flux, and hence remains approximately constant within an rf phase-cycle. Therefore, the background ionisation observed between the previously identified heating mechanisms is an indication of the temporally constant secondary electron production, whereas peak C describes the temporally varying secondary electron energy. Finally, note that as electrons produced at material surfaces have a non-zero time of flight to reach the central axis of the source leading to an observed delay between the phase of maximum ion bombardment, at most negative voltage, and when the on-axis ionisation is observed.

3.2.2 Spatially Resolved Ionisation Dynamics

Simulated phase-resolved, on-axis Ar^+ ionisation rates from upstream, at the powered electrode and downstream of the source, regions 1, 2 and 3, respectively are shown in figure 3.5 (a) for a 226 Pa (1.7 Torr) plenum pressure, 13.56 MHz, 450 V, γ-mode discharge. Here, the ionisation at each spatial location is observed independently as opposed to the axially integrated analysis discussed earlier. The associated sheath potential at each region, defined as $\phi_S(\tau) = \phi_{fp}(\tau)$ - $\phi_{dc}(\tau)$, is shown in figure 3.5 (b).

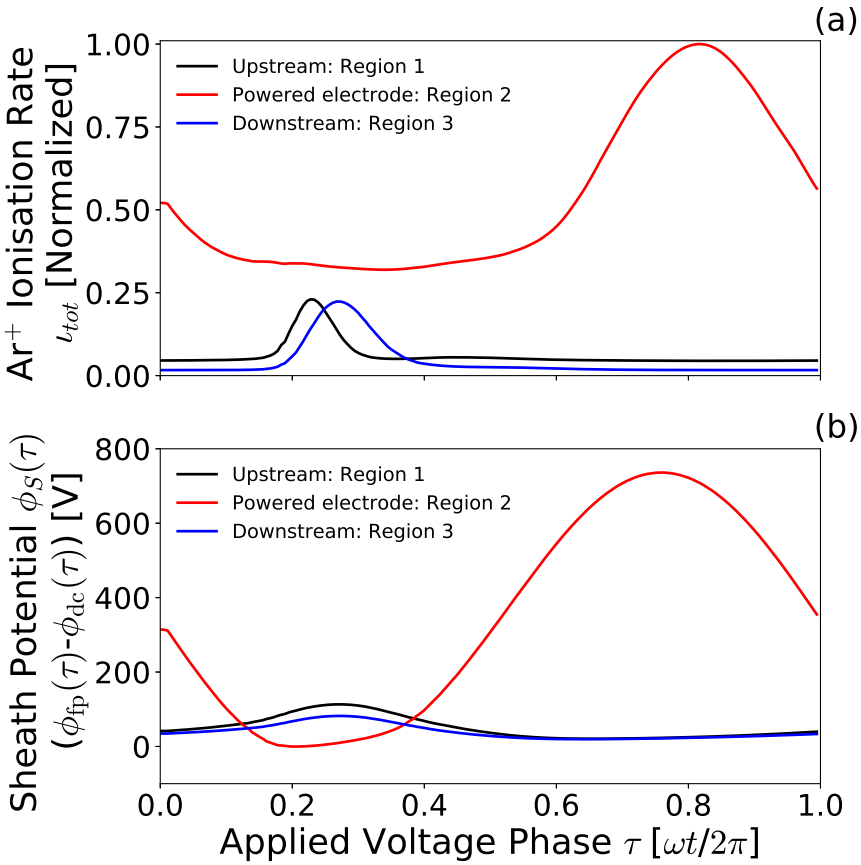

Figure 3.5: Simulated on-axis (a) Ar^+ ionisation rates ι_{tot} and (b) sheath potentials upstream, at the powered electrode and downstream, regions 1, 2 and 3, respectively. Spatially resolved ionisation is obtained by employing a zero width depth of field. Operating conditions: plenum pressure 186 Pa, 213 Pa, 226 Pa, (1.4 Torr, 1.6 Torr, 1.7 Torr) argon, 13.56 MHz, wall temperature 349 K, 687 K, 963 K, respectively.

The normalised Ar^+ ionisation rates shown in figure 3.5 (a) exhibit three notable features, a large ionisation structure adjacent to the powered electrode and two smaller ionisation structures adjacent to the upstream and downstream grounded electrodes. The ionisation adjacent to the upstream grounded electrode (region 1) peaks just prior to the maximum sheath potential, and hence maximum sheath extension, shown in figure 3.5 (b). Note that the phase of maximum sheath potential at the grounded electrodes is $\frac{\omega t}{2\pi} = 0.5$ out of phase relative to the maximum sheath drop at the powered electrode. Electron heating upstream therefore peaks during the phase of sheath expansion at the grounded electrode.

Similar behaviour is observed at the downstream electrode (region 3), albeit exhibiting a temporally wider ionisation peak that is phase-offset by approximately $\frac{\omega t}{2\pi} = 0.05$. Note also that the background ionisation rate is lower at the downstream electrode, this is likely due to a reduced radial Ar^+ flux, discussed with reference to figure 3.8 (b), and hence reduced secondary electron population. Although the maximum sheath voltage drop across the downstream grounded electrode sheath is lower than that for the upstream, it occurs

over the same region in rf phase ($0.1 \leq \frac{\omega t}{2\pi} \leq 0.5$) shown in figure 3.5 (b), and we would therefore expect to see agreement in the temporal location of the resulting ionisation. While this suggests that sheath expansion heating is likely still the primary heating mechanism, it indicates that there may be further effects from other heating mechanisms such as axial electron flux towards the collapsed powered electrode sheath. Upstream and downstream (regions 1 and 3, respectively) both demonstrate heating mechanisms that correspond to α-mode heating, where sheath expansion and collapse dictate the ionization and excitation structures.

The ionisation dynamics at the powered electrode (region 2) exhibit a $\frac{\omega t}{2\pi} = 0.5$ phase-offset from those observed at the grounded electrode, as expected. Most notably, peak ionisation occurs immediately following the phase of maximum sheath voltage drop $\frac{\omega t}{2\pi} = 0.8$, corresponding to the phase of most negative alumina surface potential. This, again, confirming that the primary ionisation mechanism in γ-mode operation arises from collisions from an increased number of high energy secondary electrons, accelerated through the sheath potential. The phase-resolved ionisation at the powered electrode (region 2) shows little evidence of either sheath expansion or sheath collapse heating during the powered electrode sheath collapse, $\frac{\omega t}{2\pi} \approx 0.25$. While these mechanisms are expected at this location, it is likely that they are hidden behind the substantial background ionisation rate. This background excitation, observed previously in figure 3.4 (a), increases with voltage due to the ion-induced secondary electron emission increasing with the phase-averaged ion flux, providing a relatively time-independent ionisation component.

3.3 Spatial Characterisation of the *Pocket Rocket* Microthruster

This section examines steady-state operation of the *Pocket Rocket* microthruster, drawing links between the ionisation dynamics discussed in section 3.2 and the resulting electron and ion densities, dc self-bias voltage and resulting ion and neutral temperatures. Spatially resolved characterisation of the *Pocket Rocket* is prohibitively difficult in experiment, owing to the limited diagnostic access and small inner dimensions of the source, as such this section employs simulated results.

3.3.1 Ionisation Dynamics and Formation of DC Self-Bias

The Ar^+ density and electron temperature within the *Pocket Rocket* are shown in figures 3.6 (a) and (c), respectively for α-mode operation at 150 V and in figures 3.6 (b) and (d), respectively for γ-mode operation at 450 V. The phase-averaged sheath extent is denoted by the white dashed lines.

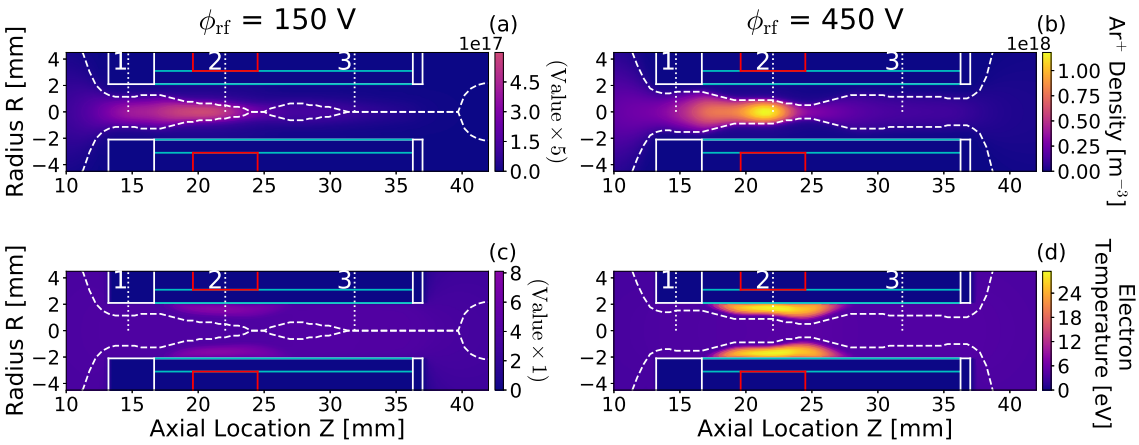

Figure 3.6: Phase-averaged Ar^+ density at (a) 150 V and (b) 450 V applied voltage amplitudes and phase-averaged fluid electron temperature at (c) 150 V and (d) 450 V. Ar^+ densities at 150 V in panel (a) have been scaled by a factor of 5 for clarity. The phase-averaged sheath extent is denoted by the white dashed lines. Regions 1, 2 and 3, denoted by the white dotted lines, are defined as upstream, powered electrode and downstream, respectively. Operating conditions: Plenum pressure 200, 226 Pa (1.5, 1.7 Torr) of argon, applied voltages of 150 V, 450 V at 13.56 MHz, wall temperatures of 349 K, 963 K.

The Ar^+ density, shown in figures 3.6 (a) and (b), reaches a maximum on-axis at the centre of the powered electrode (region 2). Larger densities are observed upstream (region 1) as compared to downstream (region 3), this decrease in Ar^+ density from upstream to downstream is primarily a result of the decreasing pressure. The inhomogeneous axial Ar^+ density results in an axial variation in sheath thickness and capacitance[79], leading to increased vari-

ations in current collected at the powered and grounded electrodes. Due to the relatively low ion density for $\phi_{rf} = 150$ V, the sheath extent is large relative to the source radius, and exceeds the source radius for axial locations of $Z \geq 30$ mm. Note that due to the cylindrically symmetric simulation geometry, the maximum computable sheath width is limited to $S_R = R$. Increasing the applied voltage results in an order of magnitude increase in the Ar^+ density from figure 3.6 (a) to (b). The increased plasma density is capable of sustaining a narrower sheath further downstream, further exaggerating the physical asymmetry of the source.

A related asymmetry is observed in the fluid electron temperature about the powered electrode, shown in figures 3.6 (c) and (d), with a region of hotter electrons extending further from the wall downstream of the powered electrode (region 3). This axial asymmetry arises due to the axially varying sheath extent resulting from the reduction in the Ar^+ density beyond Z = 24 mm and is therefore ultimately related to the location of the powered electrode and pressure gradient within the source. The protruding region of hot electrons downstream of the powered electrode is more easily observed in γ-mode at 450 V, shown in figure 3.6 (d), where the maximum electron temperature has increased by a factor of three as compared to the 150 V α-mode discharge.

The high electron temperatures observed adjacent to the wall are the result of two mechanisms. Primarily, the sheath represents a negative space charge region and hence repels low energy electrons, leaving only higher energy electrons within the sheath volume. In addition, non-thermal secondary electrons emitted as a result of ion bombardment incident upon the alumina wall further increase the average electron temperature within the sheath. Note that the secondary electrons contribute to this temperature in an indirect manner as described previously, and hence the 'bulk' electron temperature presented in figures 3.6 (c) and (d) represent a lower estimate for the secondary electron temperature at these applied voltages. The increased ionisation arising from ion-induced secondary electrons results in an increased plasma density localised adjacent the powered electrode (region 2) as shown in figure 3.7 (a). The associated on-axis (R = 0.0 cm) plasma floating potential ϕ_{fp} and alumina surface potential ϕ_{dc} are shown in figure 3.7 (b).

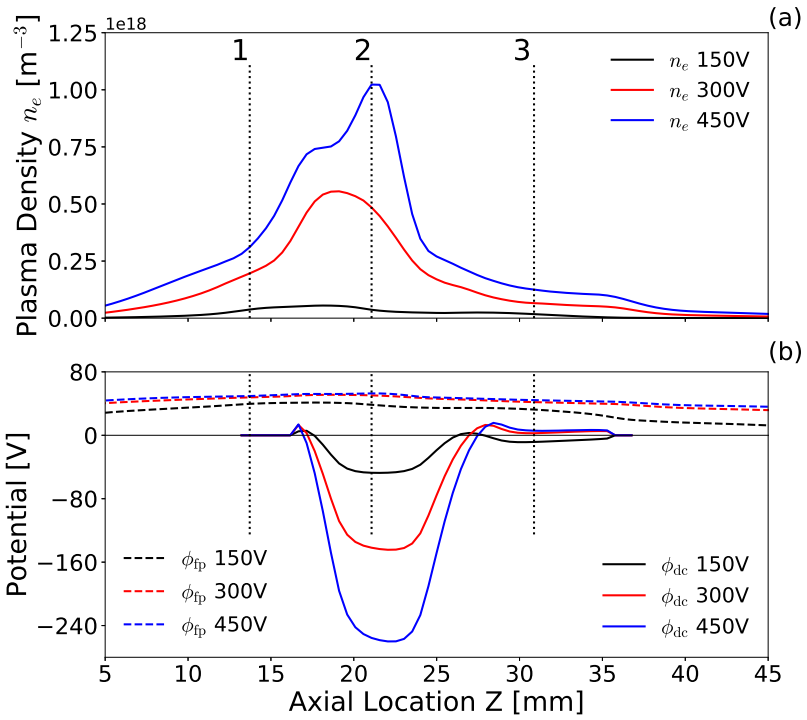

Figure 3.7: Phase-averaged (a) on-axis plasma density and (b) on-axis plasma floating potential and alumina surface potential with respect to axial location for 150 V, 300 V, and 450 V discharges. Applied voltages of 150 V and 300 V represent α-mode discharges while 450 V represents a γ-mode discharge. Regions 1, 2 and 3, denoted by the white dotted lines, are defined as upstream, powered electrode and downstream, respectively. Operating conditions: Plenum pressure 186 Pa, 213 Pa, 226 Pa, (1.4 Torr, 1.6 Torr, 1.7 Torr) of argon, applied voltages of 150 V, 450 V at 13.56 MHz, wall temperatures of 349 K, 687 K, 963 K.

The on-axis plasma density for a 150 V, α-mode discharge at 13.56 MHz, shown in figure 3.7 (a), reaches a maximum of 1.1 $\times$ 10^{17} m^{-3} upstream of the powered electrode at Z = 16 mm (between regions 1 and 2). While this agrees with the spatial distribution of the Ar^+ ion density shown previously in figure 3.6 (a), it does not coincide with the location of most negative alumina surface potential, located adjacent to the powered electrode at Z = 21 mm. This indicates two features regarding α-mode operation, firstly that the location of peak Ar^+ ion density does not align with the location of highest sheath potential, leading to inefficient ion acceleration. Secondly, that the ionisation primarily arises from bulk electron heating processes, and secondary electrons do not significantly influence the plasma density. The temporal and spatial distribution of the distinct α-mode and γ-mode heating mechanisms is described in more detail in section 3.2.

The time-averaged dielectric surface potentials in figure 3.7 (b), previously discussed with reference to figures 3.1 (e) and (f), are negative between approximately 17 $\leq$ Z $\leq$ 27 mm. Note that in traditional rf discharges, where bare metal electrodes are used and a blocking capacitor is installed in the circuit, the dc self-bias voltage forms to balance the collected currents to the grounded and powered electrodes[9]. In this geometry however, the electrodes

are not in direct contact with the plasma, and so currents to those electrodes are displacement currents. Since the bias on the blocking capacitor is small, the average applied voltage to the electrodes is essentially zero, observed in figures 3.1 (e) and (f). The charging of the alumina dielectric surface therefore functions as a dc self-bias voltage, and will be referred to as such henceforth.

Increasing the applied voltage to 300 V results in the on-axis plasma density increasing by a factor of 6, reaching a maximum value of 6×10^{17} m^{-3} upstream of the powered electrode at Z = 18 mm (between regions 1 and 2). In addition, the plasma density increases downstream of the powered electrode (region 3), dropping off sharply beyond Z $\geq$ 37 mm as the plasma expands through the thruster outlet. While the location of peak plasma density has shifted downstream by 2 mm, it remains misaligned with the location of most negative dc self-bias voltage. It is worth noting that the spatial distribution in plasma density and maximum value obtained at 300 V closely agree with previous work employing similar operating conditions [76], which observed a maximum on-axis plasma density of 5.4×10^{17} m^{-3}.

For applied voltages above 300 V the location of peak plasma density moves towards the centre of the powered electrode at Z = 21 mm (region 2) reaching a maximum value at that location of 1.03×10^{18} m^{-3} for an applied voltage of 450 V (γ-mode). The more moderate increase in plasma density upstream of the powered electrode, centred on approximately Z = 17 mm, is attributed to electron heating during sheath collapse upstream of the powered electrode (region 1), representing a non-negligible proportion of α-mode heating. However, the variation in plasma density adjacent to the powered electrode between 300 - 450 V is distinct from the increase observed between 150 - 300 V as it is highly localised, coinciding with the location of most negative dc self-bias voltage. In addition, secondary electrons preferentially undergo ionisation interactions as they typically poses a high energy ($\geq$ 50 eV) relative to the argon first ionisation potential (15.76 eV), leading to multiple ionisations per secondary released [127]. This increase in the plasma density is therefore attributed to the production of a larger number of more energetic secondary electrons, released following ion bombardment of the alumina surface, implying an increased radial ion flux incident upon the alumina wall.

The normalised dc self-bias voltage adjacent to the powered electrode (region 2) and corresponding radial Ar^+ ion flux at regions 1, 2 and 3 with respect to applied voltage are shown in figures 3.8 (a) and (b), respectively.

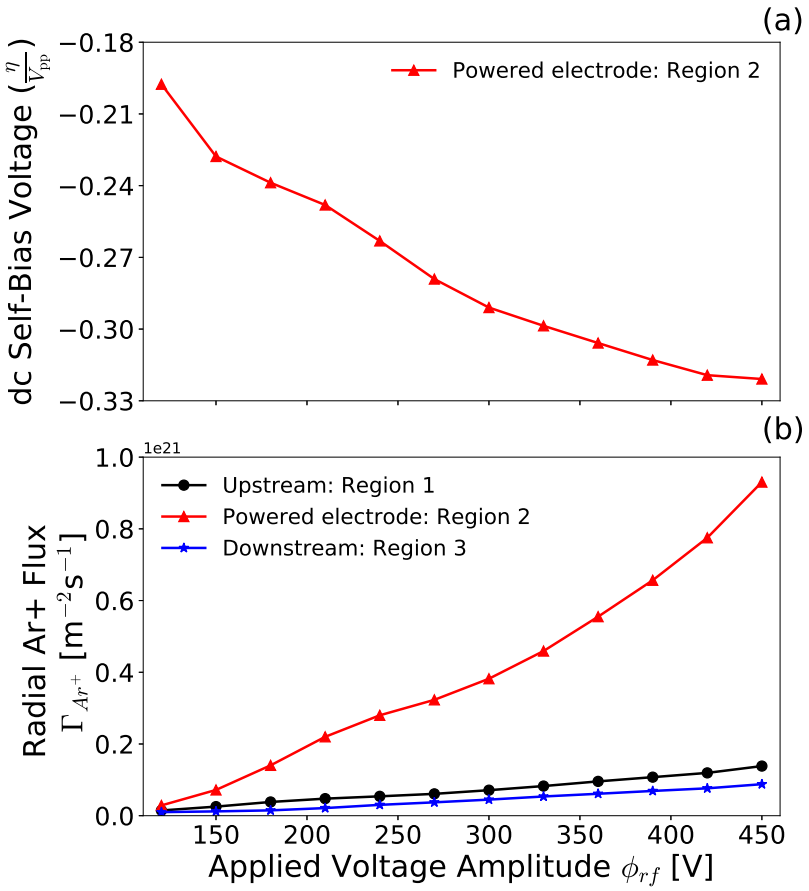

Figure 3.8: Phase-averaged (a) dc self-bias voltage and (b) radial Ar^+ flux incident upon the alumina surface with respect to applied voltage amplitude upstream (region 1), at the powered electrode (region 2) and downstream (region 3). Plenum pressure 186 - 226 Pa (1.4 - 1.7 Torr) argon, 13.56 MHz applied voltage, alumina wall temperature 349 - 967 K.

The dc self-bias voltage in figure 3.8 is normalised to the peak-to-peak voltage V_{pp} to more clearly illustrate variations in the asymmetry of the discharge. Due to the significant physical asymmetry between the powered and grounded electrode areas, the dc self-bias voltage is already a large fraction ($\approx 19\%$) of the applied peak-to-peak voltage even when the discharge is operating in α-mode at 150 V. As the applied voltage amplitude is increased through 150 - 450 V the dc self-bias approaches approximately 32% - 35% of the applied peak-to-peak voltage. This corresponds to a dc self-bias voltage of -289 V for an applied voltage of 450 V, as compared to only -68 V for an applied voltage of 150 V.

Assuming a constant current density, the dc self-bias voltage is determined by the ratio of the collecting areas of the grounded and powered electrodes, which remains unchanged. The variation in the normalised dc self-bias voltage with increasing applied voltage indicates additional mechanisms underpinning the physical asymmetry, as discussed in section 1.6.1. First, it should be stated that an increase in the driving voltage naturally produces an increase in the dc self-bias voltage, for all other conditions remaining constant, however

the ratio between the applied voltage and the dc self-bias voltage would not be expected to change. Second, with increasing applied voltage and power deposition the ion density increases, this variation is not homogeneous however and the greatest increase is observed adjacent to the powered electrode, shown in figures 3.6 (a) and (b). This reduces the powered electrode sheath extension relative to that of the grounded electrode sheaths. A narrower powered electrode sheath exhibits a greater capacitance, which enables more current to be collected by the powered electrode, thereby making the negative dc self-bias voltage a larger fraction of the applied voltage[9,79]. Third, an increase in the ion flux due to the increased density releases more secondary electrons at the radial alumina wall adjacent to the powered electrode. These secondary electrons are accelerated to higher energies through the enhanced sheath potential as the dielectric surface potential is more negative. As the dc self-bias voltage varies along the axial length of the thruster, so too does the flux and energy of ion-induced secondary electrons, which leads to an additional secondary electron induced asymmetry[196].

Indirect evidence of the axially varying secondary electron emission rate is shown in figure 3.8 (b), where the radial Ar^+ ion flux adjacent to the powered electrode exhibits a substantially greater increase with applied voltage than elsewhere in the thruster. Note that this also illustrates the purpose of the dc self-bias voltage formation, to enforce equal positive charge loss through the powered and grounded electrodes, thus nessecitating a higher Ar^+ flux through the smaller powered electrode area[9]. As the secondary electron emission coefficient employed in this model is energy independent*, the secondary electron emission is therefore directly proportional to the ion flux. Secondary electrons released adjacent to the powered electrode are also subject to a larger potential gradient due to the localised dc self-bias voltage, and are accelerated to higher energies than those produced at the grounded electrodes, resulting in a further increased ionisation rate. The dc self-bias voltage therefore plays a role in determining the ionisation rate and ion density adjacent to the powered electrode, which in-turn determines the extent and capacitance of the powered sheath resulting in a non-linear coupling between the applied voltage and the steady state dc self-bias voltage.

3.3.2 Radial Ar^+ Ion Energy Distribution

The radial Ar^+ ion flux has been shown to increase in proportion to the magnitude of the dc self-bias voltage. Flux, computed as the density velocity product through a unit area, depends not only on the Ar^+ density but also the mean Ar^+ velocity, and therefore increases with the mean Ar^+ energy $\hat{\epsilon}_{Ar^+}$. The simulated mean and modal Ar^+ energies incident upon the alumina adjacent to the powered electrode (R,Z = 2.1 mm,21 mm) for applied voltage amplitudes between 150 - 450 V are shown in figure 3.9

*This approximation is appropriate for ion energies below $\approx$ 1 keV, and therefore represents a reliable model for the ion energies observed in the *Pocket Rocket*[73].

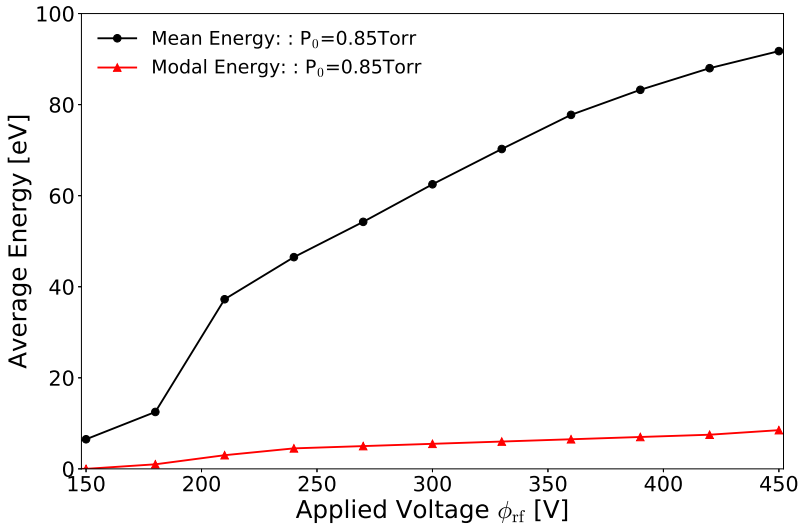

Figure 3.9: Phase-averaged mean and modal Ar^+ ion energies incident upon the alumina wall adjacent to the powered electrode at region 2 (R,Z = 2.1 mm,21 mm) for applied voltage amplitudes between 150 - 450 V. Operating Conditions: plenum pressure 186 - 226 Pa (1.4 - 1.7 Torr), 13.56 MHz, wall temperature 334 - 963 K.

The mean Ar^+ ion energy increases in proportion with the applied voltage, exhibiting a sharp increase between applied voltages of 150 V and 180 V. This transition coincides with a significant (0.3 mm) decrease in the sheath extent between these two voltages, hence resulting in an increased electric field. For reference the sheath extent reduces by approximately the same distance between applied voltages of 180 - 450 V. The modal ion energies remain comparatively low, never increasing beyond 10 eV, implying a collisionally dominated system and a Maxwellian shaped IEDF. This is beneficial as it indicates a high ion-neutral collision rate and an effective transfer of energy from the ion population to the neutral population, enhancing the neutral gas heating.

While the high radial Ar^+ ion acceleration and flux through the powered electrode sheath are desirable for neutral gas heating, high energy ions reaching the alumina surface will result in undesired etching and erosion. Figures 3.10 (a) and (b) show the angularly resolved IEDF and angle integrated IEDF incident on the alumina wall adjacent to the powered electrode (R,Z = 2.1 mm,21 mm) for a 450 V γ-mode discharge. The IEDF shown in figure 3.10 (b) is integrated through angles of incidence between $-45° \leq \theta_i \leq 45°$ and through a single 13.56 MHz phase cycle τ.

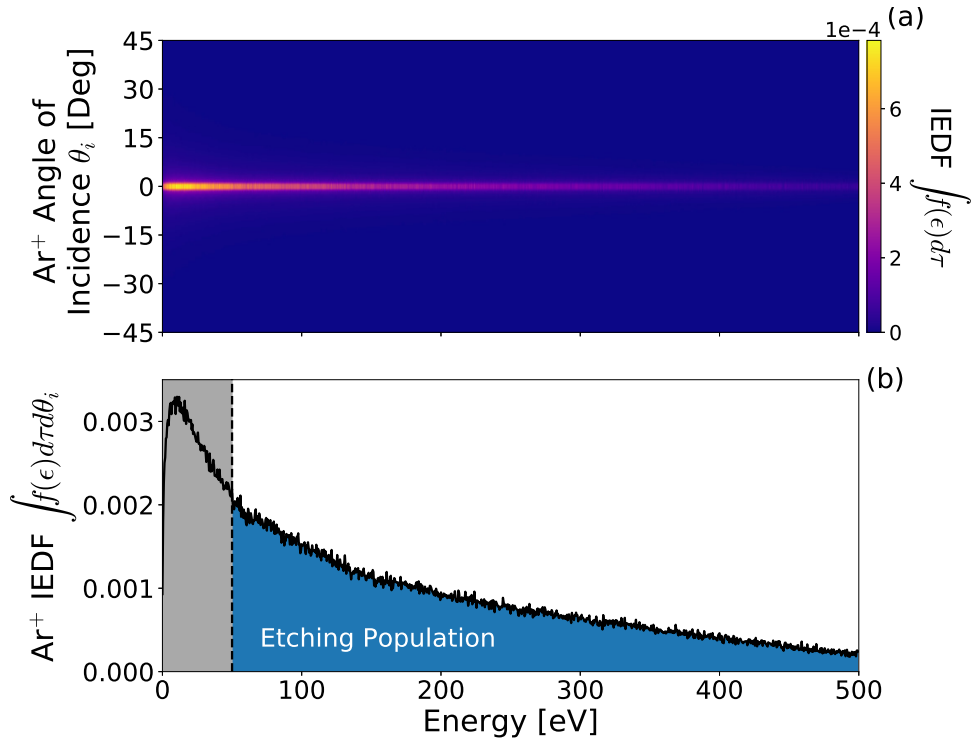

Figure 3.10: Phase-averaged (a) angularly resolved and (b) angle integrated Ar^+ ion energy distribution (IEDF) incident upon the alumina wall adjacent to the powered electrode (R,Z = 2.1 mm,21 mm) for a 450 V γ-mode discharge. Energies below the sputtering threshold for alumina (50 eV) are denoted by the grey region. The ion population capable of etching alumina is denoted by the blue fill under the IEDF in panel (b). Operating Conditions: plenum pressure 226 Pa, (1.7 Torr) argon, 13.56 MHz at 450 V, wall temperature 963 K

The angular dispersion of Ar^+ ions impacting the alumina surface is shown in figure 3.10 (a) for a 450 V γ-mode discharge, where the colour denotes the fraction of the IEDF at a given energy. The angular dispersion is very small, with over 50% of ions accelerated through the powered electrode sheath impacting the radial wall hit within 2° of normal. This indicates that the radial ion acceleration is substantial enough such that the radial ion flux is not greatly affected by the perpendicular neutral flow. The IEDF shown in figure 3.10 (b) is obtained through an angular integration of figure 3.10 (a). It is Maxwellian in profile with a modal energy of 8.5 eV, indicating a collisional sheath as discussed previously. Despite the collisional conditions, a substantial high energy tail is observed, representing a significant number of high energy ions reaching the alumina surface. Approximately three quarters (73%) of the ion population impact the alumina surface with energies above 50 eV, the sputtering threshold for alumina[197]. Therefore, sputtering of the alumina surface is likely to occur during high voltage, γ-mode, operation.

As sputtering rates scale linearly with the ion current density incident upon the target surface[79], an estimate of the etching rate in the *Pocket Rocket* can be obtained from the radial ion flux. The radial distance etched into a material surface R_{etch} in time t is given by equation 3.4 below[197].

$$\frac{R_{etch}}{t} = \left(\frac{M_s}{\rho_s N_A e}\right) S_y J_p \tag{3.4}$$

Where, M_s and ρ_s are the molar mass and density of the target material, respectively, N_A is Avogadro's constant, e is the elementary charge, S_y is the sputtering yield and J_p is the current density incident upon the target surface. From figure 3.8 (b) the radial Ar^+ flux adjacent to the powered electrode reaches a maximum value of 9.3 $\times$ 10^{20} $m^{-2}s^{-1}$ for operation at 450 V, representing a current density of 14.9 mA cm^{-2} if averaged across the 5 mm long inner area of alumina coating the powered electrode, see figure 2.6. This value represents an upper limit for the Ar^+ current density as, from figure 3.10 (b), only 73% of the ions are expected to be capable of sputtering. Assuming a spatially homogeneous alumina density of $\rho_{Al_2O_3} = 0.00395$ kg m^{-3}, where the molar weight for alumina is $M_{Al_2O_3} = 0.102$ kg mol^{-1} and assuming a conservative 25% - 50% redeposition rate, i.e. a net sputtering yield of between $0.5 \leq S_y \leq 0.75$, the final net etching rate is computed as between 0.72 - 1.08 μm/hour. This qualitatively agrees with alumina etching rates of 10 nm/min (0.6 μm/hour) demonstrated for industrial ion mills employing a 500 eV, 1 mA cm^{-2} Ar^+ beam[197]. At this rate the *Pocket Rocket* could operate for between 900 - 1400 hours before etching of the alumina wall became a significant concern. By comparison, 50 - 100 g of argon propellant at 100 sccm (1.786 μg min^{-1}) would provide between 400 - 900 hours of propellant. The lifetime of the thruster is therefore expected to be constrained primarily by propellant availability and not through component degradation.

3.3.3 Neutral Gas Heating & Fluid Dynamics

As previously noted, the neutral gas heating in the *Pocket Rocket* primarily arises from ion-neutral charge exchange collisions. Altering the radial ion flux therefore influences the ion-neutral collision frequency, the power transfer efficiency and the resulting neutral gas temperature. The spatially resolved neutral gas temperature and rf power deposition in the *Pocket Rocket* for operation at 13.56 MHz are shown in figures 3.11 (a) and (c), respectively for α-mode operation at 150 V and in figures 3.11 (b) and (d), respectively for γ-mode operation at 450 V. The associated on-axis (R = 0.0 mm) axial pressure profiles and axial neutral velocity profiles are shown in figures 3.11 (e) and (f).

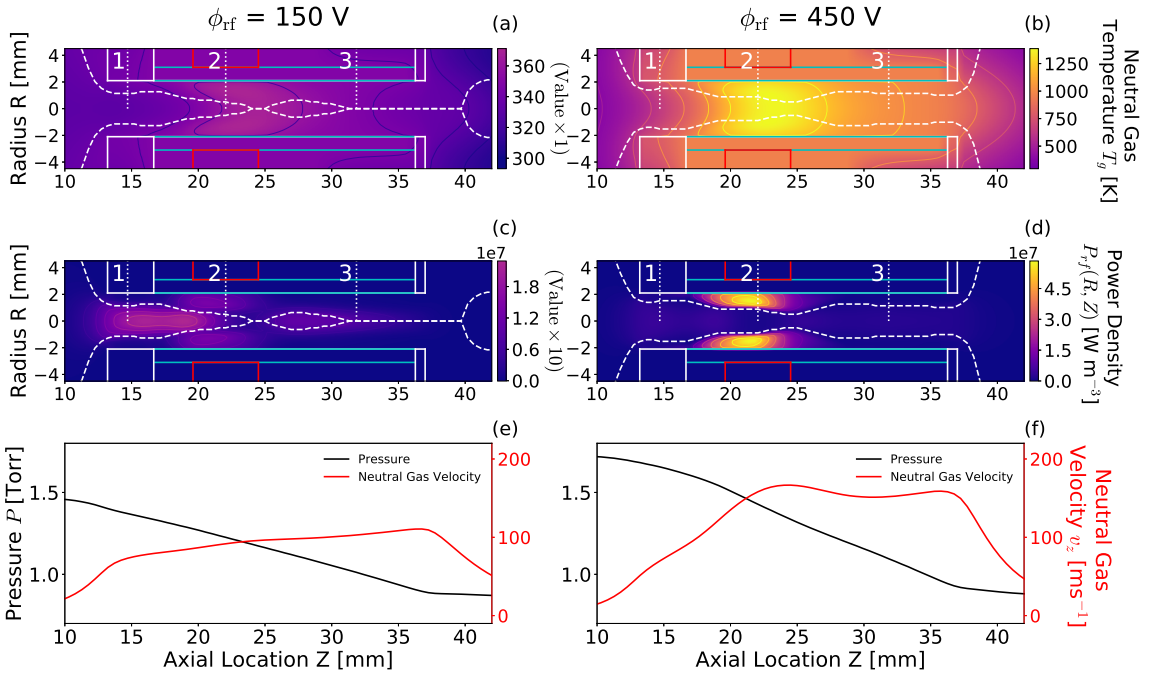

Figure 3.11: Phase-averaged neutral gas temperatures at (a) 150 V and (b) 450 V applied voltage and phase-averaged rf power deposition at (c) 150 V and (d) 450 V and on-axis gas pressure and axial neutral gas velocity at (e) 150 V and (f) 450 V. Power densities at 150 V in panel (c) have been scaled by a factor of 10 for clarity. The phase-averaged sheath extent is denoted by the white dashed lines. Regions 1, 2 and 3, denoted by the white dotted lines, are defined as upstream, powered electrode and downstream, respectively. Operating conditions: Plenum pressure 200, 226 Pa (1.5, 1.7 Torr) of argon, applied voltages of 150 V, 450 V at 13.56 MHz, wall temperatures of 349 K, 967 K.

The neutral gas temperature shown in figures 3.11 (a) and (b) peaks immediately downstream of the powered electrode (region 2). Maximum on-axis neutral gas temperatures of 369 K and 1379 K are observed at 150 V and 450 V, respectively. In both α-mode and γ-mode, neutral gas heating is primarily localised to within the sheath region, correlating with the region of highest radial Ar^+ flux, see figure 3.8 (b), and most negative dc self-bias voltage, see figure 3.7 (b). Neutral heating occurs as the Ar^+ ions first gain thermal energy in the presheath and then accelerate through the dc self-bias enhanced sheath potential, gaining a significant radial advective velocity. Both of which contribute to neutral gas heating via elastic charge exchange collisions. This is in agreement with previous observations, which have suggested that the primary neutral gas heating mechanism is through ion-neutral charge exchange collisions[65,73,146]. Localised heating close to the powered electrode reduces the local gas density, resulting in a reduction in collisionality and will be discussed with respect to figure 3.12.

For a 150 V α-mode discharge, figure 3.11 (c), the majority of the rf power is deposited on-axis downstream of the powered electrode (in between regions 1 and 2) in addition to a smaller power deposition volume within the powered electrode sheath. Note again, that the sheath width is large relative to the source radius, where $S_R \geq R$ for $Z \geq 30$ mm. The total power coupled to the plasma is 0.18 W, of which half (0.09 W) is coupled into

ions via ion acceleration in the sheath and the remaining half is coupled via the previously discussed electron heating mechanisms. As the ions only experience accelerating electric fields in the sheath regions, the power deposition on-axis must arise from electron heating in the bulk. The momentum transfer from electrons to ions is poor due to their disparate masses ($m_{Ar} \approx 73300\ m_e$), therefore no neutral gas heating is observed associated with the on-axis region of power deposition.

In contrast, operation at 450 V in γ-mode, shown in figure 3.11 (d), the total rf power coupled to the plasma increases to 3.27 W, of this 2.69 W is coupled via ion acceleration in the sheaths, and 0.58 W is coupled via electron heating. The increased fraction of power deposited into the ions reflects the increased fraction of the dc self-bias voltage to the applied voltage amplitude, shown previously in figure 3.8 (a). As such, power deposition is highest within the sheath adjacent to the powered electrode between $17 \leq Z \leq 27$ mm, aligning with the region of highest dc self-bias voltage. It is worth noting that in steady-state, the net rate of charge exchange is largest in the center of the bulk plasma where the ion density is highest. However, the heat source is largest off axis, in the sheath volume where the ions gain energy. The phase-averaged sheath extent, and hence heated volume of propellant, are related to the local pressure, plasma density, applied voltage frequency and dc self-bias voltage[9,79]. Combining these effects, the volume of the plasma into which power is deposited can be be optimized for a given thruster radius by varying the dc self-bias voltage. This could be accomplished by varying the size of the grounded electrode relative to the powered electrode, a technique used in semiconductor processing[102,115], or through the application of an electrical asymmetry[128,138], the latter of which is focus of this work and will be discussed in more detail in chapter 5.

The effects of neutral gas heating on the on-axis neutral gas pressure P and axial neutral gas velocity v_z are shown in figures 3.11 (e) and (f), respectively. The increased neutral gas heating results in a slightly elevated plenum pressure at 450 V as compared to 150 V. However, in both α-mode and γ-mode the pressure decreases linearly with respect to distance until it reaches ≈ 0.85 Torr, equal to the output pressure in the expansion region. In α-mode, figure 3.11 (e), the neutral gas velocity increases as it enters the source region (region 1), reaching a maximum of 110 ms^{-1} at the thruster outlet (Z = 37 mm). At this voltage the neutral gas heating is not sufficient to observe any appreciable change in the neutral velocity. Conversely at 450 V in figure 3.11 (f), the neutral gas velocity increases substantially between the inlet and the powered electrode (region 1 to region 2), reaching a maximum of 167 ms^{-1} at the powered electrode (region 2) correlating with the location of peak power deposition. Due to the heated walls the neutral gas temperature, and hence the neutral velocity, is maintained until the thruster aperture. In both cases the gas velocity drops sharply as it expands and cools under PdV work losses upon exiting the thruster at Z = 37 mm (region 3), where $v_z \propto \sqrt{T_g}$ as expected from equation 1.8.

3.3.4 Flow-Regime Transition

Heating a fixed volume of gas results in a reduction of the density and collision rate within the heated volume. To illustrate this effect in the *Pocket Rocket* the simulated phase-averaged on-axis (R = 0.0 cm) Knudsen number K_n is shown in figure 3.12 for three applied voltages, 150 V, 300 V, and 450 V. Note that an increase in the Knudsen number represents a reduction in the collisionality.

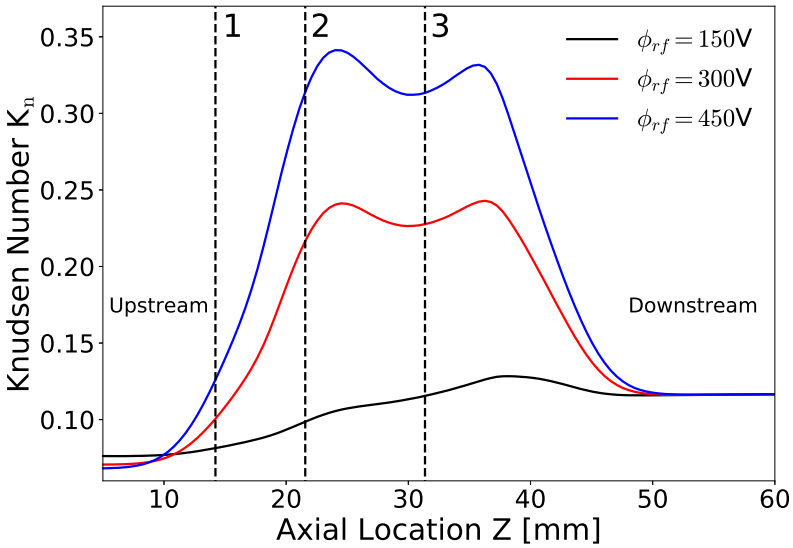

Figure 3.12: Phase-averaged on-axis (R = 0.0 cm) Knudsen number K_n profiles demonstrating a reduced collisionality in the heated region of the source. Operating conditions: Plenum pressure 186 Pa, 213 Pa, 226 Pa, (1.4 Torr, 1.6 Torr, 1.7 Torr) of argon, applied voltages of 150 V, 450 V at 13.56 MHz, wall temperatures of 349 K, 687 K, 963 K.

The Knudsen number varies between $0.03 \leq K_n \leq 0.35$ in figure 3.12, indicating a slip-flow regime[80]. At 150 V, minimal neutral gas heating results in a quasi-linear increase in the Knudsen number through the source, as expected from the pressure gradient shown previously in figure 3.11 (e). This profile shows close agreement with previous work performed for cold gas operation using CFD-ACE+[76,146].

Increasing the applied voltage beyond 150 V introduces localised neutral gas heating adjacent to the powered electrode (region 2), reducing the neutral density at that location. The subsequent reduction in the ion-neutral collision rate is reflected by an increase in the Knudsen number. A reduced collisionality reduces the rate of power transfer between the accelerated Ar^+ ions and the neutral Ar atoms, reducing the gas heating efficiency. This loss of heating efficiency is the primary self-limiting mechanism that ultimately determines the maximum neutral gas temperature achievable for a given input power. Additional losses of power arise from viscous losses to the walls, mediated by the advective neutral axial velocity, and heat lost to the walls to maintain their steady state temperature. For the case of the two step method, the latter of these two mechanisms is artificially reduced.

3.3.5 Thrust and Specific Impulse

The simulated thrust and specific impulse for the *Pocket Rocket* under lab conditions (100 sccm inlet flow, 0.85 Torr output pressure) are shown in figure 3.13. Calculation of the thrust employs the neutral axial velocity, neutral momentum flux and pressure gradient across the downstream thruster outlet (Z = 37 mm), details of the calculation are given in section 2.4.4.

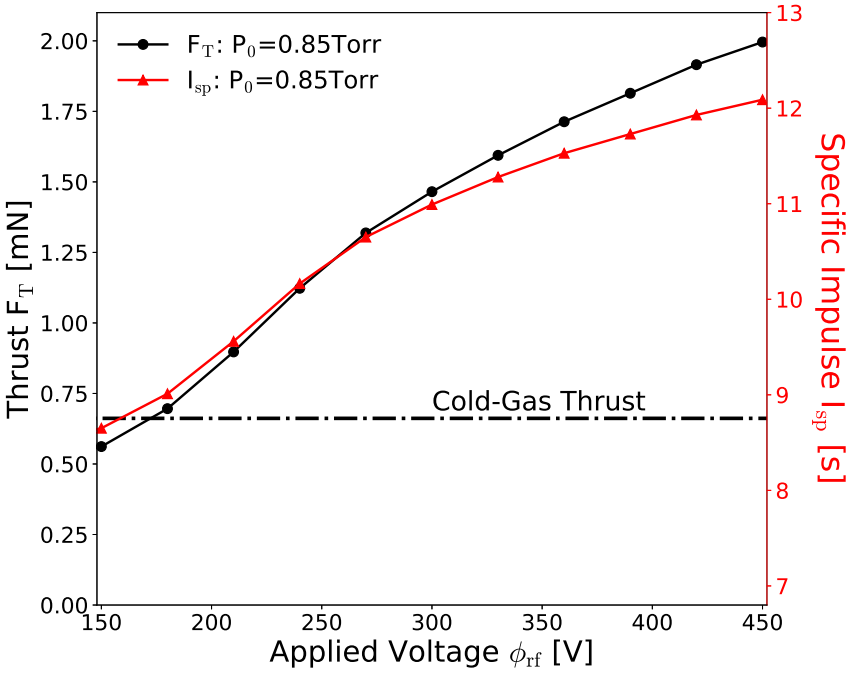

Figure 3.13: Total thrust F_T and specific impulse I_{sp} calculated across the downstream thruster outlet (Z = 37 mm) employing equations 2.19 and 1.6, respectively. Thrust produced from cold gas operation (0.66 mN) is shown by the dash-dotted line. Operating conditions: 100 sccm argon, applied voltages between 150 - 450 V at 13.56 MHz, two step method employed wall temperatures between 349 - 967 K.

The thrust and specific impulse integrated across the downstream thruster outlet (Z = 37 mm), shown in figure 3.13, both increase with increasing applied voltage amplitude. The enhanced thrust with increasing applied voltage amplitude arises primarily from the increased neutral momentum flux due to the increased neutral axial velocity, shown previously in figure 3.11 (f). This is supported by the similar trend in the specific impulse, which is dependant only on the neutral axial velocity. Employing a steady-state hot wall, a maximum simulated thrust of 1.99 mN was achieved for a 3.3 W, 13.56 MHz, 450 V argon discharge under lab conditions employing a 0.85 Torr expansion region pressure. This represents a net gain in thrust of 1.33 mN over the 0.66 mN cold gas case and a net thrust-to-power ratio of 0.40 mN/W. These values exceed thrust-to-power efficiencies commonly achieved in Hall effect (0.05 - 0.08 mN/W)[15,16] and gridded ion (0.01 - 0.02 mN/W)[16] thrusters. Further, The ability to operate the thruster with very low ($\leq$ 5 W) absolute powers provides an advantage over

techniques that require a high minimum power to operate, e.g. Arcjets[14,16]. In addition, the majority of the gas heating in the *Pocket Rocket* occurs within μs timescales[73], permitting pulsed operation with minimal loss of thrust or specific impulse. These properties make the *Pocket Rocket* desirable option for atmospheric drag compensation, station-keeping or low ΔV manoeuvres nano sized platforms with limited onboard power.

These values represent lab operating conditions employing a 0.85 Torr output pressure as measured in experiment. Operation in vacuum will exhibit the formation of a strong shock across the thruster outlet[66,76], maximising the differential pressure component in equation 2.19 and increasing the specific impulse and cold gas thrust component. Therefore, the thrusts calculated here represent lower operational limits, while the thrust-to-power efficiency likely represents an upper limit. Note that the formation of a downstream shocked boundary maintains the upstream pressure gradient through the source and as such, the electron, ion and neutral heating mechanisms discussed within this chapter are not expected to change significantly in vacuum.

3.4 Chapter Summary

To conclude, experimental measurements of the phase-resolved Ar($2p_1$) excitation rate have been compared to those generated by simulation, showing close agreement. Three excitation structures were observed within the rf voltage cycle and the primary heating mechanism responsible for each was identified, namely: electron heating at the collapsing sheath edge during sheath collapse, electron heating during sheath expansion and secondary electron induced excitation at maximum sheath extension. Sheath collapse and sheath expansion heating primarily deposit power upstream and downstream of the powered electrode, while power deposition from secondary electron collisions and ion-neutral charge exchange interactions predominately occurs within the powered electrode sheath. Neutral gas heating was observed adjacent to the powered electrode, where increasing the applied voltage resulted in enhanced neutral axial velocities, specific impulses and thrusts over cold gas operation.

A voltage induced α-γ mode transition was observed for voltages above 420 V in simulation and above 385 V in the experiment, correlating with an increased fraction of the dc self-bias voltage to the applied voltage. The resulting increase in sheath potential, coupled with enhanced ionisation from the secondary electrons, produces substantially increased radial ion fluxes, and consequentially increased neutral gas temperatures. In addition, reduced sheath extensions, higher electric fields and reduced neutral densities result in significantly higher energy ions incident upon the dielectric surface in γ-mode as compared to α-mode. These findings illustrate the inter-dependency between the ionisation dynamics, the dc self-bias voltage and neutral gas heating in capacitively coupled plasmas. Understanding and utilizing these inter-dependencies for the purposes of optimising the ion-neutral momentum transfer and obtaining control over the dominant power deposition pathways forms the focus of chapters 4 and 5, respectively.

Chapter 4

Ion Acceleration with Varying Applied Voltage Frequency

Until this point, the *Pocket Rocket* microthruster has been operated employing a 13.56 MHz applied voltage waveform. In this chapter the *Pocket Rocket* is operated at applied voltage frequencies between 13.56 - 108.48 MHz in order to better understand the interdependencies between the sheath dynamics and the resulting phase-resolved ionisation mechanisms. Experimental measurements of the phase-resolved Ar($2p_1$) excitation rates are compared to those computed employing 2D fluid/kinetic simulations, described in section 2.3, over the range 13.56 - 40.68 MHz. Simulations are then employed to investigate the ionisation dynamics, spatially resolved power deposition and ion acceleration for applied voltage frequencies between 13.56 -108.48 MHz. The formation of mid-energy (60 - 180 eV) structures between 40.68 - 54.24 MHz and additional high energy ($\gtrsim$ 180 eV) structures between 81.36 - 94.92 MHz within the ion energy distribution functions (IEDF) are discussed and a mechanism for their formation within the intermediate pressure range ($\approx$ 200 Pa, 1 Torr) is proposed. Throughout this chapter the *Pocket Rocket* is operated employing 100 sccm of argon with a 0.85 Torr outlet pressure, supplied by a 450 V amplitude voltage waveform unless otherwise stated.

The results and conclusions presented in this chapter are based upon those published by the author in Ref. 113.

4.1 Plasma Heating Mechanisms and Power Deposition

In this section, agreement between the measured and simulated Ar($2p_1$ - $1s_2$) electron impact excitation rates is demonstrated for 13.56 MHz, 27.12 MHz and 40.68 MHz applied voltage frequencies at 450 V applied voltage. Additional simulations are employed to investigate the excitation and ionisation dynamics up to 108.48 MHz. The corresponding variation in the spatially resolved Ar^+ density, radial flux and sheath dynamics, and how these influence the electron and ion power deposition are also discussed. Finally, the effects of varying ion flux and velocity on the neutral gas heating is presented with a consideration of the energy resolved ion-neutral collision cross-section.

4.1.1 Excitation and Ionisation Dynamics: Simulations and Experiments

The measured and simulated Ar($2p_1$) excitation rates for 13.56 MHz, 27.12 MHz and 40.68 MHz applied voltage frequency discharges at 450 V applied voltage amplitude are shown in figure 4.1.

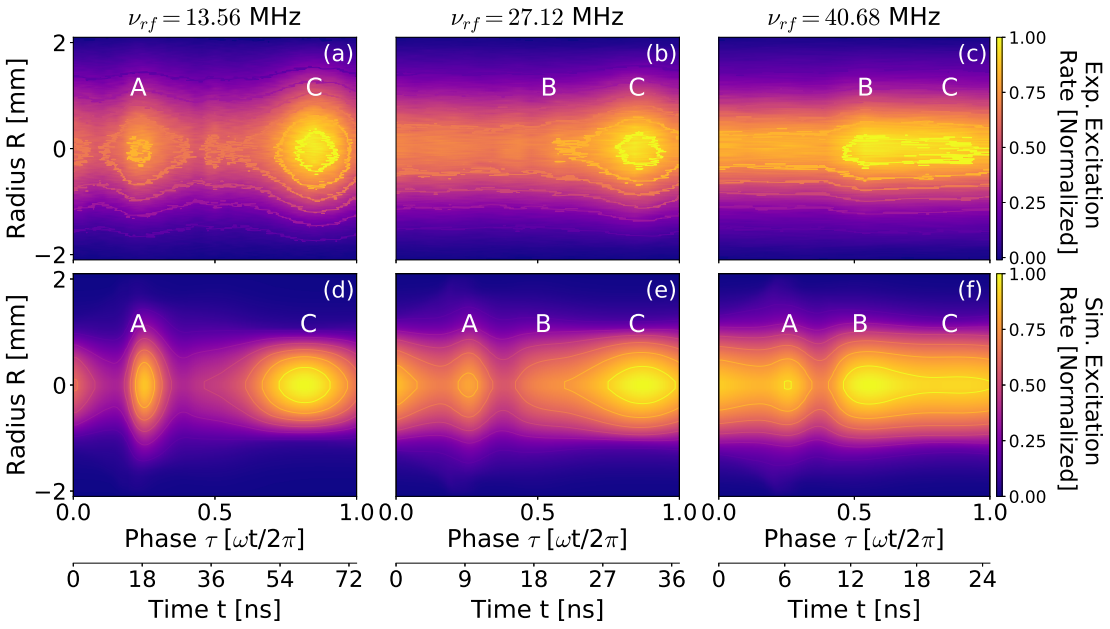

Figure 4.1: Phase-resolved Ar($2p_1$) excitation rates for 13.56 MHz, 27.12 MHz and 40.68 MHz applied voltage frequencies as measured experimentally (a-c), and via simulation (d-f). Excitation during the phase of sheath collapse (Peak A), sheath expansion (Peak B) and due to secondary electrons (Peak C) are identified. Plenum pressure 200 Pa (1.5 Torr) argon, applied voltage ϕ_{rf} = 450 V, employing wall temperatures of 963 K, 1026 K and 1061 K, respectively.

At 13.56 MHz, (figures 4.1 (a) and (d)), close agreement is observed between simulation and experiment and a similarly high level of agreement is observed over a wider voltage range of 150 - 450 V (not shown), representing the full operational range of the experiment.

Here, peak A represents electron heating due to the collapsing sheath edge[35], while peak C represents secondary electron impact excitation[101] at the phase of most negative dielectric surface potential, $\tau = 0.75$.

Similar spatio-temporal heating mechanisms are observed for 27.12 MHz, shown in figures 4.1 (b) and (e). Secondary electron excitation (peak C) remains the dominant electron heating mechanism in both the measurement and simulation. Sheath expansion heating[140] (peak B) is observed in both simulation and experiment over the phase interval $0.4 \leq \tau \leq 0.7$. Although close agreement is observed between simulation and experiment at 27.12 MHz for peaks B and C, sheath collapse heating (peak A) is overestimated in the simulation. The degree of excitation during sheath collapse is proportional to the mean electron velocity out of the plasma bulk, where the total electron flux during the phase of sheath collapse must balance the positive ion loss during phases where the sheath extent is greater than zero[79]. For a given electron-neutral collision frequency, a reduction in the electron density will enforce an increase in the average electron velocity to maintain the same flux. Therefore, the overestimation in sheath collapse heating may indicate an underestimated plasma density in the simulation as compared to the experiment[160,198].

As the applied voltage frequency is increased to 40.68 MHz, the dominant electron heating mechanism shifts from secondary electron heating (peak C) to sheath expansion heating (peak B), shown in figures 4.1 (c) and (f). This transition occurs as sheath expansion heating is dependant upon the expanding sheath velocity, which increases with increasing applied voltage frequency. In contrast, a reduction in peak C indicates a reduction in the contribution from secondary electrons, either through a reducing population or average energy. Sheath collapse heating (peak A) remains overestimated through the same reasoning as for 27.12 MHz. Sheath expansion heating and heating via secondary electrons are less sensitive to changes in the plasma density as they are to variations in the sheath dynamics[35]. Therefore, as close agreement is observed between simulation and experiment with respect to sheath expansion and secondary electron heating, and their transition at 40.68 MHz, it may be inferred that the phase-resolved sheath dynamics are being modelled appropriately, with the caveat that an underestimation in the positive ion density will likely result in a slight systematic overestimation in sheath extent[99].

Simulations are employed to model the ionisation dynamics for higher applied voltage frequencies. Simulated phase-resolved Ar^+ ionisation rates ι_{tot} and phase-averaged secondary electron energy distribution functions (EEDFs) incident upon the alumina wall at region 2 (R,Z = 2.1 mm, 21 mm) for operation at 450 V employing applied voltage frequencies between 13.56 - 108.48 MHz in harmonics of 13.56 MHz, are shown in figures 4.2 (a) and (b), respectively.

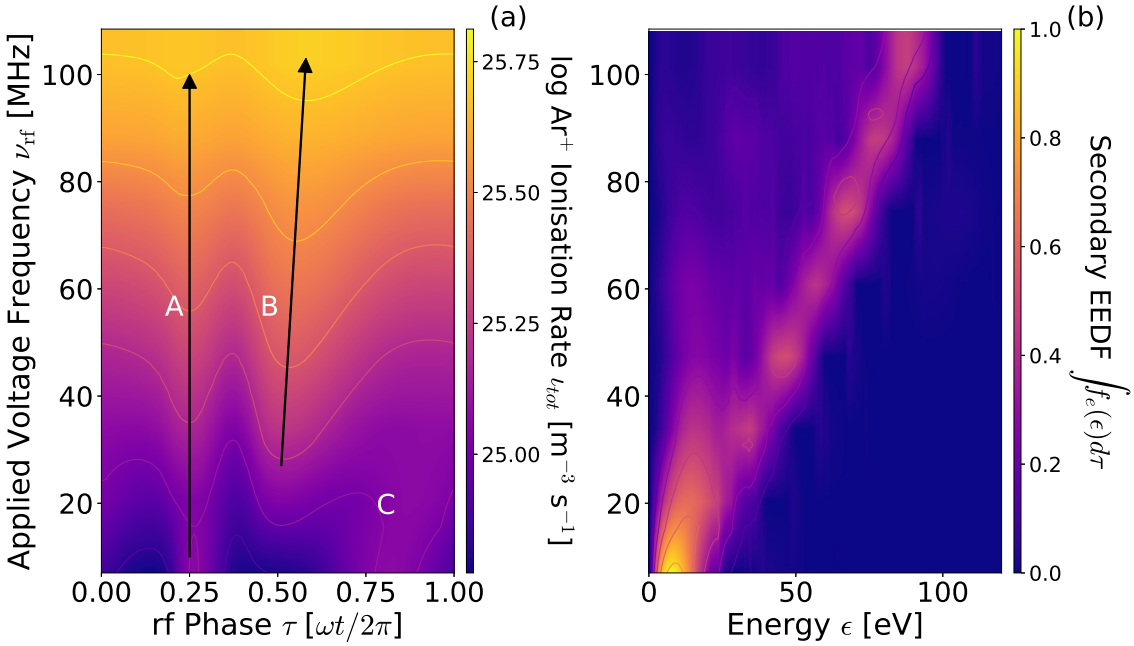

Figure 4.2: Simulated (a) Ar^+ ionisation rates and (b) phase-averaged secondary electron energy distribution functions (EEDFs) incident upon the alumina wall at region 2 (R,Z = 2.1 mm, 21 mm) for 450 V operation employing applied voltage frequencies between 13.56 - 108.36MHz. Ionisation rates are integrated through a 18 mm depth of field and a log axis is applied for clarity. Arrows in (a) denote the he phase of maximum ionisation for each heating mechanism. Plenum pressure 200 Pa (1.5 Torr) argon, applied voltage ϕ_{rf} = 450 V.

Ionisation due to sheath collapse heating (peak A) and secondary electron ionisation (peak C) is observed for operation at 13.56 MHz in figure 4.2 (a). Ionisation due to sheath expansion heating (peak B) is first observed for applied voltage frequencies of 27.12 MHz and becomes the dominant ionisation mechanism by 40.68 MHz. Sheath expansion heating increases in proportion to the sheath expansion velocity, due to the increased electron flux. Increasing the applied voltage frequency reduces the absolute time taken to complete one rf phase-cycle, resulting in an increased sheath velocity and subsequently an increase in the sheath expansion heating. Due to the increased sheath expansion heating and reduced secondary electron heating the discharge transitions out of γ-mode and into α-mode between 27.12 - 40.68 MHz. The discharge remains in α-mode for increasing applied voltage frequency, exhibiting an increased background ionisation likely due to the reduction in the absolute time between the sheath expansion and sheath collapse heating peaks. These trends indicate that the $\alpha - \gamma$ mode transition is frequency dependant, occurring at increased applied voltage amplitudes for increasing applied voltage frequencies.

As discussed previously, an $\alpha - \gamma$ mode transition occurs following an increased production of non-thermal secondary electrons, in this case arising from ion bombardment of the alumina walls. Increasing the applied voltage frequency leads to an increased Ar^+ ion density and radial flux (shown in figure 4.3), however the associated increase in secondary

electron production is not sufficient to maintain a γ-mode discharge beyond 27.12 MHz. This arises primarily due to the reduction in the absolute time taken to complete a single rf phase-cycle, reducing from 74 ns at 13.56 MHz to 9.25 ns at 108 MHz. At 13.56 MHz the electron transit time is negligible compared to the rf phase cycle, resulting in high energy electrons 'seeing' the same accelerating and retarding potential gradient. This results in electrons being reflected through the bulk multiple times, increasing their collision probability and resulting in efficient ionisation. However, as the applied voltage frequency is increased, electrons experience a difference between the accelerating and retarding sheath potentials due to the applied voltage varying on a similar timescale to the electron transit time.

Figure 4.2 (b) illustrates that for increasing applied voltage frequency, an increasing proportion of high energy secondary electrons are lost to the walls due to this difference in sheath potential. To illustrate this mechanism, consider an electron accelerated through the average sheath potential of $\phi_S = 340$ V for 108.48 MHz (see figure 4.4). If acceleration and deceleration are ignored, the transit time for a 340 eV electron across the 4.2 mm diameter source is 0.38 ns, representing 0.04 τ at 108 MHz. The applied voltage sweeps through 900 V_{pp} within 0.5 τ at 450 V amplitude, thus a phase offset of 0.04 τ represents a maximum change in the supplied voltage of $\pm$ 74 V. Therefore, electrons produced during phases of increasing applied potential ($\tau \geq 0.5$) are accelerated through a potential 74 V greater than the retarding potential 'seen' at the opposite wall. This value closely matches the 91 eV peak observed for 108 MHz operation in figure 4.2 (b), recalling that a transit time of 0.04 τ, and hence the 74 V difference, represent the minimum expected values. Electrons produced during phases of decreasing applied voltage ($\tau \leq 0.5$) experience a more negative retarding potential and are accelerated back into the bulk plasma. Therefore, increasing the applied voltage frequency results in the loss of increasingly energetic electrons for phases $\tau \geq 0.5$, resulting in a reduction of the the hollow cathode effect and subsequently reducing the proportion of ionisations resulting from secondary electrons, leading to a $\gamma - \alpha$-mode transition.

The reduction in the hollow cathode effect with increasing applied frequency results in a relatively modest increase in the Ar^+ density as ionisation primarily occurs through α-mode mechanisms. The spatial distribution in Ar^+ density for a 13.56 MHz, γ-mode discharge and a 108.48 MHz, α-mode discharge at 450 V are shown in figures 4.3 (a) and (b), respectively. The resulting variation in the radial Ar^+ flux at 450 V incident upstream, at the powered electrode and downstream (regions 1, 2 and 3, respectively) is shown with respect to applied voltage frequency in figure 4.3 (c).

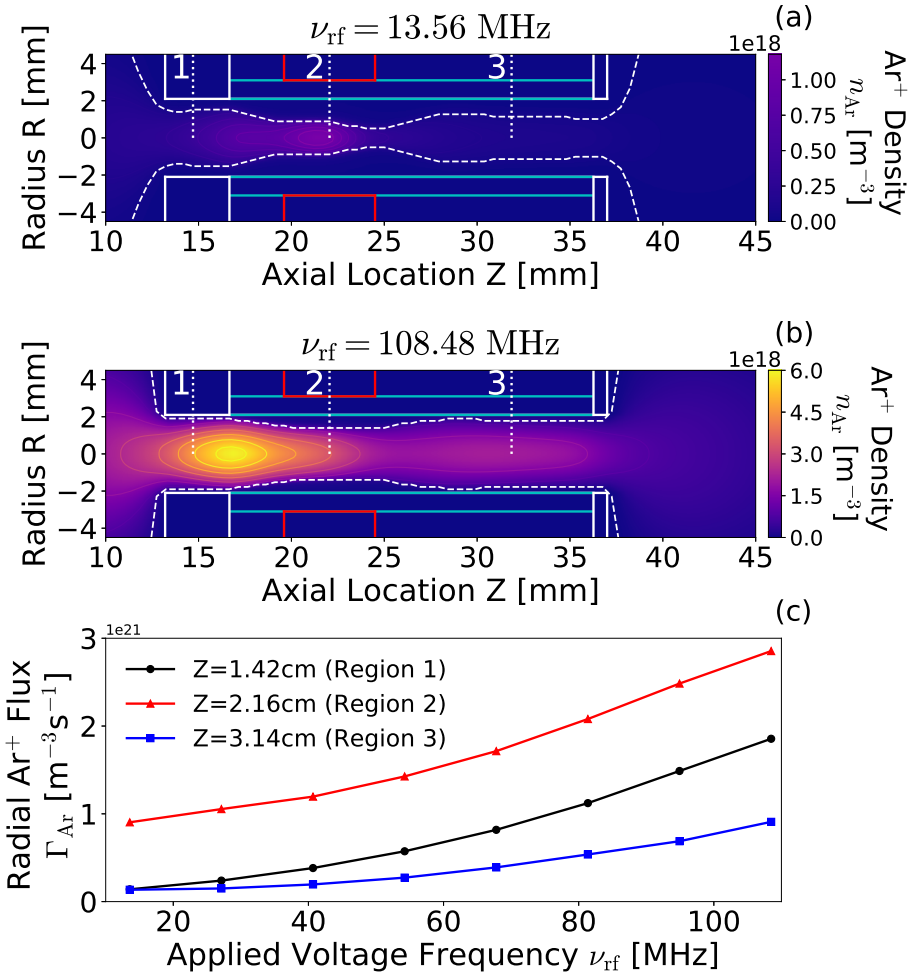

Figure 4.3: Spatially resolved Ar^+ density for (a) 13.56 MHz γ-mode operation and (b) 108.48 MHz α-mode operation at 450 V. The radial Ar^+ flux incident upon the radial wall upstream, at the powered electrode and downstream (regions 1, 2 and 3, respectively) is shown in panel (c). The phase-averaged sheath extents are denoted by the dashed lines in (a) and (b). Plenum pressure 200 Pa (1.5 Torr) argon, applied voltage ϕ_{rf} = 450 V.

The Ar^+ density for γ-mode operation at 13.56 MHz, shown in figure 4.3, reaches a maximum value of 1.18 $\times$ 10^{18} m^{-3} immediately upstream of the powered electrode (Z = 20 mm), as would be expected due to the high proportion of ionisations arising from secondary electron interactions. As the applied voltage frequency is increased from 13.56 MHz to 108.48 MHz, a γ-α mode transition occurs (see figure 4.2 (a)), where the Ar^+ density distribution for operation at 108.48 MHz is shown in figure 4.3 (b). Here, the Ar^+ density reaches a maximum of 5.9 $\times$ 10^{18} m^{-3} upstream of the powered electrode (Z = 17 mm), aligning with the intersection of the upstream grounded electrode and the alumina source tube. This shift arises in part due to the increased neutral gas heating (and hence reduced neutral density) adjacent to the powered electrode, (see figure 4.6 (b)), and in part due to the increased α-mode heating, through sheath expansion and collapse. Ionisation following sheath expansion heating

represents the primary ionisation mechanism at this frequency, and requires that electrons accelerated through sheath movement interact with neutral argon. While the sheath velocity is highest adjacent to the powered electrode, the reduced neutral argon density due to localised neutral gas heating results in a slower increase in the rate of electron-ion collisions at this location (region 2), as compared to upstream (region 1). This results in a faster increase in the Ar^+ ion density upstream as compared to at the powered electrode, resulting in the shift in peak density. This mechanism, in combination with the reduced hollow cathode effect described previously, result in the sub-linear increase in maximum density with respect to applied voltage frequency.

While the location of maximum Ar^+ density varies with applied voltage frequency, the peak radial Ar^+ flux, shown in figure 4.3 (c), remains adjacent to the powered electrode for applied voltage frequencies in the range 13.56 - 108.48 MHz. Here, the radial Ar^+ flux increases in proportion to the applied voltage frequency, increasing at approximately the same rate upstream (region 1) and at the powered electrode (region 2) and at a slower rate downstream (region 3). As previously shown, the Ar^+ density increases at a faster rate upstream, therefore to maintain the same increase in radial flux, Ar^+ ions at the powered electrode must posses a higher radial velocity. This additional velocity arises due to the dc self-bias voltage, localised adjacent to the powered electrode, resulting in a greater phase-averaged sheath potential. The degree to which an altered sheath potential affects the accelerating electric field 'seen' by the ions, and hence the ion power deposition, depends upon the sheath extent.

4.1.2 Phase-Resolved Sheath Dynamics

The phase-resolved sheath extent from the alumina wall adjacent to the powered electrode at region 2 (R,Z = 2.1 mm, 21 mm) is shown for 13.56 MHz and 108.48 MHz operation in figure 4.4 (a). The associated phase-resolved sheath potentials are shown in figure 4.4 (b), calculated as the difference between the on-axis plasma potential and the dc self-bias voltage, where: $\phi_{\mathrm{S}}(\tau) = \phi_{\mathrm{fp}}(\tau) - \phi_{\mathrm{dc}}(\tau)$. Sheath extents are calculated employing the Brinkmann criterion, discussed in detail in section 1.5.1 and smoothing is applied via a Savitzky–Golay filter.

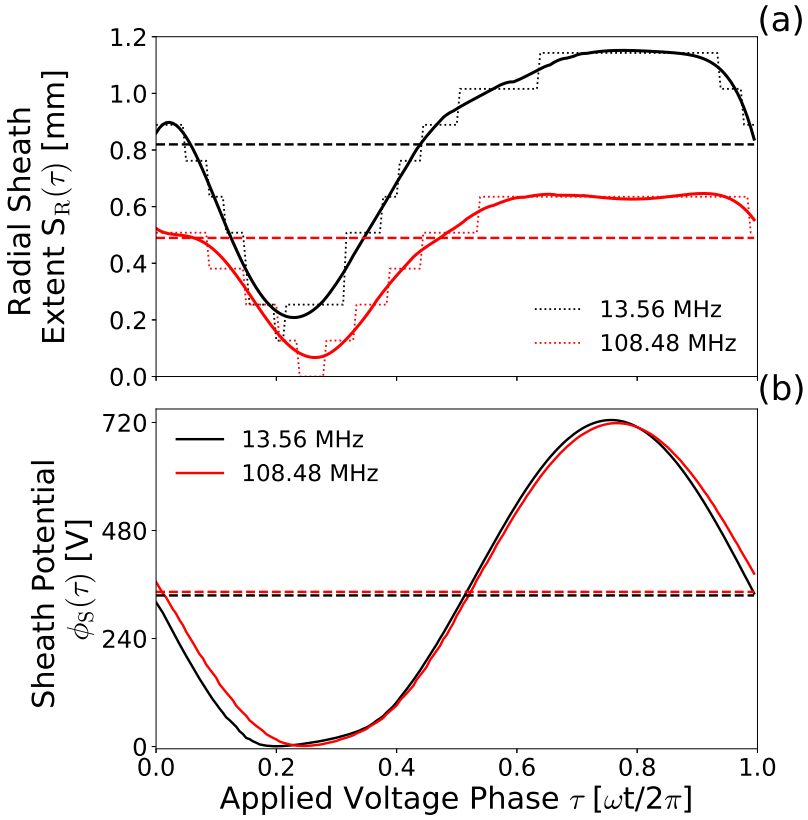

Figure 4.4: Phase-resolved (a) sheath extension and (b) sheath potential adjacent to the powered electrode (R,Z = 2.1 mm,21 mm) for 13.56 MHz and 108.36 MHz applied voltage frequencies at 450 V. Sheath edges are denoted by the solid and dotted lines, where the solid lines are smoothed employing a Savitzky–Golay filter. The phase-averaged sheath extents are denoted by the dashed lines. Plenum pressure 200 Pa (1.5 Torr) argon, applied voltage $\phi_{\mathrm{rf}} = 450$ V.

For both 13.56 MHz and 108.48 MHz operation in figure 4.4 (a), the sheath extents vary approximately sinusoidally in proportion to the sheath potentials shown in figure 4.4 (b), and in inverse proportion to the applied rf voltage waveform (not shown). The phase-averaged sheath extent, denoted by the dashed lines in figure 4.4 (a), reduces from 0.82 mm at 13.56 MHz to 0.49 mm at 108.46 MHz. In contrast, the phase-averaged sheath potentials, denoted by the dashed lines in figure 4.4 (b), remain approximately constant over the range

13.56 - 108.48 MHz. This leads to an increase in the electric field strength across the powered electrode sheath with increasing applied voltage frequency, as required by the variation in radial Ar^+ flux observed previously. Aside from the reduction in the phase-averaged sheath extent, the 108.48 MHz sheath is fully extended for a larger portion of the phase cycle, observed as a reduced separation between the mean and maximum sheath extents. This results in a smaller fraction remaining for sheath expansion and collapse, leading to higher sheath velocities. Further, the 108.48 MHz sheath collapses approximately 0.05 τ later than the 13.56 MHz sheath. The combination of these effects results in an enhanced, temporally offset, phase of sheath expansion heating with increasing applied voltage frequency, as observed previously in figure 4.4 (a).

Aside from the temporal offset and altered sheath collapse timescale, the behaviour of the sheath potentials $\phi_S(\tau)$ in figure 4.4 (b) remain approximately invariant over the range 13.56 -108.48 MHz. Any variation in the plasma potential is mirrored by the dc self-bias, maintaining the same phase-averaged sheath potential. Note that these variations are small relative to the applied voltage, where the dc self-bias reduces by only 15 V from -282 V at 13.56 MHz to -297 V at 108.48 MHz and the on-axis plasma potential increases by the same magnitude. This invariance in the phase-averaged sheath potential indicates that the reduction in the sheath extension with respect to increasing frequency likely arises from the increased Ar^+ density, shown previously. Therefore, any variation in the phase-averaged sheath dynamics, and the associated radial Ar^+ ion acceleration, with increasing applied voltage frequency are significantly influenced through the dominant ionisation mechanisms. Spatial and temporal control of the dominant ionisation mechanisms potentially provides the capability to alter the degree to which ions are accelerated within the sheath, and hence control the neutral gas heating.

4.1.3 Power Deposition and Neutral Gas Heating

Power is deposited into the plasma through the acceleration of charged particles and the subsequent collisional transfer into neutral species. In general, the ionisation rate typically scales with the power deposited into electrons P_e, while the neutral gas temperature scales with ion power deposition P_i. The radially resolved, axially integrated, electron and ion power deposition for varying applied voltage frequencies between 13.56 MHz to 108.48 MHz at 450 V are shown in figure 4.5 (a) and (b), respectively. The total power deposition P_{rf} and ion power deposition fraction $(P_{rf} - P_e)$ are shown in figure 4.5 (c).

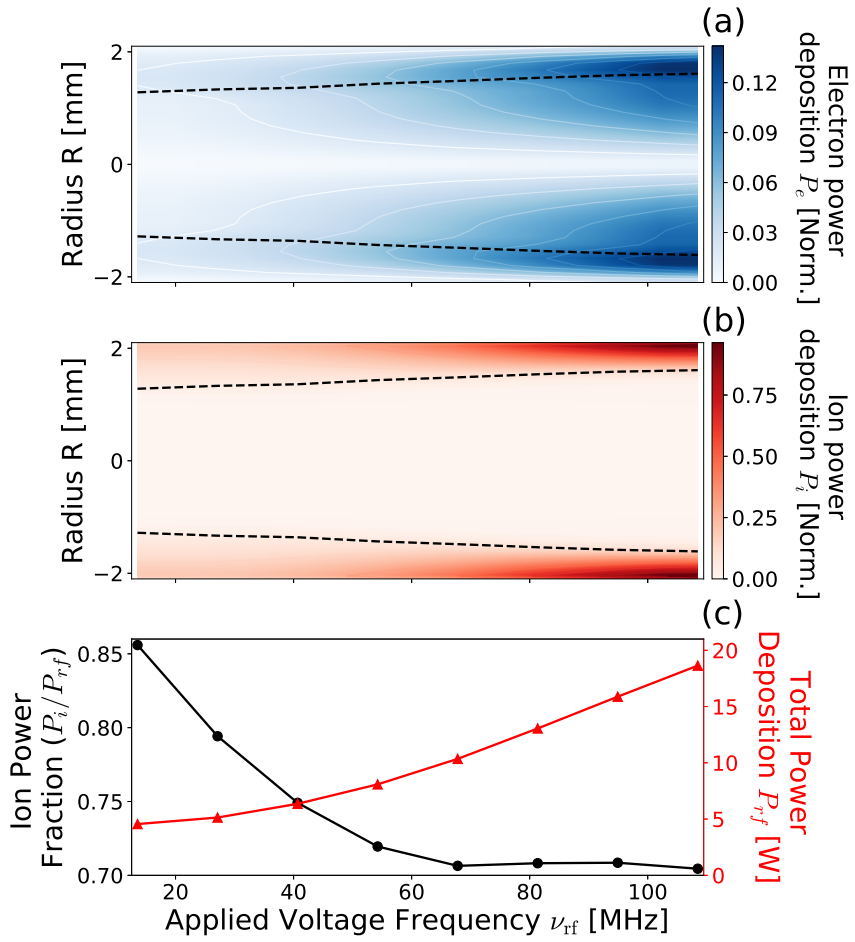

Figure 4.5: Axially integrated, radially resolved (a) electron and (b) ion power deposition fractions, normalised to the total deposited power at 108.48 MHz and (c) spatially integrated total power deposition and ion power fraction for applied voltage frequencies between 13.56 - 108.36 MHz at 450 V. The phase-averaged sheath extent S_R adjacent to the powered electrode (Z =21 mm) is denoted by dashed lines in (a) and (b). Plenum pressure 200 Pa (1.5 Torr) argon, applied voltage ϕ_{rf} = 450 V.

The radially resolved electron power deposition in figure 4.5 (a) reaches a maximum at the phase-averaged sheath extent, denoted by the dashed lines. In addition, the fraction of

the total rf power deposited into electrons, and radial extent to which rf power is deposited, increases with increasing applied voltage frequency. Electrons accelerated during sheath expansion account for the deposited power at radii below the mean sheath extent $R \leq S_R$, as these mechanisms accelerate ions towards the plasma bulk. Conversely electron power deposition at radii above the mean sheath extent $R \geq S_R$ arises from sheath collapse, as electrons are accelerated towards the wall. Secondary electrons are accelerated through the full sheath potential and therefore represent power deposition from the wall through to the pre-sheath. Extrapolating from these mechanisms, it is likely that the increasing electron power deposition for $R \leq S_R$ arises primarily due to the enhanced sheath expansion heating, with a contribution from the acceleration of secondary electrons.

Ion power deposition, shown in figure 4.5 (b), is predominately localised within the sheath $R \geq S_R$, as would be expected. However, as the sheath extent reduces with increasing applied voltage frequency, so too does the volume of plasma within which ions experience acceleration. The rate of energy transfer from ions into the neutral gas relies upon both the average ion energy and the ion-neutral collision rate. There is therefore a trade-off between the maximum radial electric field strength, which varies in proportion to ν_{rf}, and the volume of gas within which ions are accelerated by this field, which varies inversely with ν_{rf}. Finally, as neutral gas heating is performed through ion-neutral collisions, it follows that the maximum power deliverable to the neutral gas is limited by the ion power fraction.

The total rf power deposited and fraction of which is deposited into ions are shown in figure 4.5 (c) with respect to applied voltage frequency. Here, the rf power coupled into the plasma increases by 15 W over the range 13.56 - 108.48 MHz, resulting in the increased ion and electron power deposition observed in figure 4.5 (a) and (b). However, while the absolute deposited power increases, the fraction of that power deposited into ions reduces by 15% over the same range. This lost power is coupled into electrons through the aforementioned heating mechanisms, resulting in the increased ionisation rate and Ar^+ density. The ion power fraction continues to reduce until approximately 67.80 MHz, beyond which any additional coupled power is deposited into electrons and ions equally, maintaining the ion power fraction at $\approx$ 70%. The stabilisation of the ion power fraction for applied voltage frequencies of 67.80 MHz and above arises due to the formation of high energy, non-thermal, ion populations at these frequencies. These ion populations, and the mechanism by which they are formed, are discussed in more detail in section 4.2.

Power deposited into Ar^+ ions is transferred into the neutral gas primarily through ion-neutral charge exchange collisions, the rate of which is mediated by the Ar^+ density n_{Ar^+} and the energy resolved Ar^+-Ar collision cross-section $\sigma_{Ar^+}(\epsilon)$. The distribution in neutral gas temperature for operation at 13.56 MHZ and 108.48 MHz at 450 V are shown in figures 4.6 (a) and (b). The associated ranges in the Ar^+-Ar collision cross-section across the powered electrode sheath is shown in figure 4.6 (c).

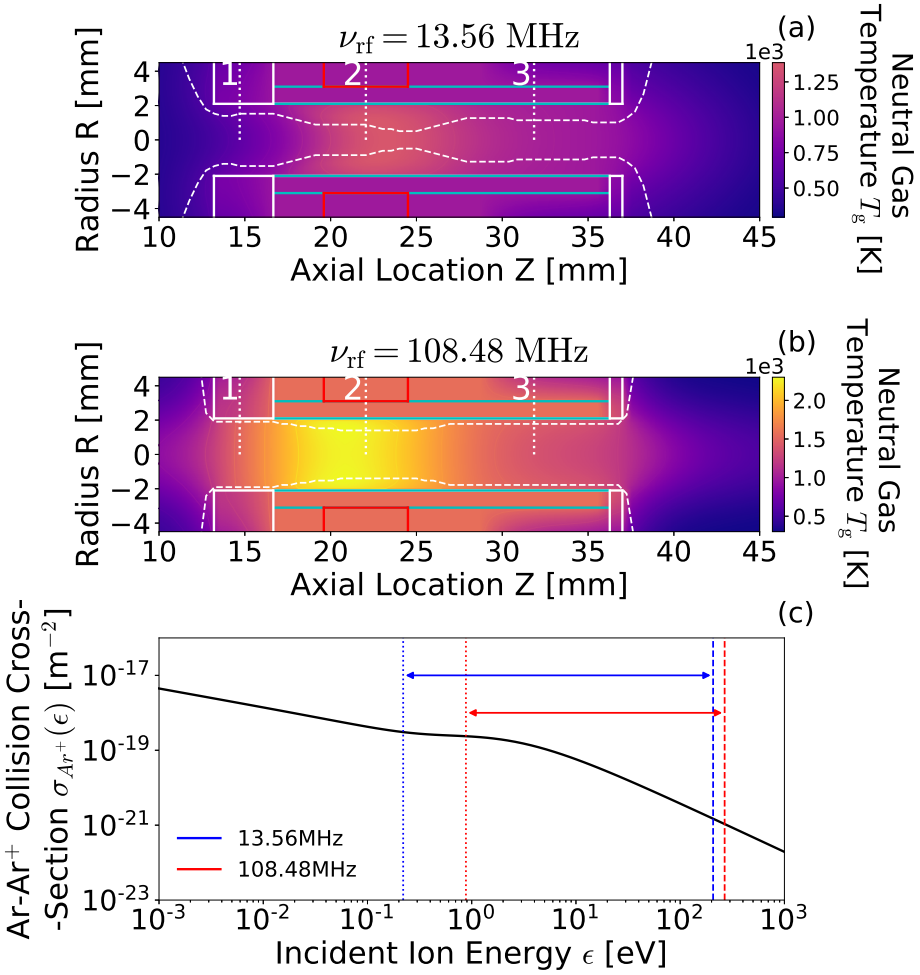

Figure 4.6: Spatially resolved neutral gas temperatures for operation at (a) 13.56 MHz and (b) 108.48 MHz, and energy resolved (c) Ar^+-Ar collision cross-sections $\sigma_{Ar^+}(\epsilon)$ across the powered electrode sheath. The dotted and dashed lines in (c) correspond to Ar^+-Ar cross-sections for the mean ion energy at the sheath edge and at the alumina wall adjacent to the powered electrode (R,Z = 2.1 mm,21 mm), respectively. Plenum pressure 200 Pa (1.5 Torr) argon, applied voltage ϕ_{rf} = 450 V, wall temperatures of 963 K and 1569 K.

Neutral gas heating in figures 4.6 (a) and (b) is localised adjacent to the powered electrode, typically between $18 \leq Z \leq 25$ mm, aligning with the location of most negative dc self-bias, shown previously in figure 3.7 (b). The maximum on-axis neutral gas temperature increases in proportion to the applied voltage frequency, varying from 1386 K at 13.56 MHz

to 2300 K at 108.48 MHz for 450 V. This increase primarily arises from the increased total deposited power, from 4.5 W - 18.6 W, resulting in an increased ion density and radial ion velocity, shown previously in figure 4.3. While increased applied voltage frequencies correspond with significantly enhanced maximum neutral gas temperatures, this is achieved at the expense of a reduction in the heating efficiency. The heating efficiency, i.e. the change in neutral gas temperature from 325 K per unit of deposited power, reduces with increasing applied voltage frequency, from 212.2 KW^{-1} at 13.56 MHz to 98.8 KW^{-1} at 108.48 MHz. This represents a 53% reduction in heating efficiency, despite only a 15% reduction in the fraction of power deposited into ions. This disparity arises from a reduction in the ion-neutral collision cross-section arising from increased ion energies, and hence resulting in a reduced ion to neutral power transfer rate.

The energy resolved Ar-Ar^+ collision cross-section $\sigma_{Ar^+}(\epsilon)$, is shown in figure 4.6 (c), as obtained from Ref. 199. Here, Ar - Ar^+ cross-sections corresponding to the mean ion energy at the sheath edge and at the alumina wall are denoted by the dotted and dashed lines respectively, for 450 V operation at 13.56 MHz and 108.48 MHz. At 13.56 MHz applied voltage frequency, the cross section remains approximately constant at 3×10^{-19} m^{-2} for as ions are initially accelerated, reducing to a minimum of 3×10^{-22} m^{-2} by the alumina wall. In contrast, the reduced sheath extent and higher electric field at 108.48 MHz result in greater ion acceleration and an associated immediate reduction in the collision cross-section, reducing to 2×10^{-22} m^{-2} by the alumina wall. In general, increasing the applied voltage frequency results in a narrower, less collisional sheath, resulting in a reduced ion to neutral power transfer efficiency. This is compensated for however, by the increased absolute power deposition and higher velocity ions, resulting in a higher absolute neutral gas temperature.

From figures 4.3, 4.5 and 4.6, ideal operation of the *Pocket Rocket* therefore relies on maximising the phase-averaged sheath extent and ion power deposition fraction to achieve a high radial ion velocity, while also maintaining a highly collisional sheath enabling efficient ion - neutral power transfer. To achieve this, multi-harmonic dual-frequency tailored voltage waveforms are employed in chapter 5, providing enhanced control over the sheath dynamics and associated ion heating mechanisms. The remainder of this chapter will focus on additional effects arising from the reduced Ar - Ar^+ collision rate and the formation of structured ion energy distribution functions.

4.2 Structured Ion Energy Distribution Functions

This section introduces and discusses the formation of structured IEDFs within the *Pocket Rocket*. Structured IEDFs differ from unstructured distributions as they exhibit additional characteristic energy peaks, typically associated with radio-frequency modulation of the sheath potential[200]. Previous work investigating structured IEDFs in rf plasmas has focused primarily on low to intermediate pressure discharges (0.65 - 67 Pa, 5 - 500 mTorr) at applied voltage frequencies of 13.56 MHz[106,200–202] and 27.12 MHz[112]. More recent work has demonstrated control of the IEDF in low-pressure (0.65 - 1.3 Pa, 5 - 10mTorr) plasmas through application of higher applied voltage frequencies in the range 12 MHz - 100 MHz[110,203,204]. For applications involving higher-pressure discharges (above 200 Pa, 1.5 Torr) relevent to this work, the increased ion-neutral collision frequency typically results in a collisionally dominated IEDF at the wall, the shape of which is largely independent of the voltage amplitude, limiting the range of accessable ion energies[110]. However, as shown previously in chapter 3, heating and rarefaction of the neutral gas plays a substantial role in determining the heavy particle collision rates, sheath extents and mean-free-paths[33,65]. Therefore, by self consistently solving for the change in gas density mediating the number of ion-neutral collisions, it is possible to model structured IEDF formation in intermediate pressure discharges.

4.2.1 Formation and Control of Structured Ion Energy Distributions

The formation of structured ion energy distribution functions necessitates the presence of discrete, non-thermal, ion populations and therefore inherently requires a kinetic approach. Here, Ar^+ macro-particles are treated kinetically within the PCMCM, where figure 4.7 shows the evolution of the Ar^+ IEDFs incident on the alumina wall adjacent to the powered electrode (R, Z = 2.1 mm, 21 mm) with respect to applied voltage for 13.56 - 108.48 MHz over the voltage range 150 - 450 V.

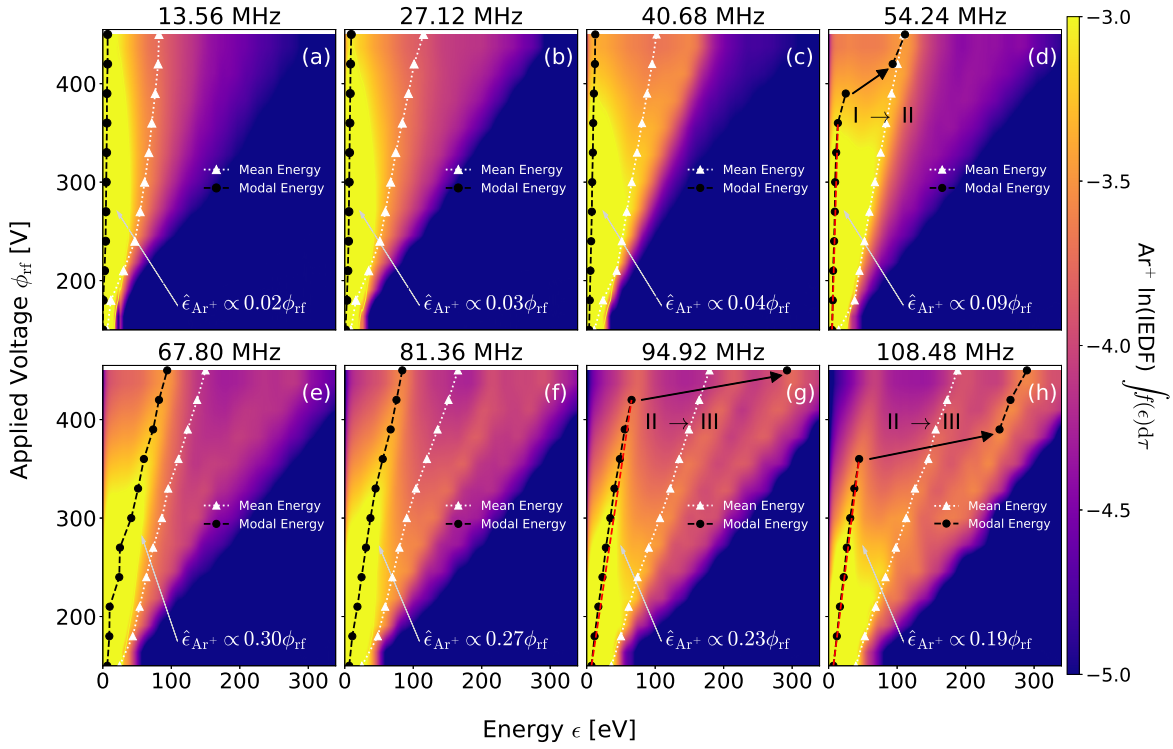

Figure 4.7: Ar^+ ion energy distribution functions incident on the alumina wall adjacent to the powered electrode (R, Z = 2.1 mm, 21 mm, see figure 2.7) for applied voltage amplitudes of 150 - 450 V and applied voltage frequencies of 13.56 - 108.48 MHz, (a-h). The mean and modal $\hat{\epsilon}_{Ar^+}$ ion energies are indicated by dotted and dashed lines, respectively, where discontinuous transitions in the modal Ar^+ energy are denoted by the black arrows in panels (d), (g) and (h). The modal energy proportionalities to the applied voltage are obtained from linear fits over the full voltage range, with the exception of 54.24 MHz, 94.92 MHz and 108.48 MHz, which are performed over the voltage ranges 150 - 360 V, 150 - 420 V and 150 - 360 V, respectively, as denoted by the red dashed lines in the associated panels. The colourbar scale has been reduced, omitting IEDF fractions above 10^{-3} and below 10^{-5} for clarity. Plenum pressure 200 Pa (1.5 Torr) in argon, ϕ_{rf} = 150 - 450 V, wall temperature 325 K.

In figure 4.7, the mean and modal $\hat{\epsilon}_{Ar^+}$ ion energies are denoted by the black and white lines, respectively. Here, the modal ion energy represents the most populous structure within the distribution, while the mean more generally characterises the entire distribution. The 13.56 MHz IEDFs in figure 4.7 (a) exhibit profiles where the majority of Ar^+ ions are maintained at low energies (0.6 eV $\leq$ $\hat{\epsilon}_{Ar^+}$ $\leq$ 6 eV), supplemented by a high energy (50 - 200 eV) tail containing relatively few ions. This structure is expected for the relatively high pressure (200 Pa, 1.5 Torr) discharge conditions, where the ion-neutral collision frequency is high[8,108,110]. As a result, the mean and modal ion energies exhibit little change with varying applied voltage amplitude. Note however, that an increase in the fraction of ions within the high energy tail is observed with increasing applied voltage amplitude.

Increasing the applied voltage frequency to 27.12 MHz, figure 4.7 (b), results in much the same behaviour as observed for the 13.56 MHz case. The first notable change in the shape of the IEDFs occurs between 40.68 MHz and 54.24 MHz, figures 4.7 (c) and (d), respectively, where the IEDFs exhibit an additional mid-energy ($\approx$ 60 - 180 eV) structure in addition to the low energy ($\leq$ 60 eV) structure observed previously. The modal ion energy transitions into this structure for applied voltage amplitudes above 390 V at 54.24 MHz, denoted by "I $\rightarrow$ II" in figure 4.7 (d), representing a distinct transition in the distribution of energies within the IEDF.

For applied voltage frequencies of 67.80 MHz and 81.36 MHz, figures 4.7 (e) and (f), the mid-energy structure represents the modal ion energy for almost the entire voltage range. Also, note that the modal ion energy exhibits an increased sensitivity to the applied voltage amplitude as a result. In addition, an increase in the fraction of ions within the high energy tail of the distribution ($\gtrsim$ 180 eV) is observed. The high energy tail begins to stratify into two further structures, positioned either side of the mean energy of the distribution, for applied voltage frequencies of 94.92 MHz and 108.48 MHz in figures 4.7 (g) and (h). Here, a structure refers to a sub-component of the IEDF that can be best approximated via a Gaussian or Lorentzian distribution as opposed to a Maxwell-Boltzmann distribution. The fraction of ions within these structures increases in proportion to the applied voltage amplitude, until the modal ion energy exhibits a transition into the highest energy structure at 450 V for 94.92 MHz ("II $\rightarrow$ III" in figure 4.7 (g)). This transition occurs at a lower voltage of 390 V for 108.48 MHz.

The trends observed in figures 4.7 (a - h) indicate the formation of mid-energy ($\approx$ 60 - 180 eV) and high energy ($\gtrsim$ 180 eV) structures (II and III, respectively) in the IEDFs, the formation and evolution of which vary with both the applied voltage frequency and amplitude. To further characterise these structures, the IEDFs incident on the alumina wall adjacent to the powered electrode (R, Z = 2.1 mm, 21 mm), for varying applied voltage frequencies between 13.56 - 108.48 MHz at an applied voltage amplitude of 450 V, are shown in figure 4.8.

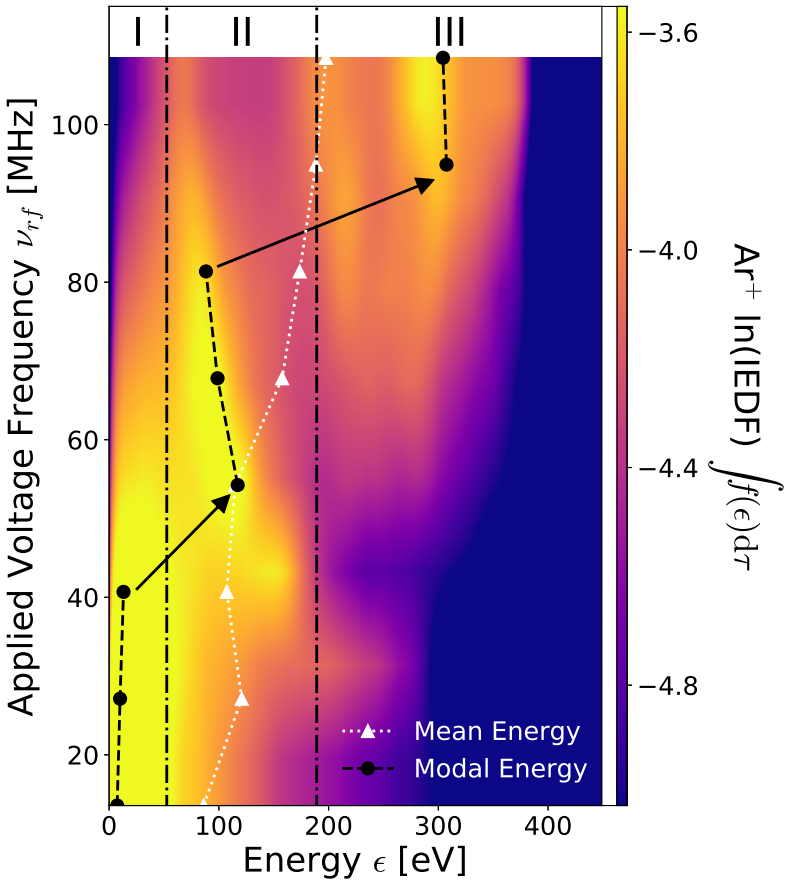

Figure 4.8: Ar^+ ion energy distribution functions incident on the alumina wall adjacent to the powered electrode (R, Z = 2.1 mm, 21 mm, see figure 2.7) for applied voltage frequencies between 13.56 - 108.48 MHz and an applied voltage amplitude of 450 V. The modal $\hat{\epsilon}_{Ar^+}$ and mean Ar^+ ion energies are denoted by the black and white dashed lines, respectively. The IEDFs can be broadly described by structures in three energy regions, seperated by the dash-dotted lines, which correspond to: I (0 - 60 eV), II (60 - 180 eV) and III ($\geq$ 180 eV). For clarity, the colourbar dynamic scale has been reduced, omitting IEDF fractions below 10^{-5}. Plenum pressure 200 Pa (1.5 Torr) in argon, 450 V applied voltage amplitude, wall temperature 325 K.

The structures within the IEDFs presented in figure 4.8 can be categorised into three energy ranges: Region I (0 - 60 eV) contains the largest fraction of ions for applied voltage frequencies between 13.56 - 40.68 MHz. This region consists primarily of low energy ions where the modal ion energy $\hat{\epsilon}_{Ar^+}$ is far below the phase-averaged sheath potential (≈ -350 V), indicating a regime in which this is determined primarily through the high ion-neutral collision frequency. Region II (60 - 180 eV) contains the largest fraction of the IEDF for applied voltage frequencies between 54.24 - 81.36 MHz, this structure becoming visible above 40.68 MHz. This region consists of a single mid-energy structure, the magnitude of which increases until approximately 67.80 MHz, and decreases thereafter. The modal energy in this region is inversely proportional to the applied voltage frequency, levelling off at $\approx$ 80 eV for frequencies above 94.92 MHz.

For applied voltage frequencies of 67.80 - 108.48 MHz two additional high energy peaks begin to form in region III, above 180 eV. The formation of these structures is observed for applied voltage frequencies above 67.80 MHz as a single broadband (80 eV energy range) structure, the centre of which approximately corresponds to 240 eV. The magnitude and energy range of this structure increases with increasing applied voltage frequency. At and above 94.92 MHz, this structure stratifies into two distinct components, with the higher energy of the two components representing the modal Ar^+ ion energy. The formation of these discrete high-energy peaks represents an increasing fraction of ions exhibiting reduced collisional losses within the sheath volume.

The modal Ar^+ ion energy exhibits sharp transitions between regions I - II (40.68 - 54.24 MHz) and II - III (81.36 - 94.92 MHz), observed previously in figures 4.7 (d), (g) and (h). A variation of 280 eV in the modal ion energy $\hat{\epsilon}_{Ar^+}$ is achieved over the applied voltage frequency range 13.56 -108.48 MHz. In comparison, the mean ion energy increases in proportion with the applied voltage frequency, varying by 106 eV over the same frequency range. The mean energy exhibits an increased proportionality to the applied voltage amplitude at applied voltage frequencies between 54.24 - 108.36 MHz, correlating with the formation of the structured IEDFs. At 94.92 MHz and upwards the modal ion energy exceeds the mean ion energy as it transitions into region III, which increasingly represents the defining region of the IEDF.

4.2.2 Mechanism for the Formation Of Structured IEDFs

The formation of the structures observed previously in figures 4.8 and 4.9 (g) and (h), suggests a reduction in the ion-neutral collision frequency within the sheath. To investigate this, IEDFs incident upon the alumina wall (R, Z = 2.1 mm, 21 mm) for 13.56 MHz and 108.48 MHz applied-voltage frequencies and 150 V, 300 V and 450 V applied voltages are shown in figures 4.9 (a) and (b). The sheath averaged neutral argon density n_{Ar} and argon ion density $n_{\mathrm{Ar^+}}$ are shown with respect to applied voltage frequency in figure 4.9 (c) and the associated $\mathrm{Ar^+}$ mean-free-path λ_{mfp} and phase-averaged sheath extent S_R are shown in figure 4.9 (d). The $\mathrm{Ar^+}$ mean-free-path was calculated by employing an Ar - $\mathrm{Ar^+}$ cross-section corresponding to the mean $\mathrm{Ar^+}$ ion velocity at the sheath edge, where the energy resolved cross-section was obtained from Ref. 199.

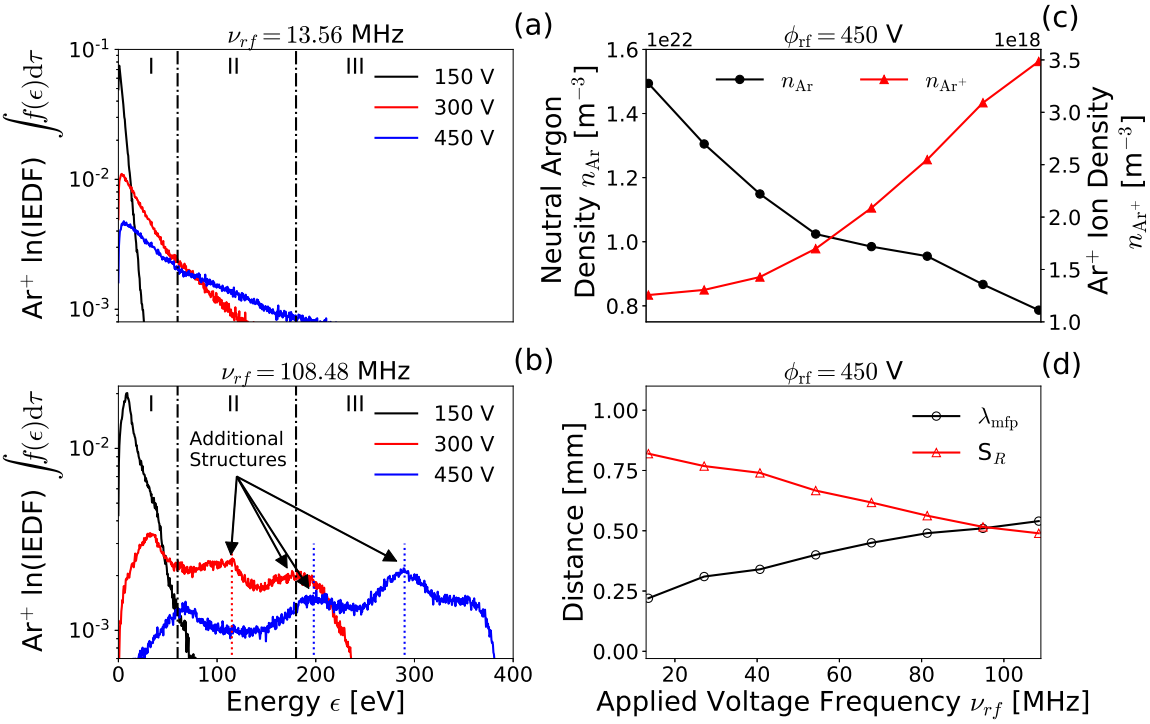

Figure 4.9: $\mathrm{Ar^+}$ ion energy distribution functions incident on the alumina wall adjacent to the powered electrode (R, Z = 2.1 mm, 21 mm, see figure 2.7) for applied voltage frequencies of (a) 13.56 MHz and (b) 108.48 MHz and increasing voltage amplitude. Panels (c) and (d) show the effects of varying the applied voltage frequency for a 450 V discharge on the (c) sheath averaged neutral argon n_{Ar} and argon ion $n_{\mathrm{Ar^+}}$ densities, and (d) $\mathrm{Ar^+}$ mean-free-path λ_{mfp} and phase-averaged sheath extent S_R. Energy regions I, II, and III are seperated by dash-dotted lines, while IEDF structures are denoted by dotted lines in (a) and (b). Plenum pressure 200 Pa (1.5 Torr) argon, ϕ_{rf} = 150 - 450 V, wall temperature 325 K.

The shape of the IEDFs at 13.56 MHz in figure 4.9 (a) are approximately independent of the applied voltage. The variation in the modal $\mathrm{Ar^+}$ ion energy at this frequency is predominately controlled by the neutral argon density (figure 4.9 (c)), which alters the ion-

neutral collision rate. Increasing the applied voltage results in an increased maximum ion energy, while the modal energy, denoted by the dashed lines, is not significantly affected ($1.9\ \text{eV} \leq \hat{\epsilon}_{Ar^+} \leq 7.7\ \text{eV}$). Increasing the applied voltage primarily results in a broadening of the distribution function, resulting in a longer high-energy tail.

In contrast to 13.56 MHz, the shapes of the IEDFs at 108.48 MHz, shown in figure 4.9 (b), exhibit a strong dependence on the applied voltage. At 150 V the IEDF is similar to 13.56 MHz, where the relatively low modal Ar^+ ion energy ($\hat{\epsilon}_{Ar^+} = 9$ eV) is dictated primarily by the high ion-neutral collision frequency and the majority of the distribution is within region I. Increasing the voltage from 150 V to 300 V results in a relatively flat distribution, now predominately within region II, exhibiting an increased modal Ar^+ ion energy of $\hat{\epsilon}_{Ar^+} = 34$ eV and evidence of two additional higher energy structures between 60 - 180 eV. The central and most well defined structure at 108 eV is highlighted in figure 4.9 (b) by the red dotted line. At an applied voltage of 450 V the IEDF consists of three distinct structures, a relatively low-energy peak in region II at 88 eV and two additional higher energy structures in region III at 190 eV and 291 eV, denoted by the blue dotted lines. The modal Ar^+ ion energy has transitioned from the low-energy region I structure into the highest energy of the two region III structure and the distribution is now weighted towards the high energy ions as shown previously in figure 4.8. In this regime, the location in energy of the IEDF structures are significantly influenced by the sheath potential via the dc self-bias voltage, while the ion-neutral collision frequency within the sheath primarily determines their broadening. Note that the dc self-bias voltage ϕ_{dc} remains approximately constant over the range of applied voltage frequencies employed, varying between $-303\ \text{V} \leq \phi_{dc} \leq 282\ \text{V}$ at 450 V applied voltage amplitude.

The sheath averaged neutral argon and plasma densities are shown with respect to applied voltage frequency in figure 4.9 (c) for an applied voltage of 450 V. Increasing the applied voltage frequency for a fixed applied voltage increases the plasma density and reduces the neutral argon density. The neutral density decreases by approximately 50% from 13.56 MHz to 108.48 MHz. This rarefaction arises from increased neutral gas heating as the deposited power increases with applied voltage frequency. A reduction in the neutral argon density reduces the Ar - Ar^+ collision frequency within the sheath, resulting in an increase in the Ar^+ mean-free-path, shown in figure 4.9 (d). While this increase in the mean-free-path can account for broadening of the IEDFs in figure 4.9 (a), it cannot independently account for the narrow and distinct structures observed in figure 4.9 (b). To describe the formation of these structures, the properties of the sheath adjacent to the powered electrode, through which ions are accelerated, is considered.

The variation in the phase-averaged sheath extension S_R with respect to applied voltage frequency is shown in figure 4.9 (d). As noted previously, increasing the applied voltage frequency leads to an increased Ar^+ density adjacent to the powered electrode, giving rise to

a reduced sheath width and an increase in the sheath capacitance[99]. The negative dc self-bias voltage at the radial wall enforces an relatively phase-independent radial Ar^+ ion flux[89,99,111]. A reducing sheath extension, coupled with an increasing Ar^+ mean-free-path results in a reduced chance for ion-neutral collisions within the sheath volume as the applied voltage frequency increases. Therefore, ion populations that are less influenced by collisions (region II) and effectively collisionless ion populations (region III) may be induced at relatively high (above 94.92 MHz at 1.5 Torr) applied voltage frequencies, enabling a greater degree of control of the range of energies within the IEDF.

As ions do not respond directly to the applied rf voltage, their velocity and acceleration through the sheath can be treated as continuous over multiple rf phase cycles. However, the proportion of ions undergoing a collision within any given rf phase-cycle will still vary in proportion to the phase-averaged Ar^+ mean-free-path. Therefore, an estimate of the relative ion population within the collisionless structures (region III) may be obtained through comparing the phase-resolved sheath extent to the phase-averaged Ar^+ mean-free-path. The fraction of the rf phase cycle for which the sheath width S_R is lower than the ion-neutral mean-free-path λ_{mfp} is plotted with respect to applied voltage for applied voltage frequencies of 13.56 - 108.48 MHz in figure 4.10.

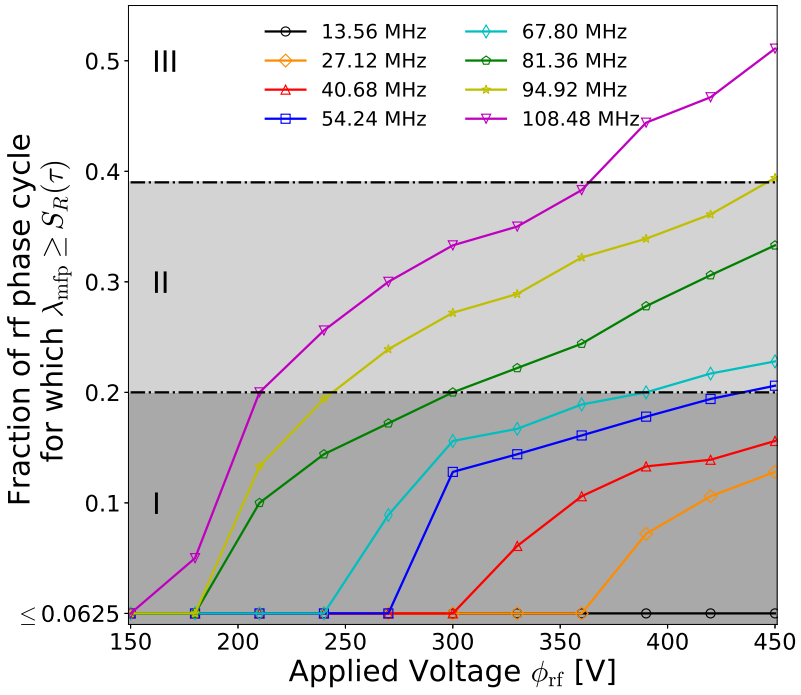

Figure 4.10: Fraction of the rf phase cycle for which the Ar^+ ion-neutral mean-free-path λ_{mfp} is greater than the sheath extension S_R with respect to applied voltage frequency between 13.56 - 108.48 MHz. Fractions corresponding to the approximate locations of regions I, II and III (see figure 4.8) are indicated by the dark grey ($\hat{\epsilon}_{Ar^+} < 60$ eV), light grey ($60 \leq \hat{\epsilon}_{Ar^+} \leq 180$ eV) and white ($\hat{\epsilon}_{Ar^+} > 180$ eV) regions, respectively. Plenum pressure 200 Pa (1.5 Torr) argon, wall temperature 325 K.

As shown in figure 4.10, the fraction of the rf phase cycle for which $\lambda_{\text{mfp}} \geq S_R$ increases in proportion to the applied voltage frequency at 450 V. As the fraction of the rf-cycle for which the phase-resolved sheath extension is below the Ar^+ mean-free-path increases, the probability for any ion already in transit through the sheath to undergo a collision decreases. Therefore, the phase-resolved proportion of the rf phase-cycle for which the sheath extent S_R is lower than the Ar - Ar^+ mean-free-path λ_{mfp} is necessarily reflective of the phase-averaged proportion of ions travelling through the sheath without undergoing a collision.

The ratio of the collisionless population relative to the collisional population increases with the applied voltage frequency, coinciding with the growth of the high energy (region III) structures observed in figures 4.8 and 4.9 (b). In addition, the minimum voltage required before a non-zero fraction of the rf cycle satisfies $\lambda_{\text{mfp}} \geq S_R$ reduces with increasing applied voltage frequency. As a result, ion populations that are less influenced by collisions (region II) and effectively collisionless ion populations (region III) may be induced over a wider voltage range at relatively high (above 94.92 MHz at 1.5 Torr) applied voltage frequencies, enabling a greater range of energies of the resulting high energy structures.

While, the treatment discussed in reference to figure 4.10 provides an estimate for the expected collisionless population, it cannot predict the expected energies of this population. In accounting for this, it is important to note that ions are not typically capable of falling through the full sheath potential unperturbed, and therefore the maximum energy an ion can reach depends upon its 'initial' distance from the wall. The radially resolved plasma potential and Ar^+ density adjacent to the powered electrode ($Z = 21$ mm) for 450 V discharges at applied voltage frequencies of 13.56 MHz and 108 MHz are shown in figures 4.11 (a) and (c), respectively. The dashed lines indicate a distance of one mean-free-path from the alumina wall. Figures 4.11 (b) and (d) show the trends in sheath potential and Ar^+ density, respectively, located at a mean-free-path from the wall and at the phase-averaged sheath extent, with varying applied voltage frequency.

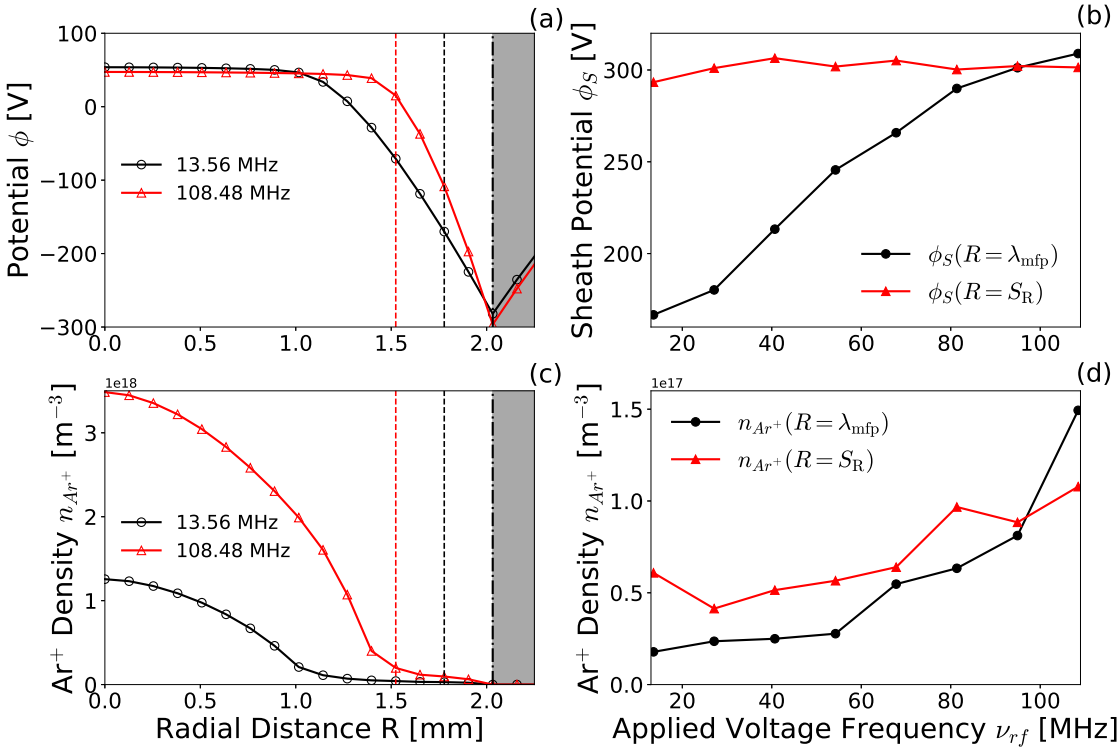

Figure 4.11: Radially resolved (a) plasma potential and (c) Ar^+ density adjacent to the powered electrode ($Z = 21$ mm) for 450 V discharges at applied voltage frequencies of 13.56 MHz and 108.48 MHz. Dashed lines represent a distance of one mean-free-path from the alumina wall, denoted by the shaded region beyond the dash-dotted line at R = 2.1 mm. Trends in (b) sheath potential and (d) Ar^+ densities located a mean-free-path from the wall and at the phase-averaged sheath extent with respect to applied voltage frequency. Plenum pressure 200 Pa (1.5 Torr) argon, $\phi_{\rm rf} = 450$ V, wall temperature 325 K.

The on-axis plasma potential and dielectric surface potential, shown in figure 4.11 (a), remain approximately constant over the applied frequency range 13.56 - 108.48 MHz at 450 V. The reduction in sheath extent with increasing applied voltage frequency is apparent from the steeper potential gradient at 108.48 MHz, as compared to 13.56 MHz. As the sheath potential is approximately frequency independent over this range, the electric field strength across the sheath increases in direct proportion to the applied voltage frequency. Ions therefore accelerate at an increased rate at higher applied voltage frequencies, reaching higher energies over a shorter distance. Also, due to the increased Ar^+ mean-free-path, ions are accelerated over a larger distance before undergoing a collision. Finally, the combination of a steeper potential gradient and larger mean-free-path result in an increase in the maximum potential gradient through which an ion can be accelerated without losing energy through collisional losses. This is observed in figure 4.11 (a) as an increase in the potential one mean-free-path from the alumina wall, denoted by the dashed lines, with increasing applied voltage frequency.

This trend is demonstrated over the frequency range 13.56 - 108.48 MHz in figure 4.10 (b), where the maximum sheath potential through which an ion can be accelerated through without a collision $\phi_S(\lambda_{\text{mfp}})$ approaches the phase-averaged sheath potential $\phi_S(S_{\text{R}})$ as the applied voltage frequency is increased. The phase-averaged sheath extension and Ar^+ mean-free-path converge at 94.92 MHz, correlating with the II - III transition frequency observed in figure 4.8 and the formation of the previously described high energy IEDF structures. At 94.92 MHz and above, ions may be accelerated through the full phase-averaged sheath potential without undergoing a collision. This results in the central energy of the highest energy region III structure (291 eV) approximately equalling the phase-averaged sheath potential (298 V), as would be expected for IEDFs in the high frequency ($\tau_{\text{rf}} >> \tau_{\text{i}}$) regime[79] and agrees with the maximum expected ion energy gain through a collisionless sheath, discussed with reference to equation 1.42, where:

$$\hat{\epsilon}_{Ar^+} = \phi_S(\lambda_{\text{mfp}}) - \phi_S(S_{\text{R}}) \tag{4.1}$$

Equation 4.1 states that the IEDF incident through a sheath is dependant upon not only the phase-averaged sheath dynamics where $\phi_S(R) \propto {}^1/_{n_i}$ but also upon the ion mean-free-path where $\lambda_{mfp} \propto {}^1/_{n_{Ar}}$. For the cases presented in figure 4.11, the sheath potential at the wall remains approximately constant with varying applied voltage frequency and we can simply state:

$$\hat{\epsilon}_{Ar^+} \propto \phi_S(\lambda_{\text{mfp}}) \tag{4.2}$$

coinciding with the trends observed in figures 4.9 (b) and (d). Crucially, equations 4.1 and 4.2 dictate that the effects of rarification arising from neutral gas heating and neutral depletion must be taken into account when determining IEDFs through intermediate pressure plasma sheaths. While this accounts for the formation of the highest energy peaks, the origin of the low and mid energy peaks is more nebulous and likely arises due to either, weakly collisional ion populations having undergone a small number of collisions, or resonant effects between the ion transit time through the sheath and the phase-resolved sheath potential, where ions are predominately accelerated from a 'preferred' distance from the wall and therefore reach similar energies[200].

The radially resolved Ar^+ ion density profiles in figure 4.11 (c) exhibit a peak density on-axis, reducing towards the alumina walls. A sharp decrease in the ion density is observed at $\approx$ 1 mm and $\approx$ 1.4 mm, marking the transition into the pre-sheath for 13.56 MHz and 108.48 MHz discharges, respectively. Due to the increased mean-free-path at higher applied voltage frequencies, there exists a larger ion density one mean-free-path from the wall at 108.48 MHz, as compared to 13.56 MHz. This results in a greater number of ions falling through a higher sheath potential towards the alumina surface at this frequency, resulting

in the formation of larger populations of high energy ions. This agrees with the transition of the modal ion energy into the higher energy structures observed in figure 4.8.

This trend is shown over the frequency range 13.56 - 108.48 MHz in figure 4.11 (d). Here, the Ar^+ ion density increases with increasing applied voltage frequency at both one mean-free-path from the wall and at the phase-averaged sheath extent due to the increasing deposited power. However, the density one mean-free-path from the wall increases at a faster rate, intercepting the density at the phase-averaged sheath extent at 94.92 MHz, again correlating with the II - III transition observed in figure 4.8. The ratio between the Ar^+ density at one mean-free-path from the wall and the Ar^+ density at the phase-averaged sheath extent correlates with the increasing proportion of collisionless ions within the resulting IEDF.

4.3 Chapter Summary

To conclude, a transition from collisional IEDFs to structured multi-peaked IEDFs exhibiting collisionless effects is observed for applied voltage frequencies above 54.24 MHz at 450 V in the *Pocket Rocket* microthruster. This transition is characterised by the formation of high energy structures within the IEDF. The formation of these structures is attributed to a reduction in the phase-averaged sheath extent in combination with an increased Ar - Ar^+ mean-free-path with increasing applied voltage frequency over 13.56 - 108.48 MHz. Two distinct transitions in the structure of the IEDF are observed at 450 V, corresponding to the formation of a single mid-energy (90 - 150 eV) structure between 40.68 - 54.24 MHz, and two additional high energy ($\approx$ 210 eV, $\approx$ 290 eV) structures which form at frequencies above 81.36 MHz. A significant degree of control of the mean and modal Ar^+ energies is achieved, varying by 97 eV and 280 eV, respectively.

Inducing and altering the shape of structured IEDF through the application of higher applied voltage frequencies enables enhanced control of the ion-neutral momentum transfer through varying the Ar - Ar^+ collision cross-section. Ions within the high energy structures respond more directly to the applied voltage, allowing a larger range of ion energies to be accessed for a given background pressure and radial ion flux. Such discrete control of the ion energy comes at the cost of a reduced fraction of power being deposited into the ions at higher applied voltage frequencies, noting that the formation of high energy structures above 67.80 MHz maintains this fraction at approximately 70%. When considering application as a propulsion source, increasing the applied frequency therefore represents a trade-off between thermal efficiency and absolute neutral gas temperature. To overcome this, and achieve independent control of the fraction of power deposited into ions and electrons, chapter 5 will investigate the application of multi-harmonic voltage waveforms to the *Pocket Rocket* microthruster.

Chapter 5

Control of Electron, Ion and Neutral Heating via Dual-Frequency Voltage Waveforms

In chapter 3, the radial ion flux through the powered electrode sheath was shown to vary in proportion to the magnitude of the dc self-bias voltage. In addition, control of the mean and modal ion energies has been demonstrated for varying single frequency operation, via modulation of the phase-averaged sheath extent. This chapter investigates the ionisation dynamics and ion heating within the *Pocket Rocket* for dual-frequency operation, where the dual-frequency voltage waveforms comprise a fundamental 13.56 MHz waveform combined with an odd or even harmonic waveform with a variable phase offset. Control of the sheath dynamics and dc self-bias voltage through varying the applied waveform shape is achieved. The resulting effects on the neutral gas heating efficiency are discussed, with a particular emphasis on the control of the relative power deposition into ion and electron species. It is also demonstrated that through dual-frequency operation, it is possible to vary the net thrust and specific impulse, enabling on-the-fly alterations to mission roles for rf driven thrusters. Finally, the formation and control of structured ion energy distributions is discussed, with respect to the application of higher fundamental frequencies with variable harmonic separation, Throughout this chapter the *Pocket Rocket* is operated employing 100 sccm of argon with a 0.85 Torr outlet pressure, supplied by a 450 V amplitude voltage waveform unless otherwise stated.

The results and conclusions presented in this chapter are based upon those published by the author in Ref. 89.

5.1 Dual-frequency Voltage Waveforms

By combining two or more sinosoidal voltage waveforms with varying amplitudes or a variable phase offset it is possible to introduce a phase-averaged electrical asymmetry to a plasma[9,128,139]. This electric asymmetry effect (EAE), introduced previously in section 1.6.3, can be employed to modify any existing physical or secondary electron induced asymmetries[196,205,206]. This provides a mechanism whereby the sheath dynamics, dc self-bias voltage and other bulk properties can be controlled in real-time for a fixed plasma source configuration, as the relative amplitude or phase offset between any two harmonics can be readily (and remotely) controlled[97,103,136–138].

The choice of frequency components determines the shape and symmetry of the resulting waveform. Non-harmonic dual-frequency voltage waveforms, involving the application of a 13.56 MHz 'carrier' frequency superimposed with a lower, typically 2 MHz, secondary frequency have been extensively studied over the last decade[97,207–209]. This technique provides the benefit that ions preferentially respond to the lower applied frequency[86], while electrons preferentially respond to the higher frequency[210], providing a quasi-independent control mechanism. However, beat effects arising from the non integer separation of the applied harmonics can introduce undesired effects and lead to drifts and instabilities. For this reason, dual-frequency waveforms composed of only harmonics of the fundamental frequency are typically more widely adopted[87,103,129,135,137,211–213].

Dual-frequency voltage waveforms employed in this work, constructed through the superposition of a fundamental 13.56 MHz sinusoid and either an odd or even harmonic sinusoid with a variable phase offset, were generated using equation 5.1, introduced previously in section 1.6.3.

$$\phi_{\mathrm{rf}}(t) = \sum_{k=1}^{n} \left(\frac{\phi_0}{n}\right) \sin(k\omega_0 \mathrm{t} + \theta_k) \tag{5.1}$$

where, as before, $\phi_{\mathrm{rf}}(t)$ is the combined voltage waveform, ϕ_0 is its maximum amplitude, $\omega_0 = 2\pi\nu_0$ is the fundamental angular frequency, θ_k is the phase offset of harmonic k and n is the total number of applied harmonics.

When evaluating $\phi_{\mathrm{rf}}(t)$, the values chosen for k influence the symmetry of the resulting waveform. Sets of k where $(2n)k \in \{k_{+1}, ..., n_{-1}, n\}$ is exclusively true produce 'odd-even' voltage waveforms, the trivial example of which is given in equation 5.2 where k = 1,2, referring to a waveform comprising 13.56 MHz and 27.12 MHz components. Conversely sets of k for which any $(2n+1)k \in \{k_{+1}, ..., n_{-1}, n\}$ produce 'odd-odd' voltage waveforms, the trivial example for which is given in equation 5.3 where k = 1,3, comprising 13.56 MHz and 40.68 MHz components.

$$\phi_{\mathrm{rf}}(t) = \left(\frac{\phi_0}{2}\right)\sin(\omega_0 \mathrm{t}) + \left(\frac{\phi_0}{2}\right)\sin(2\omega_0 \mathrm{t} + \theta_2) \qquad \text{For k} = 1, 2 \tag{5.2}$$

$$\phi_{\mathrm{rf}}(t) = \left(\frac{\phi_0}{2}\right)\sin(\omega_0 \mathrm{t}) + \left(\frac{\phi_0}{2}\right)\sin(3\omega_0 \mathrm{t} + \theta_3) \qquad \text{For k} = 1, 3 \tag{5.3}$$

As shown, phase offsets are applied only to the higher harmonic such that $\theta_1 = 0°$ and $0° < \theta_{2,3} < 360°$. For simplicity, phase offsets θ_2, θ_3, ...θ_n are referred to as θ from this point forward, unless specified otherwise.

As the harmonics $k = 2$ (27.12 MHz) and $k = 3$ (40.68 MHz) do not add in phase with the fundamental 13.56 MHz harmonic, the peak-to-peak voltage $\mathrm{V_{pp}}$ of the combined dual-frequency voltage waveform, described by $\phi_{\mathrm{rf}}(t)$, depends upon θ. Arising from this, the positive amplitude, $\phi^{+}_{\mathrm{rf}}(t)$, and negative amplitude, $\phi^{-}_{\mathrm{rf}}(t)$, are not always equal. Hence the dual-frequency voltage waveforms do not have a single voltage amplitude. For ease of discussion, waveforms in this chapter will be discussed in terms of their peak-to-peak voltage:

$$V_{\mathrm{pp}} = |\max \phi_{\mathrm{rf}}(t)| + |\min \phi_{\mathrm{rf}}(t)| \leq 2\phi_0 \tag{5.4}$$

In this work, the peak-to-peak voltage for each dual-frequency voltage waveform is allowed to vary with phase offset to more closely match experimental conditions. The variation in $\mathrm{V_{pp}}$ for odd-even and odd-odd dual-frequency voltage waveforms generated using equation 5.1 with varying phase offset θ is shown in figure 5.1.

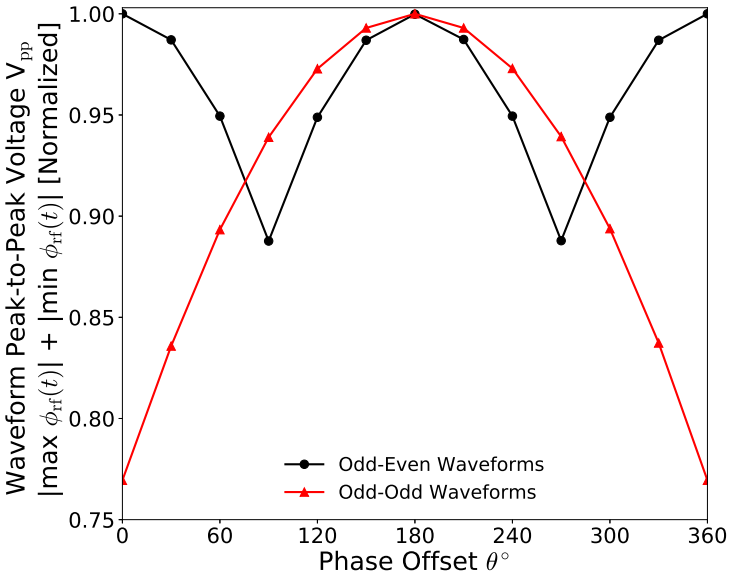

Figure 5.1: Peak-to-peak voltages $\mathrm{V_{pp}}$ for dual-frequency voltage waveforms generated using equation 5.1 for (a) odd-even ($k = 1, 2$) and (b) odd-odd ($k = 1, 3$) configurations with phase offsets $0° \leq \theta \leq 360°$ and $V_{\mathrm{pp}} = 600$ V. Odd-even and odd-odd peak-to-peak voltages are normalised to their respective maximum; odd-even: 528 V, odd-odd: 600 V.

The relationship between V_{pp} and the applied phase offset in figure 5.1 differs for odd-odd and odd-even waveforms. For odd-even waveforms ($k = 1, 2$), there is a periodic reduction in the peak-to-peak voltage for every 180° phase offset. Over a 360° range of phase offsets, two maxima and minima in V_{pp} occur, separated by 90°, where the difference between maximum and minimum represents 11% of the maximum odd-even peak-to-peak voltage ($V_{pp} = 528$ V at $\theta = 0°$, $\theta = 180°$, $\theta = 360°$). Note that for odd-even waveforms V_{pp} is always lower than $2\phi_0$, regardless of phase offset. Conversely odd-odd ($k = 1, 3$) waveforms exhibit a single approximately parabolic variation in V_{pp} over the 360° range of phase offsets. Maxima and minima are separated by 180° of phase offset, double that of the odd-even waveforms, while the variation between these increases to 26% of the maximum peak-to-peak voltage ($V_{pp} = 600$ V at $\theta = 180°$). While it is possible to avoid the effects of destructive interference in simulation, through scaling a pre-normalised waveform, it is considerably more difficult to avoid in experiment. One further practical consideration involves the requirement for matching multiple applied voltage frequencies simultaneously, the ohmic losses of which are not directly accounted for in these simulations. With these points in mind, the destructive interference between successive harmonics is maintained in simulation as a proxy for matching losses, improving the applicability of conclusions drawn from this work to real world electrothermal propulsion sources.

Examples of simulated dual-frequency voltage waveforms for three phase offsets ($\theta = 0°, \theta = 45°, \theta = 90°$) generated using equation 5.1 with odd-even ($k = 1, 2$) and odd-odd ($k = 1, 3$) voltage waveform components are shown in figures 5.2 (a) and (b), respectively.

Where, the phase offset θ refers to the temporal delay between the two superimposed waveforms, while applied voltage phase $\tau = \omega t/2\pi$ refers to temporal position within the rf cycle. Varying the phase offset of an even (k=2) harmonic relative to the fundamental frequency alters the phase-averaged RMS voltage of the resulting waveform. This is demonstrated for three odd-even waveforms in figure 5.2 (a), where the phase of the 27.12 MHz harmonic is offset from the fundamental harmonic by $\theta = 0°$, $\theta = 45°$ and $\theta = 90°$. Varying the phase offset causes the extrema in amplitude of the k=1 and k=2 harmonics to add asymmetrically, where the variation in positive amplitude need not match the variation in the negative amplitude, i.e. $\phi_{rf}^{+}(t) - \phi_{rf}^{-}(t) \neq 0$. This results in a non-zero phase-averaged voltage, denoted by the dotted lines, and is referred to as the electrical asymmetry effect (EAE)[128,138].

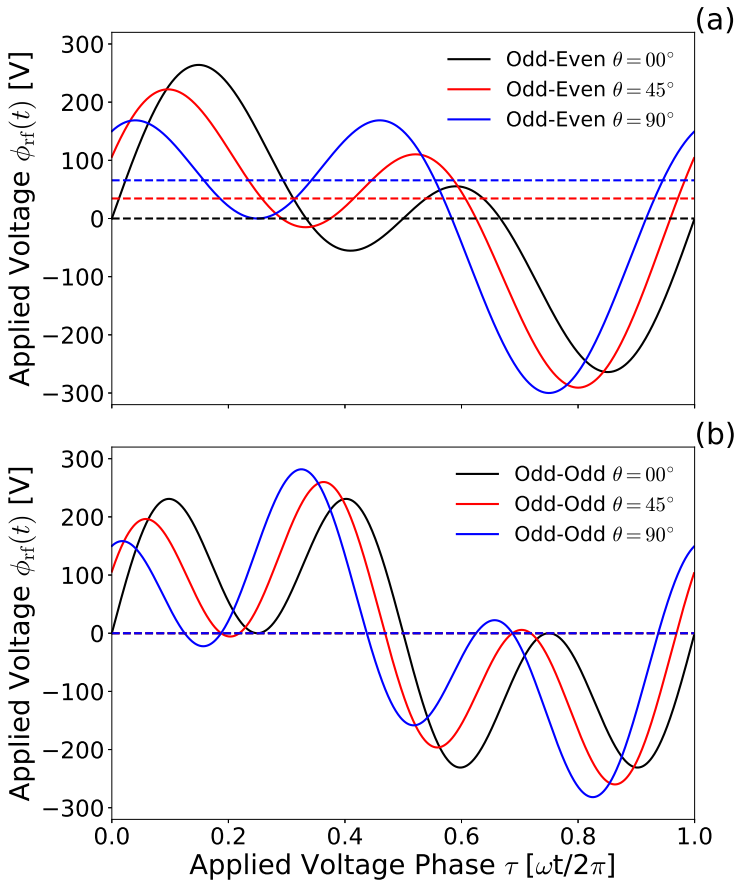

Figure 5.2: Dual-frequency voltage waveforms generated using equation 5.1 for (a) odd-even ($k = 1, 2$) and (b) odd-odd ($k = 1, 3$) configurations with phase offsets of $\theta = 0°, \theta = 45°, \theta = 90°$, with $V_{pp} = 600$ V (300 V). The difference between the most negative and most positive voltages for each waveform are denoted by the dashed lines, noting that this difference is zero in the case of odd-odd waveforms in (b).

The same effect is not observed for odd-odd waveforms, shown in figure 5.2 (b), for the same range of phase offsets as applied to the odd (k=3) 40.68 MHz harmonic. Applying a phase offset to an odd-odd waveform results in the extrema of the k=1 and k=3 harmonics superimposing symmetrically. This ensures that the extrema of the positive and negative voltages always remain equal, i.e. $\phi^{+}_{rf}(t) - \phi^{-}_{rf}(t) = 0$ and therefore no electrical asymmetry is present. While odd-odd waveforms negate any electrical asymmetry, destructive interference between the two harmonics is still observed, albeit symmetric about the RMS voltage. Therefore odd-odd waveforms employing phase offsets still exhibit a varying peak-to-peak voltage, presenting the capability to alter the sheath dynamics without imposing an EAE[168,214]. Finally, note that for both odd-odd and odd-even voltage waveforms, varying the phase offset alters the location and magnitude of the peak change in voltage, $\mathrm{d}V/\mathrm{d}t$, and therefore alters the phase-resolved sheath dynamics.

The voltage amplitude asymmetries ($\phi^{+}_{rf}(t) - \phi^{-}_{rf}(t)$) for odd-even and odd-odd dual-frequency waveforms of increasing harmonic separation are shown in figure 5.3 with respect

to varying upper harmonic phase offset. The difference between the minimum and maximum voltage amplitude asymmetries, denoted the symmetry parameter ϵ_s, is shown for odd-even waveforms of increasing harmonic separation in the inlay.

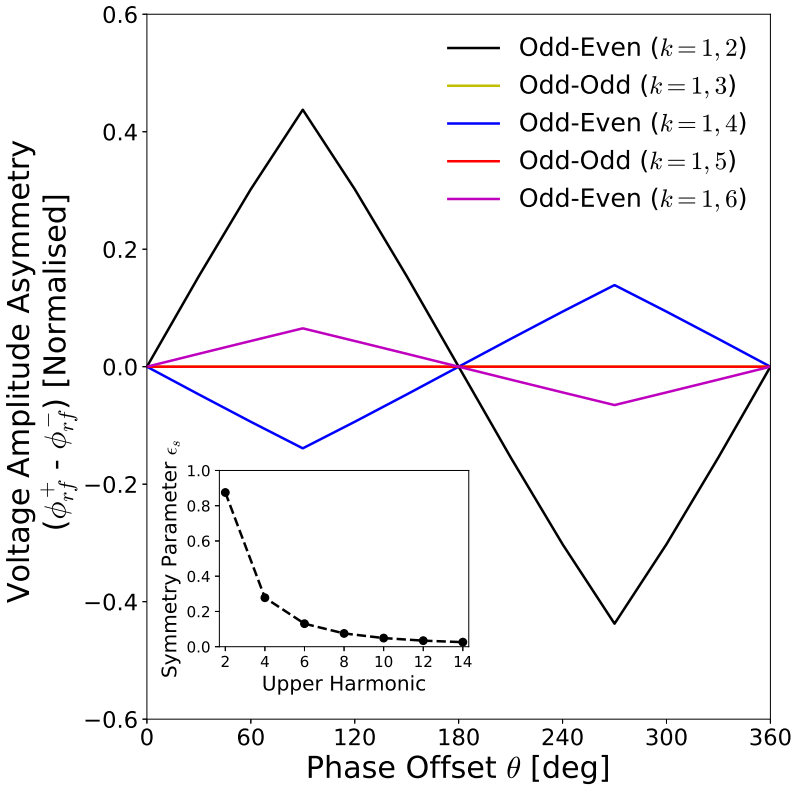

Figure 5.3: Voltage amplitude asymmetries $(\phi_{\mathrm{rf}}^{+}(t) - \phi_{\mathrm{rf}}^{-}(t))$ for odd-even and odd-odd dual-frequency waveforms with varying applied upper harmonic phase offsets in the range $0° \leq \theta \leq 360°$. The difference between the minimum and maximum voltage amplitude asymmetries is denoted by the symmetry parameter ϵ_s as introduced in equation 1.39 and is shown for odd-even waveforms of increasing harmonic seperation in the inlay.

Here, the voltage amplitude asymmetry represents the maximum value of $\phi_{\mathrm{rf}}^{+}(t) - \phi_{\mathrm{rf}}^{-}(t)$ over a single rf phase cycle. Odd-odd voltage waveforms possess no voltage amplitude asymmetry, regardless of phase offset or harmonic separation, as expected. In contrast, the voltage amplitude asymmetries for odd-even voltage waveforms exhibit a sawtooth shape, varying linearly between two extrema for $\theta = 90°$ and $\theta = 270°$. The 'parity' of these extrema in voltage amplitude asymmetry flips for every successive odd-even waveform, where the most positive separation for $k = 1, 2$ waveforms corresponds to the most negative for $k = 1, 4$ waveforms and visa-versa. In describing these patterns, it is helpful to re-introduce the symmetry parameter ϵ_s, first introduced in equation 1.39, here representing the difference between the minimum and maximum voltage amplitude asymmetries for a given harmonic pair. The greater the symmetry parameter, the greater the range of achievable electrical asymmetries imposed by voltage waveforms constructed from these harmonics. As shown in the inset, the

symmetry parameter varies in inverse proportion to the harmonic separation, reducing exponentially with increasing upper harmonic frequency. For this reason dual-frequency voltage waveforms employing the minimum harmonic separation, namely $k = 1, 2$ and $k = 1, 3$, will form the focus of this study. Effects arising from dual-frequency waveforms employing higher fundamental frequencies and increased harmonic separation will be considered in section 5.4.

5.2 Electrical Asymmetry Effect via Harmonic Phase-Offset

This section will address the extent to which the electrical asymmetry effect influences the phase resolved sheath dynamics within the *Pocket Rocket* and how this alters the dc self-bias voltage for dual-frequency operation employing odd-even ($k = 1, 2$) and odd-odd ($k = 1, 3$) voltage waveforms.

5.2.1 Dual-Frequency Sheath Dynamics

The phase-resolved sheath extent $S_R(\tau)$ and sheath potential $\phi_S(\tau)$ adjacent to the powered electrode at region 2 (Z = 21 mm) are shown in figures 5.4 (b) and (c) for operation employing 900 V_{pp} (450 V), odd-even ($k = 1, 2$) dual-frequency waveforms, shown in figure 5.4 (a).

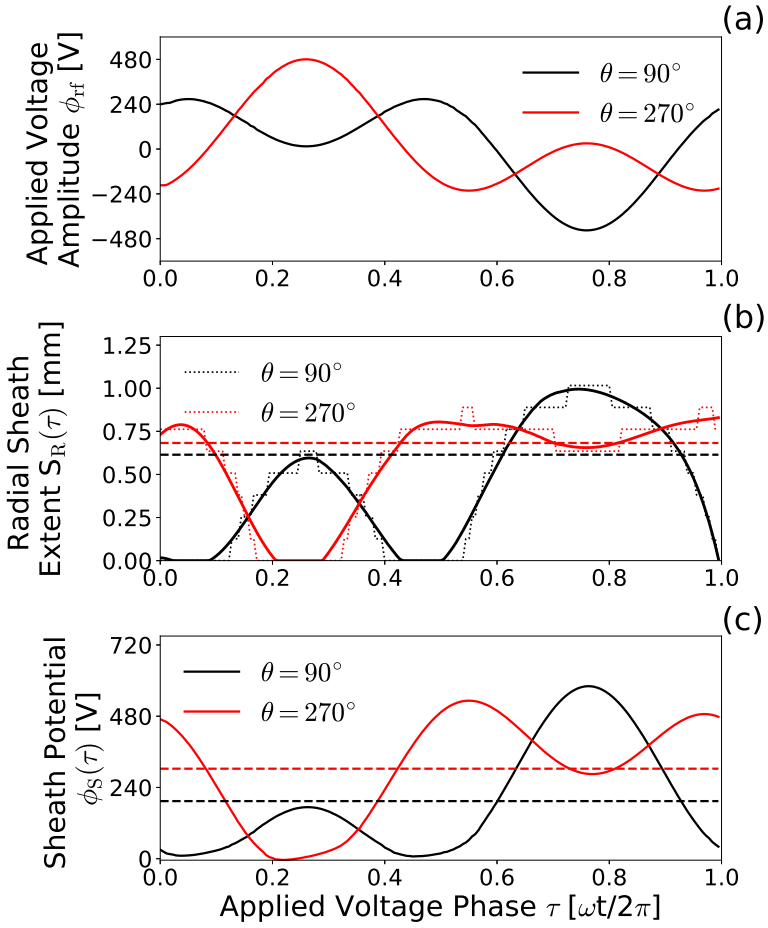

Figure 5.4: Phase-resolved (b) sheath extent $S_R(\tau)$ adjacent to the powered electrode at region 2 (Z = 21 mm), (c) sheath potential $\phi_{\S}(\tau)$ through full sheath extent for operation employing (a) 900 V_{pp} (450 V), odd-even ($k = 1, 2$) dual-frequency waveforms with phase-offsets of $\theta = 90°$ and $\theta = 270°$, representing the most positive and negative dc self-bias voltages, respectively. The phase-averaged sheath extent and sheath potentials are denoted by the dashed lines in (b) and (c). Plenum pressure 200 Pa (1.5 Torr) argon, V_{pp} = 900 V (450 V), wall temperature 325 K.

The dual-frequency voltage waveforms in figure 5.4 (a) employ phase offsets of $\theta = 90°$ and $\theta = 270°$ to correspond with the minimum and maximum expected voltage amplitude asymmetries, see figure 5.3. The two waveforms are effectively phase-offset mirror images of each-other, owing to the 180° phase separation, each possessing a relatively flat region and a single large amplitude peak. The amplitude of this peak is approximately ± 240 V separated from the flat region for both waveforms, leading to the electrical asymmetry. Note that due to the similar shapes, the magnitude of peak $\mathrm{d}V/\mathrm{d}t$ is the same for both waveforms.

The sheath adjacent to the powered electrode varies in inverse proportion to the applied rf voltage amplitude, as shown in figure 5.4 (b). Here, as before, the sheath extents are determined through the Brinkmann criterion, and smoothed through a Savitzky–Golay filter, denoted as the dotted and solid lines, respectively. The phase-averaged sheath extent ϕ_S, denoted by the dashed lines, does is not greatly affected by phase offset, varying between $0.61 \leq \phi_S \leq 0.68$ mm. This represents a 10% variation, as compared to the 40% variation previously observed with varying applied voltage frequency in figure 4.4 (a). Note that while the sheaths exhibit approximately similar minimum and maximum extents, the frequency and duration of sheath collapse are not equal for the two waveforms. Specifically, the $\theta = 270°$ waveform sheath collapses once for 8.3% of the rf cycle, while the $\theta = 90°$ waveform collapses twice for a combined 13.3% of the rf cycle. Low energy electrons are therefore more easily able to leave the plasma for a $\theta = 90°$ offset waveform, as compared to the $\theta = 270°$ waveform, resulting in a reduction in the electron velocity during sheath collapse. In addition, the sheath extent varies by a greater total distance for $\theta = 90°$, and therefore the average sheath velocity is necessarily higher. The impacts of these changes to the sheath dynamics are discussed in more detail in section 5.3.

The sheath potentials shown in figure 5.4 (c), computed as $\phi_{\mathrm{S}}(\tau) = \phi_{\mathrm{fp}}(\tau) - \phi_{\mathrm{dc}}(\tau)$, vary in proportion to the sheath extent. The phase-averaged sheath potential varies significantly with phase offset, reducing from 303 V for $\theta = 270°$ to 194 V for $\theta = 90°$. This arises from two effects: firstly, the increased duration and frequency of sheath collapse for for $\theta = 90°$ results in an increased proportion of the phase cycle for which the sheath potential is zero, reducing the average. Secondly, the negative electrical asymmetry imposed by the $\theta = 270°$ waveform enforces a more negative dc self-bias voltage, shown in 5.5, resulting in an increased sheath potential. Note that this behaviour differs from that experienced when varying the applied voltage frequency, where the sheath potential remains approximately constant for a fixed applied voltage amplitude, see figure 4.4 (b). To summarise, varying the applied voltage frequency alters plasma behaviour through modulating the sheath extent, while varying the phase offset between applied voltage frequencies influences the plasma through varying the sheath potential directly.

The dc self-bias voltage η_{dc}, forms to balance the positive and negative fluxes lost to the powered and grounded electrodes, as previously discussed. Varying the phase-offset for

an odd-even voltage waveform influences the dc self-bias voltage directly through the time-averaged electrical asymmetry, as shown in figure 5.3 (a). The resulting modulation in the dc self-bias voltage adjacent to the powered electrode (region 2, Z = 21 mm), normalized to V_{pp}, is shown in figure 5.5 (a), for operation at 900 V_{pp} (450 V) employing odd-even ($k = 1, 2$) and odd-odd voltage ($k = 1, 3$) waveforms. The maximum Ar^+ density adjacent to the powered electrode and radial Ar^+ flux incident upon the powered electrode are shown in figures 5.5 (b) and (c) respectively.

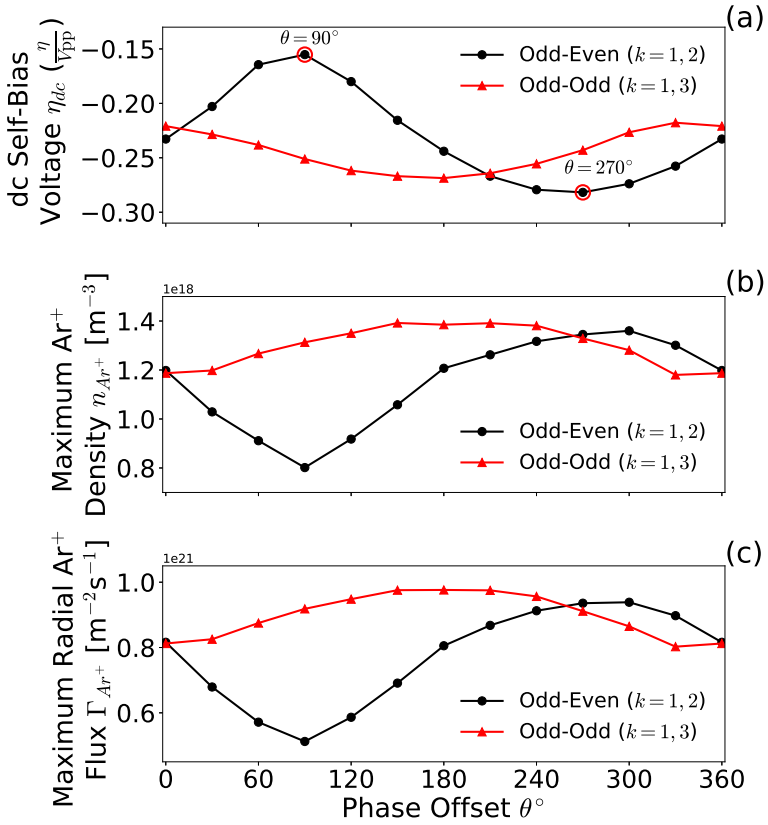

Figure 5.5: Phase-averaged (a) dc self-bias voltage adjacent to the powered electrode (R = 2.1 mm), (b) Ar^+ density adjacent to the powered electrode and (c) radial Ar^+ flux incident upon the powered electrode with respect to phase offset θ for odd-even ($k = 1, 2$) and odd-odd ($k = 1, 3$) voltage waveforms. Radial Ar^+ flux and secondary electron impact ionisation rates are taken at the dielectric surface adjacent to the powered electrode (R,Z = 2.1 mm, 21 mm). The phase offsets which correspond to the most positive and most negative dc self-bias voltages are identified with red circles in (a). Plenum pressure 200 Pa (1.5 Torr) argon, V_{pp} = 900 V (450 V), wall temperature 325 K.

Varying the phase offset between $0° \leq \theta \leq 360°$ for resulted in an approximately sinusoidal modulation of the dc self-bias voltage, shown in figure 5.5 (a). Modulations of 13% V_{pp} and 5% V_{pp} were achieved employing odd-even ($k = 1, 2$) and odd-odd ($k = 1, 3$) voltage waveforms, respectively. Note that, despite the odd-odd voltage waveform applying no direct electrical asymmetry to the plasma, there is still a non-zero modulation in the dc

self-bias voltage. The mechanism for this modulation is attributed to the variation in the peak-to-peak voltage, see figure 5.1, and associated variation in the power deposited with phase offset. While the peak-to-peak voltage also varies for odd-even waveforms, any effects arising from this are overshadowed by the variation in the electrical asymmetry.

The dc self-bias voltage varies about $\eta_{dc} \approx -0.25$ V_{pp} due to the inherent physical asymmetry between the powered and grounded electrode areas and the voltage induced asymmetry between the powered and grounded sheath extents. This 'baseline' dc self-bias differs by 6% from the $\eta_{dc} \approx -0.31$ V_{pp} dc self-bias voltage observed for 900 V_{pp} (450 V) operation at 13.56 MHz, shown in figure 3.7 (b). This disparity arises due to increased ionisation upstream and downstream of the powered electrode for dual-frequency operation as compared to 13.56 MHz operation, discussed in more detail in section 5.3. This reduces the difference between the powered and grounded electrode sheath extents, reducing the voltage induced asymmetry and correspondingly also the magnitude of the dc self-bias.

The Ar^+ density adjacent to the powered electrode, shown in figure 5.5 (b), also exceeds the densities observed for 13.56 MHz operation and varies in inverse proportion to the dc self-bias voltage. Odd-odd ($k = 1, 3$) voltage waveforms achieve the highest Ar^+ density, at 1.39×10^{18} m^{-3}. However the greatest control is achieved via the odd-even ($k = 1, 2$) waveforms where the Ar^+ density varies by $\approx 70\%$ between 0.8×10^{18} m^{-3} to 1.35×10^{18} m^{-3} over the range $90° \leq \theta \leq 270°$, representing the most positive to most negative dc self-bias voltages, respectively. This variation in the Ar^+ coincides with an increased radial Ar^+ flux incident on the powered electrode, shown in figure 5.5 (c). Here, the radial Ar^+ flux was modulated by $\approx$ 80% over the range $90° \leq \theta \leq 270°$ for odd-even waveform operation. This closely matches the $\approx 70\%$ modulation in the Ar^+ density over the same range of phase offsets, suggesting that the variation in the mean Ar^+ ion velocity, and hence energy, is relatively small. As the sheath potential has been shown to vary significantly with phase offset, see figure 5.4 (c), this indicates a high rate of collisional loss within the sheath, to maintain a low mean Ar^+ ion velocity. Enhanced control of the radial Ar^+ flux through this means therefore represents an effective method for altering power deposition into the neutral gas. Further, from previous discussion regarding figures 3.8 and 3.5, an increased radial Ar^+ flux results in an increased production of secondary electrons, leading to a higher 'background' ionisation rate.

5.3 Influence of Phase Offset on Electron Heating Mechanisms

Dual-frequency voltage waveforms have been shown to influence both the phase-resolved sheath dynamics and phase averaged dc self-bias voltage. The effects that these parameters have on the electron heating and ionisation dynamics are investigated in this section, including a discussion on the extent to which these mechanisms can be controlled through dual-frequency phase offset.

5.3.1 Evolution of Ar($2p_1$) Excitation Rates With Phase Offset: Comparison With Experiment

Before progressing further into an analysis of the dual-frequency driven electron heating mechanisms, the validity of the simulations must first be scrutinised. As before, this is performed through a comparison of the measured and simulated phase-resolved Ar($2p_1$) excitation rates, the agreement of which provides confidence that the sheath dynamics are being modelled reliably.

Measurements were taken as previously described in section 2.1.1. Dual-frequency waveforms were produced in experiment through the superposition and subsequent amplification of two sinusoidal 'seed' ($\leq$ 1 V) voltage waveforms. Owing to the narrow resonance range of the matching network, the resulting dual-frequency waveforms were not impedance matched to the *Pocket Rocket*, resulting in a high ($\geq$ 50%) reflected power to the amplifier, see figure 2.3. For this reason the dual-frequency experimental validation was carried out employing waveforms with a peak-to-peak voltage of 600 V_{pp} (300 V), as unmatched operation at 900 V_{pp} (450 V) resulted in an unsustainably high reflected power to the amplifier. Following validation, simulations are employed to investigate dual-frequency operation employing applied voltages between 300 - 900 V_{pp} (150 - 450 V).

The simulated and measured Ar($2p_1$) excitation rates within the *Pocket Rocket* for operation employing 600 V_{pp} (300 V) odd-even ($k = 1, 2$) dual-frequency voltage waveforms with varying upper harmonic phase offset are shown in figures 5.6 (a) and (b), respectively. Here, PROES images are spatially integrated for each phase offset and the resulting profiles combined to show the evolution of the temporally resolved electron heating mechanisms with respect to phase offset.

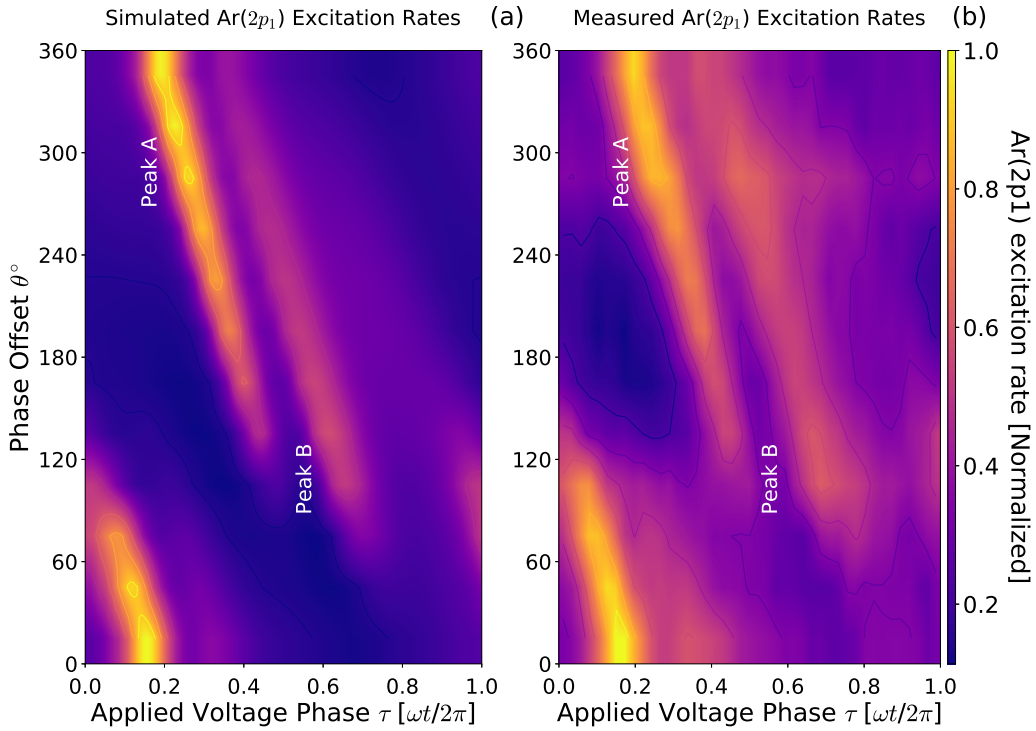

Figure 5.6: Spatially integrated (a) simulated and (b) measured $\mathrm{Ar}(2p_1)$ excitation rates for odd-even ($k = 1, 2$) dual-frequency waveforms with phase offsets in the range $0° \leq \theta \leq 360°$ with respect to rf phase. Simulation plenum pressure 200 Pa (1.5 Torr), experiment plenum pressure 207 Pa (1.55 Torr) argon, odd-even ($k = 1, 2$) voltage waveforms, $V_{\mathrm{pp}} = 600$ V (300 V), wall temperatures between 421 K - 634 K

The measured $\mathrm{Ar}(2p_1)$ excitation rates in figure 5.6 (b) show a close agreement with the simulated rates in 5.6 (a). Excitation arising from both sheath collapse heating (peak A) and sheath expansion heating (peak B) are visible for the same range of rf phases over the same range of applied phase offsets. Additionally, the relative difference between the 'magnitudes' of sheath collapse heating and sheath expansion heating is approximately the same for the simulated and measured PROES. Evidence for the control afforded through dual-frequency operation is observed in both the simulated and measured PROES through a significant ($\approx 50\%$) reduction in the sheath collapse (peak A) heating mechanism between $120° \leq \theta \leq 150°$. The reduction in sheath collapse heating for waveforms with these phase offsets arises, perhaps counterintuitively, from an increase in the frequency and duration of sheath collapse, as shown previously for a $k = 1, 2$, $\theta = 90°$ voltage waveform in figure 5.4 (b). As the fraction of the rf cycle for which the sheath is collapsed increases, the electron flux to the wall required to maintain quasineutrality reduces, resulting in a reduced excitation and ionisation during phases of sheath collapse. Conversely, waveforms resulting in a reduced sheath collapse fraction, for example $\theta = 270°$, accumulate more negative charge within the plasma bulk over the larger period of time between sheath collapses. To maintain quasineutrality the electron flux during sheath collapse must increase proportionally, leading

to substantial electron heating during the shorter phase of sheath collapse.

While control of sheath collapse heating is demonstrated in figures 5.6 (a) and (b), sheath expansion heating is influenced to a lesser extent. This arises as the degree to which electrons are heated during sheath expansion relies upon the sheath velocity, which varies in proportion to the sheath extent for a fixed applied voltage frequency. As the sheath extent has been shown to be only weakly dependent on the phase offset for odd-even ($k = 1, 2$) dual-frequency operation, see figure 5.4 (b), the control afforded over sheath expansion heating is limited. Increased control could be achieved through the application of a higher even harmonic, 54.24 MHz for example, however as shown in figure 5.3, an increased harmonic separation reduces the magnitude of the applied electrical asymmetry effect.

The influence of secondary electrons is not easily observed in either figure 5.6 (a) or (b), with the exception of an increased background excitation rate between applied voltage phases of $0.75 \leq \tau \leq 0.95$, most easily discerned in figures 5.6 (a) and 5.7 (a). The lack of a clear secondary electron excitation peak arises primarily as, at 600 V_{pp} (300 V), the discharge is in α-mode, where the majority of electron heating occurs during sheath movement. In addition, as previously mentioned, secondary electrons preferentially undergo ionisation interactions due to their high energy ($\approx$ 50 eV) relative to the Ar($2p_1$) excitation potential ($\approx$ 11 eV), resulting in a reduced excitation component from the secondary electron population regardless of the discharge mode. Note however, that the measured background excitation between phase offsets $240° \leq \theta \leq 300°$ in figure 5.6 (b), is higher than would be expected from the simulation. This range of phase offsets coincides with discharges with the most negative dc self-bias voltages, see figure 5.5 (a). This could indicate an underestimation in the time-resolved secondary electron induced Ar($2p_1$) excitation rate, likely arising due the phase-averaged secondary electron ionisation rate.

5.3.2 Dual-Frequency Ionisation Dynamics

Having validated the model for dual-frequency operation, it is now possible to investigate further the mechanisms underpinning the change in Ar^+ density observed with varying phase-offset. Varying the applied voltage at 13.56 MHz in chapter 3 altered the Ar^+ density primarily through increased secondary electron emission, while increasing the applied frequency in chapter 4 resulted in increased ionisation primarily through sheath expansion heating. Dual-frequency excitation introduces elements from both of these previously examined cases, and therefore warrants further analysis.

Here, control of the spatio-temporal ionisation dynamics in an odd-even ($k = 1, 2$) 900 V_{pp} (450 V) dual-frequency discharge are investigated for varying phase-offset. The simulated PROES images in figures 5.7 (a) and (b) show the phase-resolved, radially integrated Ar^+ ionisation rates ι_{tot} within the *Pocket Rocket* source between $10 \leq Z \leq 40$ mm, for odd-even ($k = 1, 2$) dual-frequency operation with phase offsets of $\theta = 90°$ and $\theta = 270°$,

respectively. Note that, while the 'bulk' ionisation rate is phase-resolved, the secondary electron ionisation rate represents a phase-averaged value. The associated voltage waveforms and dielectric surface potentials adjacent to the powered electrode (R,Z = 2.1 mm,21 mm) are shown in figures 5.7 (c) and (d), respectively.

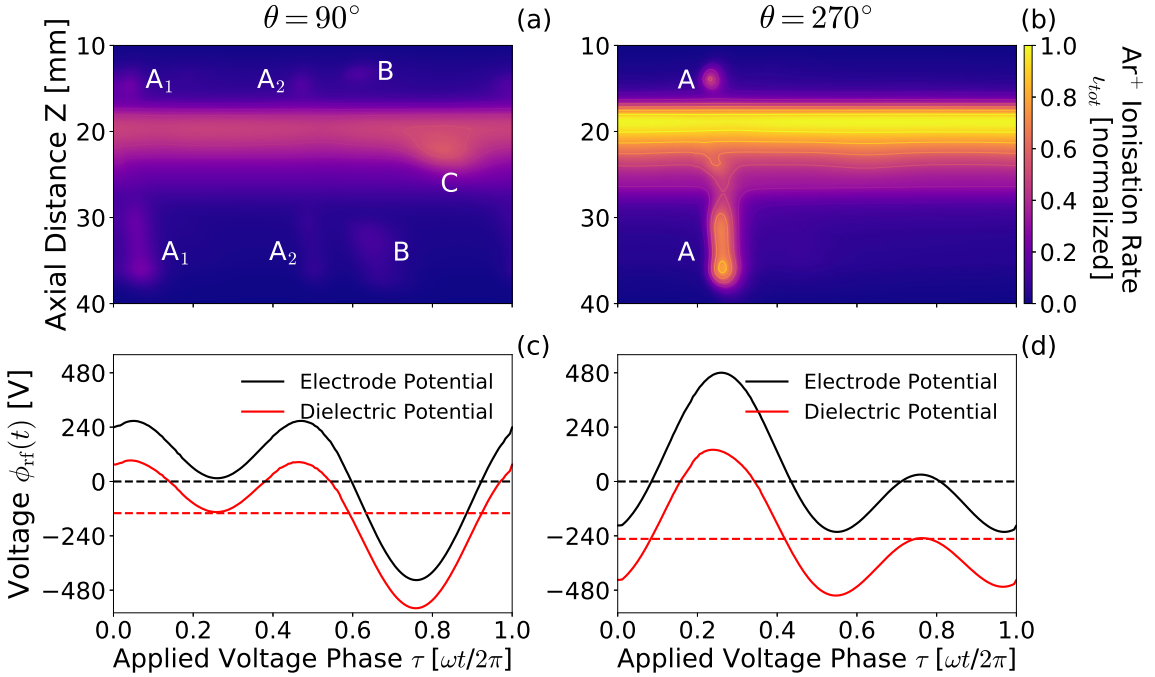

Figure 5.7: Phase-resolved radially integrated Ar^+ ionisation rates ι_{tot} with associated applied voltage $\phi_{\mathrm{rf}}(t)$, and dielectric potential adjacent to the powered electrode (R,Z = 2.1 mm,21 mm) for an odd-even dual-frequency driven discharge with (a) (c) $\theta = 90°$ phase offset and (b) (d) $\theta = 270°$ phase offset. Plenum pressure 200 Pa (1.5 Torr) argon, odd-even ($k = 1, 2$) voltage waveform, $V_{\mathrm{pp}} = 900$ V (450 V), wall temperature 325 K.

The phase-resolved ionisation rate for $\theta = 90°$, representing the most positive dc self-bias voltage case, is shown in figure 5.7 (a) and exhibits four ionization structures (A_1, A_2, B and C). However the majority of the ionisation arises from a relatively phase-independent 'background' ionisation between 18 mm $\leq Z \leq$ 24 mm. While peaks A_1 and A_2, coincide with phases for which the applied voltage is most positive, $\omega t/2\pi = 0.05$ and $\omega t/2\pi = 0.5$, any evidence of sheath collapse heating adjacent to the powered electrode (region 2, Z = 21 mm) is hidden by the secondary electron background ionisation. Instead, peaks A_1, A_2 are observed upstream and downstream of the powered electrode, and correspond to axial electron flux away from the upstream and downstream regions (regions 1 and 3) and towards the, now collapsed, powered electrode sheath at Z = 21 mm. This occurs due to the rapid depletion in the electron density at region 2 during the powered electrode sheath collapse. The same spatial distribution in ionisation is also observed for sheath expansion heating (peak B) observed between $0.6 \leq \omega t/2\pi \leq 0.8$, corresponding to the most negative $\mathrm{d}V/\mathrm{d}t$ in figure 5.7 (c). Here, the opposite effect occurs, where the large influx of electrons into region 2

due to sheath expansion results in a net axial electron flux into regions 1 and 3. Returning to the sheath collapse heating, note that the magnitude of the A_1 peak in figure 5.7 (a) is greater than that of A_2. This likely results from the increased production of secondary electrons between $0.7 \leq \omega t/2\pi \leq 0.9$. The increased electron flux into the plasma bulk during interval C necessitates a larger electron flux out of the bulk during sheath collapse at A_1, resulting in the increased ionisation.

Peak C is observed between $0.7 \leq \omega t/2\pi \leq 0.9$, coenciding with the phases of most negative dielectric potential in figure 5.7 (c) and hence represents ionisation from energetic secondary electrons, accelerated through the full sheath potential. Note that while only the phase-averaged direct secondary ionisations are shown here, phase-resolved indirect effects from secondary electrons can be seen through electron-electron collisions and as secondary electrons 'relax' back into the bulk population when their energy drops below 3 eV [165]. The phase-independent 'background' secondary electron ionisation is observed adjacent to the powered electrode between 18 mm $\leq Z \leq$ 24 mm. This corresponds to the spatial extent of the most negative dc self-bias voltage, see figure 3.7 (b), and region of highest radial ion flux, see figure 3.8 (b), confirming the previous assertion that this 'background' ionisation arises from the phase-independent release of secondary electrons arising from radial ion bombardment.

The phase-resolved ionisation dynamics for $\theta = 270°$ are shown in figure 5.7 (b), where the reduction in the dc self-bias voltage is exhibited as a larger difference between the electrode potential and dielectric potential in figure 5.7 (d). Here, the $\theta = 270°$ voltage waveform exhibits positive amplitude asymmetry, i.e. the magnitude of the most positive amplitude $\omega t/2\pi \approx 0.2$ is greater than the magnitude of the most negative amplitude $\omega t/2\pi \approx 0.95$. This alters the ionisation structures in figure 5.7 (b) substantially, notably through an increased secondary electron 'background' ionisation and a relative increase in ionisation during sheath collapse between $0.21 \leq \omega t/2\pi$ 0.27, (peak A). The increase in sheath collapse heating arises due to the reduced fraction of the rf phase cycle for which the sheath is collapsed, as previously described with reference to figures 5.4 (b) and 5.6. This results in a larger radial electron flux at the powered electrode (region 2) and consequentially a larger axial electron flux towards the powered electrode (regions 1 and 3).

To more clearly illustrate the change in the electron heating mechanisms with varying phase offset, the ionisation dynamics have been spatially integrated to produce figure 5.8. Here, the combined 'bulk' and secondary electron Ar^+ ionisation rates ι_{tot} are shown for odd-even ($k = 1, 2$) and odd-odd ($k = 1, 3$) dual-frequency operation at 900 V_{pp} (450 V) for varying phase offset are shown with respect to applied voltage phase in figures 5.8 (a) and (b), respectively.

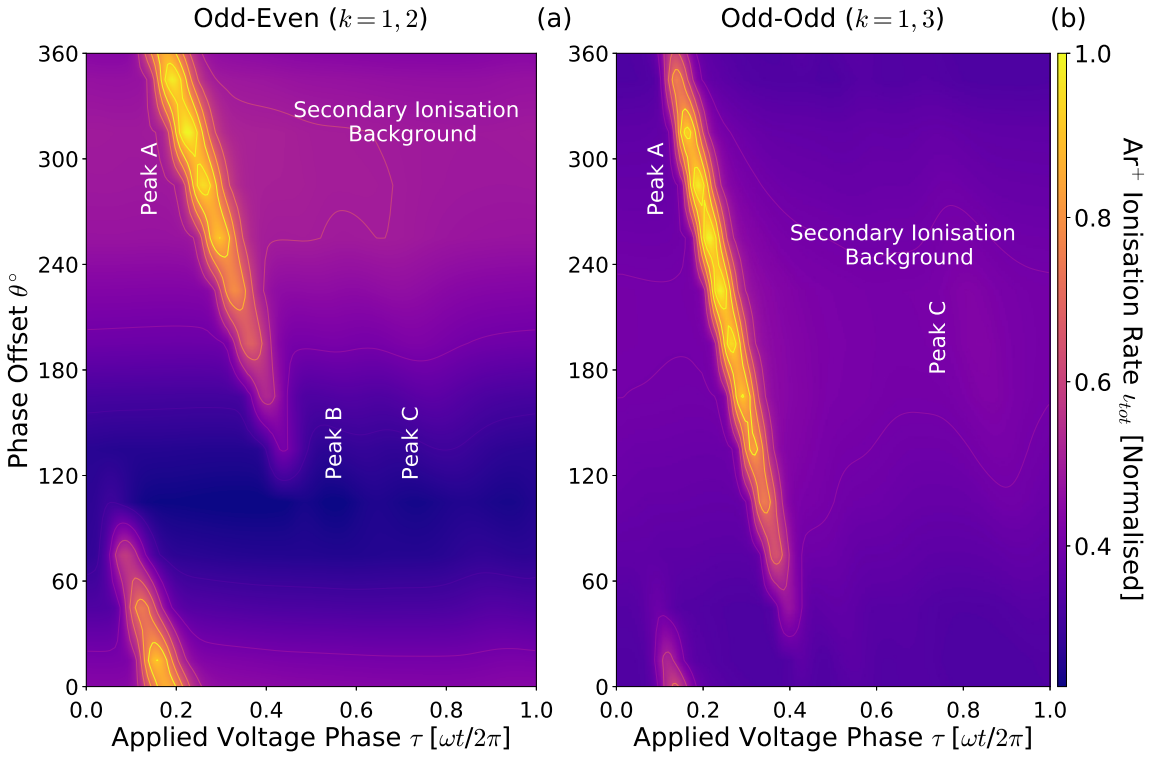

Figure 5.8: Simulated, spatially integrated, phase-resolved 'bulk' ionisation rate $\iota_\alpha(\tau)$ and phase-averaged secondary ionisation rate ι_γ for (a) odd-even ($k = 1, 2$) and (b) odd-odd ($k = 1, 3$) dual-frequency operation at 900 V_{pp} (450 V) for varying upper harmonic phase-offset. Plenum pressure of 200 Pa (1.5 Torr) argon, 13.56 MHz - 27.12 MHz, V_{pp} = 900 V (450 V), wall temperature 325 K.

The variation in the secondary electron background ionisation is readily observed in figures 5.8 (a) and (b), reaching a maximum between phase offsets of $270° \leq \theta \leq 300°$, for odd-even ($k = 1, 2$) operation and between $150° \leq \theta \leq 210°$, for odd-odd ($k = 1, 3$) operation. These correlate with the most negative dc self-bias voltages for the odd-even and odd-odd voltage waveforms, shown previously for phase offsets of $\theta = 270°$ and $\theta = 180°$, respectively. Direct control of the dc self-bias voltage afforded by the odd-even waveforms results in a greater modulation in the maximum total ionisation rate, varying by 62% (1.9×10^{24} - 5.0×10^{24} m^{-3} s^1) as compared to only 23% (3.7×10^{24} - 4.8×10^{24} m^{-3} s^1) for odd-odd waveforms. This reflects the higher absolute steady-state Ar^+ densities achieved for odd-even operation, shown previously in figure 5.5 (b).

In addition to the background ionisation, three further ionisation structures are visible in figures 5.8 (a) and (b). Previously identified as arising from heating during sheath collapse (peak A), heating during sheath expansion (peak B) and heating via secondary electron impacts (peak C). Varying the phase offset alters both the relative magnitude of the observed ionisation mechanisms and the phase at which they occur. Increasing the phase offset results in ionisation structures occurring later in the rf phase-cycle, as would be expected. A high degree of control over the electron heating mechanisms is achievable as evidenced

by an approximately 70% reduction in the total ionisation rate associated with sheath collapse heating (peak A) for odd-even ($k = 1, 2$) waveforms employing phase offsets between $90° \leq \theta \leq 150°$ in figure 5.8 (a). This arises due to the aforementioned increase in the fraction of the rf phase cycle for which the sheath is collapsed, and therefore represents control of the phase-resolved sheath dynamics. A lesser degree of control is observed for odd-odd ($k = 1, 3$) waveforms in figure 5.8 where sheath collapse heating is reduced by only 30% over a smaller range of phase offsets between $30° \leq \theta \leq 60°$. This reduction in the control arises from the generally narrower timescale over which the sheath is collapsed for odd-odd operation, owing to the higher frequency 40.68 MHz second harmonic adding constructively with the fundamental 13.56 MHz harmonic for a shorter period of the rf cycle as compared to 27.12 MHz.

Dual-frequency waveforms therefore achieve control of the ionisation dynamics in tandem through varying the phase-resolved sheath dynamics, and hence the electron fluxes during α-mode heating, but also through modulation of phase-averaged properties, i.e. the dc self-bias voltage, via the electrical asymmetry effect. This differs from the control achieved with single frequency operation, where varying voltage at a fixed frequency predominately affects the dc self-bias, see figure 3.8 (a), while varying the applied frequency at a fixed voltage predominately affects the phase-resolved sheath dynamics, resulting in the observed γ - α transition in figure 4.2 (a). Multi-frequency operation therefore provides the unique capability to alter both the phase-averaged and phase-resolved discharge properties in real time, enhancing the control over the ionisation and power deposition mechanisms.

5.4 Application of Higher Harmonic Dual-Frequency Components

Control of the phase-resolved ionisation dynamics via dual-frequency phase offset has been demonstrated for odd-even ($k = 1, 2$) and odd-odd ($k = 1, 3$) dual-frequency waveforms through varying the phase-resolved sheath extent and the phase-averaged dc self-bias voltage. This section furthers investigates changes to the IEDFs incident upon material surfaces within the *Pocket Rocket*, when operated employing dual-frequency voltage waveforms with varying phase offset. Following this, the application of dual-frequency waveforms employing a higher fundamental frequency and larger harmonic separations between the component frequencies will be addressed. Finally, expanding upon the work performed in chapter 4, the capability to produce and control structured IEDFs through dual-frequency phase offset is investigated.

5.4.1 Control of Ion Energy Distribution Functions

Previously, control of the IEDF was demonstrated for varying applied voltage frequencies through reducing the difference between the phase-averaged sheath extent and the Ar - Ar+ mean-free-path, see figure 4.9. For dual-frequency operation the phase-averaged sheath extent has been shown to be approximately invariant with varying phase-offset. Control of the IEDF will therefore be achieved through varying the sheath potential, via the imposed electrical asymmetry. The Ar^+ IEDFs incident on the radial wall at region 2 (R,Z = 2.1 mm, 21 mm) are shown in figures 5.9 (a) and (b) for operation employing odd-even ($k = 1, 2$) and odd-odd ($k = 1, 3$) dual-frequency voltage waveforms, respectively.

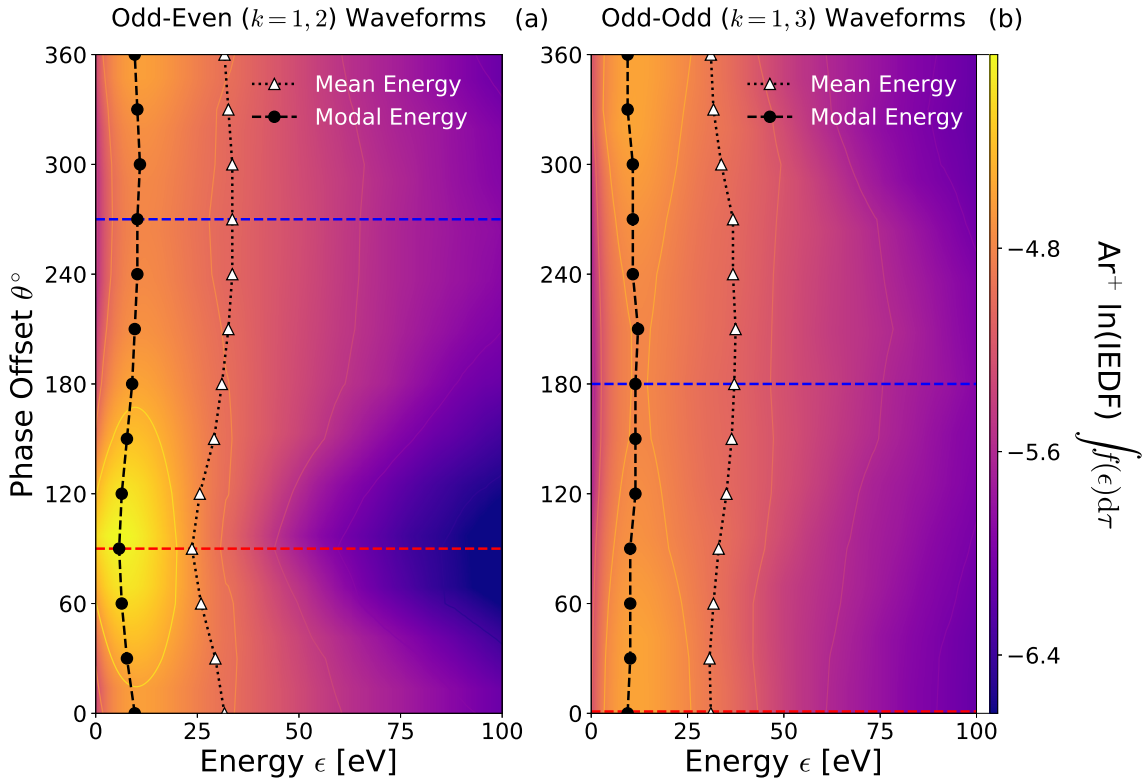

Figure 5.9: Phase-averaged Ar^+ incident upon the radial wall adjacent to the powered electrode (R,Z = 2.1 mm, 21 mm) for (a) odd-even ($k = 1, 2$) and (b) odd-odd ($k = 1, 3$) dual-frequency voltage waveforms. Mean and modal Ar^+ ion energies are denoted by the dashed black and dotted white lines, respectively. Phase offsets corresponding to the most positive and negative dc self-bias voltages are denoted by the red and blue dash-dotted lines, respectively, see figure 5.5 (a). Plenum pressure of 200 Pa (1.5 Torr) argon, V_{pp} = 900 V (450 V), wall temperatures 325 K.

The IEDFs presented in figures 5.9 (a) and (b) exhibit a Maxwellian-like distribution for all applied phase offsets, where the majority of ions impact the alumina wall at energies below the mean energy. For odd-even ($k = 1, 2$) voltage waveforms, increasing the phase offset from $\theta = 90^\circ$ to $\theta = 270^\circ$ achieves a 30% modulation in the mean Ar^+ energy, between 23.7 eV to 33.6 eV, and a 47% modulation in the modal Ar^+ energy, from 5.8 eV to 10.9 eV. Meanwhile, the sheath potential increases by 56% from 194 V to 303 V, see figure 5.4 (c). A reduced degree of control is afforded by odd-odd ($k = 1, 3$) voltage waveforms, shown in figure 5.9 (b), which achieve modulations of only 18% and 22% for the mean and modal Ar^+ energies for respectively. For both odd-even ($k = 1, 2$) and odd-odd ($k = 1, 3$) voltage waveforms, the largest increase in the mean ion energy coincides with the phase offset resulting in the most negative dc self-bias voltage, and therefore greatest sheath potential.

The disparity between the modulation in the sheath potential ($\Delta\phi_S$ =109 V for $k = 1, 2$) and the modulation in the mean Ar^+ energy ($\Delta\hat{\epsilon}_{Ar^+} = 9.9$ eV for $k = 1, 2$) with varying phase offset arises as ions lose the majority of their energy via ion-neutral charge-exchange collisions as they transit through the sheath. Recall, however, that the ion-neutral charge

exchange cross-section reduces with increasing ion energy[101], and that excessively high mean ion energies actually reduce the neutral gas heating efficiency, see figure 5.16 (a). However, for sufficiently collisional discharges, the reduction in the cross-section with increasing Ar^+ energy is secondary to the increased energy transferred in an average collision, resulting in the increased neutral gas heating efficiencies observed in figure 5.16 (b). Therefore, dual-frequency operation enables fine-tuning of the Ar^+ energy, optimising the increasing energy transferred per ion-neutral collision against the reducing collision rate for a given set of operating conditions.

The mean Ar^+ energy and associated ion-neutral collision cross-section adjacent to the powered electrode at region 2 (R,Z = 2.1 mm, 21 mm) are shown with respect to phase offset in figures 5.10 (a) and (b), respectively. The resulting Ar - Ar^+ mean-free-paths, calculated at the powered sheath edge, are shown in figure 5.10 (c).

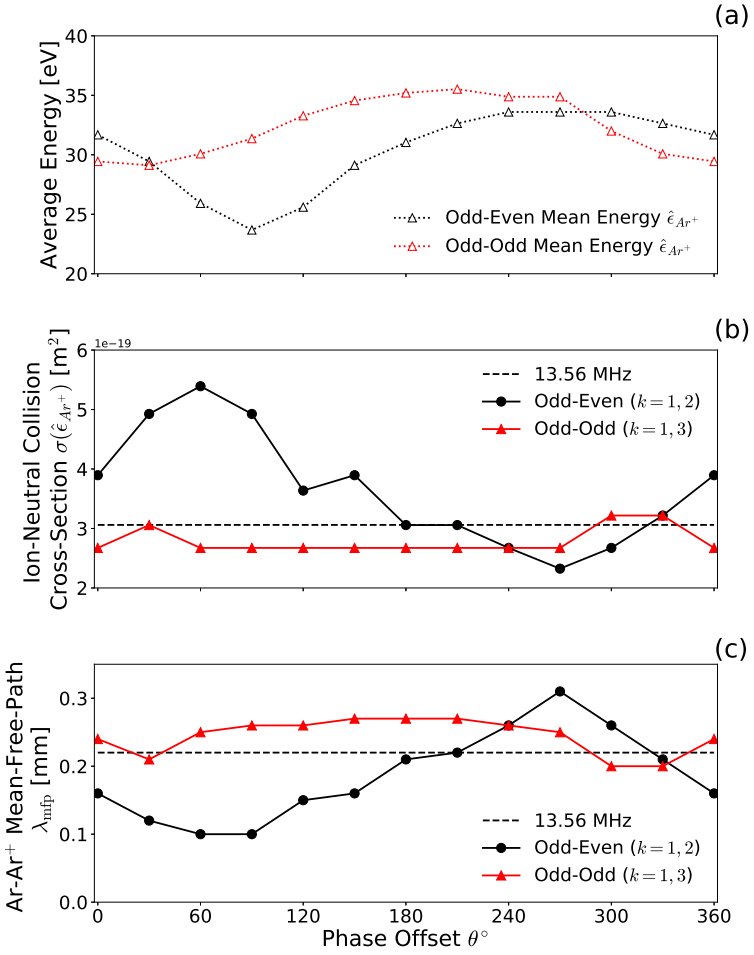

Figure 5.10: Phase averaged (a) mean Ar^+ energies $\hat{\epsilon}_{Ar^+}$, (b) ion-neutral collision cross-sections $\sigma(\hat{\epsilon}_{Ar^+})$ and (c) Ar - Ar^+ mean-free-paths λ_{mfp} adjacent to the powered electrode (R,Z = 2.1 mm, 21 mm) with respect to phase offset for 900 V_{pp} (450 V) odd-even ($k = 1, 2$) and odd-odd ($k = 1, 3$) dual-frequency operation. Plenum pressure of 200 Pa (1.5 Torr) argon, V_{pp} = 900 V (450 V), wall temperatures 325 K.

The mean Ar^+ energies in figure 5.10 (a), taken from figure 5.9 (a), exhibit an approximately sinusoidal variation with varying phase-offset, in proportion to the sheath potential as discussed previously. Phase offsets resulting in larger sheath potentials result in a greater ion acceleration through the sheath, increasing the mean ion energy and reducing the ion-neutral collision cross-section, shown in figure 5.10 (b). Here, the Ar - Ar^+ collision cross sections are calculated employing ion energies at the phase-averaged sheath extent, where the energy resolved cross-section is as shown previously in figure 4.6 (c), originally obtained from Ref. 199. The ion-neutral collision cross-section varies in inverse proportion to the mean ion energy within the sheath, being modulated by 57% and 17% for odd-even ($k = 1, 2$) and odd-odd ($k = 1, 3$) waveforms, respectively. Further, the ion-neutral collision cross-section varies in direct proportion to the thermal efficiency, see figure 5.16 (c). A higher ion-neutral cross-section leads to a higher ion-neutral charge exchange collision rate, and therefore, all else being equal, more effectively thermalises the ion and neutral populations, leading to a more efficient transfer of power.

Note however, that the ion-neutral collision cross-section varies in inverse proportion to the neutral gas temperature, see figure 5.15 (c), where for $\theta = 270°$ odd-even ($k = 1, 2$) voltage waveforms the minimum ion-neutral cross section corresponds to the maximum on-axis neutral gas temperature. This relationship arises from two factors: (1), the increased Ar^+ density arising from the enhanced secondary ionisation rate discussed in section 5.3.2 counteracts the reduced cross-section, maintaining the ion-neutral collision frequency. And (2), the increased Ar^+ mean-free-path, shown in figure 5.10 (c), results in ions being accelerated to higher energies before undergoing a collision, therefore each ion-neutral collision transfers a greater amount of energy into the neutral population. While these effects result in enhanced neutral gas heating and higher on-axis temperatures, a larger fraction of ions pass through the sheath without undergoing a collision, evidenced by the larger mean Ar^+ energy incident upon the alumina wall, leading to more inefficient neutral gas heating.

In summary, the trends observed in figures 5.10 (b) and (c) indicate that ion-neutral momentum transfer is most efficient for a higher number of less energetic collisions, i.e. the thermal efficiency can be optimised by selectively choosing low ion energies. Note that the highest neutral gas temperatures are still expected for conditions selectively choosing the highest ion energy, as the energy transferred in each ion-neutral collision scales with the ion velocity squared, while the reduction in ion-neutral cross section scales approximately linearly with ion velocity over the range 1 - 1000 eV. Selective control of the ion energy therefore provides a mechanism to directly control the efficiency of the ion-neutral momentum transfer via modulation of the imposed EAE altering the phase-averaged sheath potential. Note that this control is primarily localised to the sheath and, to a lesser extent, the pre-sheath regions, while ion-neutral cross-sections and collision rates within the bulk remain predominately unaffected.

5.4.2 Enhanced Control of IEDF via Increased Fundamental Harmonic

The dual-frequency voltage waveforms investigated thus-far have employed the fundamental 13.56 MHz voltage frequency and either the first or second harmonic. While the application of higher harmonics has been shown to enable control of the shape of the IEDF, described in chapter 4, an increased harmonic separation between the dual-frequency components results in a reduced symmetry parameter ϵ_s and hence a reduced EAE, see figure 5.3. To mitigate this effect, both the fundamental frequency and first harmonic are scaled to produce integer multiples of the odd-even ($k = 1, 2$) voltage waveform.

Here, figures 5.11 (a), (b) and (c) show the Ar^+ IEDF incident upon the alumina wall adjacent to the powered electrode (R,Z = 2.1 mm, 21 mm) for three ϕ_0 = 900 V (450 V) odd-even dual-frequency waveforms comprised of 27.12 MHz & 54.24 MHz ($k = 2, 4$), 40.68 MHz & 81.36 MHz ($k = 3, 6$), and 54.24 MHz & 108.48 MHz ($k = 4, 8$), respectively, with varying upper harmonic phase offsets. Odd-even waveforms were chosen as they maximise the applied EAE and have been demonstrated to provide the greatest degree of control over the IEDF, as shown in figure 5.9 (a).

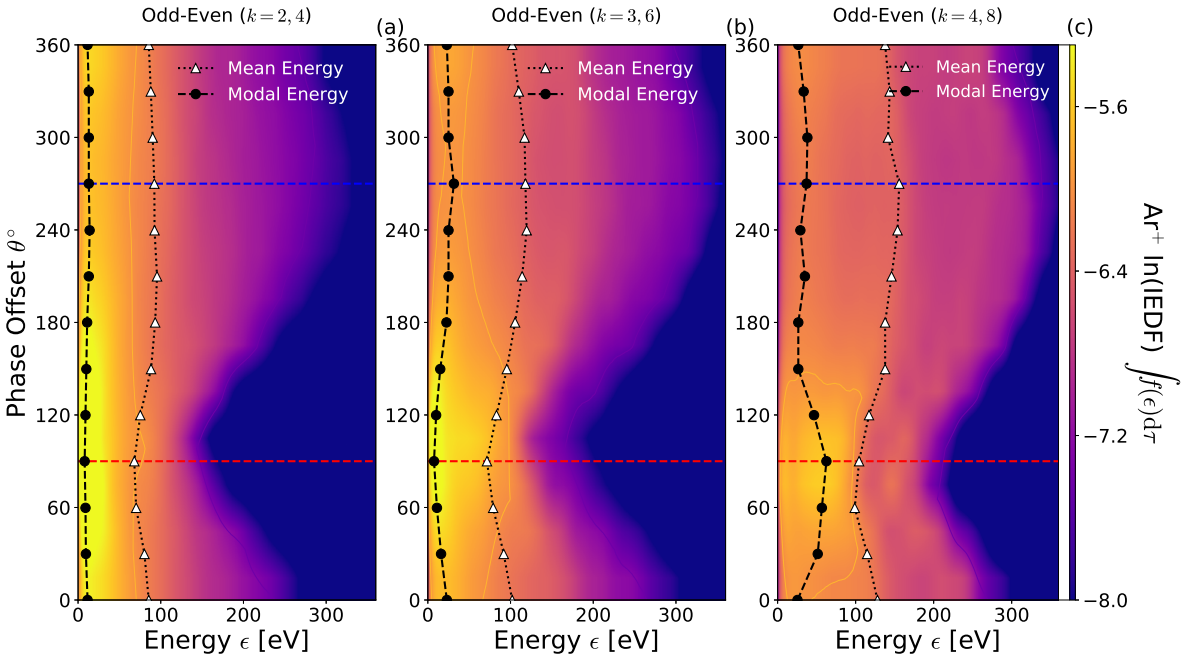

Figure 5.11: IEDFs incident upon the alumina wall adjacent to the powered electrode (R,Z = 2.1 mm, 21 mm) for odd-even dual-frequency waveforms comprising frequencies of (a) 27.12 MHz & 54.24 MHz ($k = 2, 4$), (b) 40.68 MHz & 81.36 MHz ($k = 3, 6$), and (c) 54.24 MHz & 108.48 MHz ($k = 4, 8$). Phase offsets resulting in the most positive and negative dc self-bias voltages are denoted by the red and blue dashed lines, respectively. Plenum pressure of 200 Pa (1.5 Torr) argon, V_{pp} = 900 V (450 V), wall temperatures 325 K.

The mean and modal Ar^+ ion energies for the odd-even ($k = 2, 4$) and ($k = 3, 6$) waveforms, shown in figures 5.11 (a) and (b), exhibit a similar sinusoidal variation with phase

offset as seen previously, varying in proportion to the magnitude of the dc self-bias voltage. Increasing the fundamental harmonic for a fixed applied voltage increases the deposited power, reduces the phase-averaged sheath width and results in increased mean and modal Ar^+ ion energies for all phase offsets, as compared to lower applied harmonics. The degree of control afforded over the mean Ar^+ ion energy increases with increasing fundamental harmonic, where $\hat{\epsilon}_{Ar^+}$ is modulated by 30% (23.7 - 33.6 eV), increasing to 40% (68 - 95.5 eV) and 67% (71.5 - 119.5 eV) for $(k = 1, 2)$, $(k = 2, 4)$ and $(k = 3, 6)$ voltage waveforms, respectively. Similar trends are observed for modulations in the modal ion energy, increasing from 47% (5.8 - 10.9 eV) to 75% (8 - 14 eV) and to 320% (7.5 - 31.5 eV) for $(k = 1, 2)$, $(k = 2, 4)$ and $(k = 3, 6)$ voltage waveforms, respectively. The significant increase in modulation observed for $(k = 3, 6)$ voltage waveforms arises due to a broadening of the low energy peak for phase offsets between $210° \leq \theta \leq 360°$, discussed in more detail in figure 5.12.

Operation employing $(k = 4, 8)$ voltage waveforms, shown in figure 5.11 (c), exhibits a break in the trends observed for $k = 1, 2$ to $k = 3, 6$ waveforms. Here the mean and modal Ar^+ ion energies are modulated by, 58% (93 - 147 eV) and 146% (24 - 59 eV), respectively, representing a decrease in the control afforded through phase offset. Notably, while the peak mean Ar^+ energy is observed for a phase offset of $\theta = 270°$, agreeing with previous results, the peak modal Ar^+ energy is observed for $\theta = 90°$, distinct from previous results. Further, the mean Ar^+ ion energy closely follows a 'ridge' separating a low energy plateau ($\approx 0 - 150\ eV$) from a high energy plateau ($\geq 160\ eV$). This behaviour represents the emergence of structured IEDFs, similar to those previously observed in chapter 4. The emergence of structured IEDFs presents further potential control mechanisms, in addition to the modulation in the mean and modal Ar^+ ion energies afforded via the EAE.

To further investigate the emergence of structured IEDFs in high fundamental frequency dual-frequency discharges, the IEDFs incident upon the alumina wall adjacent to the powered electrode (R,Z = 2.1 mm, 21 mm) have been plotted in figure 5.12 for six $\phi_0 = 900$ V (450 V) odd-even waveforms of varying fundamental harmonic between $k = 2, 4$ to $k = 4, 8$, for phase offsets of $\theta = 90°$ and $\theta = 270°$, representing the most positive and most negative dc self-bias voltages, respectively.

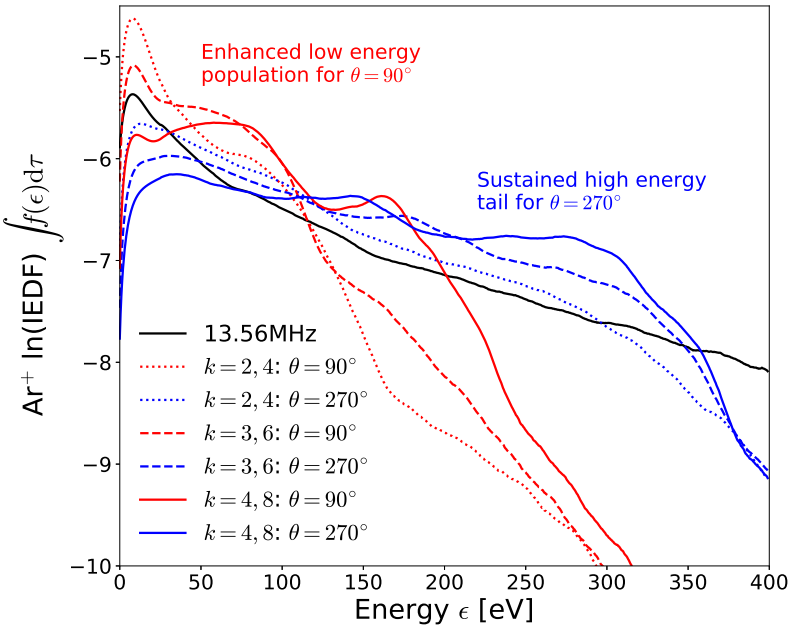

Figure 5.12: IEDFs incident upon the alumina wall adjacent to the powered electrode (R,Z = 2.1 mm, 21 mm) for odd-even waveforms of varying fundamental harmonic between $k = 2, 4$ to $k = 4, 8$, for phase offsets of $\theta = 90°$ and $\theta = 270°$. IEDFs plotted in red correspond to $\theta = 90°$, while those in blue correspond to $\theta = 270°$, representing phase offsets resulting in the most positive and most negative dc self-bias voltages, respectively. The IEDF resulting from 13.56 MHz operation is denoted by the black line for comparison. Plenum pressure of 200 Pa (1.5 Torr) argon, $V_{pp} = 900$ V (450 V), wall temperatures 325 K.

The shape of the IEDFs presented in figure 5.12 vary significantly with respect to the applied phase offset. While all of the IEDFs can be generally described as 'Maxwellian-like', possessing a dominant low-energy population with a high energy tail, the precise energy range and relative magnitude of these two components exhibits substantial variation over the range of phase offsets $0° \leq \theta \leq 360°$.

Phase offsets resulting in more positive dc self-bias voltages, $0° \leq \theta \leq 180°$, produce IEDFs exhibiting an enhanced low energy ($\lessapprox 150$ eV) Ar^+ ion population. For $k = 1, 2$ (not shown), $k = 2, 4$ and $k = 3, 6$ dual-frequency voltage waveforms, this is observed as a narrow low-energy peak centred at approximately 20 eV. For $k = 4, 8$ dual-frequency operation, an additional, broad, low-energy structure is observed between $\approx$ 25 - 100 eV, resulting in the enhanced modal ion energies observed between $30° \leq \theta \leq 120°$ previously in figure 5.11.

Phase offsets resulting in a more negative dc self-bias voltages, $180° \leq \theta \leq 360°$, produce IEDFs exhibiting an enhanced high energy Ar^+ population, observed as a flattening of the high energy tail. The degree to which the high energy tail is sustained increases proportionally with the fundamental harmonic. For example a $k = 4, 8$, $\theta = 270°$ dual-frequency voltage waveform produces an approximately flat high energy plateau between $\approx$ 160 - 300 eV, in contrast to the narrow $\approx$ 170 eV peak observed for $k = 4, 8$, $\theta = 90°$. The IEDFs for both $\theta = 90°$ and $\theta = 270°$ also exhibit a sharper drop off in the ion

population beyond either the low energy peak or high energy plateau as compared to the approximately linear decrease in ion population for single frequency operation at 13.56 MHz.

Varying the phase offset enables access to a wide range of IEDF shapes, bounded between the most positive and most negative achievable dc self-bias voltages (red and blue lines) for a given fundamental harmonic. Increasing the fundamental harmonic for a fixed phase offset increases both the upper and lower energy bounds and enables flatter IEDFs, resulting in higher mean and modal ion energies, see figure 5.11. This increased selectivity enables tailoring of the ion energies to optimise the ion-neutral charge exchange collision rate in electrothermal propulsion. Further, varying the phase-offset has been demonstrated to modulate the dc self-bias voltage and resulting radial ion flux adjacent to the powered electrode in figure 5.5, influencing the maximum neutral gas temperature. The extent to which the ion flux and ion energy can be decoupled therefore influences the extent to which the maximum neutral gas temperature and maximum thermal efficiency can be decoupled.

This decoupling is presented in figure 5.13 where the mean Ar^+ ion energy and radial Ar^+ ion flux are plotted for discharges employing six $\phi_0 = 900$ V (450 V) odd-even and odd-odd dual-frequency waveforms of varying fundamental harmonic between $k = 1, 2$ to $k = 4, 8$ with upper harmonic phase offsets between $0° \leq \theta \leq 360°$.

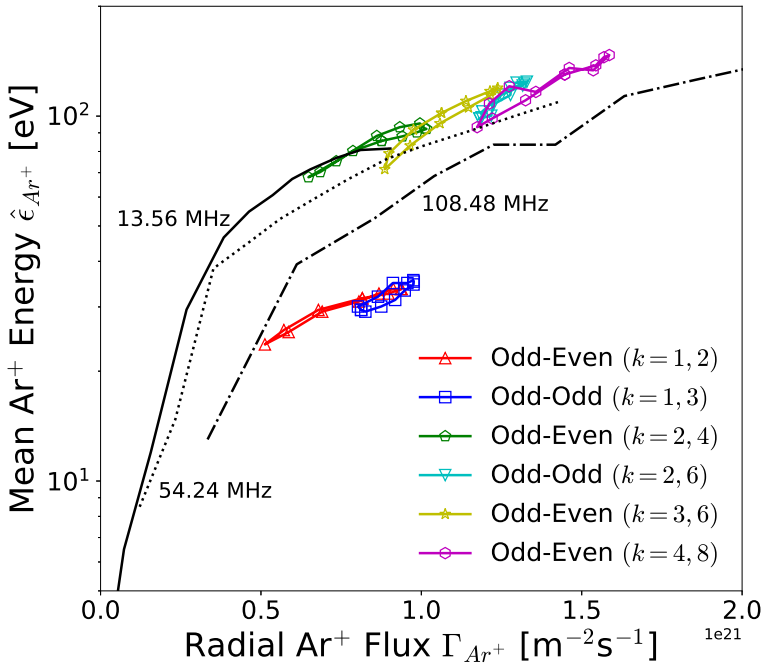

Figure 5.13: Ion energies incident upon the radial wall adjacent to the powered electrode (R,Z = 2.1 mm, 21 mm) with respect to ion flux at the same location for varying phase offset employing odd-even ($k = 1, 2$, $k = 2, 4$, $k = 3, 6$, $k = 4, 8$) and odd-odd ($k = 1, 3$, $k = 2, 6$) dual-frequency voltage waveforms. Single frequency curves are obtained from data underpinning figure 4.8. Plenum pressure of 200 Pa (1.5 Torr) argon, $V_{pp} = 900$ V (450 V), wall temperatures 325 K.

For discharges employing a single voltage frequency in figure 5.13, the ion energy and ion flux are co-dependant, i.e. increasing the applied voltage amplitude necessarily increases both the energy and flux, this agrees with previous findings presented in 1.12 from Ref. 105. In contrast, discharges employing dual-frequency voltage waveforms exhibit a range of ion energy/flux combinations for a single applied voltage amplitude. Varying the phase offset 'rotates' the ion energy/flux combination clockwise in an approximately elliptical shape about a central point, determined by the harmonic composition and voltage amplitude of the dual-frequency voltage waveform. Focusing on dual-frequency voltage waveforms employing a 13.56 MHz fundamental harmonic ($k = 1, 2$, $k = 1, 3$), it can be seen that the odd-even ($k = 1, 2$) waveform exhibits a greater range of attainable ion energies and fluxes as compared to the odd-odd waveform ($k = 1, 3$). The extent to which the ion energy and ion flux are decoupled remains approximately constant with varying fundamental harmonic, noting that fundamental harmonics above 13.56 MHz exhibit generally higher mean Ar^+ energies due to the increased power deposition and narrower sheath extents.

From figures 5.12 and 5.13 it can be seen that dual-frequency voltage waveforms offer a unique degree of control over ion dynamics as compared to single frequency voltage waveforms. Crucially, the results presented in figure 5.13 demonstrate the capacity for dual-frequency voltage waveforms to optimise the radial ion flux for a given ion energy, or visa-versa. For electrothermal applications this translates into the capability to selectively optimise both the thermal efficiency, via the mean Ar^+ energy, and the maximum neutral gas temperature, via the radial Ar^+ flux. Investigating to what extent these parameters can be independently optimised, and the ultimate impact on the thrust and specific impulse of the *Pocket Rocket* microthruster, forms the basis of sections 5.5.1 and 5.5.2.

5.5 Control of Ion Power Deposition and Neutral Heating

The control afforded by dual-frequency voltage waveforms on the ionisation dynamics, ion acceleration and resulting IEDF within the *Pocket Rocket* microthruster have been discussed. This section will address how these changes affect the spatial power deposition into charged species, and the extent to which this power is transferred into the neutral gas, specifically with regards to neutral gas temperature and neutral flow velocity. The prospect of variable thrust and specific impulse operation for plasma thrusters employing dual-frequency waveforms is discussed, with reference to lab based and space based operating conditions.

5.5.1 RF Power Deposition Pathways

The ion power fraction, defined as the ratio between power deposited into Ar^+ and the total rf-power deposited, has been shown to vary with increasing applied voltage frequency and amplitude, see figures 4.5 and figure 5.14 (a) respectively. In the former example, the inability of ions to respond to the high voltage frequencies results in the fractional ion power deposition reduces with increasing applied frequency, the excess power being deposited into the highly mobile electrons. In the latter the increasing proportion of the dc self-bias voltage to the applied voltage, results in an increased the fractional ion power deposition arising from a higher radial phase-averaged electric field. As the dual-frequency waveforms discussed in this chapter posses elements from both of these previous examples, the degree of control afforded is not immediately obvious.

The ion power fraction is shown with respect to applied voltage for a single frequency, 13.56 MHz discharge in figure 5.14 (a) and with respect to phase offset for 900 V_{pp} (450 V) odd-even ($k = 1, 2$) and odd-odd ($k = 1, 3$) dual-frequency voltage waveforms, in figures 5.14 (b) and (c), respectively. The total power deposited and ion power fraction for 13.56 MHz operation at 900 V_{pp} (450 V) is denoted in figures 5.14 (b) and (c) by the dashed line for comparison.

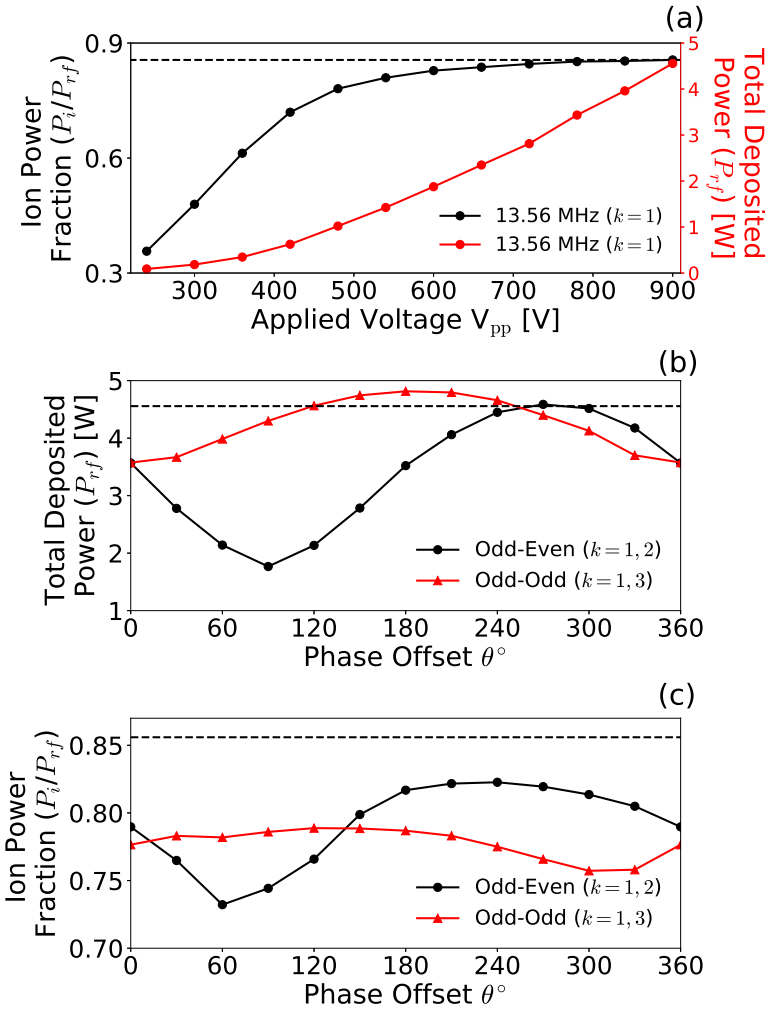

Figure 5.14: Ion power fraction for (a) single frequency operation at 13.56 MHz with respect to applied voltage as compared to (b) the total power deposited and (c) the ion power fraction for operation employing odd-even ($k = 1, 2$) and odd-odd ($k = 1, 3$) dual-frequency voltage waveforms with respect to phase offset. The dashed lines on (a) and (b) represent the total power deposition and ion power fraction for 13.56 MHz operation at 900 V_{pp} (450 V). Plenum pressure 200 Pa (1.5 Torr) argon, V_{pp} = 900 V (450 V), wall temperature 325 K.

For single frequency operation at 13.56 MHz the ion power fraction increases with respect to the applied voltage as shown in figure 5.14 (a). The ion power fraction increases in proportion with the magnitude of the dc self-bias voltage, which also exhibits the greatest proportionality to applied voltage between 240 - 600 V_{pp} (120, 300 V). This illustrates that the maximum ion power fraction achievable in the *Pocket Rocket* through varying the dc self-bias voltage plateaus at approximately 86% of the total deposited power by 900 V_{pp} (450 V). Since the total deposited power continues to increase with increasing applied voltage, this plateau represents approximately equal power deposition between electrons and ions for increasing applied voltage in γ -mode, above $\approx$ 720 V_{pp} (360 V).

The total rf power deposited for dual-frequency operation in figure 5.14 (b) varies with

respect to the phase offset for both odd-even ($k = 1, 2$) and odd-odd ($k = 1, 3$) waveforms. For the odd-even ($k = 1, 2$) waveforms the total rf power deposited varies between $1.8 \leq P_{rf} \leq 4.6$ W, in proportion to the dc self-bias voltage, and therefore primarily arises from the altered electrical asymmetry. Note that the power deposited for odd-even dual-frequency operation is typically below that of 13.56 MHz operation due to the slightly reduced dc self-bias magnitude. In contrast, the $3.6 \leq P_{rf} \leq 4.8$ W power variation observed for odd-odd ($k = 1, 3$) waveforms is accounted for by recalling that although $\phi_0 = 900$ V is maintained when creating the waveform harmonics, the peak-to-peak voltage of the resulting dual-frequency waveform is typically slightly lower due to destructive interference, see figure 5.1. In both cases, the ultimate effect is to increase the sheath potential adjacent to the powered electrode, resulting in enhanced ion and secondary electron acceleration through the powered electrode sheath. Finally, note that due to the higher voltage specific power deposition of the 40.68 MHz component as compared to the 27.12 MHz component the power deposited via odd-odd waveforms is typically higher than that of the odd-even waveforms.

The ion power fractions shown in figure 5.14 (c) for 900 V_{pp} (450 V) operation, vary in direct proportion to the magnitude of the dc self-bias voltage, as expected from previous findings at 13.56 MHz. The greatest degree of control over the ion power fraction is achieved for odd-even ($k = 1, 2$) voltage waveforms where the ion power fraction varies by 10%, compared with only a 3% modulation for the odd-odd ($k = 1, 3$) voltage waveforms. The degree of control increases for lower applied voltage amplitudes (not shown), where modulations of 20% and 6% were achieved for 600 V_{pp} (300 V) odd-even ($k = 1, 2$) and odd-odd ($k = 1, 3$) voltage waveforms, respectively, albeit for reduced absolute power depositions.

Finally, note that the up-moderated section of the ion power fraction ($180° \leq \theta \leq 300°$) is 'flatter' than the down-moderated section ($0° \leq \theta \leq 150°$). This is mirrored in the dc self-bias voltage shown previously in figure 5.5 (a). This asymmetry arises due to the constructive - destructive interaction between the change in peak-to-peak voltage and change in the EAE with varying phase offset, see figures 5.3 and 5.1, respectively. For phase offsets between $0° \leq \theta \leq 180°$ both the symmetry parameter ϵ_s, i.e. the magnitude of the EAE, and the change in V_{pp} add constructively to reduce the dc self-bias voltage, and hence also the ion power fraction. The EAE reduces the magnitude of the dc self-bias voltage directly, while the reduced peak-to-peak voltage acts indirectly via a reduction in the powered to grounded sheath extent ratio, described previously with reference to figure 3.8 (a). However, for phase offsets between $180° \leq \theta \leq 360°$ the 'parity' of the symmetry parameter flips, resulting in a more positive dc self-bias voltage, while the contribution from the change in V_{pp} remains negative. This causes the EAE and change in V_{pp} to add destructively to the dc self-bias voltage, resulting in the more gradual change to the ion power fraction for these phase-offsets. This destructive interference also limits the maximum attainable ion power fraction for dual-frequency operation below that which would be expected from a single frequency

discharge of the same peak-to-peak voltage, as observed in figure 5.14 (c).

Figure 5.15 shows the radial power deposition into Ar^+ ions and electrons adjacent to the powered electrode (Z = 21 mm) and the resulting neutral gas temperature with respect to phase offset for odd-even ($k = 1, 2$) voltage waveforms. These waveforms were chosen as they had the largest effect on neutral gas temperature. Axially integrated ion P_i and electron P_e power densities, normalised to the maximum total rf power density occurring at $\theta = 270\,°$, are shown in figures 5.15 (a) and (b), with respect to phase offset. The corresponding ion power fraction and maximum on-axis neutral gas temperature are shown in figure 5.15 (c).

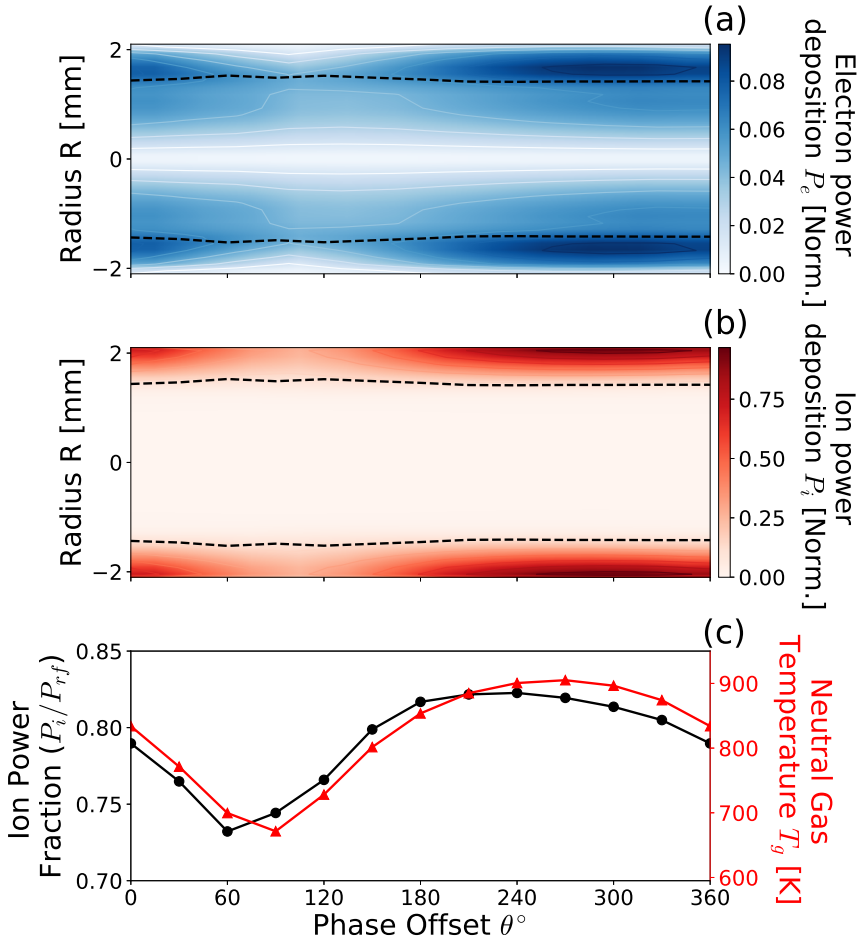

Figure 5.15: Phase-averaged, axially integrated (a) electron and (b) ion rf-power densities, normalised to the maximum total rf-power density at $\theta = 270°$ and (c) the ion power fraction and maximum on-axis neutral gas temperature with respect to phase offset $0° \leq \theta \leq 360°$. Axial integration in (a) and (b) is performed within the source tube between 13 mm $\leq Z \leq$ 37 mm. Phase-averaged sheath extents in (a) and (b) are denoted by the dashed lines. Plenum pressure 200 Pa (1.5 Torr) argon, odd-even ($k = 1, 2$) dual-frequency voltage waveform, $V_{pp} = 900$ V (450 V), wall temperature 325 K.

Power is deposited into electrons both within the sheath and the bulk plasma, as shown

in figure 5.15 (a). The increased electron power deposition within the sheath between $240° \leq \theta \leq 360°$ correlates with the increased ionisation due to secondary electrons observed previously in figure 5.8 (a). In contrast, power deposited close to the central axis of the *Pocket Rocket* exhibits negligible variation with varying phase offset and arises primarily from the axial electron flux towards the powered electrode during sheath expansion and collapse. As such, modulation in the electron power fraction is primarily attributed to the variation in the secondary electron emission, and subsequent acceleration, with varying radial ion flux. Note that, while volumetrically diffuse, the electron power deposition typically constitutes less than 20% of the total rf-power deposition.

The spatially-resolved ion power deposition is shown in figure 5.15 (b). Here power is almost exclusively deposited into Ar^+ ions within the sheath, denoted by the dashed lines. The ion power deposition varies in proportion to the sheath potential, and hence the magnitude of the dc self-bias voltage, as mentioned previously. This differs subtly from the mechanism observed for varying the applied voltage frequency, see figure 4.5, where the increased electric field arises from a reduced sheath width for constant sheath potential. As the sheath extent is approximately invariant with varying phase offset, the volume of plasma into which power is deposited remains approximately constant for dual-frequency operation.

The maximum on-axis neutral gas temperature and ion power fraction with varying phase offset for odd-even ($k = 1, 2$) operation are shown in figure 5.15 (c). The neutral gas temperature varies in proportion to the ion power fraction for both odd-even ($k = 1, 2$) and odd-odd ($k = 1, 3$) voltage waveforms (not shown). Here, a 10% modulation in the ion power fraction, normalised to the total deposited power, correlates with a 35% variation in the neutral gas temperature, from 671 K to 905 K for odd-even ($k = 1, 2$) operation. Note that the majority of this additional heating arises from the variation in the total deposited power, increasing from 1.77 W to 4.58 W from $\theta = 60°$ to $\theta = 270°$. However, as both the total deposited power and ion power fraction increase over this range of phase offsets, the effect is amplified, resulting in a higher degree of control over the resulting neutral gas temperature for odd-even ($k = 1, 2$) dual-frequency waveforms. This control is achieved at the expense of a slightly reduced maximum neutral gas temperature of 905 K as compared to 964 K for cold wall operation at 13.56 MHz, due to the aforementioned destructive interference.

In general the thermal efficiency of a closed system is defined as the ratio between the useful output work from a device W_{out}, in this case the work expended in increasing the neutral gas temperature, and the energy input E_{in} required to attain it, as defined in equation 5.5.

$$\eta_{th} = \frac{W_{out}}{E_{in}} \approx \frac{c_{Ar}\dot{m}_{Ar}\Delta T_g}{P_{rf}} \tag{5.5}$$

Here, ΔT_g is the change in neutral gas temperature, $c_{Ar} = 0.52$ J g^{-1} K^{-1} is the specific heat capacity for argon gas and $\dot{m}_{Ar}$ is the mass flow rate, where $\dot{m}_{Ar} = 29.7$ mg s^{-1} for

100 sccm of argon*. The thermal efficiency represents a useful metric for comparing variations in the degree of ion heating and ion-neutral charge exchange achieved for the range of operating conditions considered thus-far. Thermal efficiencies for 13.56 MHz operation with varying applied voltage and for operation with varying applied voltage frequency between 13.56 MHz $\leq \nu_{rf} \leq$ 108.48 MHz at V_{pp} = 900 V (450 V) are shown in figure 5.16 (a). For comparison, the thermal efficiencies employing odd-even ($k = 1, 2$) and odd-odd ($k = 1, 3$) dual-frequency voltage waveforms at V_{pp} = 900 V (450 V) with varying phase offset are shown in figure 5.16 (b). Wall temperatures are determined by employing the two-step method described in section 2.4.3 to better reflect steady-state operation efficiencies.

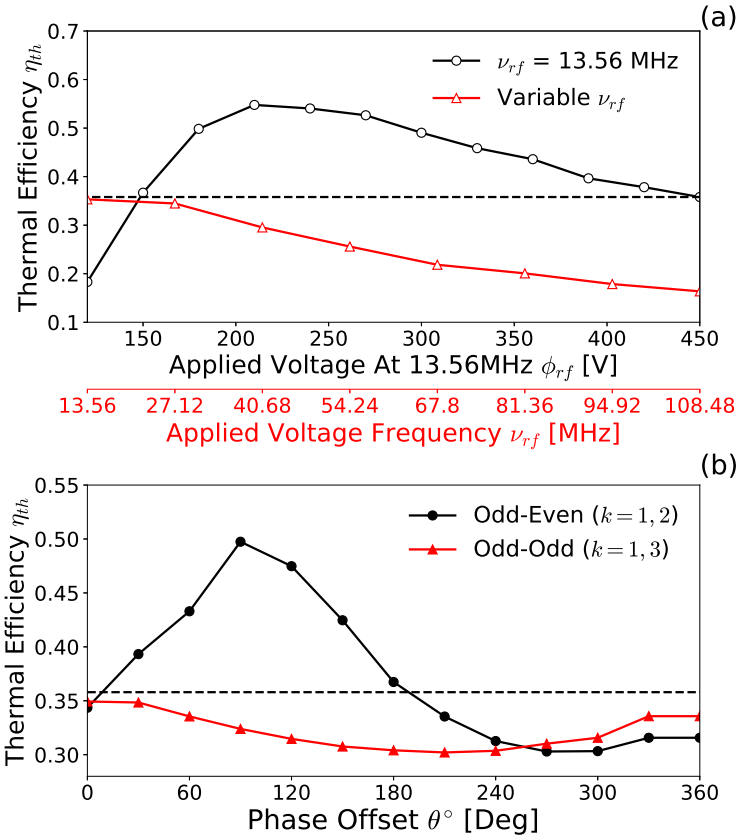

Figure 5.16: Thermal efficiencies for (a) varying applied voltage at 13.56 MHz and varying applied voltage frequency at V_{pp} =900 V (450 V) and (b) odd-even ($k = 1, 2$) and odd-odd ($k = 1, 3$) dual-frequency voltage waveforms with variable phase offset. The thermal efficiency for V_{pp} =900 V (450 V), 13.56 MHz operation is denoted by the dashed lines in (a) and (b), for comparison. Plenum pressure 200 Pa (1.5 Torr) argon, odd-even ($k = 1, 2$) dual-frequency voltage waveform, V_{pp} = 900 V (450 V), wall temperatures determined via the two-step method.

The thermal efficiency achieved for operation at 13.56 MHz varies from 19% to 36% over the range 240 - 900 V_{pp} (120 - 450 V), shown in figure 5.16 (a), reaching a maximum of

*ΔT_g is calculated relative to 'room temperature' (325 K), note that this will change for operation in space due to additional heating and cooling mechanisms including: (1) heating relative to the angle and presence of incident sunlight, (2) ohmic dissipation of heat from onboard electronics, (3) cooling via removal of latent heat of vaporisation upon conversion from liquid storage to gaseous propellant and (4) cooling through the subsequent PdV expansion into the source.

$\eta_{th} = 0.55$ for an applied voltage of 240 V, reducing thereafter. This trend in thermal efficiency is typical for electrothermal propulsion, where higher neutral temperatures and thrusts are achieved at the expense of reduced efficiency[16]. This typically arises as higher thermal efficiencies represent an increased degree of thermalisation between the electrostatically accelerated Ar^+ ions and the neutral gas, indicating effective collisional power transfer. Recall that the neutral gas temperature increases approximately linearly with applied voltage over this range, see figure 2.9. As discussed previously, increasing the neutral gas temperature reduces the neutral density and subsequently also the ion-neutral collision rate, see figure 4.6, self-limiting the maximum achievable neutral gas temperature and thermal efficiency. This effect is also observed as a reduction in the heating efficiency for increasing applied voltage frequencies in figure 5.16 (a), coinciding with the increased Ar^+ ion mean-free-path in figure 4.9 (d). Note also that as all neutral heating occurs following ion acceleration, the thermal efficiency is limited by the ion power fraction, resulting in a theoretical upper limit of between $0.75 \leq \eta_{th} \leq 0.90$, depending upon the precise operating conditions.

The thermal efficiencies achievable by the *Pocket Rocket* compare well to other similar micro propulsion sources. Operating at a higher deposited power (40 - 90 W), micro-arcjets have been demonstrated to achieve thermal efficiencies in the range $0.50 \leq \eta_{th} \leq 0.70$ utilizing nitrogen propellant[38]. Similarly high powered ($\approx$ 100 W) resistojets employing hydrazine can achieve thermal efficiencies of $\eta_{th} = 0.65$, only slightly higher than that achievable in the *Pocket Rocket*[14,37]. While higher than the *Pocket Rocket*, the nature of operation of resistojets and arcjets results in increased erosion of internal components and reduced operational lifetimes. On the other end of the scale, micro-electro-mechanical systems (MEMS) thrusters, employing lower powers in the range 0.5 - 2 W, typically achieve thermal efficiencies between $0.04 \leq \eta_{th} \leq 0.17$, for operation employing argon and xenon[41]. The *Pocket Rocket* therefore occupies a middle-ground position, achieving slightly lower efficiencies than comparable resistojets and arcjets, albeit it at deposited powers more akin to MEMS style thrusters. For a more detailed comparison over a wider range of operating parameters, refer to table 1.1 in section 1.2.2.

Complimenting this middle-ground position, dual-frequency operation enables control of the ion power fraction, and therefore also the peak thermal efficiency, of the *Pocket Rocket*. Figure 5.16 (b) shows the thermal efficiency achieved for odd-even ($k = 1, 2$) and odd-odd ($k = 1, 3$) dual-frequency operation at 900 V_{pp} (450 V). Here, the thermal efficiency is modulated by 67%, between $0.3 \leq \eta_{th} \leq 0.5$ and by 17%, between $0.3 \leq \eta_{th} \leq 0.35$ for odd-even ($k = 1, 2$) and odd-odd ($k = 1, 3$) voltage waveforms respectively. These thermal efficiencies are achieved for total deposited powers in the range $1.8 \leq P_{rf} \leq 4.8$ W, where the thermal efficiency varies in proportion to the both the total deposited power and the ion power fraction. Note that phase offsets which increase the heating efficiency result in reduced neutral gas temperatures, for the same reasoning as described with regards to ion-neutral

momentum transfer related to figures 5.10 (b) and (c). This control enables operation in either a high temperature - low power efficiency mode ($180° \leq \theta \leq 360°$ for $k = 1, 2$) or in a high power efficiency - low temperature mode ($0° \leq \theta \leq 180°$ for $k = 1, 2$) for an approximately constant applied voltage amplitude. Crucially, this represents the capability to de-couple the heating efficiency from the applied voltage amplitude for dual-frequency operation, not achievable through single frequency operation. Quasi-independent control of the neutral gas temperature and the thermal efficiency, enables optimisation of the peak heating efficiency for a given applied voltage. Further, it presents the potential for remotely varying the thrust and specific impulse of radio-frequency coupled electrothermal thrusters, significantly increasing the in-mission versatility of satellites equipped with such propulsion sources.

5.5.2 Variable Thrust and Specific Impulse

It has been established that dual-frequency operation enables control of the neutral gas heating within the *Pocket Rocket*, mediated via the dc self-bias voltage and rf power deposition. This control potentially enables variable thrust and specific impulse through modulating the neutral axial flux Γ_{Ar} and exit velocity v_e. To produce thrusts and specific impulses comparable to steady state operation, wall temperatures throughout this section are determined employing the two-step method as described in section 2.4.3.

Figure 5.17 shows the spatially resolved neutral gas temperature and corresponding neutral axial velocity for odd-even ($k = 1, 2$) dual-frequency operation at 900 V_{pp} (450 V), employing a downstream pressure of 0.85 Torr. Here, panels (a), (c) and (e) show operation employing a phase offset of $\theta = 90°$, corresponding to the most positive dc self-bias voltage, while panels (b), (d) and (f) show operation where $\theta = 270°$, corresponding to the most negative dc self-bias voltage.

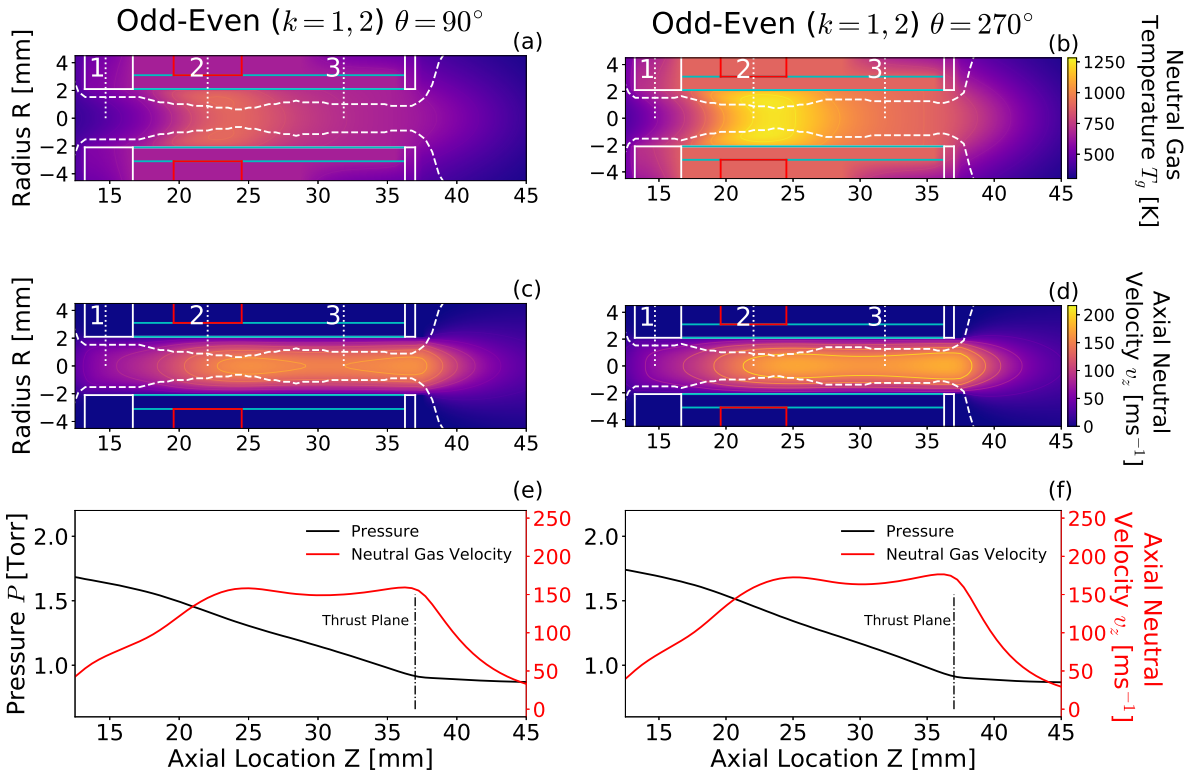

Figure 5.17: Phase-averaged (a), (b) neutral gas temperature and (c), (d) axial neutral velocity for odd-even ($k = 1, 2$) dual-frequency discharges employing 90° and 270° phase offsets, representing the closest stable discharge to most positive and negative dc self-bias voltages, respectively. The associated on-axis (R = 0.0 mm) pressure and neutral axial velocity are shown in (e) and (f), for phase offsets of 90° and 270°, respectively. The dashed white lines in (a-d) represent the phase-averaged sheath edge. Plenum pressure 226 Pa (1.7 Torr), outlet pressure 0.85 Torr, odd-even voltage waveforms, V_{pp} = 900 V (450 V), wall temperatures determined via the two-step method.

While control of the maximum neutral gas temperature has been demonstrated for dual-

frequency operation, the spatial temperature distribution, shown in figures 5.17 (a) and (b), remains approximately independent of phase offset. For all phase offsets, the neutral gas heating is predominately localised within the powered electrode sheath (region 2), coinciding with the location of highest ion power deposition in figure 5.15 (b). Here, the maximum on-axis neutral gas temperature varies by 27% (from 895 - 1231 K) over the full range of phase offsets, exceeding the cold wall cases shown previously. Radial heat diffusion and wall losses are observed downstream of the powered electrode, resulting in a slightly cooler homogeneous radial temperature profile at the thrust plane (Z = 37 mm). The on-axis neutral gas temperature at the thrust plane varies by 24% (from 637 - 841 K), demonstrating that the control afforded via dual-frequency waveforms at the heated region (Z = 21 mm) is propagated forward to the thrust plane (Z = 31 mm).

The spatially resolved neutral gas axial velocity (parallel to the source axis), shown in figures 5.17 (c) and (d), exhibits variation with respect to applied phase-offset. For all phases, laminar slip flow is observed where the fluid flow at the wall is maintained at approximately 50 m s^{-1}, mediated by viscous forces, resulting in a Gaussian radial velocity profile where the axial neutral velocity is highest on-axis. The on-axis neutral velocity across the thrust plane (Z = 37 mm) increases in proportion to the local neutral gas temperature, varying by 10% (from 158 - 175 m s^{-1}) between $\theta = 90°$ to $\theta = 270°$. This increase is maintained through the full axial length of the source, observed more clearly in figures figures 5.17 (e) and (f). In both cases, the neutral gas velocity increases as it enters the source region, reaching a maximum at the powered electrode (region 2). The axial neutral velocity remains approximately constant through the source before reducing beyond the thrust plane. This profile is maintained for both phase offsets, with the enhanced neutral heating for $\theta = 270°$ uniformally increasing the neutral axial velocity throughout the source tube.

It should be noted that the degree of modulation achieved in the neutral axial velocity is is below what would be expected given the increase in neutral gas temperature observed between figures 5.17 (a) and (b). For an ideal gas the average particle velocity varies in proportion to the square root of the gas temperature, see equation 1.8. Therefore, the ratio between the square roots of the neutral gas temperature should equal the ratio between the neutral axial velocities, assuming a Maxwellian velocity distribution. However, the variation in the on-axis neutral gas temperatures at the thrust plane for figures 5.17 (a) and (b) yields a ratio of 1.15, while the ratio between the resulting on-axis neutral velocity at the same location 5.17 (c) and (d) is only 1.10.

This discrepancy is attributed to the relatively high expansion region pressure of 0.85 Torr, coupled with the shallow pressure gradient across the thrust plane, leading to a significant proportion of the pressure thrust being converted into radial momentum at the outlet due to the formation of off-axis turbulent flow, as discussed in section 2.4.4. This results in an anisotropic neutral velocity distribution at the outlet, where the axial velocity component

increases at a reduced rate than would be expected from an isotropic Maxwellian distribution. This mechanism is not expected to occur for operation in space, where the steeper pressure gradient and choked neutral velocity ($v_e \geq c_s$) maintain a laminar flow through the thruster outlet[66,76,77].

The thrust F_T and specific impulse I_{sp} produced by the *Pocket Rocket* are calculated employing equation 2.19 as described in section 2.4.4. The total thrust comprises two components; (1) the summation of the integrated ion Γ_i and neutral Γ_{Ar} momentum fluxes across the exit plane (Z = 37 mm) and (2) the differential pressure ΔP between the exit plane (Z = 37 mm) and the output pressure, here maintained at 133 Pa (0.85 Torr). The simulated thrust and specific impulse for operation employing odd-even ($k = 1, 2$) and odd-odd ($k = 1, 3$) dual-frequency voltage waveforms employing phase offsets between $0° \leq \theta \leq 360°$ are shown in figures 5.18 (a) and (b), respectively.

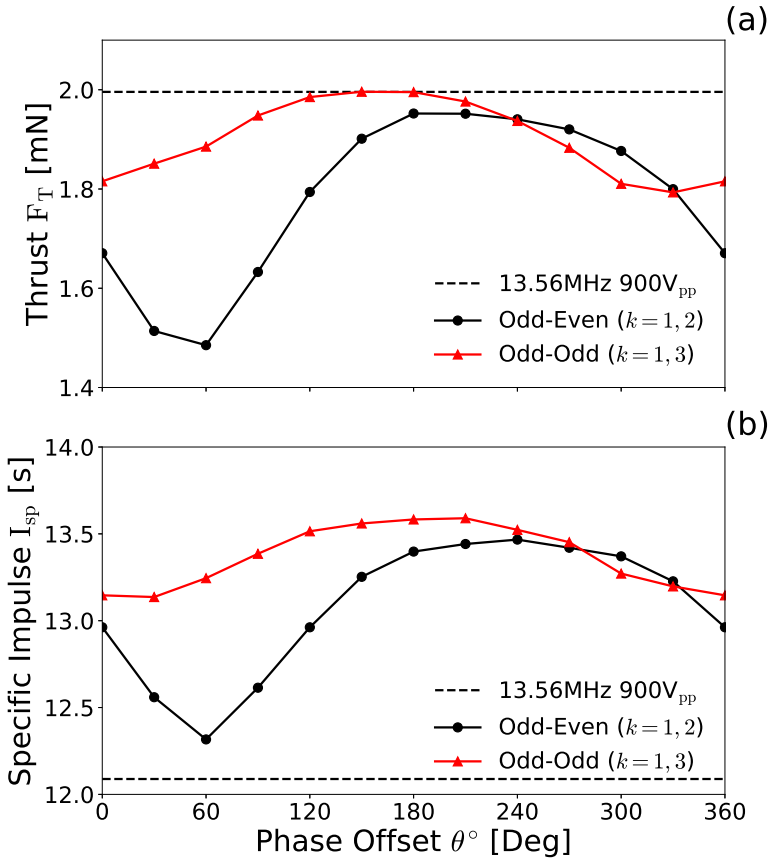

Figure 5.18: Simulated (a) total thrust F_T and (b) specific impulse I_{sp} across the outlet plane (Z = 37 mm) for V_{pp} = 900 V (450 V) odd-even ($k = 1, 2$) and odd-odd ($k = 1, 3$) dual-frequency operation for phase-offsets between $0° \leq \theta \leq 360°$. Thrust and specific impulse produced for a 900 V_{pp} (450 V), 13.56 MHz single frequency discharge are denoted by the dashed lines. Plenum pressure 226 Pa (1.7 Torr) argon, V_{pp} = 900 V (450 V), wall temperatures determined via the two-step method.

The thrusts presented in figure 5.18 (a) exhibit modulations of 29% (1.43 - 1.93 mN) and

12% (1.79 - 2.0 mN) for odd-even ($k = 1, 2$) and odd-odd ($k = 1, 3$) dual-frequency operation, respectively, demonstrating the prospect for variable thrust operation. Odd-even ($k = 1, 2$) waveforms demonstrated the greatest degree of control, while odd-odd ($k = 1, 3$) waveforms exhibited the greatest thrust, on-par with that achieved during single frequency operation at 13.56 MHz. The disparity between the specific impulse resulting from odd-even and odd-odd voltage waveform operation is explained through the odd-odd waveforms exhibiting a greater average peak-to-peak voltage and power deposition, as discussed previously with reference to figure 5.3. The variation in thrust for dual-frequency operation arises primarily from variations in the neutral axial velocity, and hence neutral momentum flux. This differs from operation in single frequency, where the majority of the change in thrust arises due to variations in the upstream pressure, see figure 3.11. In both cases the pressure thrust provides the largest component to the total thrust output. The capability to remotely modulate the thrust by 30% offers an increased capability to perform short timescale collision avoidance manoeuvrers. Translating this into mission relevant parameters, a 30% increase in thrust equates to an additional 1 ms^{-1} of Δv per low earth orbit ($\tau_{LEO} \approx 40$ mins) for a 1U cubesat, significantly reducing the chance of collision. Following the manoeuvre, the thrust can be remotely altered for optimal thermal efficiency, saving power and propellant for longer burns, e.g. for drag compensation.

Varying the thrust via the neutral axial velocity has the added consequence that the specific impulse, shown in shown in figure 5.18 (b), varies in proportion to the thrust. For operation employing a 0.85 Torr outlet pressure, the specific impulse was modulated by 9% (12.32 - 13.55 s) and 3% (13.14 - 13.59 s) for odd-even ($k = 1, 2$) and odd-odd ($k = 1, 3$) operation, respectively. The relatively high expansion region pressure leads to relatively low neutral axial velocities across the thrust plane, as described with respect to figures 3.13 and 5.17. This results in underestimated specific impulses as compared to what would be expected for operation in space. Identical simulations (not shown) employing a 0.35 Torr output pressure, ensuring a choked flow ($v_e \geq c_s$) across the thrust plane (Z = 37 mm), produce specific impulses in the range $33\ s \leq I_{sp} \leq 40\ s$, closely matching previous work performed by Ho[66,76,77] and Greig[72,73,75].

The thrust and specific impulse both vary in proportion to the ion power deposition fraction in figure 5.15 (c), and in inverse proportion to the thermal efficiencies shown in figure 5.16 (b). All of these effects are ultimately mediated by the magnitude of the dc self-bias as modulated via the symmetry of the applied voltage waveform. Electrothermal propulsion utilizing dual-frequency voltage waveforms therefore present the prospect of 'on-the-fly' variations in the thrust, specific impulse and thrust efficiency. Prospective applications range from high thrust, low efficiency operational modes for time sensitive burns, e.g. debris avoidance manoeuvrers, or low thrust, high efficiency manoeuvrers for station keeping.

5.6 Chapter Summary

Control of the species specific power deposition, neutral gas heating, thrust and specific impulse have been demonstrated in the *Pocket Rocket* microthruster employing dual-frequency voltage waveforms. Two types of dual-frequency voltage waveforms were investigated, comprising the combination of a 13.56 MHz fundamental waveform with either a 27.12 MHz or 40.68 MHz waveform applied with a variable phase offset. Varying the phase offset through $0^\circ \leq \theta \leq 360^\circ$ produced a dc self-bias voltage modulation of 11% V_{pp} and 3% V_{pp} of the maximum applied V_{pp} for the odd-even and odd-odd voltage waveforms, respectively. Through varying the phase offset in an odd-even ($k = 1, 2$) waveform discharge the ion power fraction was varied from 57% to 77% of the total rf-power deposited, resulting in a 35% variation in the on-axis neutral gas temperature and a 30% variation in the modal ion energy adjacent to the powered electrode wall. Consequentially, variations in the neutral density and ion-neutral collision cross-section resulted in a 67% modulation in the thermal efficiency, and a 29% modulation in the thrust, demonstrating remotely variable operation.

The application of dual-frequency waveforms to plasma sources for spacecraft propulsion provides the ability to selectively enhance specific heating mechanisms within the plasma by controlling the phase-resolved sheath dynamics. Such control allows for an optimisation of electron, ion and neutral heating mechanisms and power deposition relevant to the desired source function, e.g. optimisation of neutral gas heating mechanisms for spacecraft propulsion or enhancement of ionisation rate and surface incident ion fluxes for industrial applications. Further work into exploring the effects of higher harmonic waveforms could allow for separate control of ion densities and energies in hollow cathode geometries, further increasing the degree of control afforded.

Chapter 6

Conclusions and Further Work

The work presented in this thesis demonstrates the capability to influence and alter the particle heating mechanisms in hollow cathode rf electrothermal micropropulsion sources via the application of variable frequency and multi-harmonic driving voltages. These outcomes were achieved in tandem through the application of the HPEM 2D hybrid fluid/kinetic code with comparison to experimental measurements of the lab-based prototype *Pocket Rocket* hollow cathode microthruster.

6.1 Conclusions

An initial characterisation of the *Pocket Rocket* microthruster was undertaken employing a single 13.56 MHz radio-frequency voltage waveform, this provided baseline for comparison. Varying the applied voltage amplitude at 13.56 MHz, resulted in significant variation of the electron and ion heating dynamics, leading to a voltage induced α-γ mode transition for voltages above 420 V in simulation and above 385 V in experiment. It was determined that this transition corresponded to an increase in the secondary electron emission arising from an enhanced dc self-bias voltage with increasing applied voltage amplitude. This is supported by nanosecond imaging of the *Pocket Rocket* discharge, where experimental measurements of the phase-resolved Ar($2p_1$) excitation rate have been compared to simulations using the Hybrid Plasma Equipment Model, showing close agreement. Three excitation structures were observed within the rf voltage cycle, each corresponding to a distinct electron heating mechanism, identified as follows: A) collisional electron heating during the phase of sheath collapse arising from the electron flux associated with loss of electrons to the wall, B) collisional electron heating during sheath expansion arising from the electron flux associated with the reformation of the sheath volume, and C) the acceleration of non-thermal secondary electrons released from material surfaces following ion bombardment, primarily observed during phases of maximum sheath extension. Sheath collapse and sheath expansion heating mechanisms primarily deposit power on-axis at the upstream and downstream ends of the thruster,

while power deposition from secondary electron collisions predominately occurs within the powered electrode sheath. The reduced powered electrode sheath extent arising from the enhanced plasma densities adjacent to the powered electrode were determined as the primary cause of the variation in the dc self-bias voltage with increasing applied voltage. Ion acceleration and radial flux within the sheath volume were found to increase in proportion with the dc self-bias voltage, localised to the powered electrode sheath. Correspondingly the maximum neutral gas temperature was also found to increase with the dc self-bias voltage, arising from increasingly energetic ion-neutral charge exchange collisions within the sheath volume. For γ-mode operation under lab conditions, a maximum thrust of 2 mN at 13 s specific impulse was achieved for an input power of 3.3 W, representing a net thrust-to-power ratio of 0.40 mN/W over the cold gas thrust of 0.66 mN.

In an attempt to vary the power deposited into ion and electron species, and hence alter the neutral gas heating, the *Pocket Rocket* was operated for varying applied voltage frequencies in the range 13.56 - 108.48 MHz. A frequency induced γ-α mode transition was observed between applied voltage frequencies of 27.12 MHz and 40.68 MHz. The increasing sheath velocity and reducing absolute time for which the sheath is collapsed with increasing applied voltage frequency resulted in enhanced α-mode heating mechanisms, while increased loss of secondary electrons to the source walls resulted in reduced γ-mode heating mechanisms. Despite this, and due primarily to the increased deposited power, the maximum plasma density was observed to increase with increasing applied voltage frequency, leading to reduced phase-averaged sheath extensions and enhanced radial ion fluxes. Consequentially the electron power deposition was found to vary with the phase-resolved sheath dynamics, while ion and neutral power deposition responded to properties arising from the phase-averaged sheath dynamics, i.e. the dc self-bias voltage. The fraction of power deposited into ion species reduced with increasing applied voltage frequency,converging towards 70% of the total deposited power for applied voltage frequencies of 54.24 MHz at 450 V. This stabilization of the ion power fraction arises due to the formation of high energy, non-thermal, ion populations exhibiting weakly collisional and collisionless behaviour. The transition from collisional IEDFs to structured multi-peaked IEDFs exhibiting collisionless effects was observed for applied voltage frequencies above 54.24 MHz at 450 V, agreeing with the ion energy plateau. This transition was characterised by the formation of high energy structures within the IEDFs incident on plasma facing material surfaces. The formation of these structures was attributed to a reduction in the phase-averaged sheath extent in combination with an increased Ar - Ar^+ mean-free-path with increasing applied voltage frequency over 13.56 - 108.48 MHz. Two distinct transitions in the structure of the IEDF were observed at 450 V, corresponding to the formation of a single mid-energy (90 - 150 eV) structure between 40.68 - 54.24 MHz, and two additional high energy ($\approx$ 210 eV, $\approx$ 290 eV) structures which form at frequencies above 81.36 MHz. A significant degree of control of the mean and modal

Ar^+ energies was achieved, varying by 97 eV and 280 eV, respectively. Ions within the high energy structures responded more directly to the applied voltage, enabling a larger range of ion energies, and associated collision cross-sections, to be accessed for a given radial ion flux.

Building upon the control achieved employing variable single frequency excitation, the *Pocket Rocket* was operated employing dual-frequency voltage waveforms with a variable phase offset. Two types of dual-frequency voltage waveforms were investigated, comprising the combination of a 13.56 MHz fundamental waveform with either an even or odd harmonic, typically 27.12 MHz and 40.68 MHz, respectively. Control of the dc self-bias voltage was demonstrated for both odd-even and odd-odd voltage waveforms, the former being achieved directly through the application of an electrical asymmetry and the latter achieved indirectly through a variation in the deposited power. Through these mechanisms, dc self-bias voltage modulations of 13% V_{pp} and 5% V_{pp} were achieved employing odd-even and odd-odd voltage waveforms with upper harmonic phase offsets between $0^\circ \leq \theta \leq 360^\circ$, respectively. Through varying the phase offset in an odd-even waveform discharge the ion power fraction varied from 57% to 77% of the total rf-power deposited, correlating with a 35% variation in the on-axis neutral gas temperature and a factor of 5 variation in the modal ion energy through the powered electrode sheath. Additionally, enhanced α-mode ionisation during sheath collapse, afforded via modulation of the phase-resolved sheath dynamics, resulted in a 70% variation in the Ar^+ density and radial flux. A comparison of measured and simulated phase-resolved $Ar(2p_1)$ excitation rates showed close agreement, confirming the numerically asserted sheath dynamics. Both the increased ionisation and altered ion power deposition arise from a reduction in the fraction of the rf-cycle for which the sheath is collapsed and the resultant increase in the phase-averaged sheath potential and electric field strength. The capability to selectively enhance specific ion and electron heating mechanisms was employed to demonstrate variable thrust and specific impulse operation of the *Pocket Rocket* microthruster. Two modes of operation were identified: a high thrust, high specific impulse, low thermal efficiency mode and a low thrust, low specific impulse, high thermal efficiency mode, where the thrust and thermal efficiency were modulated by 26% and 67%, respectively. The capability to remotely alter the propulsive characteristics offers a substantial increase in the flexibility of satellites equipped with radio-frequency propulsion sources. Exploring the effects of higher fundamental dual-frequency waveforms allowed for significant variation of the mean ion energy and ion-neutral collision cross-section, enabling enhanced control of the ion to neutral power transfer efficiency.

In conclusion, the work presented herein has furthered the understanding of power deposition in multi-frequency hollow cathode enhanced discharges through the use of experimentally validated numerical simulations. It has been demonstrated that control of the electron heating through altering the dominant ionisation mechanisms can alter the ion power deposition via manipulation of the phase-averaged physical and electrical asymme-

tries. This feedback between electron heating, varying ionisation rates, altered ion densities and the resulting sheath dynamics creates a highly non-linear system, which must be carefully considered when modelling strongly asymmetric plasma discharges. However, while this non-linearity enforces careful modelling of such systems, it also enables significant degrees of control over the resulting ion energy distributions and spatially resolved ion and electron fluxes through direct modulation of the sheath dynamics via tailored voltage waveforms. Such control allows for an optimisation of electron, ion and neutral heating mechanisms and power deposition relevant to the desired outcomes, e.g. enhancement of spatially resolved ionisation rates for industrial applications or optimisation of ion and neutral gas heating mechanisms for spacecraft propulsion. Application of the control mechanisms afforded via tailored voltage waveforms detailed in this work has the potential to enable the development of more power efficient electrothermal thrusters for use on increasingly miniaturized satellite platforms.

6.2 Ongoing Work

As this thesis represents work from an evolving research project, there are a number of ongoing investigations that, while pertinent to the conclusions presented here, are not yet at the fidelity required for inclusion in the main text. Of these ongoing projects, the most relevant to the arguments put forward in this thesis involves the application of higher harmonic ($n \geq 3$) tailored voltage waveforms to the *Pocket Rocket* microthruster.

6.2.1 Application of $n \geq 3$ Harmonic Tailored Voltage Waveforms

A natural extension from the application of dual-frequency voltage waveforms involves the addition of further harmonics, resulting in more finely structured voltage waveforms. These truly 'tailored' voltage waveforms present the capability to enhance the control already demonstrated for dual-frequency operation. Ongoing work aims to demonstrate enhanced neutral heating, variable spatial power deposition and increasingly independent control of the ion energies and fluxes towards material surfaces.

Three classes of tailored voltage waveform are currently under investigation, constructed through the superposition of a 13.56 MHz fundamental waveform and between 1 to 9 additional harmonics with varying amplitudes phase offsets. These consist of 'sawtooth' waveforms, 'peak' waveforms and 'nanosecond pulse' waveforms, generated employing equations 6.1, 6.2, and 6.3, respectively.

$$\phi_{rf}(t) = \sum_{k=0}^{n} \left(\frac{\phi_0}{nk} \right) sin(k\omega_0 t + \theta_k) \tag{6.1}$$

$$\phi_{rf}(t) = \sum_{k=0}^{n} \left(\frac{\phi_0}{n} \right) sin(k\omega_0 t + \theta_k) \tag{6.2}$$

$$\phi_{rf}(t) = \sum_{k=0}^{n} \left(\frac{k\phi_0}{n!} \right) sin(k\omega_0 t + \theta_k) \tag{6.3}$$

The symbols used in equations 6.1 through 6.3, are the same as previously employed for dual-frequency operation: where $\phi_{\mathrm{rf}}(t)$ is the combined voltage waveform, ϕ_0 is its maximum amplitude, $\omega_0 = 2\pi\nu_0$ is the fundamental angular frequency, θ_k is the phase offset of harmonic k and n is the total number of applied harmonics. As before, the shape and symmetry of the resulting waveform can be altered through varying the phase-offset between individual harmonics. However, due the intractable growth in the parameter space with increasing harmonic number, the same global phase offset θ is applied applied to each harmonic component, i.e. $\theta_k = \theta \; \forall \; k$.

The 'parity' of a waveform, defined as the direction of the largest change in voltage, may be positive or negative. Employing the sawtooth waveforms as an example, a 'rising-

sawtooth' consists of a single rapid positive change in voltage followed by a long shallow decrease in voltage. Altering the parity of the waveform is achieved through varying the global phase offset, where a 'rising-sawtooth' or a 'falling-sawtooth' may be generated from equation 6.1 for $\theta = 0$ or $\theta = \pi$, respectively. Similarly, 'peak' and 'valley' voltage waveforms are generated from equation 6.2 where $\theta = \frac{\pi}{2}$ or $\theta = \frac{3\pi}{2}$, respectively, and 'rising-pulse' and 'falling-pulse' waveforms from equation 6.3 where $\theta = 0$ or $\theta = \pi$, respectively.

Experimental agreement between measured and simulated phase-resolved Ar($2p_1$) excitation structures has been achieved for all three classes of tailored waveforms introduced above, for brevity only the sawtooth comparison will be presented here. The phase-resolved measured Ar($2p_1$) excitation rates for 240 V operation employing a single 13.56 MHz sinosoid, an $n = 5$ rising sawtooth and an $n = 5$ falling sawtooth are shown in figures 6.1 (a-c), respectively, while the associated simulated excitation rates are shown in figures 6.1 (d-f). The measured and simulated phase-resolved electrode potentials ϕ_{rf} and simulated dielectric potentials ϕ_{dc} are shown in figures 6.1 (g-i), where the phase-averaged dc self-bias voltage is denoted by the dashed red line.

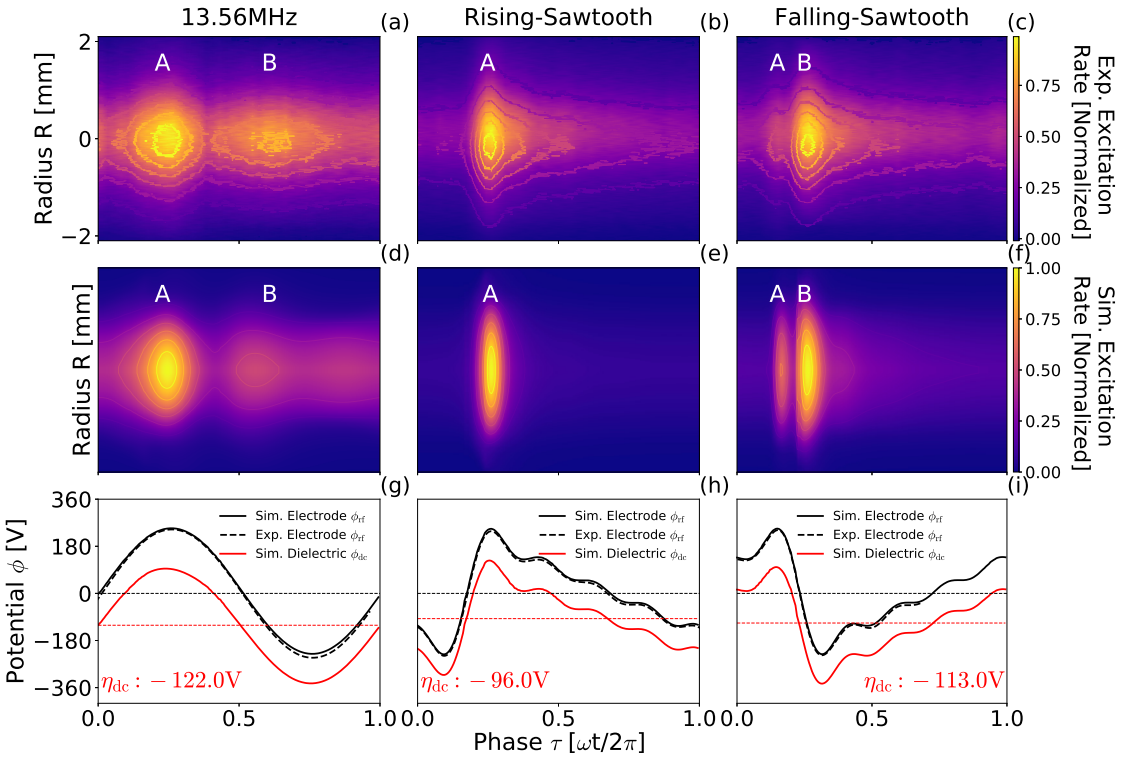

Figure 6.1: Phase-resolved measured and simulated Ar($2p_1$) excitation rates for 240 V operation employing (a),(d) a single 13.56 MHz frequency driving waveform (b),(e) an $n = 5$, 'rising'-sawtooth waveform and (c),(f) an $n = 5$, 'falling'-sawtooth waveform. Associated measured and simulated electrode and dielectric potentials are shown in (g-i), where the dc self-bias voltage is denoted by the dashed red line. Rising-sawtooth and falling-sawtooth waveforms were generated employing equation 6.1, employing $\theta_k = 0$ and $\theta_k = \pi$, respectively. Operating conditions, plenum pressure 200 pa (1.5 Torr) argon, $\phi_0 = 240$ V, fundamental frequency of 13.56 MHz.

The comparisons shown in figure 6.1 were performed at 240 V as this represented a stable α-mode operating voltage for 13.56 MHz and all six tailored voltage waveforms, enabling a more equal comparison of excitation mechanisms. As a baseline for comparison, the measured and simulated Ar($2p_1$) excitation rates for 13.56 MHz are shown in figures 6.1 (a) and (b) and show a good agreement. Excitation is observed during phases of sheath collapse (Peak A) and sheath expansion (Peak B), confirming α-mode operation. Close agreement is also observed between the measured and simulated excitation structures for operation employing $n = 5$ rising and falling sawtooth waveforms, shown in figures 6.1 (b) & (c) and 6.1 (e) & (f), respectively.

The application of rising and falling sawtooth waveforms alters the temporal location and extent of these excitation structures significantly, demonstrating variations in the sheath dynamics. Operation employing a rising-sawtooth voltage waveform exhibits enhanced sheath collapse heating, arising from the substantial increase in the electrode and dielectric potential between phases $0.1 \leq \tau \leq 0.2$, resulting in a high sheath collapse velocity. In contrast falling-sawtooth operation preferentially enhances sheath expansion heating, arising from analogous reasoning where the rapid drop in potential between $0.1 \leq \tau \leq 0.2$ results in a high sheath expansion velocity.

As discussed above, real-time alterations to the shape and symmetry of the sawtooth waveform are possible through varying the phase offset θ in equation 6.1. Inverting the sawtooth waveform from a rising-sawtooth to a falling-sawtooth via this method, achieves a 15% modulation ($-113 \leq \eta_{dc} \leq -96\ V$) in the dc self-bias voltage, while altering the predominant electron heating mechanism from sheath collapse to sheath expansion heating. For sawtooth waveforms, the degree of control achieved over the sheath dynamics and associated α-mode electron heating mechanisms is greater that that achieved through dual-frequency operation, at the expense of a slightly reduced modulation in the dc self-bias voltage. Note however, that the most negative dc self-bias voltage is still achieved for a single frequency 13.56 MHz discharge, mirroring the gain in control at the expense of peak performance as observed with dual-frequency voltage waveforms.

Modulation of the ionisation mechanisms and dc self-bias voltage naturally lead to alteration of the mean ion energy and flux, through the same mechanisms as described with dual-frequency waveforms. Specifically, the enhanced control achieved via $n \geq 3$ harmonic tailored voltage waveforms leads to further decoupling of the ion energy and ion flux, enabling increasingly independent optimisation of these parameters. Figure 6.2 shows the mean Ar^+ ion energy and radial Ar^+ ion flux for phase offsets between $0° \leq \theta \leq 360°$ employing $n = 5$, $\phi_0 = 900$ V (450 V) sawtooth, peak and ns-pulse tailored voltage waveforms.

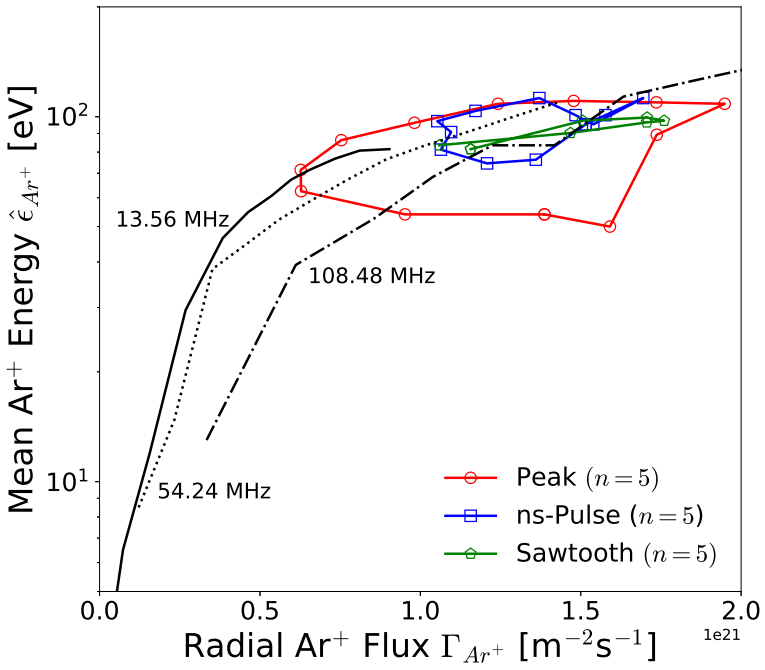

Figure 6.2: Ion energies incident upon the radial wall adjacent to the powered electrode (R,Z = 2.1 mm, 21 mm) with respect to ion flux at the same location employing sawtooth, peak and ns-pulse tailored voltage waveforms with phase offsets between between $0° \leq \theta \leq 360°$. Single frequency curves are obtained from data underpinning figure 4.8. Plenum pressure of 200 Pa (1.5 Torr) argon, V_{pp} = 900 V (450 V), wall temperatures 325 K.

Discharges employing $n \geq 3$ harmonic tailored voltage waveforms in figure6.2 exhibit a substantially increased range of obtainable ion energy/flux combinations as compared to single frequency discharges. As observed previously in figure 6.2, the phase offset determines the 'modulation angle' around from a central 'modulation origin' point in $\hat{\epsilon}_{Ar^+}\Gamma_{Ar^+}$ space, itself determined by the tailored waveform shape, harmonic composition and voltage amplitude. Sawtooth waveforms exhibit a similar degree of control as observed previously for dual-frequency voltage waveforms, with a relatively flat elliptical range of attainable values. In contrast, ns-pulse and peak voltage waveforms exhibit increased control as compared to dual-frequency voltage waveforms, resulting in increasingly circular modulations in $\hat{\epsilon}_{Ar^+}\Gamma_{Ar^+}$ space with peak shaped waveforms achieving the largest modulation in both ion energy and flux. Figure 6.2 demonstrates that peak shaped voltage waveforms are capable of further separating the high flux, low energy, thermally efficient regimes and high energy, low flux, high temperature regimes previously demonstrated via dual-frequency operation. Continued development and modelling of higher harmonic ($n \geq 3$) tailored voltage waveforms for use in aerospace applications therefore enables a greater degree of control and optimisation of ion, neutral and electron heating mechanisms, expanding upon that achieved and demonstrated for dual-frequency operation.

6.3 Recommendations for future work

Building upon the conclusions outlined in this thesis, it would be interesting to address the prospective application of kHz pulsed voltage waveforms. Through varying the pulse duty cycle, a significant reduction in the applied power could be achieved. Determining the effects on the ionisation dynamics and neutral gas heating would be essential for a determination of the effectiveness of this technique. In addition, a more in-depth analysis on the capability to induce collisionless ion populations within intermediate pressure ($\approx$ 1.0 Torr) discharges prospectively enables the production of high flux, high energy ion beams. There also remain a number of open questions regarding the optimal internal geometry of the *Pocket Rocket* microthruster. Specifically regarding the axial placement of the powered electrode, thickness of the dielectric layer and the internal diameter of the source for a given propellant flow rate. While outside of the scope of this thesis, some thought has been given to the internal geometry and scalability of the *Pocket Rocket* source.

6.3.1 Nested Hollow Cathode Thrusters

The *Pocket Rocket* microthruster is designed for operation employing powers in the range 1 - 40 W, roughly coinciding with available powers on 1 - 12U CubeSat systems. For deployment on larger satellites, multiple *Pocket Rocket* sources could be employed to scale with the available power and required thrust. While an easy to implement scaling solution, using multiple sources represents an inefficient use of mass, volume and power, all strictly limited on satellite platforms. To enable effective scaling for larger systems, the prospect of Nested Hollow Cathode (NHC) geometries presents a possible solution. An example of a prospective nested *Pocket Rocket* geometry is shown in figure 6.3.

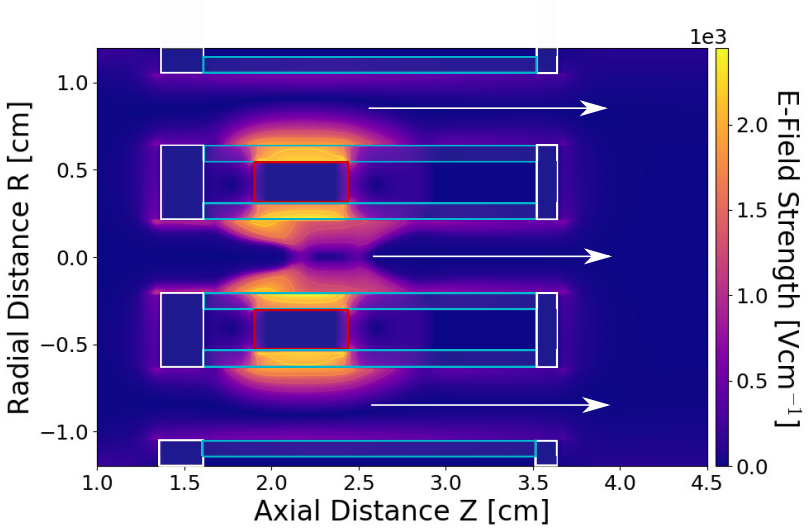

Figure 6.3: Nested Hollow Cathode (NHC) source geometry, employing a single inner radial powered electrode configuration. Electric field strength reaches a maximum on-axis, reducing towards the outer nested cavity. Operating conditions, plenum pressure 200 pa (1.5 Torr) argon, 300 V, 13.56 MHz.

Here, in addition to the central unaltered *Pocket Rocket* source, an outer co-axial dielectric lined channel has been included. This geometry exposes the electric field from both the inner and outer radial sides of the powered electrode to the propellant. The volume within which ions are accelerated and ion-neutral charge exchange may occur is therefore increased substantially. The configuration shown in figure 6.3 utilizes only one inner powered ring, it is entirely feasible that nested powered rings may also be employed in situations where the power is available. Note also, as the outer channel sweeps through a larger volume, prospective geometries will likely employ reducing cavity widths at higher radii. This would maintain an approximately equal volume of gas within each nested cavity, enabling homogeneous neutral gas heating.

In addition to the nesting of hollow cathode sources, the prospect of internal 'rifling' of the dielectric surface, i.e. the carving 3D helical grooves, represents an additional possible optimisation to the *Pocket Rocket* microthruster. The addition of such helical grooves increases the dielectric surface area, resulting in the collection of a greater surface charge, enhancing the dc self-bias voltage and increasing the sheath potential through which ions are accelerated. Further, if the cross-section of the rifling groove is greater than the phase-averaged sheath extension, then the high sheath velocities at the rifled edges will enhance α-mode ionisation mechanisms, resulting in enhanced ion densities. Finally, as the majority of gas heating is observed adjacent to the dielectric surface, the greatly increased surface area will result in a larger volume of neutral gas heated.

In summary, further investigation into the applicability of exotic three dimensional hollow cathode geometries enables scalable source configurations and presents the prospect of further optimising the ionisation and neutral heating processes for aerospace and industrial applications.

Chapter 7

Biblography

[1] Hero of Alexandria. *The Pneumatics of Hero of Alexandria*. Taylor Walton And Maberly, London, 1851. ISBN 1449562876.

[2] K. Tsiolkovsky. Exploration of the Universe with Reaction Machines. *Nauchnoe Obozrenie*, 5(3), 1903.

[3] M. J. L. Turner. *Rocket and spacecraft propulsion*. Springer-Praxis, Chichester, UK, 2nd edition, 2006. ISBN 3540221905.

[4] D. M. Goebel and I. Katz. *Fundamentals of Electric Propulsion: Ion and Hall Thrusters*. John Wiley, Hoboken, 2008.

[5] C. Charles. Plasmas for spacecraft propulsion. *Journal of Physics D: Applied Physics*, 42(16):163001, 2009. ISSN 0022-3727. doi:10.1088/0022-3727/42/16/163001.

[6] D. Platt. A Monopropellant Milli-Newton Thruster System for Attitude Control of Nanosatellites. *16th Annual USU Conference on Small Satellites*, pages 1–6, 2002.

[7] A. Makled and H. Belal. Modeling of Hydrazine Decomposition for Monopropellant Thrusters. *Aerospace Science & aviation technology*, (September):1–17, 2009.

[8] V. Godyak, R. Piejak, and B Alexandrovich. Measurements of electron energy distribution in low-pressure R F discharges. *Plasma Sources Science and Technology*, 1(1):36–58, 1992. doi:10.1088/0963-0252/1/1/006.

[9] P. Chabert and N. Braithwaite. *Physics of Radio-Frequency Plasmas*. Cambridge University Press, Cambridge, 3rd edition, 2014.

[10] E. Y. Choueiri. A Critical History of Electric Propulsion : The First Fifty Years (1906-1956). *Journal of Propulsion and Power*, 20(2):1–21, 2004. doi:10.2514/1.9245.

[11] I. Adamovich, S. D. Baalrud, A. Bogaerts, P. J. Bruggeman, M. Cappelli, V. Colombo, U. Czarnetzki, U. Ebert, J. G. Eden, P. Favia, D. B. Graves, S. Hamaguchi, G. Hieftje, M. Hori, I. D. Kaganovich, U. Kortshagen, M. J. Kushner, N. J. Mason, S. Mazouffre, S. Mededovic Thagard, H. R. Metelmann, A. Mizuno, E. Moreau, A. B. Murphy, B. A. Niemira, G. S. Oehrlein, Z. Lj Petrovic, L. C. Pitchford, Y. K. Pu, S. Rauf, O. Sakai, S. Samukawa, S. Starikovskaia, J. Tennyson, K. Terashima, M. M. Turner, M. C.M. Van De Sanden, and A. Vardelle. The 2017 Plasma Roadmap: Low temperature plasma science and technology. *Journal of Physics D: Applied Physics*, 50(32):323001, 2017. ISSN 13616463. doi:10.1088/1361-6463/aa76f5.

[12] D. B. Scharfe and A. D. Ketsdever. A Review of High Thrust , High Delta-V Options for Microsatellite Missions. *45th AIAA/ASME/SAE/ASEE Joint Propulsion Conference*, 15(August):1–14, 2009.

[13] I. Hrbud, E. Kemp, A. Yan, and J. Gedrimas. Review of RF Plasma Thruster Development. *Iepc-2007-309*, pages 1–10, 2007.

[14] M. Martinez-Sanchez and J. E. Pollard. Spacecraft Electric Propulsion-An Overview. *Journal of Propulsion and Power*, 14(5):688–699, 1998. ISSN 0748-4658. doi:10.2514/2.5331.

[15] L Garrigues and P Coche. Electric propulsion: comparisons between different concepts. *Plasma Physics and Controlled Fusion*, 53(12):124011, 2011. ISSN 0741-3335. doi:10.1088/0741-3335/53/12/124011.

[16] S. Mazouffre. Electric propulsion for satellites and spacecraft: established technologies and novel approaches. *Plasma Sources Science and Technology*, 25(3):033002, 2016. ISSN 0963-0252. doi:10.1088/0963-0252/25/3/033002.

[17] A. Aanesland, A. Meige, and P. Chabert. Electric propulsion using ion-ion plasmas. *Journal of Physics: Conference Series*, 162:012009, 2009. ISSN 1742-6596. doi:10.1088/1742-6596/162/1/012009.

[18] A. Aanesland, D. Rafalskyi, J. Bredin, P. Grondein, N. Oudini, P. Chabert, D. Levko, L. Garrigues, and G. Hagelaar. The PEGASES Gridded Ion – Ion Thruster Performance and Predictions. *IEEE Transactions of Plasma Science*, 43(1):321–326, 2015.

[19] T. Lafleur and P. Chabert. Is collisionless heating in capacitively coupled plasmas really collisionless? *Plasma Sources Science and Technology*, 24(4):044002, 2015. ISSN 13616595. doi:10.1088/0963-0252/24/4/044002.

[20] M. Tajmar, A. Genovese, and W. Steiger. Indium Field Emission Electric Propulsion Microthruster Experimental Characterization. *Journal of Propulsion and Power*, 20(2), 2004. doi:10.2514/1.9247.

[21] A. Genovese, M. Tajmar, N. Buldrini, and W. Steiger. 2000-Hour Endurance Test of Indium Field Emission. *Journal of Propulsion and Power*, 20(2), 2004. doi:10.2514/1.9250.

[22] M. J. Mueller and D. A. Ketsdever. *Micropropulsion For Small Spacecraft*. American Institute of Astronautics and Aeronautics, 1st edition, 2000. ISBN 1-56347-448-4. doi:10.2514/4.866586.

[23] M. S. Alexander, J. Stark, and K. L. Smith. Electrospray Performance of Microfabricated Colloid Thruster Arrays. *Journal of Propulsion and Power*, 22(3), 2006. doi:10.2514/1.15190.

[24] V V Zhurin, H R Kaufman, and R S Robinson. Physics of closed drift thrusters. *Plasma Sources Science and Technology*, 8(1):R1–R20, 1999. ISSN 0963-0252. doi:10.1088/0963-0252/8/1/021.

[25] C Charles and R Boswell. Current-free double-layer formation in a high-density helicon discharge. *Applied Physics Letters*, 82(9):1356–1358, 2003. ISSN 00036951. doi:10.1063/1.1557319.

[26] C. Charles and R. W. Boswell. Laboratory evidence of supersonic ion beam generated by a current-free "helicon" double-layer. *Physics of Plasmas*, 11(4):1706–1714, 2004. ISSN 1070664X. doi:10.1063/1.1652058.

[27] A. Bennet, C. Charles, and R. Boswell. In situ electrostatic characterisation of ion beams in the region of ion acceleration. *Physics of Plasmas*, 25(2), 2018. ISSN 10897674. doi:10.1063/1.5017049.

[28] K. Takahashi. *Helicon-type radiofrequency plasma thrusters and magnetic plasma nozzles*, volume 3. Springer Singapore, 2019. ISBN 0123456789. doi:10.1007/s41614-019-0024-2.

[29] R. W. Boswell. Plasma production using a standing helicon wave. *Physics Letters A*, 33(7):457–458, 1970. ISSN 03759601. doi:10.1016/0375-9601(70)90606-7.

[30] T. Lafleur, K. Takahashi, C. Charles, and R. W. Boswell. Direct thrust measurements and modelling of a radio-frequency expanding plasma thruster. *Physics of Plasmas*, 18(8):1–4, 2011. ISSN 1070664X. doi:10.1063/1.3610570.

[31] T. Lafleur, C. Charles, and R. W. Boswell. Ion beam formation in a very low magnetic field expanding helicon discharge. *Physics of Plasmas*, 17(4):1–6, 2010. ISSN 1070664X. doi:10.1063/1.3381093.

[32] F. F. Chen. Helicon discharges and sources: A review. *Plasma Sources Science and Technology*, 24(1), 2015. ISSN 13616595. doi:10.1088/0963-0252/24/1/014001.

[33] A. Agarwal, S. Rauf, and K. Collins. Gas heating mechanisms in capacitively coupled plasmas. *Plasma Sources Science and Technology*, 21:055012, 2012. ISSN 0963-0252. doi:10.1088/0963-0252/21/5/055012.

[34] L. Blackhall and J. Khachan. A simple electric thruster based on ion charge exchange. *Journal of Physics D: Applied Physics*, 40:2491–2494, 2007. ISSN 0022-3727. doi:10.1088/0022-3727/40/8/011.

[35] J. Schulze, Z. Donkó, B. G. Heil, D. Luggenhölscher, T. Mussenbrock, R. P. Brinkmann, and U. Czarnetzki. Electric field reversals in the sheath region of capacitively coupled radio frequency discharges at different pressures. *Journal of Physics D: Applied Physics*, 41(10):105214, 2008. ISSN 15735052. doi:10.1007/s11258-017-0772-4.

[36] W. E. Morren and S. S. Hay. Performance Characterizations of an Engineering Model Multipropellant Resistojet. *Journal of Propulsion and Power*, 5(2):197–203, 1989. doi:10.2514/3.23136.

[37] R. H. Frisbee. Advanced Space Propulsion for the 21st Century. *Journal of Propulsion and Power*, 19 (6), 2003. doi:10.2514/2.6948.

[38] H. Horisawa and I. Kimura. Very low-power arcjet testing. *Vacuum*, 59:106–117, 2000. doi:10.1016/S0042-207X(00)00260-8.

[39] G. F. Willmes and R. L. Burton. Low-Power Helium Pulsed Arcjet. *Journal of Propulsion and Power*, 15(3), 1999. doi:10.2514/2.5446.

[40] J. Mueller, C. Marrese, J. Polk, E.-H. Yang, A. Green, V. White, D. Bame, I. Chakraborty, and S. Vargo. An Overview of Mems-Based Micropropulsion Development at JPL. *Acta Astronautica*, 52: 881–895, 2003. doi:http://hdl.handle.net/2014/36757.

[41] K. Palmer, H. Nguyen, and G. Thornell. Fabrication and evaluation of a free molecule micro-resistojet with thick silicon dioxide insulation and suspension. *Journal of Micromechanics and Microengineering*, 23:065006, 2013. doi:10.1088/0960-1317/23/6/065006.

[42] S. Muncheberg, M. Krischke, and N. Lemke. Nanosatellites and micro systems technology - capabilities limitations and applications. In *International Electric Propulsion Conference*, volume 39, pages 799–808, 1996.

[43] R. A. Arakoni, J. J. Ewing, and M. J. Kushner. Microdischarges for use as microthrusters: modelling and scaling. *Journal of Physics D: Applied Physics*, 41(10):105208, 2008. ISSN 0022-3727. doi:10.1088/0022-3727/41/10/105208.

[44] C. Charles, R. W. Boswell, A. Bish, V. Khayms, and E. F. Scholz. Direct Measurement of Axial Momentum Imparted by an Electrothermal Radiofrequency Plasma Micro-Thruster. *Frontiers in Physics*, 4(May):1–6, 2016. ISSN 2296-424X. doi:10.3389/fphy.2016.00019.

[45] A. Dunaevsky, Y. Raitses, and N. J. Fisch. Plasma acceleration from radio-frequency discharge in dielectric capillary. *Applied Physics Letters*, 88(25):10–13, 2006. ISSN 00036951. doi:10.1063/1.2214127.

[46] K. K. Jameson, D. M. Goebel, and R. M. Watkins. Hollow Cathode and Thruster Discharge Chamber Plasma Measurements Using High-Speed Scanning Probes. *Proceedings of the International Electric Propulsion Conference 2005 (IEPC05)*, pages 1–16, 2005.

[47] I. Levchenko, K. Bazaka, Y. Ding, Y. Raitses, S. Mazouffre, T. Henning, Peter J. Klar, S. Shinohara, J. Schein, L. Garrigues, M. Kim, D. Lev, F. Taccogna, R. W. Boswell, C. Charles, H. Koizumi, Y. Shen, C. Scharlemann, M. Keidar, and S. Xu. Space micropropulsion systems for Cubesats and small satellites: From proximate targets to furthermost frontiers. *Applied Physics Reviews*, 5(1):011104, 2018. ISSN 19319401. doi:10.1063/1.5007734.

[48] K. Woellert, P. Ehrenfreund, A. J. Ricco, and H. Hertzfeld. Cubesats : Cost-effective science and technology platforms for emerging and developing nations. *Advances in Space Research*, 47(4):663–684, 2011. ISSN 0273-1177. doi:10.1016/j.asr.2010.10.009.

[49] A. Mehrparvar and J. Carnahan. CubeSat Design Specification: Revision 13. Technical report, California Polytechnic State University, 2014.

[50] A. Scholz and J.-N. Juang. Toward open source CubeSat design. *Acta Astronautica*, 115(June 2003): 384–392, 2015. ISSN 0094-5765. doi:10.1016/j.actaastro.2015.06.005.

[51] E. Kulu. Nanosats Database, 2019. URL `https://www.nanosats.eu/`.

[52] D. Selva and D. Krejci. A survey and assessment of the capabilities of Cubesats for Earth observation. *Acta Astronautica*, 74:50–68, 2012. ISSN 0094-5765. doi:10.1016/j.actaastro.2011.12.014.

[53] R. Sandau, K. Brieß, and M. D. Errico. ISPRS Journal of Photogrammetry and Remote Sensing Small satellites for global coverage : Potential and limits. *ISPRS Journal of Photogrammetry and Remote Sensing*, 65(6):492–504, 2010. ISSN 0924-2716. doi:10.1016/j.isprsjprs.2010.09.003.

[54] A. Kirilin, E. Shakhmatov, V. Soifer, R. Akhmetov, A. Prokofev, V. Salmin, and N. Stratilatov. Small satellites " AIST " constellation - design , construction and program of scientific and technological experiments. *Procedia Engineering*, 104:43–49, 2015. ISSN 1877-7058. doi:10.1016/j.proeng.2015.04.095.

[55] E. Gill, P. Sundaramoorthy, J. Bouwmeester, B. Zandbergen, and R. Reinhard. Formation flying within a constellation of nano-satellites : The QB50 mission. *Acta Astronautica*, 82(1):110–117, 2013. ISSN 0094-5765. doi:10.1016/j.actaastro.2012.04.029.

[56] K. Takahashi, C. Charles, R. W. Boswell, and A. Ando. Demonstrating a new technology for space debris removal using a bi-directional plasma thruster. *Scientific Reports*, 8(1):1–10, 2018. ISSN 20452322. doi:10.1038/s41598-018-32697-4.

[57] G. Benedetti, N. Bloise, D. Boi, F. Caruso, A. Civita, S. Corpino, E. Garofalo, G. Governale, L. Mascolo, G. Mazzella, M. Quarata, D. Riccobono, G. Sacchiero, D. Teodonio, and P. M. Vernicari. Interplanetary CubeSats for asteroid exploration : Mission analysis and. *Acta Astronautica*, 154(April 2018):238–255, 2019. ISSN 0094-5765. doi:10.1016/j.actaastro.2018.05.011.

[58] A. Poghosyan and A. Golkar. CubeSat evolution: Analyzing CubeSat capabilities for conducting science missions. *Progress in Aerospace Sciences*, 88(November 2016):59–83, 2017. ISSN 03760421. doi:10.1016/j.paerosci.2016.11.002.

[59] Y. Ulybyshev. Satellite Constellation Design for Complex Coverage. *Journal of Spacecraft and Rockets*, 45(4):843–849, 2008. doi:10.2514/1.35369.

[60] W. Zhaokui, X. Yun, J. Chao, and Z. Yulin. Self-organizing control for satellite clusters using artificial potential function in terms of relative orbital elements. *Aerospace Science and Technology*, 84:799–811, 2019. ISSN 1270-9638. doi:10.1016/j.ast.2018.11.033.

[61] S. Nag and L. Summerer. Behaviour based , autonomous and distributed scatter manoeuvres for satellite swarms. *Acta Astronautica*, 82(1):95–109, 2013. ISSN 0094-5765. doi:10.1016/j.actaastro.2012.04.030.

[62] M. Keidar, T. Zhuang, A. Shashurin, G. Teel, D. Chiu, J. Lukas, S. Haque, and L. Brieda. Electric propulsion for small satellites. *Plasma Physics and Controlled Fusion*, 57(1):014005, 2015. ISSN 13616587. doi:10.1088/0741-3335/57/1/014005.

[63] N. H. Crisp, K. Smith, and P. Hollingsworth. Launch and deployment of distributed small satellite systems. 114:65–78, 2015. doi:10.1016/j.actaastro.2015.04.015.

[64] D. Rafalskyi and A. Aanesland. Brief review on plasma propulsion with neutralizer-free systems. *Plasma Sources Science and Technology*, 25(4):043001, 2016. ISSN 13616595. doi:10.1088/0963-0252/25/4/043001.

[65] S. J. Doyle, A. R. Gibson, J. Flatt, T. S. Ho, R. W. Boswell, C. Charles, P. Tian, M. J. Kushner, and J. Dedrick. Spatio-temporal plasma heating mechanisms in a radio-frequency electrothermal microthruster. *Plasma Sources Science and Technology*, 27:085011, 2018. doi:10.1088/1361-6595/aad79a.

[66] T. S. Ho, C. Charles, and R. W. Boswell. Performance modelling of plasma microthruster nozzles in vacuum. *Journal of Applied Physics*, 123(17):173301, 2018. ISSN 0021-8979. doi:10.1063/1.5012765.

[67] E. H. Kim, H. D. Kim, and H. J. Kim. A Study on the collision avoidance maneuver optimization with multiple space debris. *Journal of Astronomy and Space Science*, 29(1):11–21, 2012. ISSN 20935587. doi:10.5140/JASS.2012.29.1.011.

[68] L. Hall. The History of Space Debris. In *Space Traffic Management Conference 19*, pages 1–10, 2014.

[69] L. Gremyachikh, D. Dubov, N. Kazeev, A. Kulibaba, A. Skuratov, A. Tereshkin, A. Ustyuzhanin, L. Shiryaeva, and S. Shishkin. Space Navigator: a Tool for the Optimization of Collision Avoidance Maneuvers. In *Advances in the Astronomical Sciences*, pages 1–14, 2019.

[70] C. Charles, R. W. Boswell, and K Takahashi. Investigation of radiofrequency plasma sources for space travel. *Plasma Physics and Controlled Fusion*, 54(12):124021, 2012. ISSN 0741-3335. doi:10.1088/0741-3335/54/12/124021.

[71] C. Charles and R. W. Boswell. Measurement and modelling of a radiofrequency micro-thruster. *Plasma Sources Science and Technology*, 21(2):022002, 2012. ISSN 0963-0252. doi:10.1088/0963-0252/21/2/022002.

[72] A. Greig, C. Charles, R. Hawkins, and R. Boswell. Direct measurement of neutral gas heating in a radio-frequency electrothermal plasma micro-thruster. *Applied Physics Letters*, 103(7):1–7, 2013. ISSN 00036951. doi:10.1063/1.4818657.

[73] A. Greig, C. Charles, N. Paulin, and R. W. Boswell. Volume and surface propellant heating in an electrothermal radio-frequency plasma micro-thruster. *Applied Physics Letters*, 105(5):054102, 2014. ISSN 0003-6951. doi:10.1063/1.4892656.

[74] A. Greig, C. Charles, and R. W. Boswell. Simulation of main plasma parameters of a cylindrical asymmetric capacitively coupled plasma micro-thruster using computational fluid dynamics. *Frontiers in Physics*, 2(January):1–9, 2015. ISSN 2296-424X. doi:10.3389/fphy.2014.00080.

[75] A. Greig, C. Charles, and R. W. Boswell. Neutral gas temperature estimates and metastable resonance energy transfer for argon-nitrogen discharges. *Physics of Plasmas*, 23(1), 2016. ISSN 10897674. doi:10.1063/1.4939028.

[76] T. S. Ho, C. Charles, and R. W. Boswell. A Comprehensive Cold Gas Performance Study of the Pocket Rocket Radiofrequency Electrothermal Microthruster. *Frontiers in Physics*, 4(January):1–16, 2017. ISSN 2296-424X. doi:10.3389/fphy.2016.00055.

[77] T. S. Ho. *Supersonic Constricted Plasma Flows*. PhD thesis, Australian National University, 2018.

[78] C. Charles, W. Liang, L. Raymond, J. Rivas-Davila, and R. W. Boswell. Vacuum Testing of a Miniaturized Switch Mode Amplifier Powering an Electrothermal Plasma Micro-Thruster. *Frontiers in Physics*, 5(August):1–8, 2017. ISSN 2296-424X. doi:10.3389/fphy.2017.00036.

[79] M. A. Lieberman and A. J. Lichtenberg. *Principles of Plasma Discharges and Materials Processing*. John Wiley & Sons, New Jersey, 2nd edition, 2005. ISBN 0-471-72001-1. doi:10.1017/CBO9781107415324.004.

[80] X. Chen and E. Pfender. Effect of the Knudsen number on heat transfer to a particle immersed into a thermal plasma. *Plasma Chemistry and Plasma Processing*, 3(1):97–113, 1983. ISSN 02724324. doi:10.1007/BF00566030.

[81] M. Shigeta and A. B. Murphy. Thermal plasmas for nanofabrication. *Journal of Applied Physics D*, 44:174025, 2011. doi:10.1088/0022-3727/44/17/174025.

[82] E. Pfender. Thermal Plasma Technology : Where Do We Stand and Where Are We Going? *Plasma Chemistry and Plasma Processing*, 19(1):1–31, 1999. doi:10.1023/A:1021899731587.

[83] C. Charles. Grand challenges in low-temperature plasma physics. *Frontiers in Physics*, 2(June):1–5, 2014. ISSN 2296-424X. doi:10.3389/fphy.2014.00039.

[84] S. Samukawa, M. Hori, S. Rauf, K. Tachibana, P. Bruggeman, G. Kroesen, J. C. Whitehead, A. B. Murphy, A. F. Gutsol, S. Starikovskaia, U. Kortshagen, J.-P. Boeuf, T. J. Sommerer, M. J. Kushner, U. Czarnetzki, and N. Mason. The 2012 Plasma Roadmap. *Journal of Physics D: Applied Physics*, 45 (25):253001, 2012. ISSN 0022-3727. doi:10.1088/0022-3727/45/25/253001.

[85] H. Conrads and M. Schmidt. Plasma generation and plasma. *Plasma Sources Science and Technology*, 9:441, 2000. doi:10.1088/0963-0252/9/4/301.

[86] J. K. Lee, O. V. Manuilenko, N. Yu. Babaeva, H. C. Kim, and J. W. Shon. Ion energy distribution control in single and dual frequency capacitive plasma sources. *Plasma Sources Science and Technology*, 14(1):89–97, 2005. ISSN 0963-0252. doi:10.1088/0963-0252/14/1/012.

[87] J. Schulze, E. Schüngel, U. Czarnetzki, and Z. Donko. Optimization of the electrical asymmetry effect in dual-frequency capacitively coupled radio frequency discharges: Experiment, simulation, and model. *Journal of Applied Physics*, 106(6):092005, 2009. ISSN 00218979. doi:10.1063/1.3223310.

[88] T. Lafleur and J.-P. Booth. Control of the ion flux and ion energy in CCP discharges using non-sinusoidal voltage waveforms. *Journal of Physics D: Applied Physics*, 45(39):395203, 2012. ISSN 0022-3727. doi:10.1088/0022-3727/45/39/395203.

[89] S. J. Doyle, A. R. Gibson, R. W. Boswell, C. Charles, and J. P. Dedrick. Control of electron, ion and neutral heating in a radio-frequency electrothermal microthruster via dual-frequency voltage waveforms. *Plasma Sources Science and Technology*, 28(3):035019, 2019. doi:10.1088/1361-6595/ab0984.

[90] W. Steckelmacher. Knudsen flow 75 years on: The current state of the art for flow of rarefied gases in tubes and systems. *Reports on Progress in Physics*, 49(10):1083–1107, 1986. ISSN 00344885. doi:10.1088/0034-4885/49/10/001.

[91] A. Schuetze, J. Y. Jeong, S. E. Babayan, J. Park, G. S. Selwyn, and R. F. Hicks. The Atmospheric-Pressure Plasma Jet : A Review and Comparison to Other Plasma Sources. *IEEE Transactions on Plasma Science*, 26(6):1685–1694, 1998. doi:10.1109/27.747887.

[92] H.-B. Valentini. Bohm criterion for the collisional sheath. *Physics of Plasmas*, 3(4):1459, 1996. ISSN 1070664X. doi:10.1063/1.871736.

[93] M. S. Benilov. The Child-Langmuir law and analytical theory of collisionless to collision-dominated sheaths. *Plasma Sources Science and Technology*, 18(1), 2009. ISSN 09630252. doi:10.1088/0963-0252/18/1/014005.

[94] A. Salabaş and R. P. Brinkmann. Non-neutral/quasi-neutral plasma edge definition for discharge models: A numerical example for dual frequency hydrogen capacitively coupled plasmas. *Japanese Journal of Applied Physics, Part 1: Regular Papers and Short Notes and Review Papers*, 45(6 A): 5203–5206, 2006. ISSN 00214922. doi:10.1143/JJAP.45.5203.

[95] J. Schulze, B. G. Heil, D. Luggenhölscher, R. P. Brinkmann, U. Czarnetzki, and D. Luggenh. Stochastic heating in asymmetric capacitively coupled RF discharges. *Journal of Physics D: Applied Physics*, 41 (19):195212, 2008. ISSN 0022-3727. doi:10.1088/0022-3727/41/19/195212.

[96] V. A. Godyak. Statistical heating of electrons at an oscillating plasma boundary. *Sov. Phys. -Tech. Phys.*, 16:1073, 1972.

[97] J. Schulze, Z. Donkó, D. Luggenhölscher, and U. Czarnetzki. Different modes of electron heating in dual-frequency capacitively coupled radio frequency discharges. *Plasma Sources Science and Technology*, 18: 034011, 2009. ISSN 0963-0252. doi:10.1088/0963-0252/18/3/034011.

[98] J. Schulze, A. Derzsi, K. Dittmann, T. Hemke, J. Meichsner, and Z. Donkó. Ionization by drift and ambipolar electric fields in electronegative capacitive radio frequency plasmas. *Physical Review Letters*, 107(27):1–5, 2011. ISSN 00319007. doi:10.1103/PhysRevLett.107.275001.

[99] M.A. Lieberman. Analytical solution for capacitive RF sheath. *IEEE Transactions on Plasma Science*, 16(6):638–644, 1988. ISSN 00933813. doi:10.1109/27.16552.

[100] K. H. Schoenbach, A. El-habachi, W. Shi, and M. Ciocca. High-pressure hollow cathode discharges. *Plasma Sources Science and Technology*, 6:468–477, 1997. doi:10.1088/0963-0252/6/4/003.

[101] A. V. Phelps and Z. Lj Petrović. Cold-cathode discharges and breakdown in argon: surface and gas phase production of secondary electrons. *Plasma Sources Science and Technology*, 8(3):R21–R44, 1999. ISSN 09630252. doi:10.1088/0963-0252/8/3/201.

[102] T. Lafleur, R. W. Boswell, and J.-P. Booth. Enhanced sheath heating in capacitively coupled discharges due to non-sinusoidal voltage waveforms. *Applied Physics Letters*, 100(19):194101, 2012. ISSN 00036951. doi:10.1063/1.4712128.

[103] S. J. Doyle, T. Lafleur, A. R. Gibson, P. Tian, M. J. Kushner, and J. Dedrick. Enhanced control of the ionization rate in radio-frequency plasmas with structured electrodes via tailored voltage waveforms. *Plasma Sources Science and Technology*, 26:125005, 2017. doi:10.1088/1361-6595/aa96e5.

[104] H. D. Hagstrum. Theory of auger ejection of electrons from metals by ions. *Physical Review*, 96(2): 336–365, 1954. ISSN 0031899X. doi:10.1103/PhysRev.96.336.

[105] A. Perret, P. Chabert, J. Jolly, and J. P. Booth. Ion energy uniformity in high-frequency capacitive discharges. *Applied Physics Letters*, 86(2):10–13, 2005. ISSN 00036951. doi:10.1063/1.1848183.

[106] A. Manenschijn, G. C.A.M. Janssen, E. Van Der Drift, and S. Radelaar. Measurement of ion impact energy and ion flux at the rf electrode of a parallel plate reactive ion etcher. *Journal of Applied Physics*, 69(3):1253–1262, 1991. ISSN 00218979. doi:10.1063/1.347311.

[107] S. B. Wang and A. E. Wendt. Control of ion energy distribution at substrates during plasma processing. *Journal of Applied Physics*, 88(2):643–646, 2000. ISSN 00218979. doi:10.1063/1.373715.

[108] D. O'Connell, R. Zorat, A. R. Ellingboe, and M. M. Turner. Comparison of measurements and particle-in-cell simulations of ion energy distribution functions in a capacitively coupled radio-frequency discharge. *Physics of Plasmas*, 14(10), 2007. ISSN 1070664X. doi:10.1063/1.2795634.

[109] M. Zeuner, H. Neumann, and J. Meichsner. Ion energy distributions in a dc biased rf discharge. *Journal of Applied Physics*, 81(7):2985–2994, 1997. ISSN 00218979. doi:10.1063/1.364331.

[110] E. Schüngel, S. Mohr, J. Schulze, U. Czarnetzki, and M. J. Kushner. Ion distribution functions at the electrodes of capacitively coupled high-pressure hydrogen discharges. *Plasma Sources Science and Technology*, 23(1):015001, 2013. ISSN 09630252. doi:10.1088/0963-0252/23/1/015001.

[111] M. J. Kushner. Distribution of ion energies incident on electrodes in capacitively coupled rf discharges. *Journal of Applied Physics*, 58(11):4024–4031, 1985. ISSN 00218979. doi:10.1063/1.335580.

[112] W. C. Chen, X. M. Zhu, S. Zhang, and Y. K. Pu. Reconstruction of ion energy distribution function in a capacitive rf discharge. *Applied Physics Letters*, 94(21):211503, 2009. ISSN 00036951. doi:10.1063/1.3147216.

[113] S. J. Doyle, A. R. Gibson, R. W. Boswell, C. Charles, and J. P. Dedrick. Inducing locally structured ion energy distributions in intermediate-pressure plasmas Inducing locally structured ion energy distributions in intermediate-pressure plasmas. *Physics of Plasmas*, 7(July):073519, 2019. doi:10.1063/1.5111401.

[114] G. J.M. Hagelaar and L. C. Pitchford. Solving the Boltzmann equation to obtain electron transport coefficients and rate coefficients for fluid models. *Plasma Sources Science and Technology*, 14(4):722–733, 2005. ISSN 09630252. doi:10.1088/0963-0252/14/4/011.

[115] C. M. O. Mahony, R. Al Wazzan, and W. G. Graham. Sheath dynamics observed in a 13.56 MHz-driven plasma. *Applied Physics Letters*, 71(5):608, 1997. ISSN 00036951. doi:10.1063/1.119808.

[116] L. Bárdoš. Radio frequency hollow cathodes for the plasma processing technology. *Surface and Coatings Technology*, 86-87(PART 2):648–656, 1996. ISSN 02578972. doi:10.1016/S0257-8972(96)03056-3.

[117] K. H. Schoenbach, R. Verhappen, T. Tessnow, F. E. Peterkin, and W. W. Byszewski. Microhollow cathode discharges. *Applied Physics Letters*, 13(1996):13, 1995. ISSN 00036951. doi:10.1063/1.116739.

[118] M. J. Kushner. Modeling of microdischarge devices: Pyramidal structures. *Journal of Applied Physics*, 95(3):846–859, 2004. ISSN 00218979. doi:10.1063/1.1636251.

[119] R. Mavrodineanu. Hollow Cathode Discharges - Analytical Applications. *Journal of Research of the National Bureau of Standards*, 89(2):143, 1984. ISSN 0160-1741. doi:10.6028/jres.089.009.

[120] C. Lazzaroni, P. Chabert, A. Rousseau, and N. Sadeghi. Sheath and electron density dynamics in the normal and self-pulsing regime of a micro hollow cathode discharge in argon gas. *European Physical Journal D*, 60(3):555–563, 2010. ISSN 14346060. doi:10.1140/epjd/e2010-00259-4.

[121] S. Dixon, C. Charles, R. W. Boswell, W. Cox, J. Holland, and R. Gottscho. Interactions between arrayed hollow cathodes. *Journal of Physics D: Applied Physics*, 46(14):145204, 2013. ISSN 0022-3727. doi:10.1088/0022-3727/46/14/145204.

[122] N. Schmidt, U. Czarnetzki, E. Schüngel, and J. Schulze. The effect of structured electrodes on heating and plasma uniformity in capacitive discharges. *Journal of Physics D: Applied Physics*, 46:505202, 2013. ISSN 0022-3727. doi:10.1088/0022-3727/46/50/505202.

[123] C. M. Horwitz. Hollow cathode etching and deposition. *Journal of Vacuum Science & Technology A: Vacuum, Surfaces, and Films*, 6(3):1837, 1988. doi:http://dx.doi.org/10.1116/1.575265.

[124] O. Taylan and H. Berberoglu. Dissociation of carbon dioxide using a microhollow cathode discharge plasma reactor: effects of applied voltage, flow rate and concentration. *Plasma Sources Science and Technology*, 24(1):015006, 2015. ISSN 0963-0252. doi:10.1088/0963-0252/24/1/015006.

[125] S. Takashima, M. Hori, T. Goto, A. Kono, M. Ito, and K. Yoneda. Vacuum ultraviolet absorption spectroscopy employing a microdiacharge hollow-cathode lamp for absolute density measurements of hydrogen atoms in reactive plasmas. *Applied Physics Letters*, 75(1999):3929, 1999. ISSN 00036951. doi:10.1063/1.125497.

[126] C. Charles, R. Hawkins, and R. W. Boswell. Particle in cell simulation of a radiofrequency plasma jet expanding in vacuum. *Applied Physics Letters*, 106(9):093502, 2015. ISSN 0003-6951. doi:10.1063/1.4914109.

[127] T. Lafleur and R. W. Boswell. Particle-in-cell simulations of hollow cathode enhanced capacitively coupled radio frequency discharges. *Physics of Plasmas*, 19(2), 2012. ISSN 1070664X. doi:10.1063/1.3685709.

[128] B. G. Heil, U. Czarnetzki, R. P. Brinkmann, and T. Mussenbrock. On the possibility of making a geometrically symmetric RF-CCP discharge electrically asymmetric. *Journal of Physics D: Applied Physics*, 41(16):165202, 2008. ISSN 0022-3727. doi:10.1088/0022-3727/41/16/165202.

[129] E. Schüngel, D. Eremin, J. Schulze, T. Mussenbrock, and U. Czarnetzki. The electrical asymmetry effect in geometrically asymmetric capacitive radio frequency plasmas. *Journal of Applied Physics*, 112 (5):053302, 2012. ISSN 00218979. doi:10.1063/1.4747914.

[130] H. H. Goto, M. Sasaki, T. Ohmi, T. Shibata, A. Yamagami, N. Okamura, and O. Kamiya. Related content Minimizing Wafer Surface Damage and Chamber Material Contamination in New Plasma Processing Equipment. *Japanese Journal of Applied Physics*, 29(12):2395–2397, 1990. doi:10.1143/JJAP.29.L2395.

[131] H. H. Goto, H.-D. Lowe, and T. Ohmi. Independent Control of Ion Density and Ion Bombardment Energy in a Dual RF Excitation Plasma. *IEEE Transactions on Semiconductor Manufacturing*, 6(1): 58–64, 1993. doi:10.1109/66.210658.

[132] P. C. Boyle, A. R. Ellingboe, and M. M. Turner. Independent control of ion current and ion impact energy onto electrodes in dual frequency plasma devices. *Journal of Physics D: Applied Physics*, 37: 697–701, 2004. ISSN 0022-3727. doi:10.1088/0022-3727/37/5/008.

[133] X.-M. Zhu, W.-C. Chen, S. Zhang, Z.G. Guo, D.-W. Hu, and Y.-K. Pu. Electron density and ion energy dependence on driving frequency in capacitively coupled argon plasmas. *Journal of Physics D: Applied Physics*, 40(22):7019–7023, 2007. ISSN 0022-3727. doi:10.1088/0022-3727/40/22/023.

[134] C. O'Neill, J. Waskoenig, and T. Gans. Tailoring electron energy distribution functions through energy confinement in dual radio-frequency driven atmospheric pressure plasmas. *Applied Physics Letters*, 101 (15):154107, 2012. ISSN 00036951. doi:10.1063/1.4758463.

[135] Y. Du and Y. Li. Plasma Density Distribution in Asymmetric Geometry Capacitive Coupled Plasma Discharge System. *World Academy of Science, Engineering and Technology*, 6(11):919–922, 2012.

[136] J. Schulze, E. Schüngel, Z. Donkó, and U. Czarnetzki. The electrical asymmetry effect in multi-frequency capacitively coupled radio frequency discharges. *Plasma Sources Science and Technology*, 20(1):015017, 2011. ISSN 09630252. doi:10.1088/0963-0252/20/1/015017.

[137] B. Bruneau, T. Gans, D. O'Connell, A. Greb, E. V. Johnson, and J.-P. Booth. Strong Ionization Asymmetry in a Geometrically Symmetric Radio Frequency Capacitively Coupled Plasma Induced by Sawtooth Voltage Waveforms. *Physical Review Letters*, 114(12):125002, 2015. ISSN 0031-9007. doi:10.1103/PhysRevLett.114.125002.

[138] T. Lafleur. Tailored-waveform excitation of capacitively coupled plasmas and the electrical asymmetry effect. *Plasma Sources Science and Technology*, 25(1):013001, 2016. ISSN 0963-0252. doi:10.1088/0963-0252/25/1/013001.

[139] T Lafleur, P Chabert, M M Turner, and J P Booth. Theory for the self-bias formation in capacitively coupled plasmas excited by arbitrary waveforms. *Plasma Sources Science and Technology*, 22(6):065013, 2013. ISSN 0963-0252. doi:10.1088/0963-0252/22/6/065013.

[140] J. Schulze, E. Schüngel, Z. Donkó, D. Luggenhölscher, and U. Czarnetzki. Phase resolved optical emission spectroscopy: a non-intrusive diagnostic to study electron dynamics in capacitive radio frequency discharges. *Journal of Physics D: Applied Physics*, 43(12):124016, 2010. ISSN 0022-3727. doi:10.1088/0022-3727/43/12/124016.

[141] A. Derzsi, T. Lafleur, J.-P. Booth, A. Derzsi, B. Bruneau, and A. R. Gibson. Power coupling mode transitions induced by tailored voltage waveforms in capacitive oxygen discharges. *Plasma Sources Science and Technology*, 26:034002, 2017. doi:10.1088/1361-6595/aa56d6.

[142] B. Bruneau, T. Lafleur, T. Gans, D. O'Connell, A. Greb, I. Korolov, A. Derzsi, Z. Donkó, S. Brandt, E. Schüngel, J. Schulze, P. Diomede, D. J. Economou, S. Longo, E. Johnson, and J.-P. Booth. Effect of gas properties on the dynamics of the electrical slope asymmetry effect in capacitive plasmas: comparison of Ar, H$_{2}$ and CF$_{4}$. *Plasma Sources Science and Technology*, 25(1):01LT02, 2016. ISSN 0963-0252. doi:10.1088/0963-0252/25/1/01LT02.

[143] J. Franek, S. Brandt, B. Berger, M. Liese, M. Barthel, E. Schüngel, and J. Schulze. Power supply and impedance matching to drive technological radio-frequency plasmas with customized voltage waveforms. *Review of Scientific Instruments*, 86(5), 2015. ISSN 10897623. doi:10.1063/1.4921399.

[144] B. Bruneau, T. Novikova, T. Lafleur, J.-P. Booth, and E. V. Johnson. Control and optimization of the slope asymmetry effect in tailored voltage waveforms for capacitively coupled plasmas. *Plasma Sources Science and Technology*, 24:015021, 2015. ISSN 0963-0252. doi:10.1088/0963-0252/24/1/015021.

[145] C. Charles, J. Dedrick, R. W. Boswell, D. O'Connell, and T. Gans. Nanosecond optical imaging spectroscopy of an electrothermal radiofrequency plasma thruster plume. *Applied Physics Letters*, 103 (12):124103, 2013. ISSN 00036951. doi:10.1063/1.4821738.

[146] T. S. Ho, C. Charles, and R. Boswell. Neutral gas heating and ion transport in a constricted plasma flow. *Physics of Plasmas*, 24(8):8–13, 2017. ISSN 10897674. doi:10.1063/1.4996014.

[147] T. Lafleur, P. A. Delattre, J. P. Booth, E. V. Johnson, and S. Dine. Radio frequency current-voltage probe for impedance and power measurements in multi-frequency unmatched loads. *Review of Scientific Instruments*, 84(1):015001, 2013. ISSN 00346748. doi:10.1063/1.4773540.

[148] V. A. Godyak and R. B. Piejak. Insitu simultaneous radio frequency discharge power measurements. *Journal of Vacuum Science & Technology A: Vacuum, Surfaces, and Films*, 8(5):3833–3837, 1990. ISSN 0734-2101. doi:10.1116/1.576457.

[149] D. Marinov and N. St J. Braithwaite. Power coupling and electrical characterization of a radio-frequency micro atmospheric pressure plasma jet. *Plasma Sources Science and Technology*, 23(6):3–9, 2014. ISSN 13616595. doi:10.1088/0963-0252/23/6/062005.

[150] T Gans, C C Lin, V Schulz-von der Gathen, and H F Döbele. Phase-resolved emission spectroscopy of a hydrogen rf discharge for the determination of quenching coefficients. *Phys. Rev. A*, 67:12707, 2003. ISSN 1050-2947. doi:10.1103/PhysRevA.67.012707.

[151] T. Gans, D. O'Connell, V. Schulz-von der Gathen, and J. Waskoenig. The challenge of revealing and tailoring the dynamics of radio-frequency plasmas. *Plasma Sources Science and Technology*, 19(3): 034010, 2010. ISSN 0963-0252. doi:10.1088/0963-0252/19/3/034010.

[152] J. E. Chilton, J. B. Boffard, R. S Schappe, and C. C. Lin. Measurement of electron-impact excitation into the 3p^{5}4p levels of argon using Fourier-transform spectroscopy. *Physical Review A*, 57(1): 267–277, 1998. ISSN 1050-2947. doi:10.1103/PhysRevA.57.267.

[153] K. Niemi, S. Reuter, L. M. Graham, J. Waskoenig, N. Knake, V. Schulz-Von Der Gathen, and T. Gans. Diagnostic based modelling of radio-frequency driven atmospheric pressure plasmas. *Journal of Physics D: Applied Physics*, 43(12):124006, 2010. ISSN 00223727. doi:10.1088/0022-3727/43/12/124006.

[154] S. Siepa and U. Czarnetzki. Line integration and spatial resolution in optical imaging of plasmas. *Journal of Physics D: Applied Physics*, 48:385201, 2015. doi:10.1088/0022-3727/48/38/385201.

[155] R. H. Huddlestone and S. L. Leonard. *Plasma Diagnostic Techniques.pdf*. Academic Press, New York, 1965.

[156] A. Anders. *A Formulary for Plasma Physics*. Akademie-Verlag, Berlin, 1990. ISBN 3055012631.

[157] D. Vender and R. Boswell. Numerical modeling of low-pressure RF plasmas. *Trans. Plasma Sci.*, 18 (4), 1990.

[158] V. Vahedi, G. DiPeso, C. K. Birdsall, T. D. Rognlien, and M. A. Lieberman. Capacitive RF discharges modelled by particle-in-cell Monte Carlo simulation. I. Analysis of numerical techniques. *Plasma Sources Science and Technology*, 2(4):261–272, 1993. ISSN 0963-0252. doi:10.1088/0963-0252/2/4/006.

[159] A. Sun, M. M. Becker, and D. Loffhagen. PIC/MCC simulation of capacitively coupled discharges: Effect of particle management and integration. *Computer Physics Communications*, 206:35–44, 2016. ISSN 00104655. doi:10.1016/j.cpc.2016.05.003.

[160] A. R. Gibson, Z. Donkó, L. Alelyani, L. Bischoff, G. Hübner, J. Bredin, S. J. Doyle, I. Korolov, K. Niemi, T. Mussenbrock, P. Hartmann, J. P. Dedrick, J. Schulze, T. Gans, and D. O. Connell. Disrupting the spatio-temporal symmetry of the electron dynamics in atmospheric pressure plasmas by voltage waveform tailoring. 28:01LT01, 2019. doi:10.1088/1361-6595/aaf535.

[161] J. Van Dijk, G. M. W. Kroesen, and A. Bogaerts. Plasma modelling and numerical simulation. *Journal of Physics D: Applied Physics*, 42(19), 2009. ISSN 00223727. doi:10.1088/0022-3727/42/19/190301.

[162] A. Greb, K. Niemi, D. O'Connell, G. J. Ennis, N. Macgearailt, and T. Gans. Improved fluid simulations of radio-frequency plasmas using energy dependent ion mobilities. *Physics of Plasmas*, 20(5), 2013. ISSN 1070664X. doi:10.1063/1.4804280.

[163] L. L. Alves and L. Marques. Fluid modelling of capacitively coupled radio-frequency discharges: A review. *Plasma Physics and Controlled Fusion*, 54(12), 2012. ISSN 07413335. doi:10.1088/0741-3335/54/12/124012.

[164] G. Chen and L. L. Raja. Fluid modeling of electron heating in low-pressure, high-frequency capacitively coupled plasma discharges. *Journal of Applied Physics*, 96(11):6073–6081, 2004. ISSN 00218979. doi:10.1063/1.1818354.

[165] M. J. Kushner. Hybrid modelling of low temperature plasmas for fundamental investigations and equipment design. *Journal of Physics D: Applied Physics*, 42(19):194013, 2009. ISSN 0022-3727. doi:10.1088/0022-3727/42/19/194013.

[166] S. W. Hwang and H. J. Lee. Effect of electron Monte Carlo collisions on a hybrid simulation of a low-pressure capacitively coupled plasma. *Plasma Sources Science and Technology*, 23(6), 2014. ISSN 13616595. doi:10.1088/0963-0252/23/6/065040.

[167] S.-H. Song and M. J. Kushner. Control of electron energy distributions and plasma characteristics of dual frequency, pulsed capacitively coupled plasmas sustained in Ar and Ar/CF4/O2. *Plasma Sources Science and Technology*, 21(5):55028, 2012. ISSN 0734-2101. doi:10.1088/0963-0252/21/5/055028.

[168] A. R. Gibson, A. Greb, W. G. Graham, and T. Gans. Tailoring the nonlinear frequency coupling between odd harmonics for the optimisation of charged particle dynamics in capacitively coupled oxygen plasmas. *Applied Physics Letters*, 106(5):054102, 2015. ISSN 00036951. doi:10.1063/1.4907567.

[169] D. L. Scharfetter and H. K. Gummel. Large-Signal Analysis of a Silicon Read Diode Oscillator. *IEEE Transactions on Electron Devices*, 16(1):64–77, 1969. ISSN 15579646. doi:10.1109/T-ED.1969.16566.

[170] P. Tian and M. J. Kushner. Controlling VUV photon fluxes in low-pressure inductively coupled plasmas. *Plasma Sources Science and Technology*, 24:34017, 2015. ISSN 0963-0252. doi:10.1088/0963-0252/24/3/034017.

[171] M. Hayashi. Report No. IPPJ-AM-19. Technical report, Nagoya Institute of Technology, 1991.

[172] K. Tachibana. Excitation of the $1s_5$, $1s_4$, $1s_3$ and $1s_2$ levels of argon by low-energy electrons. *Physical Review A*, 34(2):451, 1986. doi:10.1103/PhysRevA.34.1007.

[173] D. Rapp and P. Englander-Golden. Total Cross Sections for Ionization and Attachment in Gases by Electron Impact. I. Positive Ionization. *The Journal of Chemical Physics*, 43(5):1464–1479, 1965. ISSN 0021-9606. doi:10.1063/1.1696957.

[174] N. A. Dyatko, Y. Z. Ionikh, I. V. Kochetov, D. L. Marinov, A. V. Meshchanov, A. P. Napartovich, F. B. Petrov, and S. A. Starostin. Experimental and theoretical study of the transition between diffuse and contracted. *J. Phys. D: Appl. Phys*, 41:055204, 2008. doi:10.1088/0022-3727/41/5/055204.

[175] A. Bogaerts, R. G. V. Serikov, and V. V. Serikov. Calculation of gas heating in direct current argon glow discharges. *Journal of Applied Physics*, 87:8334, 1999. doi:10.1063/1.373545.

[176] M. A. Furman and M. T. F. Pivi. Probabilistic model for the simulation of secondary electron emission. *Physical Review Special Topics - Accelerators and Beams*, 5(12):82–99, 2002. ISSN 10984402. doi:10.1103/PhysRevSTAB.5.124404.

[177] A. Marcak, C. Corbella, T. De los Arcos, and A. Von keudell. Ion-induced secondary electron emission from oxidized metal surfaces measured in a particle beam reactor. *Review of Scientific Instruments*, 86 (10):106102, 2015. ISSN 10897623. doi:10.1063/1.4932309.

[178] M. Nikolić, J. Newton, C. I. Sukenik, L. Vušković, and S. Popović. Measurements of population densities of metastable and resonant levels of argon using laser induced fluorescence. *Journal of Applied Physics*, 117(2):023304, 2015. ISSN 10897550. doi:10.1063/1.4905611.

[179] H. W. Ellis, R. Y. Pai, E. W. McDaniel, E. A. Mason, and L. A. Viehland. Transport Properties of Gaseous Ions Over a Wide Energy Range. *Atomic Data and Nuclear Data Tables*, 17(3):177–210, 1976. doi:10.1016/0092-640X(76)90001-2.

[180] Precision ceramics alumina datasheet. *https://www.precision-ceramics.co.uk*, 2017. URL `https://www.precision-ceramics.co.uk/wp-content/uploads/2016/04/CeramAlox-Downloadable-Data-Sheet.pdf`.

[181] Precision ceramics macor datasheet. *https://www.precision-ceramics.co.uk*, 2017. URL `https://www.precision-ceramics.co.uk/wp-content/uploads/2016/04/macor-brochure-english.pdf`.

[182] A. Fruchtman, G. Makrinich, P. Chabert, and J. M. Rax. Enhanced plasma transport due to neutral depletion. *Physical Review Letters*, 95(11):1–4, 2005. ISSN 00319007. doi:10.1103/PhysRevLett.95.115002.

[183] J. L. Raimbault, L. Liard, J. M. Rax, P. Chabert, A. Fruchtman, and G. Makrinich. Steady-state isothermal bounded plasma with neutral dynamics. *Physics of Plasmas*, 14(1):013503, 2007. ISSN 1070664X. doi:10.1063/1.2424558.

[184] L. Liard, J. L. Raimbault, J. M. Rax, and P. Chabert. Plasma transport under neutral gas depletion conditions. *Journal of Physics D: Applied Physics*, 40(17):5192–5195, 2007. ISSN 00223727. doi:10.1088/0022-3727/40/17/026.

[185] A. Fruchtman. Energizing and depletion of neutrals by a collisional plasma. *Plasma Sources Science and Technology*, 17(2):024016, 2008. ISSN 09630252. doi:10.1088/0963-0252/17/2/024016.

[186] P. A. Thompson. *Compressible Fluid Dynamics*. McGraw-Hill, New York, 2nd edition, 1994. ISBN 9780070644052.

[187] L. Wu. A slip model for rarefied gas flows at arbitrary Knudsen number. *Applied Physics Letters*, 93 (25):2006–2009, 2008. ISSN 00036951. doi:10.1063/1.3052923.

[188] H. Yamaguchi, K. Kanazawa, Y. Matsuda, T. Niimi, A. Polikarpov, and I. Graur. Investigation on heat transfer between two coaxial cylinders for measurement of thermal accommodation coefficient. *Physics of Fluids*, 24(6):062002, 2012. ISSN 10706631. doi:10.1063/1.4726059.

[189] A. R. Gibson, M. Foucher, D. Marinov, P. Chabert, T. Gans, M. J. Kushner, and J.-P. Booth. The role of thermal energy accommodation and atomic recombination probabilities in low pressure oxygen plasmas. *Plasma Physics and Controlled Fusion*, 59:024004, 2017. doi:10.1088/1361-6587/59/2/024004.

[190] A. J. Lofthouse, L. C. Scalabrin, and I. D. Boyd. Velocity Slip and Temperature Jump in Hypersonic Aerothermodynamics. *Journal of Thermophysics and Heat Transfer*, 22(1):38–49, 2008. ISSN 0887-8722. doi:10.2514/1.31280.

[191] W. M. Trott, J. N. Castaeda, J. R. Torczynski, M. A. Gallis, and D. J. Rader. An experimental assembly for precise measurement of thermal accommodation coefficients. *Review of Scientific Instruments*, 82 (3):035120, 2011. ISSN 00346748. doi:10.1063/1.3571269.

[192] S. Dixon, J. Dedrick, C. Charles, T. Gans, D. O Connell, and R. Boswell. Phase Resolved Imaging of a Repetitive Extrusion of Hydrogen Plasma From a Hollow Cathode Source. *IEEE Transactions of Plasma Science*, 16(9):1–2, 2014.

[193] M. Daksha, A. Derzsi, S. Wilczek, J. Trieschmann, T. Mussenbrock, P. Awakowicz, Z. Donkó, and J. Schulze. The effect of realistic heavy particle induced secondary electron emission coef fi cients on the electron power absorption dynamics in single- and dual-frequency capacitively coupled plasmas. *Plasma Sources Science and Technology*, 26:085006, 2017. doi:10.1088/1361-6595/aa7c88.

[194] A. Derzsi, I. Korolov, E. Schüngel, Z. Donkó, and J. Schulze. Effects of fast atoms and energy-dependent secondary electron emission yields in PIC/MCC simulations of capacitively coupled plasmas. *Plasma Sources Science and Technology*, 24(3):034002, 2015. ISSN 13616595. doi:10.1088/0963-0252/24/3/034002.

[195] J. Schulze, E. Schüngel, Z. Donkó, and U. Czarnetzki. Charge dynamics in capacitively coupled radio frequency discharges. *Journal of Physics D: Applied Physics*, 43:225201, 2010. ISSN 0022-3727. doi:10.1088/0022-3727/43/22/225201.

[196] T. Lafleur, P. Chabert, and J.-P. Booth. Secondary electron induced asymmetry in capacitively coupled plasmas. *Journal of Physics D: Applied Physics*, 46(13):135201, 2013. ISSN 0022-3727. doi:10.1088/0022-3727/46/13/135201.

[197] K. R. Williams, K. Gupta, and M. Wasilik. Etch Rates for Micromachining Processing II. *Journal of Microelectromechanical systems*, 12(6):761–777, 2003. ISSN 1098-6596. doi:10.1017/CBO9781107415324.004.

[198] J. Schulze, Z. Donkó, T. Lafleur, S. Wilczek, and R. P. Brinkmann. Spatio-temporal analysis of the electron power absorption in electropositive capacitive RF plasmas based on moments of the Boltzmann equation. *Plasma Sources Science and Technology*, 27(5):055010, 2018. ISSN 13616595. doi:10.1088/1361-6595/aabebc.

[199] A. V. Phelps. The application of scattering cross sections to ion flux models in discharge sheaths. *Journal of Applied Physics*, 76(2):747–753, 1994. ISSN 00218979. doi:10.1063/1.357820.

[200] C. Wild and P. Koidl. Structured ion energy distribution in radio frequency glow-discharge systems. *Applied Physics Letters*, 54(6):505–507, 1989. ISSN 00036951. doi:10.1063/1.100913.

[201] J. Liu, G. L. Huppert, and H. H. Sawin. Ion bombardment in rf plasmas. *Journal of Applied Physics*, 68(8):3916–3934, 1990. ISSN 00218979. doi:10.1063/1.346278.

[202] C. Wild and P. Koidl. Ion and electron dynamics in the sheath of radio-frequency glow discharges. *Journal of Applied Physics*, 69(5):2909–2922, 1991. ISSN 00218979. doi:10.1063/1.348601.

[203] S. Sharma, A. Sen, N. Sirse, M. M. Turner, and A. R. Ellingboe. Plasma density and ion energy control via driving frequency and applied voltage in a collisionless capacitively coupled plasma discharge. *Physics of Plasmas*, 25(8):080705, 2018. ISSN 1070-664X. doi:10.1063/1.5045816.

[204] J. T. Gudmundsson, D. I. Snorrason, and H. Hannesdottir. The effect of pressure and driving frequency on electron heating in a capacitively coupled oxygen discharge. *Plasma Source Sciences and Technologies*, 27:025009, 2018.

[205] I. Korolov, A. Derzsi, and J. Schulze. Asymmetry effect in capacitively coupled plasmas The influence of the secondary electron induced asymmetry on the electrical asymmetry effect in capacitively coupled plasmas. *Applied Physics Letters*, 064102(2013):1–5, 2014. doi:10.1063/1.4817920.

[206] I. Korolov, A. Derzi, Z. Donkó, E. Schüngel, and J. Schulze. The influence of electron reflection / sticking coefficients at the electrodes on plasma parameters in particle-in-cell simulations of capacitive radio-frequency plasmas. *Plasma Sources Science and Technology*, 25:015024, 2016. doi:10.1088/0963-0252/25/1/015024.

[207] D. O'Connell, T. Gans, E. Semmler, and P. Awakowicz. The role of the relative voltage and phase for frequency coupling in a dual-frequency capacitively coupled plasma. *Applied Physics Letters*, 93(8): 2006–2009, 2008. ISSN 00036951. doi:10.1063/1.2972117.

[208] Z. Donkó, J. Schulze, B. G. Heil, and U. Czarnetzki. PIC simulations of the separate control of ion flux and energy in CCRF discharges via the electrical asymmetry effect. *Journal of Physics D: Applied Physics*, 42(2):025205, 2009. ISSN 0022-3727. doi:10.1088/0022-3727/42/2/025205.

[209] Y. Zhang, M. J. Kushner, N. Moore, P. Pribyl, and W. Gekelman. Space and phase resolved ion energy and angular distributions in single- and dual-frequency capacitively coupled plasmas. *Journal of Vacuum Science & Technology A: Vacuum, Surfaces, and Films*, 31(6):061311, 2013. ISSN 0734-2101. doi:10.1116/1.4822100.

[210] T Gans, J Schulze, D O'Connell, U Czarnetzki, R Faulkner, A R Ellingboe, and M M Turner. Frequency coupling in dual frequency capacitively coupled radio-frequency plasmas. *Applied Physics Letters*, 89 (26):13–16, 2006. ISSN 00036951. doi:10.1063/1.2425044.

[211] S. Brandt, B. Berger, E. Schüngel, I. Korolov, A. Derzsi, B. Bruneau, E. Johnson, T. Lafleur, D. O'Connell, M. Koepke, T. Gans, J. P. Booth, Z. Donkó, and J. Schulze. Electron power absorption dynamics in capacitive radio frequency discharges driven by tailored voltage waveforms in CF4. *Plasma Sources Science and Technology*, 25(4):45015, 2016. ISSN 13616595. doi:10.1088/0963-0252/25/4/045015.

[212] Y. Zhang, A. Zafar, D. J. Coumou, S. C. Shannon, and M. J. Kushner. Control of ion energy distributions using phase shifting in multi-frequency capacitively coupled plasmas. *Journal of Applied Physics*, 117(23):1–15, 2015. ISSN 10897550. doi:10.1063/1.4922631.

[213] E. Schüngel, J. Schulze, Z. Donkó, and U. Czarnetzki. Power absorption in electrically asymmetric dual frequency capacitive radio frequency discharges. *Physics of Plasmas*, 18(1):013503, 2011. ISSN 1070664X. doi:10.1063/1.3535542.

[214] A.R. Gibson and T. Gans. Controlling plasma properties under differing degrees of electronegativity using odd harmonic dual frequency excitation. *Plasma Sources Science and Technology*, 26(11):115007, 2017. ISSN 13616595. doi:10.1088/1361-6595/aa8dcd.

Chapter 8

Appendices

8.1 Appendix A: CUSTOM RFVOLT USER(M) Subroutine

Additions were made to the CUSTOM RFVOLT USER(M) subroutine in HPEM to enable the application of tailored voltage waveforms to material surfaces within the numerical model. The following comprises the verbatim additions to the CUSTOM RFVOLT USER(M) subroutine:

```
C*********************************************************************
C
C*********************************************************************
C    AUTHOR: SCOTT J DOYLE, LAST CHANGE: 22/02/2019
C    PERFORMS CONSTRUCTIVE ADDITION OF PREDEFINED WAVEFORMS FOR N HARMONICS
C    SHAPE DEFINED BY ICUSTOM NUMBER, AMP BY VRFM, BASE FREQUENCY BY FREQM
C    ALSO ALLOWS FOR PULSED OPERATION THROUGH REDUCED DUTY CYCLE
C
C    INITIATE ANY REQUIRED ARRAYS OR VARIABLES
    ALLOCATE( WAVEFORM_ARRAY(1000) )    #NUM.GT.(IMOVIE_FRAMES*2)
    ALLOCATE( VCUSTOM_ARRAY(5) )        #NUMBER OF HARMONICS
    IHARMONICS(IMATERIALDIM)            #ADDED IN COMMON FOR icp.f
VRFM_ON=1.0
DTNORMAL=0.0
NORMALIZE=0.0
HARMONICS=5

C   QUICK AND DIRTY FACTORIAL OF HARMONICS, NEED GAMMA FUNCTION TO WORK!
HARMONICSBANG=1
DO i=1,HARMONICS
HARMONICSBANG = HARMONICSBANG*i
END DO
HARMONICSBANG = real(HARMONICSBANG)
```

```
C
C   CCCCCCCCCCCCCCCCCCCCCC
C   CCCCCCCCCCCCCCCCCCCCCC
C
C   DEFINE IF PULSE POWER IS ON OR OFF, GENERATES INT COEFFICIENT FOR WAVEFORMS
IF (ICUSTOM(IMET0).EQ.-10) THEN
ICYCLE=INT((DTACTUAL+TUP)/TCYCLE_CUSTOM(IMET0))
TIME_LEFT=(DTACTUAL+TUP)-TCYCLE_CUSTOM(IMET0)*DFLOAT(ICYCLE)
FRAC_CYCLE=TIME_LEFT/TCYCLE_CUSTOM(IMET0)
C       VRFM_ON FOR FRACTION OF PULSE FREQUENCY LESS THAN DUTY CYCLE
IF (FRAC_CYCLE.LE.DUTY_CYCLE_CUSTOM(IMET0)) THEN
VRFM_ON=1.0
C       FORCE VRFM_ON FOR FINAL ITERATION FOR CORRECT AVERAGING
ELSE IF (ITERATION.EQ.(ITERATIONS)) THEN
VRFM_ON=1.0
ELSE
VRFM_ON=0.0
END IF
C       DEFAULT SINE WAVEFORM WITH DUTY CYCLE IF (ICUSTOM.GT.-10)
VCUSTOM(IMET0)=DSIN((DTACTUAL+TUP)*DBLE(FREQM(IMET0)*PI2))
VCUSTOM(IMET0)=VCUSTOM(IMET0)*VRFM(IMET0)*VRFM_ON
C       write(*,*) FRAC_CYCLE, VCUSTOM(IMET0)
END IF
C
C
C   CCCCCCCCCCCCCCCCCCCCCC
C   CCCCCCCCCCCCCCCCCCCCCC
C
C   CUSTOM WAVEFORM APPLIED IF REQUESTED
IF (ICUSTOM(IMET0).LE.-10) THEN
C
C OBTAIN PHASE OFFSET FOR REQUESTED WAVEFORM SHAPE, WHERE:
C [-11,FALLING-SAWTOOTH],[-12,RISING-SAWTOOTH]
C [-13,PEAK],[-14,VALLEY],
C [-15,FALLING-NSPULSE],[-16,RISING-NSPULSE],FLAT INTERMEDIATE
C [-17,FALLING-SAW-NSPULSE],[-18,RISING-SAW-NSPULSE] EQUAL PARITY INTERMEDIATE
IF (ICUSTOM(IMET0).EQ.-11) THEN
PHASEOFFSET = DBLE(PI)
ELSE IF (ICUSTOM(IMET0).EQ.-12) THEN
PHASEOFFSET = 0
ELSE IF (ICUSTOM(IMET0).EQ.-13) THEN
PHASEOFFSET = DBLE(PI)/2
ELSE IF (ICUSTOM(IMET0).EQ.-14) THEN
```

```
PHASEOFFSET = 3*DBLE(PI)/2
ELSE IF ((ICUSTOM(IMET0).EQ.-15).OR.(ICUSTOM(IMET0).EQ.-17)) THEN
PHASEOFFSET = 0
ELSE IF ((ICUSTOM(IMET0).EQ.-16).OR.(ICUSTOM(IMET0).EQ.-18)) THEN
PHASEOFFSET = DBLE(PI)
ELSE
PHASEOFFSET = 0
ENDIF
C
C   CCCCCCCCCCCCCCCCCCCCCC
C   CCCCCCCCCCCCCCCCCCCCCC
C
C       IF NO NORMALIZATION FACTOR SET, GENERATE FULL WAVEFORM AND OBTAIN ONE
IF (NORMALIZE.EQ.0.0) THEN
C           GENERATE WAVEFORM OVER DTNORMAL, PRESERVING DTACTUAL
DTNORMAL = DTACTUAL
C
DO i=1,1000
DTNORMAL = DTNORMAL+DBLE(0.001)
C
C               CALCULATE VOLTAGE OF EACH HARMONIC COMPONENT SEPERATELY
DO j=1,HARMONICS
VCUSTOM_ARRAY(j)=
     +                DSIN((DTNORMAL+TUP)*
     +                DBLE(j*FREQM(IMET0)*PI2)+PHASEOFFSET)
ENDDO
C
C               CONSTRUCT NORMALIZED SAWTOOTH WAVEFORMS
IF ((ICUSTOM(IMET0).EQ.-11).OR.(ICUSTOM(IMET0).EQ.-12)) THEN
VCUSTOM(IMET0)=0.0
DO j=1,HARMONICS
VCUSTOM(IMET0) = VCUSTOM(IMET0)+(VCUSTOM_ARRAY(j)/real(j))
ENDDO
C
C               CONSTRUCT NORMALZIED PEAK OR VALLEY WAVEFORMS
ELSE IF ((ICUSTOM(IMET0).EQ.-13).OR.(ICUSTOM(IMET0).EQ.-14)) THEN
VCUSTOM(IMET0)=0.0
DO j=1,HARMONICS
VCUSTOM(IMET0) = VCUSTOM(IMET0)+VCUSTOM_ARRAY(j)
ENDDO
C
C               CONSTRUCT NORMALIZED FLAT NSPULSE WAVEFORMS
ELSE IF ((ICUSTOM(IMET0).EQ.-15).OR.(ICUSTOM(IMET0).EQ.-16)) THEN
```

```
C                   HARMONICSBANG = FACTORIAL(HARMONICS)
VCUSTOM(IMET0)=0.0
DO j=1,HARMONICS
VCUSTOM(IMET0)=
     +                    VCUSTOM(IMET0)+
     +                    (j*(VCUSTOM_ARRAY(j)/HARMONICSBANG))
ENDDO
C
C               CONSTRUCT NORMALIZED SAME PARITY SAW-NSPULSE WAVEFORMS
ELSE IF ((ICUSTOM(IMET0).EQ.-17).OR.(ICUSTOM(IMET0).EQ.-18)) THEN
VCUSTOM(IMET0)=0.0
DO j=1,HARMONICS
FLIPFLOP=((-1)**j)
VCUSTOM(IMET0) = VCUSTOM(IMET0)+(FLIPFLOP*VCUSTOM_ARRAY(j))
ENDDO
ENDIF
C               SAVE FULL WAVEFORM TO ARRAY FOR PROCESSING
WAVEFORM_ARRAY(i) = VCUSTOM(IMET0)
ENDDO
C
C           UPDATE AND RETURN NORMALIZATION FACTOR
NORMALIZE=(MAXVAL(WAVEFORM_ARRAY)+ABS(MINVAL(WAVEFORM_ARRAY)))/2
ENDIF
C
C       CCCCCCCCCCCCCCCCCCCCCC
C       CCCCCCCCCCCCCCCCCCCCCC
C
C       CALCULATE VOLTAGE OF EACH REQUIRED HARMONIC COMPONENT SEPERATELY
DO j=1,HARMONICS
VCUSTOM_ARRAY(j)=
     +        DSIN((DTACTUAL+TUP)*
     +        DBLE(j*FREQM(IMET0)*DBLE(PI2))+PHASEOFFSET)
END DO
C
C       CONSTRUCT SAWTOOTH WAVEFORMS AND STRETCH BY REQUIRED VRFM(IMET0)
IF ((ICUSTOM(IMET0).EQ.-11).OR.(ICUSTOM(IMET0).EQ.-12)) THEN
VCUSTOM(IMET0)=0.0
DO j=1,HARMONICS
VCUSTOM(IMET0) = VCUSTOM(IMET0)+(VCUSTOM_ARRAY(j)/real(j))
END DO
VCUSTOM(IMET0)=(VCUSTOM(IMET0)/NORMALIZE)*VRFM(IMET0)*VRFM_ON
C
C       CONSTRUCT PEAK OR VALLEY WAVEFORMS AND STRETCH BY REQUIRED VRFM(IMET0)
```

```
ELSE IF ((ICUSTOM(IMET0).EQ.-13).OR.(ICUSTOM(IMET0).EQ.-14)) THEN
VCUSTOM(IMET0)=0.0
DO j=1,HARMONICS
VCUSTOM(IMET0) = VCUSTOM(IMET0)+VCUSTOM_ARRAY(j)
END DO
VCUSTOM(IMET0)=(VCUSTOM(IMET0)/NORMALIZE)*VRFM(IMET0)*VRFM_ON
C
C       CONSTRUCT FLAT NSPULSE WAVEFORMS AND STRETCH BY REQUIRED VRFM(IMET0)
ELSE IF ((ICUSTOM(IMET0).EQ.-15).OR.(ICUSTOM(IMET0).EQ.-16)) THEN
C           HARMONICSBANG = FACTORIAL(HARMONICS)
VCUSTOM(IMET0)=0.0
DO j=1,HARMONICS
VCUSTOM(IMET0) = VCUSTOM(IMET0)+(j*(VCUSTOM_ARRAY(j)/HARMONICSBANG))
END DO
VCUSTOM(IMET0)=(VCUSTOM(IMET0)/NORMALIZE)*VRFM(IMET0)*VRFM_ON
C
C       CONSTRUCT SAME PARITY SAW-NSPULSE WAVEFORMS AND STRETCH BY REQUIRED VRFM(IMET0)
ELSE IF ((ICUSTOM(IMET0).EQ.-17).OR.(ICUSTOM(IMET0).EQ.-18)) THEN
VCUSTOM(IMET0)=0.0
DO j=1,HARMONICS
FLIPFLOP=((-1)**j)
VCUSTOM(IMET0) = VCUSTOM(IMET0)+(FLIPFLOP*VCUSTOM_ARRAY(j))
END DO
VCUSTOM(IMET0)=(VCUSTOM(IMET0)/NORMALIZE)*VRFM(IMET0)*VRFM_ON
END IF
END IF
C
C   CCCCCCCCCCCCCCCCCCCCCC
C   CCCCCCCCCCCCCCCCCCCCCC
C
RETURN
END
C
```